



Modelling and Prediction of Breast Cancer Treatment Response

Improved Drug Induced Mechanically Coupled Reaction Diffusion model to predict tumour response for HER2+ patients

Diede Room

Modelling and Prediction of Breast Cancer Treatment Response

Improved Drug Induced Mechanically Coupled
Reaction Diffusion model to predict tumour
response for HER2+ patients

by

Diede Room

to obtain the degree of Master of Science,
in Computational Science and Engineering,
at the Delft University of Technology,
to be defended publicly on Friday October 4th, 2024 at 14:00.

Project duration:	December 11, 2023 – October 4, 2024
Supervisors:	Dr. Ir. M.B. van Gijzen, TU Delft Dr. Ir. E.G. Rens, TU Delft Dr. A. Jager, Erasmus MC Dr. J.F. Veenland, Erasmus MC
Thesis Committee:	Dr. M.E. Kootte TU Delft

Preface

This thesis marks the end of my Master of Applied Mathematics at Delft University of Technology, a milestone that feels surreal. From the very beginning of my bachelor's, I always wanted to apply mathematics in a meaningful way, ideally creating a societal impact, with a strong preference for the medical field. When Martin van Gijzen introduced me to several medical topics for my master's thesis, this project immediately stood out. It felt as a valuable opportunity to work with real patient data to model breast cancer treatment response and to collaborate with both an oncologist and a radiologist. I would like to thank the Erasmus Medical Centre, Martin van Gijzen, and Agnes Jager for making this project possible.

This master's thesis would not have been achievable without the support of my great team of supervisors. First, I would like to thank Lisanne Rens and Martin van Gijzen, my supervisors from Delft, for our weekly meetings. These sessions provided a platform to present and discuss my findings, which greatly improved my results and helped me manage setbacks with perspective. I also appreciated the informal conversations, motivational quotes and parenting wisdom from Martin, as well as Lisanne's support and quick reviewing in the last weeks. Second, I would like to thank Jifke Veenland, whose expertise in biomedical imaging was essential to the image processing aspects of this research. I am grateful for all our meetings, your patience in answering my numerous questions, and the extra resources you provided, such as slides and tutorials, which helped me read in into the field of biomedical imaging and gain a deeper understanding of it. Third, I would like to thank Agnes Jager, oncologist, for offering medical insights that we, as mathematicians, might otherwise overlook. Your efforts to expand the dataset were invaluable to this project. I am also grateful for the opportunity to sit in on breast cancer patient consultations, which provided me with a unique and valuable perspective.

In addition, I would like to thank radiologist Cecile de Monyé, who significantly contributed to my research by segmenting the patients' tumours. I really enjoyed our sessions, where I had the opportunity to ask many questions about breast cancer and other medical specifics during the segmenting of the scans. Finally, I want to express my thanks to my friends, roommates, and family for their support—whether it was proofreading, providing ICT assistance for the EMC cluster, or simply keeping me motivated throughout this journey.

*Diede Room
Delft, September 2024*

Abstract

HER2+ breast cancer patients, as observed by oncologist Agnes Jager from Erasmus Medical Centre (EMC), often achieve radiologic complete response (rCR) earlier than expected under standard treatments. To address this, Jager has partnered with Delft University of Technology to develop a computational model aimed at personalizing treatment schedules, potentially reducing chemotherapy cycles and minimizing side effects.

Building on previous MSc theses by Nathalie Oudhof, Eva Slingerland, and Rutger Engelberts, this thesis aims to improve the predictive capability of the Drug-Induced Mechanically Coupled Reaction-Diffusion (DI-MRCD) model and test its performance on a larger dataset consisting of 13 patients. The DI-MRCD model combines dynamic contrast-enhanced (DCE) and diffusion-weighted imaging (DWI) magnetic resonance imaging (MRI) data with patient-specific parameters to simulate the reaction of breast cancer tumours on chemotherapy. Key improvements include optimizing and generalizing the pre-processing pipeline for a larger patient cohort and enhancing input reliability by independently computing apparent diffusion coefficients (ADC).

Further refinements to the DI-MRCD model include updates to chemotherapy and shear modulus parameters, switching to a Trust Region Reflective (TRF) optimization method, and introducing a tissue-specific proliferation rate and natural cell death term. Despite these enhancements providing more insight, control, and making the model biologically more realistic, the model struggled to converge, highlighting the challenge of fitting patient-specific parameters with limited data points.

Future improvements could include resolving the convergence issues, incorporating additional calibration parameters, allowing the proliferation rate to travel with tumour cells as they diffuse, incorporating chemotherapy doses into the chemotherapy term, using Bayesian optimization for better parameter estimation, and making the results more explanatory by integrating other patient data.

Contents

Preface	i
Abstract	ii
1 Introduction	1
2 Medical Context	3
2.1 Breast Cancer	3
2.2 Tumour Growth	4
2.3 Treatment	5
2.4 MRI Scans	6
2.4.1 DWI-MRI	6
2.4.2 DCE-MRI	7
3 Data Pre-Processing	8
3.1 Data Acquisition	8
3.1.1 Previous Studies	8
3.1.2 Current Approach	9
3.2 Tumour Segmentation	10
3.2.1 Previous Studies	10
3.2.2 Current Approach	11
3.3 Registration	11
3.3.1 Previous Studies	12
3.3.2 Current Approach	12
3.3.3 Registration results	14
3.4 ROI	17
3.4.1 Previous Studies	17
3.4.2 Current Approach	17
3.5 Number of Tumour Cells Calculation	17
3.5.1 Previous Studies	17
3.5.2 Current Approach	18
3.6 Segmentation Breast Tissue	19
3.6.1 Previous Studies	20
3.6.2 Current Approach	20
3.7 Concluding	20
4 DI-MCRD Model	21
4.1 Current Model	21
4.1.1 Diffusion Term	21
4.1.2 The First Reaction Term	22
4.1.3 The Second Reaction Term	22
4.1.4 Baseline Model	25
4.1.5 Discretization & Numerical Methods	26
4.1.6 Parameter Calibration	27
4.1.7 Variables & Parameters	28
4.1.8 Baseline Results	29
4.2 Model Cycle I: Positive Parameters	37
4.2.1 Model Cycle Ia: Updated Prediction Parameters & DL with Positive Bounds	37
4.2.2 Model Cycle Ib: TRF	39
4.3 Model Cycle II: Tissue-Specific Parameters	41
4.4 Model Cycle III: Inclusion of Death Term	43

4.5 Overview of the Modelling Cycles	46
5 Conclusion & Discussion	47
5.1 Pre-Processing Pipeline	47
5.2 DI-MRCD Model	48
5.3 Concluding & Future Research	50
References	50
Appendices	55
A Exponential and Gompertz Model for Tumour Growth	55
A.1 Exponential model	55
A.2 Gompertz model	55
A.3 Results of Simple Experiments	56
B Chemotherapy schedules	57
C Full DI-MCRD Model Results	59
C.1 Baseline Results	59
C.1.1 Total Number of Tumour Cells Over Time	59
C.1.2 Slices Visualization	60
C.1.3 3D Visualization	71
C.2 Cycle I Results	75
C.2.1 Cycle Ia	75
C.2.2 Cycle Ib	80
C.3 Cycle II Results	90
C.4 Cycle III Results	101

List of Figures

2.1	Anatomy of the breast composed mostly of fibroglandular and fat tissues, which have distinct mechanical properties	3
2.2	Treatment schedule of p_1	6
3.1	Segmentation of the tumours of p_1 at t_0 using ITK snap.	11
3.2	MRI image along with the registration structure for aligning all images to the DCE images at t_1 . The registration process involves three steps, step ①: DCE images are registered to the DWI images within the same time step t_i , step ②: DWI images at t_0 and t_2 are registered to the DWI image at t_1 , step ③: DCE images from t_0 and t_2 are registered to the DWI at t_1 using the parameter map derived from step ②.	14
3.3	Checkerboard representation of DWI image at t_1 and DCE image at t_0 , before and after registration with and without different masks. These images correspond to p_1 and the middle slices are shown.	15
3.4	DCE image from t_0 of p_1 with masks applied, showing only the masked parts of the middle slices.	16
3.5	ROI and breast mask of patient p_1 displayed overlaid on the fixed reference image. . . .	17
3.6	Computed ADC maps generated by the MRI scanner and analytically derived ADC values using (3.4) (a), along with the absolute error between the two maps (b). The results are of p_1 at t_1 , showing the middle slice in the z -direction.	18
3.7	Number of tumour cells of p_1 at t_1 using different ADC maps: ADC computed by MRI (left) and analytic ADC (right).The middle slice in the z -direction is shown.	19
3.8	Tissue segmentation of p_1 at t_0 using global histogram equalization together with a simple threshold (=150). The middle z -slices are shown.	20
4.1	Total amount of tumour cells over time for three different patients obtained using baseline model.	32
4.2	Baseline results for p_8 visualized using slices. (a) shows the N_{data} representation at t_1 and t_2 , along with $N_{\text{model}}(t_1)$, the calibrated number of tumour cells at t_1 , and $N_{\text{model}}(t_2)$, the prediction made by the DI-MCRD model at t_2 . (b) presents the errors between N_{data} and N_{model} at t_1 and t_2 . (c) visualizes the proliferation rate $k(\bar{x})$, (d) displays the shear modulus $G(\bar{x})$, and (e) displays the drug distribution $C_{\text{drug}}(\bar{x}, t_0)$	33
4.3	Baseline results for p_{12} visualized using slices. (a) shows the N_{data} representation at t_1 and t_2 , along with $N_{\text{model}}(t_1)$, the calibrated number of tumour cells at t_1 , and $N_{\text{model}}(t_2)$, the prediction made by the DI-MCRD model at t_2 . (b) presents the errors between N_{data} and N_{model} at t_1 and t_2 . (c) visualizes the proliferation rate $k(\bar{x})$, (d) displays the shear modulus $G(\bar{x})$, and (e) displays the drug distribution $C_{\text{drug}}(\bar{x}, t_0)$	34
4.4	Baseline results for p_{17} visualized using slices. (a) shows the N_{data} representation at t_1 and t_2 , along with $N_{\text{model}}(t_1)$, the calibrated number of tumour cells at t_1 , and $N_{\text{model}}(t_2)$, the prediction made by the DI-MCRD model at t_2 . (b) presents the errors between N_{data} and N_{model} at t_1 and t_2 . (c) visualizes the proliferation rate $k(\bar{x})$, (d) displays the shear modulus $G(\bar{x})$, and (e) displays the drug distribution $C_{\text{drug}}(\bar{x}, t_0)$	35
4.5	3D representation of the number of tumour cells for patients p_8 and p_{12} obtained using the baseline model. Within each subfigure, the top row shows the N_{data} representation at t_1 and t_2 , while the bottom row displays $N_{\text{model}}(t_1)$, the calibrated number of tumour cells at t_1 , and $N_{\text{model}}(t_2)$, the prediction made by the DI-MCRD model at t_2 . In the bottom row, all voxels with a tumour cell count less than N_{min} are removed.	36

4.6	3D representation of the number of tumour cells for patient p_{17} obtained using the baseline model. The top row shows the N_{data} representation at t_1 and t_2 , while the bottom row displays $N_{\text{model}}(t_1)$, the calibrated number of tumour cells at t_1 , and $N_{\text{model}}(t_2)$, the prediction made by the DI-MCRD model at t_2 . In the bottom row, all voxels with a tumour cell count less than N_{min} are removed.	37
4.7	Total amount of tumour cells over time for three different patients obtained using model cycle Ia model.	39
4.8	Total number of tumour cells over for three different patients using both DL and TRF optimization using the model from cycle Ib. The results are obtained using model cycle Ib model.	40
4.9	Total number of tumour cells over for three different patients using both DL and TRF optimization using the model from cycle IIa.	43
4.10	Total number of tumour cells over for three different patients for different initial values γ_0 using the model from cycle III.	46
A.1	Evaluation of exponential and Gompertz models for three patients. The models were calibrated on the first two time points to predict tumour cell from the second point to the third time point.	56
C.1	Total number of tumour cells over time for the first subset of the dataset.	59
C.2	Total number of tumour cells over time for the second and final subset of the dataset.	60
C.3	Baseline results for p_1 visualized using slices. (a) shows the N_{data} representation at t_1 and t_2 , along with $N_{\text{model}}(t_1)$, the calibrated number of tumour cells at t_1 , and $N_{\text{model}}(t_2)$, the prediction made by the DI-MCRD model at t_2 . (b) presents the errors between N_{data} and N_{model} at t_1 and t_2 . (c) visualizes the proliferation rate $k(\bar{x})$, (d) displays the shear modulus $G(\bar{x})$, and (e) displays the drug distribution $C_{\text{drug}}(\bar{x}, t_0)$	61
C.4	Baseline results for p_3 visualized using slices. (a) shows the N_{data} representation at t_1 and t_2 , along with $N_{\text{model}}(t_1)$, the calibrated number of tumour cells at t_1 , and $N_{\text{model}}(t_2)$, the prediction made by the DI-MCRD model at t_2 . (b) presents the errors between N_{data} and N_{model} at t_1 and t_2 . (c) visualizes the proliferation rate $k(\bar{x})$, (d) displays the shear modulus $G(\bar{x})$, and (e) displays the drug distribution $C_{\text{drug}}(\bar{x}, t_0)$	62
C.5	Baseline results for p_4 visualized using slices. (a) shows the N_{data} representation at t_1 and t_2 , along with $N_{\text{model}}(t_1)$, the calibrated number of tumour cells at t_1 , and $N_{\text{model}}(t_2)$, the prediction made by the DI-MCRD model at t_2 . (b) presents the errors between N_{data} and N_{model} at t_1 and t_2 . (c) visualizes the proliferation rate $k(\bar{x})$, (d) displays the shear modulus $G(\bar{x})$, and (e) displays the drug distribution $C_{\text{drug}}(\bar{x}, t_0)$	63
C.6	Baseline results for p_6 visualized using slices. (a) shows the N_{data} representation at t_1 and t_2 , along with $N_{\text{model}}(t_1)$, the calibrated number of tumour cells at t_1 , and $N_{\text{model}}(t_2)$, the prediction made by the DI-MCRD model at t_2 . (b) presents the errors between N_{data} and N_{model} at t_1 and t_2 . (c) visualizes the proliferation rate $k(\bar{x})$, (d) displays the shear modulus $G(\bar{x})$, and (e) displays the drug distribution $C_{\text{drug}}(\bar{x}, t_0)$	64
C.7	Baseline results for p_{10} visualized using slices. (a) shows the N_{data} representation at t_1 and t_2 , along with $N_{\text{model}}(t_1)$, the calibrated number of tumour cells at t_1 , and $N_{\text{model}}(t_2)$, the prediction made by the DI-MCRD model at t_2 . (b) presents the errors between N_{data} and N_{model} at t_1 and t_2 . (c) visualizes the proliferation rate $k(\bar{x})$, (d) displays the shear modulus $G(\bar{x})$, and (e) displays the drug distribution $C_{\text{drug}}(\bar{x}, t_0)$	65
C.8	Baseline results for p_{11} visualized using slices. (a) shows the N_{data} representation at t_1 and t_2 , along with $N_{\text{model}}(t_1)$, the calibrated number of tumour cells at t_1 , and $N_{\text{model}}(t_2)$, the prediction made by the DI-MCRD model at t_2 . (b) presents the errors between N_{data} and N_{model} at t_1 and t_2 . (c) visualizes the proliferation rate $k(\bar{x})$, (d) displays the shear modulus $G(\bar{x})$, and (e) displays the drug distribution $C_{\text{drug}}(\bar{x}, t_0)$	66
C.9	Baseline results for p_{15} visualized using slices. (a) shows the N_{data} representation at t_1 and t_2 , along with $N_{\text{model}}(t_1)$, the calibrated number of tumour cells at t_1 , and $N_{\text{model}}(t_2)$, the prediction made by the DI-MCRD model at t_2 . (b) presents the errors between N_{data} and N_{model} at t_1 and t_2 . (c) visualizes the proliferation rate $k(\bar{x})$, (d) displays the shear modulus $G(\bar{x})$, and (e) displays the drug distribution $C_{\text{drug}}(\bar{x}, t_0)$	67

C.10	Baseline results for p_{16} visualized using slices. (a) shows the N_{data} representation at t_1 and t_2 , along with $N_{\text{model}}(t_1)$, the calibrated number of tumour cells at t_1 , and $N_{\text{model}}(t_2)$, the prediction made by the DI-MCRD model at t_2 . (b) presents the errors between N_{data} and N_{model} at t_1 and t_2 . (c) visualizes the proliferation rate $k(\bar{x})$, (d) displays the shear modulus $G(\bar{x})$, and (e) displays the drug distribution $C_{\text{drug}}(\bar{x}, t_0)$	68
C.11	Baseline results for p_{18} visualized using slices. (a) shows the N_{data} representation at t_1 and t_2 , along with $N_{\text{model}}(t_1)$, the calibrated number of tumour cells at t_1 , and $N_{\text{model}}(t_2)$, the prediction made by the DI-MCRD model at t_2 . (b) presents the errors between N_{data} and N_{model} at t_1 and t_2 . (c) visualizes the proliferation rate $k(\bar{x})$, (d) displays the shear modulus $G(\bar{x})$, and (e) displays the drug distribution $C_{\text{drug}}(\bar{x}, t_0)$	69
C.12	Baseline results for p_{19} visualized using slices. (a) shows the N_{data} representation at t_1 and t_2 , along with $N_{\text{model}}(t_1)$, the calibrated number of tumour cells at t_1 , and $N_{\text{model}}(t_2)$, the prediction made by the DI-MCRD model at t_2 . (b) presents the errors between N_{data} and N_{model} at t_1 and t_2 . (c) visualizes the proliferation rate $k(\bar{x})$, (d) displays the shear modulus $G(\bar{x})$, and (e) displays the drug distribution $C_{\text{drug}}(\bar{x}, t_0)$	70
C.13	Visualization of the results from the baseline model using a 3D representation for a subset of the dataset (part 1).	71
C.14	Visualization of the results from the baseline model using a 3D representation for a subset of the dataset (part 2).	72
C.15	Visualization of the results from the baseline model using a 3D representation for a subset of the dataset (part 3).	73
C.16	Visualization of the results from the baseline model using a 3D representation for a subset of the dataset (part 4).	74
C.17	Visualization of the results from the baseline model using a 3D representation for a subset of the dataset (part 5).	75
C.1	Results from cycle Ia for p_3 visualized using slices. (a) shows the N_{data} representation at t_1 and t_2 , along with $N_{\text{model}}(t_1)$, the calibrated number of tumour cells at t_1 , and $N_{\text{model}}(t_2)$, the prediction made by the DI-MCRD model from cycle Ia at t_2 . (b) presents the errors between N_{data} and N_{model} at t_1 and t_2 . (c) visualizes the proliferation rate $k(\bar{x})$, (d) displays the shear modulus $G(\bar{x}, t_0)$, (e) displays the shear modulus $G(\bar{x}, t_1)$, (f) drug distribution $C_{\text{drug}}(\bar{x}, t_0)$, and drug distribution $C_{\text{drug}}(\bar{x}, t_1)$	76
C.2	Results from cycle Ia for p_8 visualized using slices. (a) shows the N_{data} representation at t_1 and t_2 , along with $N_{\text{model}}(t_1)$, the calibrated number of tumour cells at t_1 , and $N_{\text{model}}(t_2)$, the prediction made by the DI-MCRD model from cycle Ia at t_2 . (b) presents the errors between N_{data} and N_{model} at t_1 and t_2 . (c) visualizes the proliferation rate $k(\bar{x})$, (d) displays the shear modulus $G(\bar{x}, t_0)$, (e) displays the shear modulus $G(\bar{x}, t_1)$, (f) drug distribution $C_{\text{drug}}(\bar{x}, t_0)$, and drug distribution $C_{\text{drug}}(\bar{x}, t_1)$	77
C.3	Results from cycle Ia for p_{10} visualized using slices. (a) shows the N_{data} representation at t_1 and t_2 , along with $N_{\text{model}}(t_1)$, the calibrated number of tumour cells at t_1 , and $N_{\text{model}}(t_2)$, the prediction made by the DI-MCRD model from cycle Ia at t_2 . (b) presents the errors between N_{data} and N_{model} at t_1 and t_2 . (c) visualizes the proliferation rate $k(\bar{x})$, (d) displays the shear modulus $G(\bar{x}, t_0)$, (e) displays the shear modulus $G(\bar{x}, t_1)$, (f) drug distribution $C_{\text{drug}}(\bar{x}, t_0)$, and drug distribution $C_{\text{drug}}(\bar{x}, t_1)$	78
C.4	3D representation of the number of tumour cells for patients p_3 and p_8 obtained using the model from cycle Ia. Within each subfigure, the top row shows the N_{data} representation at t_1 and t_2 , while the bottom row displays $N_{\text{model}}(t_1)$, the calibrated number of tumour cells at t_1 , and $N_{\text{model}}(t_2)$, the prediction made by the DI-MCRD model at t_2 . In the bottom row, all voxels with a tumour cell count less than N_{min} are removed.	79
C.5	3D representation of the number of tumour cells for patient p_{10} obtained using the model from cycle Ia. The top row shows the N_{data} representation at t_1 and t_2 , while the bottom row displays $N_{\text{model}}(t_1)$, the calibrated number of tumour cells at t_1 , and $N_{\text{model}}(t_2)$, the prediction made by the DI-MCRD model at t_2 . In the bottom row, all voxels with a tumour cell count less than N_{min} are removed.	80

- C.6 Results from cycle Ib for p_3 using DL optimization visualized using slices. (a) shows the N_{data} representation at t_1 and t_2 , along with $N_{\text{model}}(t_1)$, the calibrated number of tumour cells at t_1 , and $N_{\text{model}}(t_2)$, the prediction made by the DI-MCRD model from cycle Ib at t_2 . (b) presents the errors between N_{data} and N_{model} at t_1 and t_2 . (c) visualizes the proliferation rate $\mathbf{k}(\bar{x})$ (d) displays the shear modulus $G(\bar{x}, t_0)$ and (e), displays the drug distribution $C_{\text{drug}}(\bar{x}, t_0)$ 81
- C.7 Results from cycle Ib for p_8 using DL optimization visualized using slices. (a) shows the N_{data} representation at t_1 and t_2 , along with $N_{\text{model}}(t_1)$, the calibrated number of tumour cells at t_1 , and $N_{\text{model}}(t_2)$, the prediction made by the DI-MCRD model from cycle Ib at t_2 . (b) presents the errors between N_{data} and N_{model} at t_1 and t_2 . (c) visualizes the proliferation rate $\mathbf{k}(\bar{x})$, (d) displays the shear modulus $G(\bar{x}, t_0)$ and (e), displays the drug distribution $C_{\text{drug}}(\bar{x}, t_0)$ 82
- C.8 Results from cycle Ib for p_{10} using DL optimization visualized using slices. (a) shows the N_{data} representation at t_1 and t_2 , along with $N_{\text{model}}(t_1)$, the calibrated number of tumour cells at t_1 , and $N_{\text{model}}(t_2)$, the prediction made by the DI-MCRD model from cycle Ib at t_2 . (b) presents the errors between N_{data} and N_{model} at t_1 and t_2 . (c) visualizes the proliferation rate $\mathbf{k}(\bar{x})$, (d) displays the shear modulus $G(\bar{x}, t_0)$ and (e), displays the drug distribution $C_{\text{drug}}(\bar{x}, t_0)$ 83
- C.9 3D representation of the number of tumour cells for patients p_3 and p_8 obtained using the model from cycle Ib with DL optimization. Within each subfigure, the top row shows the N_{data} representation at t_1 and t_2 , while the bottom row displays $N_{\text{model}}(t_1)$, the calibrated number of tumour cells at t_1 , and $N_{\text{model}}(t_2)$, the prediction made by the DI-MCRD model at t_2 . In the bottom row, all voxels with a tumour cell count less than N_{min} are removed. 84
- C.10 3D representation of the number of tumour cells for patient p_{10} obtained using the model from cycle Ib with DL optimization. The top row shows the N_{data} representation at t_1 and t_2 , while the bottom row displays $N_{\text{model}}(t_1)$, the calibrated number of tumour cells at t_1 , and $N_{\text{model}}(t_2)$, the prediction made by the DI-MCRD model at t_2 . In the bottom row, all voxels with a tumour cell count less than N_{min} are removed. 85
- C.11 Results from cycle Ib for p_3 using TRF optimization visualized using slices. (a) shows the N_{data} representation at t_1 and t_2 , along with $N_{\text{model}}(t_1)$, the calibrated number of tumour cells at t_1 , and $N_{\text{model}}(t_2)$, the prediction made by the DI-MCRD model from cycle Ib at t_2 . (b) presents the errors between N_{data} and N_{model} at t_1 and t_2 . (c) visualizes the proliferation rate $\mathbf{k}(\bar{x})$, (d) displays the shear modulus $G(\bar{x}, t_0)$ and (e), displays the drug distribution $C_{\text{drug}}(\bar{x}, t_0)$ 86
- C.12 Results from cycle Ib for p_8 using TRF optimization visualized using slices. (a) shows the N_{data} representation at t_1 and t_2 , along with $N_{\text{model}}(t_1)$, the calibrated number of tumour cells at t_1 , and $N_{\text{model}}(t_2)$, the prediction made by the DI-MCRD model from cycle Ib at t_2 . (b) presents the errors between N_{data} and N_{model} at t_1 and t_2 . (c) visualizes the proliferation rate $\mathbf{k}(\bar{x})$, (d) displays the shear modulus $G(\bar{x}, t_0)$ and (e), displays the drug distribution $C_{\text{drug}}(\bar{x}, t_0)$ 87
- C.13 Results from cycle Ib for p_{10} using TRF optimization visualized using slices. (a) shows the N_{data} representation at t_1 and t_2 , along with $N_{\text{model}}(t_1)$, the calibrated number of tumour cells at t_1 , and $N_{\text{model}}(t_2)$, the prediction made by the DI-MCRD model from cycle Ib at t_2 . (b) presents the errors between N_{data} and N_{model} at t_1 and t_2 . (c) visualizes the proliferation rate $\mathbf{k}(\bar{x})$, (d) displays the shear modulus $G(\bar{x}, t_0)$ and (e), displays the drug distribution $C_{\text{drug}}(\bar{x}, t_0)$ 88
- C.14 3D representation of the number of tumour cells for patients p_3 and p_8 obtained using the model from cycle Ib with TRF optimization. Within each subfigure, the top row shows the N_{data} representation at t_1 and t_2 , while the bottom row displays $N_{\text{model}}(t_1)$, the calibrated number of tumour cells at t_1 , and $N_{\text{model}}(t_2)$, the prediction made by the DI-MCRD model at t_2 . In the bottom row, all voxels with a tumour cell count less than N_{min} are removed. 89
- C.15 3D representation of the number of tumour cells for patient p_{10} obtained using the model from cycle Ib with TRF optimization. The top row shows the N_{data} representation at t_1 and t_2 , while the bottom row displays $N_{\text{model}}(t_1)$, the calibrated number of tumour cells at t_1 , and $N_{\text{model}}(t_2)$, the prediction made by the DI-MCRD model at t_2 . In the bottom row, all voxels with a tumour cell count less than N_{min} are removed. 90

- C.1 Results from cycle II for p_3 using DL optimization visualized using slices. (a) shows the N_{data} representation at t_1 and t_2 , along with $N_{\text{model}}(t_1)$, the calibrated number of tumour cells at t_1 , and $N_{\text{model}}(t_2)$, the prediction made by the DI-MCRD model from cycle II at t_2 . (b) presents the errors between N_{data} and N_{model} at t_1 and t_2 . (c) visualizes the proliferation rate $k(\bar{x})$, (d) displays the shear modulus $G(\bar{x}, t_0)$, and (e) displays the drug distribution $C_{\text{drug}}(\bar{x}, t_0)$ 91
- C.2 Results from cycle II for p_8 using DL optimization visualized using slices. (a) shows the N_{data} representation at t_1 and t_2 , along with $N_{\text{model}}(t_1)$, the calibrated number of tumour cells at t_1 , and $N_{\text{model}}(t_2)$, the prediction made by the DI-MCRD model from cycle II at t_2 . (b) presents the errors between N_{data} and N_{model} at t_1 and t_2 . (c) visualizes the proliferation rate $k(\bar{x})$, (d) displays the shear modulus $G(\bar{x}, t_0)$, and (e) displays the drug distribution $C_{\text{drug}}(\bar{x}, t_0)$ 92
- C.3 Results from cycle II for p_{10} using DL optimization visualized using slices. (a) shows the N_{data} representation at t_1 and t_2 , along with $N_{\text{model}}(t_1)$, the calibrated number of tumour cells at t_1 , and $N_{\text{model}}(t_2)$, the prediction made by the DI-MCRD model from cycle II at t_2 . (b) presents the errors between N_{data} and N_{model} at t_1 and t_2 . (c) visualizes the proliferation rate $k(\bar{x})$, (d) displays the shear modulus $G(\bar{x}, t_0)$, and (e) displays the drug distribution $C_{\text{drug}}(\bar{x}, t_0)$ 93
- C.4 3D representation of the number of tumour cells for patients p_3 and p_8 obtained using the model from cycle II with DL optimization. Within each subfigure, the top row shows the N_{data} representation at t_1 and t_2 , while the bottom row displays $N_{\text{model}}(t_1)$, the calibrated number of tumour cells at t_1 , and $N_{\text{model}}(t_2)$, the prediction made by the DI-MCRD model at t_2 . In the bottom row, all voxels with a tumour cell count less than N_{min} are removed. 94
- C.5 3D representation of the number of tumour cells for patient p_{10} obtained using the model from cycle II with DL optimization. The top row shows the N_{data} representation at t_1 and t_2 , while the bottom row displays $N_{\text{model}}(t_1)$, the calibrated number of tumour cells at t_1 , and $N_{\text{model}}(t_2)$, the prediction made by the DI-MCRD model at t_2 . In the bottom row, all voxels with a tumour cell count less than N_{min} are removed. 95
- C.6 Results from cycle II for p_3 using TRF optimization visualized using slices. (a) shows the N_{data} representation at t_1 and t_2 , along with $N_{\text{model}}(t_1)$, the calibrated number of tumour cells at t_1 , and $N_{\text{model}}(t_2)$, the prediction made by the DI-MCRD model from cycle II at t_2 . (b) presents the errors between N_{data} and N_{model} at t_1 and t_2 . (c) visualizes the proliferation rate $k(\bar{x})$, (d) displays the shear modulus $G(\bar{x}, t_0)$ and (e), displays the drug distribution $C_{\text{drug}}(\bar{x}, t_0)$ 96
- C.7 Results from cycle II for p_8 using TRF optimization visualized using slices. (a) shows the N_{data} representation at t_1 and t_2 , along with $N_{\text{model}}(t_1)$, the calibrated number of tumour cells at t_1 , and $N_{\text{model}}(t_2)$, the prediction made by the DI-MCRD model from cycle II at t_2 . (b) presents the errors between N_{data} and N_{model} at t_1 and t_2 . (c) visualizes the proliferation rate $k(\bar{x})$, (d) displays the shear modulus $G(\bar{x}, t_0)$ and (e), displays the drug distribution $C_{\text{drug}}(\bar{x}, t_0)$ 97
- C.8 Results from cycle II for p_{10} using TRF optimization visualized using slices. (a) shows the N_{data} representation at t_1 and t_2 , along with $N_{\text{model}}(t_1)$, the calibrated number of tumour cells at t_1 , and $N_{\text{model}}(t_2)$, the prediction made by the DI-MCRD model from cycle II at t_2 . (b) presents the errors between N_{data} and N_{model} at t_1 and t_2 . (c) visualizes the proliferation rate $k(\bar{x})$, and (d) displays the shear modulus $G(\bar{x}, t_0)$ 98
- C.9 3D representation of the number of tumour cells for patients p_3 and p_8 obtained using the model from cycle II with TRF optimization. Within each subfigure, the top row shows the N_{data} representation at t_1 and t_2 , while the bottom row displays $N_{\text{model}}(t_1)$, the calibrated number of tumour cells at t_1 , and $N_{\text{model}}(t_2)$, the prediction made by the DI-MCRD model at t_2 . In the bottom row, all voxels with a tumour cell count less than N_{min} are removed. 99
- C.10 3D representation of the number of tumour cells for patient p_{10} obtained using the model from cycle II with TRF optimization. The top row shows the N_{data} representation at t_1 and t_2 , while the bottom row displays $N_{\text{model}}(t_1)$, the calibrated number of tumour cells at t_1 , and $N_{\text{model}}(t_2)$, the prediction made by the DI-MCRD model at t_2 . In the bottom row, all voxels with a tumour cell count less than N_{min} are removed. 100

C.1	Results from cycle III with $\gamma_0 = 0.05$ for p_3 using TRF optimization visualized using slices. (a) shows the N_{data} representation at t_1 and t_2 , along with $N_{\text{model}}(t_1)$, the calibrated number of tumour cells at t_1 , and $N_{\text{model}}(t_2)$, the prediction made by the DI-MCRD model from cycle II at t_2 . (b) presents the errors between N_{data} and N_{model} at t_1 and t_2 . (c) visualizes the proliferation rate $k(\bar{x})$, (d) displays the shear modulus $G(\bar{x}, t_0)$ and (e), displays the drug distribution $C_{\text{drug}}(\bar{x}, t_0)$	101
C.2	Results from cycle III for p_8 with $\gamma_0 = 0.05$ using TRF optimization visualized using slices. (a) shows the N_{data} representation at t_1 and t_2 , along with $N_{\text{model}}(t_1)$, the calibrated number of tumour cells at t_1 , and $N_{\text{model}}(t_2)$, the prediction made by the DI-MCRD model from cycle II at t_2 . (b) presents the errors between N_{data} and N_{model} at t_1 and t_2 . (c) visualizes the proliferation rate $k(\bar{x})$, (d) displays the shear modulus $G(\bar{x}, t_0)$ and (e), displays the drug distribution $C_{\text{drug}}(\bar{x}, t_0)$	102
C.3	Results from cycle III with $\gamma_0 = 0.05$ for p_{10} using TRF optimization visualized using slices. (a) shows the N_{data} representation at t_1 and t_2 , along with $N_{\text{model}}(t_1)$, the calibrated number of tumour cells at t_1 , and $N_{\text{model}}(t_2)$, the prediction made by the DI-MCRD model from cycle II at t_2 . (b) presents the errors between N_{data} and N_{model} at t_1 and t_2 . (c) visualizes the proliferation rate $k(\bar{x})$, and (d) displays the shear modulus $G(\bar{x}, t_0)$	103
C.4	3D representation of the number of tumour cells for patients p_3 and p_8 obtained using the model from cycle III with $\gamma_0 = 0.05$ with TRF optimization. Within each subfigure, the top row shows the N_{data} representation at t_1 and t_2 , while the bottom row displays $N_{\text{model}}(t_1)$, the calibrated number of tumour cells at t_1 , and $N_{\text{model}}(t_2)$, the prediction made by the DI-MCRD model at t_2 . In the bottom row, all voxels with a tumour cell count less than N_{min} are removed.	104
C.5	3D representation of the number of tumour cells for patient p_{10} obtained using the model from cycle III with $\gamma_0 = 0.05$ with TRF optimization. The top row shows the N_{data} representation at t_1 and t_2 , while the bottom row displays $N_{\text{model}}(t_1)$, the calibrated number of tumour cells at t_1 , and $N_{\text{model}}(t_2)$, the prediction made by the DI-MCRD model at t_2 . In the bottom row, all voxels with a tumour cell count less than N_{min} are removed.	105
C.6	Results from cycle III with $\gamma_0 = 0.005$ for p_3 using TRF optimization visualized using slices. (a) shows the N_{data} representation at t_1 and t_2 , along with $N_{\text{model}}(t_1)$, the calibrated number of tumour cells at t_1 , and $N_{\text{model}}(t_2)$, the prediction made by the DI-MCRD model from cycle II at t_2 . (b) presents the errors between N_{data} and N_{model} at t_1 and t_2 . (c) visualizes the proliferation rate $k(\bar{x})$, (d) displays the shear modulus $G(\bar{x}, t_0)$ and (e), displays the drug distribution $C_{\text{drug}}(\bar{x}, t_0)$	106
C.7	Results from cycle III for p_8 with $\gamma_0 = 0.005$ using TRF optimization visualized using slices. (a) shows the N_{data} representation at t_1 and t_2 , along with $N_{\text{model}}(t_1)$, the calibrated number of tumour cells at t_1 , and $N_{\text{model}}(t_2)$, the prediction made by the DI-MCRD model from cycle II at t_2 . (b) presents the errors between N_{data} and N_{model} at t_1 and t_2 . (c) visualizes the proliferation rate $k(\bar{x})$, (d) displays the shear modulus $G(\bar{x}, t_0)$ and (e), displays the drug distribution $C_{\text{drug}}(\bar{x}, t_0)$	107
C.8	Results from cycle III with $\gamma_0 = 0.005$ for p_{10} using TRF optimization visualized using slices. (a) shows the N_{data} representation at t_1 and t_2 , along with $N_{\text{model}}(t_1)$, the calibrated number of tumour cells at t_1 , and $N_{\text{model}}(t_2)$, the prediction made by the DI-MCRD model from cycle II at t_2 . (b) presents the errors between N_{data} and N_{model} at t_1 and t_2 . (c) visualizes the proliferation rate $k(\bar{x})$, and (d) displays the shear modulus $G(\bar{x}, t_0)$	108
C.9	3D representation of the number of tumour cells for patients p_3 and p_8 obtained using the model from cycle III with $\gamma_0 = 0.005$ with TRF optimization. Within each subfigure, the top row shows the N_{data} representation at t_1 and t_2 , while the bottom row displays $N_{\text{model}}(t_1)$, the calibrated number of tumour cells at t_1 , and $N_{\text{model}}(t_2)$, the prediction made by the DI-MCRD model at t_2 . In the bottom row, all voxels with a tumour cell count less than N_{min} are removed.	109
C.10	3D representation of the number of tumour cells for patient p_{10} obtained using the model from cycle III with $\gamma_0 = 0.005$ with TRF optimization. The top row shows the N_{data} representation at t_1 and t_2 , while the bottom row displays $N_{\text{model}}(t_1)$, the calibrated number of tumour cells at t_1 , and $N_{\text{model}}(t_2)$, the prediction made by the DI-MCRD model at t_2 . In the bottom row, all voxels with a tumour cell count less than N_{min} are removed.	110

- C.11 Results from cycle III with $\gamma_0 = 0.0005$ for p_3 using TRF optimization visualized using slices. (a) shows the N_{data} representation at t_1 and t_2 , along with $N_{\text{model}}(t_1)$, the calibrated number of tumour cells at t_1 , and $N_{\text{model}}(t_2)$, the prediction made by the DI-MCRD model from cycle II at t_2 . (b) presents the errors between N_{data} and N_{model} at t_1 and t_2 . (c) visualizes the proliferation rate $k(\bar{x})$, (d) displays the shear modulus $G(\bar{x}, t_0)$ and (e), displays the drug distribution $C_{\text{drug}}(\bar{x}, t_0)$ 111
- C.12 Results from cycle III for p_8 with $\gamma_0 = 0.0005$ using TRF optimization visualized using slices. (a) shows the N_{data} representation at t_1 and t_2 , along with $N_{\text{model}}(t_1)$, the calibrated number of tumour cells at t_1 , and $N_{\text{model}}(t_2)$, the prediction made by the DI-MCRD model from cycle II at t_2 . (b) presents the errors between N_{data} and N_{model} at t_1 and t_2 . (c) visualizes the proliferation rate $k(\bar{x})$, (d) displays the shear modulus $G(\bar{x}, t_0)$ and (e), displays the drug distribution $C_{\text{drug}}(\bar{x}, t_0)$ 112
- C.13 Results from cycle III with $\gamma_0 = 0.0005$ for p_{10} using TRF optimization visualized using slices. (a) shows the N_{data} representation at t_1 and t_2 , along with $N_{\text{model}}(t_1)$, the calibrated number of tumour cells at t_1 , and $N_{\text{model}}(t_2)$, the prediction made by the DI-MCRD model from cycle II at t_2 . (b) presents the errors between N_{data} and N_{model} at t_1 and t_2 . (c) visualizes the proliferation rate $k(\bar{x})$, and (d) displays the shear modulus $G(\bar{x}, t_0)$ 113
- C.14 3D representation of the number of tumour cells for patients p_3 and p_8 obtained using the model from cycle III with $\gamma_0 = 0.0005$ with TRF optimization. Within each subfigure, the top row shows the N_{data} representation at t_1 and t_2 , while the bottom row displays $N_{\text{model}}(t_1)$, the calibrated number of tumour cells at t_1 , and $N_{\text{model}}(t_2)$, the prediction made by the DI-MCRD model at t_2 . In the bottom row, all voxels with a tumour cell count less than N_{min} are removed. 114
- C.15 3D representation of the number of tumour cells for patient p_{10} obtained using the model from cycle III with $\gamma_0 = 0.0005$ with TRF optimization. The top row shows the N_{data} representation at t_1 and t_2 , while the bottom row displays $N_{\text{model}}(t_1)$, the calibrated number of tumour cells at t_1 , and $N_{\text{model}}(t_2)$, the prediction made by the DI-MCRD model at t_2 . In the bottom row, all voxels with a tumour cell count less than N_{min} are removed. 115

List of Tables

3.1	Patient data for the group with scans at three time points. Note that p_4 has tumours in both breasts.	9
3.2	Patient data for the group with scans at two time points.	10
3.3	General dimensions and voxel sizes of the different types of MRI scans provided by EMC.	10
4.1	Description of the variables of the DI-MCRD model system equations (4.17)–(4.19).	29
4.2	Description of the parameters of the DI-MCRD model system described in equations (4.17)–(4.19). These values correspond to those used by Engelberts [12] in the most recent version of his code.	29
4.3	Baseline results of the DI-MCRD model applied to the entire dataset.	30
4.4	Cycle Ia results of the DI-MCRD model applied for three patients.	38
4.5	Cycle Ib results of the DI-MCRD model applied for three patients.	39
4.6	Cycle II results of the DI-MCRD model applied for three patients.	42
4.7	Cycle III results of the DI-MCRD model applied for three patients for different initial values of γ	45
4.8	This table shows the differences between the models cycles taken within this chapter. Here method(s) refers to the optimization methods used/compared, α_0 refers to the initial value of α , $\alpha \in$ and $k(\bar{x}) \in$ refer to the trust region bounds of the optimization methods, t^* refers to the time points where the parameters $C_{drug}(\bar{x}, t^*)$ and $G(\bar{x}, t^*)$ are updated, # params refers to the number of patient-specific parameters that need to be fitted.	46
B.1	Chemotherapy schedules for each patient, detailing the 9-cycle regimen with dosages (in mg) of carboplatin (C), paclitaxel (Pa), pertuzumab (Pe), and trastuzumab (T) administered on Day 1 (D1) and Day 8 (D8) of each cycle. An asterisk (*) indicates subcutaneous administration.	58

1

Introduction

Breast cancer has emerged as the most often diagnosed disease globally, with almost 2.3 million new cases documented in 2020. This statistic indicates that breast cancer represents approximately one in every eight cancer diagnoses across all genders [1]. Furthermore, in 2020, it comprised a notable 25% of all cancer cases in women, emerging as the most common cancer for women [2]. In the Netherlands annually 18,000 women are diagnosed with breast cancer [3].

Standard approaches to treating breast cancer typically involve a combination of chemotherapy and surgery. While chemotherapy is effective in shrinking tumours, it also damages healthy tissues, highlighting the need for an optimal, patient-specific, tailored chemotherapy schedule. Determining the optimal treatment schedule is patient-specific and complex. Magnetic Resonance Imaging (MRI) is often used to assess tumour size, morphology and location before, during and after chemotherapy. Mathematical studies have used MRI images to calibrate patient-specific models, enabling the prediction of individual treatment responses [4–9]. This allows for the creation of patient-specific treatment schedules, which can be used to optimize the rounds of chemotherapy to effectively treat cancer.

Agnes Jager, medical oncologist at the Erasmus Medisch Centrum (EMC), observed that for a particular type of breast cancer, human epidermal growth factor receptor 2 positive (HER2+), patients achieved radiologic complete response (rCR) much earlier than expected with the standard treatment schedule. In other words, MRI scans showed no visible tumour lesion after early courses of treatment. Consequently, she has collaborated with Delft University of Technology (TU Delft) to develop a model capable of simulating the response of breast cancer tumours to treatment, aiming to devise a personalised treatment schedule for each patient. The ultimate objective is to personalize the treatment schedule by reducing the number of cycles required to achieve rCR, thereby reducing the potential harm to healthy tissues and discomfort to the patient.

Before this master's thesis, three other students, Nathalie Oudhof [10], Eva Slingerland [11], and Rutger Engelberts [12], contributed to this project. They used studies conducted by a research institute based in Texas, comprising diverse departments dedicated to mathematical modelling in oncology. The model of this research group, referred to as the Texas research group, served as the foundation of their work. Building upon studies conducted by the Texas research group [4–9], Oudhof and Slingerland formulated a three-dimensional Drug-Incorporated-Mechanically-Coupled-Reaction-Diffusion (DI-MCRD) model tailored for patient data from EMC which was made numerical efficient by Engelberts. This model uses MRI scans from two distinct time points to calibrate patient-specific parameters. Subsequently, it predicts tumour evolution up to a third-time point, which can be validated with a corresponding MRI scan. The model has been applied to a dataset from EMC comprising three patients. While it successfully predicts treatment response for one patient, it fails for the other two when compared to the results at the third time point. The objective of this research is to evaluate the model on a larger data set and to improve its performance by adapting the model.

This research is structured as follows: it begins with an introductory chapter about the medical context necessary for understanding the project after which it continues with three main chapters. The first main

chapter covers the preprocessing pipeline, which consists of the steps required to transform MRI scan data into input data for the DI-MCRD model. Each step within the preprocessing pipeline is reassessed, drawing on the Texas research group, the thesis from Oudhof [10], and insights from Jifke Veenland, a member of the Biomedical Imaging Group Rotterdam (BIGR). The second main chapter covers the DI-MCRD model. First the model from Engelberts [12] is used to create a baseline by applying it to all patients inside the larger dataset. Subsequently, various enhancements to his model are executed through modelling cycles, followed by an assessment of the improved model against the data. The research concludes with a conclusion and discussion, including recommendations for future research.

2

Medical Context

Within this chapter, the medical context needed for this research is explained. First, breast cancer and the HER2+ type will be discussed, followed by an explanation of tumour growth and treatment. Finally, the two types of MRI scans used in this research are described.

2.1. Breast Cancer

Breast cancer is a heterogeneous disease, comprising multiple types associated with distinctive histological and biological features, clinical presentations, and responses to therapy [13]. Within the Netherlands, it occurs most commonly in the ducts (80%) or lobules (15%) [3]. In the remaining 5%, breast cancer may arise in less common areas such as the nipple, areola, and breast skin. Ductal carcinomas are formed in the cells lining the milk ducts, while lobular ones are made in the glands that produce the milk. Carcinomas are a specific type of cancer that originates in epithelial cells, which line the inside and outside surfaces of the body. In Figure 2.1 the location of the ducts and lobules in the breast can be seen. This Figure also illustrates that the human breast primarily consists of fibroglandular and adipose tissue. Adipose tissue consists of adipocytes that store lipids and offer cushioning and insulation. Conversely, fibroglandular tissue consists of connective tissue, ducts, and lobules that are essential for breast support and lactation.

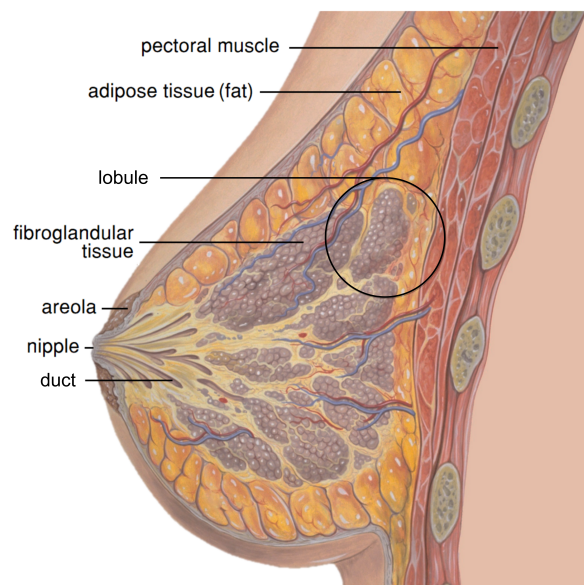


Figure 2.1: Anatomy of the breast composed mostly of fibroglandular and fat tissues, which have distinct mechanical properties

Breast cancer classification contains several key factors: clinical stage, tumour type, grade, and receptor status, regulated by specific rules [14]. The clinical stage is defined using the TNM classification system, which classifies cancer staging according to three primary criteria: the size of the primary tumour (T category), the extent of spread to adjacent lymph nodes (N category), and the presence of distant metastasis (M category). In this system, T0, N0, and M0 represent the absence of detectable tumour, lymph node involvement, and distant metastasis, respectively. Higher values (T1-T4, N1-N3, M1) represent progressively severe conditions, characterized by larger tumours, increased lymph node involvement, and the presence of distant metastasis, respectively. Mammography and MRI are commonly used by radiologists to evaluate this clinical classification of the tumour. Pathological confirmation, achieved via biopsy, is indicated by prefixing a lowercase 'p' to the category (e.g., pN0). Pathological assessments conducted post-treatment use 'yp' (e.g., ypT1), whereas clinical evaluations via imaging are denoted by a lowercase 'c' (e.g., cT2).

The second key factor is the breast tumour type, which is also detected via mammography and in certain instances, MRI scans. Tumour types include, among others, invasive carcinoma of no special type (IC-NST) and ductal carcinoma in situ (DCIS). IC-NST is the most common kind of breast cancer which originates in the milk ducts and infiltrates adjacent tissue. In contrast, DCIS is non-invasive and stays within the ducts. In mammograms, DCIS is generally observed as clusters of small, irregular dots lacking a defined mass, whereas IC-NST is commonly identified as a spiky or irregular mass. It must be noted that although DCIS may be suspected, it may not always be clinically proven by a radiologist. The appearance of the breast tumour is also assessed through grading (from grade 1 to 3), which helps guide treatment decisions based on tumour growth as well as aggressiveness.

Tumour receptor types can be classified as hormone receptor-positive (HR+) or hormone receptor-negative (HR-). HR+ tumours proliferate in reaction to the female hormones estrogen (ER) and progesterone (PR), requiring the incorporation of anti-hormonal therapy in the treatment regimen. In contrast, HR-negative tumours do not express these receptors and are unresponsive to such treatments. Another classification of receptor status is based on whether a tumour is HER2-positive (HER2+) or HER2-negative (HER2-). HER2+ indicates that the tumour is responsive to the human epidermal growth factor receptor 2 protein. HER2-positive breast cancer is generally more aggressive compared to other breast cancer subtypes. However, advancements in targeted therapies, including HER2-targeted monoclonal antibodies such as trastuzumab and pertuzumab, have markedly enhanced outcomes for patients with this subtype of breast cancer [15]. Targeted therapies block the action of the HER2 protein, consequently slowing or stopping the proliferation of cancer cells. A tumour may exhibit both HR+ and HER2+ characteristics, referred to as triple-positive, or it can be classified as the less prevalent triple-negative breast cancer (HER2-/HR-), which is associated with limited treatment alternatives and a worse prognosis. Combinations such as HER2+/HR- and HER2-/HR+ are also present within this classification.

Oncologist Agnes Jager noted a positive response to targeted therapies in HER2-positive patients, as indicated in the introduction. She seeks to acquire a more profound understanding of this subtype of breast cancer. This project will focus on HER2-positive patients, specifically examining the tumour's response to targeted therapies, with the goal of minimizing the number of chemotherapy cycles. To highlight the importance of this subtype of breast cancer, in the Netherlands, 12 percent of the women who are diagnosed with invasive breast cancer have a HER2-positive tumour [3].

2.2. Tumour Growth

To model breast tumour growth, it is important to understand its dynamics. Tumours originate from genetic mutations disrupting normal cell growth, often caused by carcinogens or inherited predispositions. Mutations in genes regulating cell division, apoptosis, or DNA repair lead to uncontrolled cell proliferation, driving tumour growth and spread [16].

As the tumour proliferates, it necessitates a vascular supply to support its growth. This requires angiogenesis, the process by which new blood vessels are generated. Angiogenesis enhances the tumour's vascularity, improving the network of blood vessels that supply essential oxygen and nutrients for its growth. Vascularity, defined as the density of blood vessels in a tissue or organ, directly impacts the tumour's capacity to proliferate. Nonetheless, the tumour's proliferation is limited by variables including nutrition availability and spatial constraints [?].

Moreover, it is important to know the interaction between a tumour and the surrounding breast tissue to understand the physical dynamics of tumour growth. The fact that fibroglandular tissue is denser and twice as stiff as adipose tissue [17] is particularly relevant in this context. A growing tumour imparts an external force on the surrounding tissue, inducing tissue deformation—a phenomenon known as the “mass effect” [4, 5]. This deformation increases the total mechanical distortion energy within the tissue, which is influenced by the local mechanical properties of the surrounding area. Tumours have been shown to be sensitive to their mechanical microenvironment, exhibiting reduced outward growth and expansion in regions of high stress [18].

Stress denotes the internal force per unit area generated within the tissue as a reaction to the tumour’s growth, whereas distortion energy represents the energy stored in the tissue as a result of its deformation. In fibroglandular tissue, increased stiffness results in greater stress and distortion energy, hence creating less favourable conditions for tumour proliferation. Conversely, adipose tissue, characterized by its reduced stiffness, leads to decreased stress and lower distortion energy, hence creating a more favourable environment for tumour proliferation.

Investigations have been conducted to determine which mathematical model best suits tumour growth dynamics [19]. Initially, exponential growth models were used. However, with the support of in vitro cancer cell population data, it became clear that exponential growth was not suitable for accurately describing cancer progression beyond the earliest phases of population growth [20]. Subsequently, logistic growth models were found to represent tumour growth more accurately. These models can simulate the fact that tumour growth is limited by nutritional, immunological, or spatial constraints by incorporating a carrying capacity into the model at which the tumour volume plateaus [19]. In addition to logistic models, the Gompertz model has also been shown to be effective in capturing the slowing growth rate as the tumour size increases [21].

At the beginning of this research, initial simple tests were conducted using the previous data available, using a logistic model and Gompertz model [21] with the total number of tumour cells at each time point. Note that the current DI-MCRD model uses logistic growth; therefore, alternative methods were explored. Appendix A presents the results of these preliminary tests. From these tests, it was concluded that these models are incapable of approximating the third timestep using only the first two time steps for calibration. Exponential growth particularly failed to capture the third point effectively, whereas the Gompertz model showed potential but would require additional parameters for better calibration. Moreover, since the Gompertz model only captures growth and does not account for the decay of tumour cells due to chemotherapy or the spread, it would need to be expanded with additional terms.

2.3. Treatment

Cancer treatment options include surgery, radiation therapy, immunotherapy, and chemotherapy, often used in combination. Neoadjuvant therapy (NAT) is commonly given to patients with locally advanced breast cancer to reduce the tumour’s size before surgery. NAT often results in a pathological complete response (pCR), indicating that pathological examination of the removed tissue after surgery shows no remaining tumour. Patients who achieve pCR typically demonstrate a significantly improved disease-free survival rate [22]. Consequently, achieving pCR is vital for patient outcomes, making the understanding of the tumour’s response to NAT important. Each patient shows different tumour growth and treatment responses, influenced by several characteristics such as the patient’s weight and age, along with the tumour’s location, receptors, and stage. Consequently, a tailored treatment strategy for the patient would be ideal.

In the case of HER2-positive breast cancer patients, NAT also often results in pCR [23], a favourable outcome also observed in patients from the EMC by Agnes Jager. Moreover, numerous studies in the medical field have investigated the potential predictive value of radiologic complete response (rCR), indicating the absence of visible tumours on radiologic imaging [23]. These investigations have shown that rCR and pCR frequently correspond in HER2+ individuals [24]. Consequently, if a mathematical model can accurately predict rCR, it can be used to devise a patient-specific treatment plan.

Currently, at the EMC, all HER2+ patients are treated with a similar protocol, namely the TRAIN-2 scheme [25]. This protocol consists of nine rounds of intravenous therapy that include trastuzumab, pertuzumab, carboplatin, and paclitaxel. Both carboplatin and paclitaxel are chemotherapy treatments,

meaning that they kill fast-growing cells, which are usually tumour cells as they grow quicker and faster than normal cells [26]. Trastuzumab and pertuzumab as mentioned before (See Section 2.1) are targeted therapies. A single therapy cycle lasts for three weeks. During the first week, patients get trastuzumab, pertuzumab, carboplatin, and paclitaxel; in the second week, generally, paclitaxel is the only medication used; and in the third week, there is no treatment. Starting the following week, all four medications will be used again in the subsequent cycle of therapy. Every component can have a different dosage every week and is patient-dependent. Following three or four treatments, an MRI is performed to see whether the tumour has shrunk in response to the therapy. Surgery, including pathological testing, follows after the completion of nine treatment rounds. In Figure 2.2 the treatment schedule of a patient from the Erasmus MC is visualised as an example.

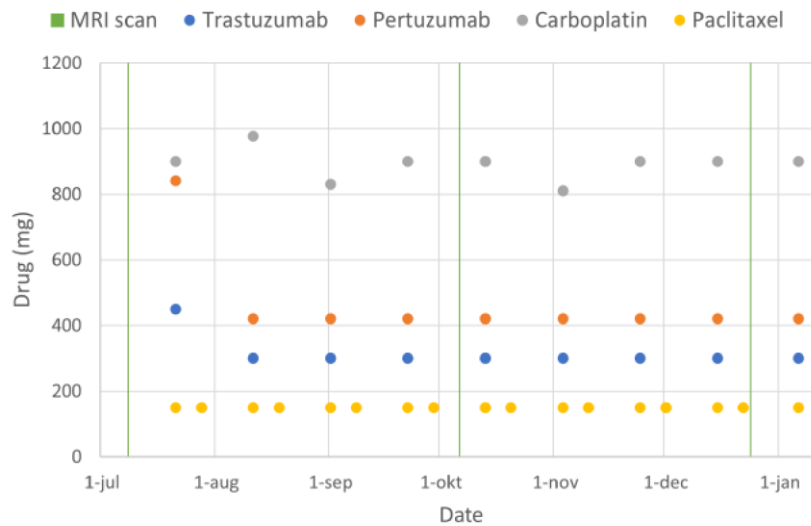


Figure 2.2: Treatment schedule of p_1 .

2.4. MRI Scans

As mentioned earlier in Section 2.1, medical imaging techniques such as MRI scans and ultrasounds are often used to assess and classify a tumour. In addition, these imaging techniques can also be used in the later stages of a patient's treatment to evaluate the efficacy of the tumour's response to therapy. In this research, MRI scans are used. MRI is a non-invasive technique which uses strong magnetic fields and radio waves to generate detailed images of the body's internal structures. The water molecules in the human body respond to these magnetic fields and emit signals that are then converted into images. Advancements in technology have led to the development of new types of MRI scans. This research uses Diffusion-weighted MRI (DWI-MRI) and dynamic contrast-enhanced MRI (DCE-MRI) to obtain information about the response to treatment and will be used to initialize the DI-MRCD model.

2.4.1. DWI-MRI

DWI-MRI is a specialised MRI technique that measures the random motion of water molecules within tissues using the principles of Brownian motion [27]. This imaging technique enhances MRI pictures to detect the movement of water molecules, enabling the visualization and quantification of their natural diffusion throughout biological tissues. When water molecules encounter barriers such as cell membranes, their diffusion becomes restricted. DWI-MRI is capable of detecting and quantifying this restriction.

DWI-MRI is especially valuable in neurological and oncological imaging. In neurological applications, diffusion-weighted scans enable the visualization of nerve pathways in the brain by highlighting areas of restricted diffusion. Disruptions in these pathways, indicated by areas of less restricted diffusion, can signal the occurrence of a stroke. In oncology, DWI-MRI plays a crucial role in tumour characterization

and monitoring treatment response, as tumours typically show distinct diffusion patterns compared to normal tissues.

The degree of diffusion sensitivity in DWI-MRI is controlled by the b -value, which determines the strength of diffusion weighting applied to the image. Often multiple scans with different b -values are taken. Higher b -values correspond to stronger diffusion weighting, enhancing the detection of subtle differences in water movement, particularly in tissues where diffusion is more restricted, such as dense tumour cells. Lower b -values, on the other hand, are more sensitive to faster water movement in tissues with less diffusion restriction. However, lower b -values are also more sensitive to perfusion effects, which can affect the accuracy of diffusion measurements.

Using multiple DWI scans with different diffusion weightings allows for the estimation of the apparent diffusion coefficient (ADC), which describes the rate of water diffusion in cellular tissue. Based on these ADC values, the number of tumour cells for each voxel, which is needed for the DI-MRCD model, can be estimated. This ADC value can be calculated in several ways which will be elaborated upon in Section 3.5. Note that the movement of water is hindered by cells and thus ADC is inversely correlated with tumour cellularity [28].

2.4.2. DCE-MRI

DCE-MRI (Dynamic Contrast-Enhanced MRI) is a specialized imaging technique used to assess blood flow and the permeability of blood vessels within tissues. In DCE-MRI, a gadolinium-based contrast agent (CA) is injected into the patient's bloodstream, and a series of images is captured over time. These images include pre-contrast scans, taken before the contrast agent is introduced, and post-contrast scans, taken afterwards. This dynamic imaging shows how the contrast agent moves through blood vessels and tissues, creating enhanced contrast between different tissues on the MRI, thus improving the quality of the scan [29].

In the context of tumours, DCE-MRI is particularly useful due to the unique characteristics of tumour vasculature. Tumour blood vessels are often poorly formed, with endothelial cells lining the vessel walls that are not tightly connected. This allows the small molecular CA to easily leak from the vessels into the surrounding tissue. Tumours use this feature to rapidly acquire nutrients and expel waste products back into the bloodstream. As a result, tumours typically show much more pronounced enhancement on DCE-MRI compared to the surrounding normal tissue, aiding in the identification and characterization of tumours.

Therefore, DCE-MRI is often used in oncology. It provides valuable information about tumour vasculature, helping in the diagnosis, characterisation, and monitoring of cancer. It can also differentiate between various types of tissues based on their perfusion characteristics. Therefore, in our case, DCE-MRI will be used to detect a region of interest (ROI) that contains the tumour, segmenting different tissues and estimating the distribution of drugs in tumour tissue (see Sections 3.2, 3.2 and 4.1.3).

3

Data Pre-Processing

A critical stage of the modelling pipeline is the preprocessing of patient data received from the EMC. The preprocessing phase determines the initial values of the model, thereby forming the basis of the subsequent results. The preprocessing pipeline consists of the following steps:

1. Data acquisition
2. Tumour segmentation
3. Registration
4. Identifying region of interest (ROI)
5. Calculation of the number of tumour cells per voxel
6. Segmentation of the breast tissue

Each of these steps involves various choices that influence both the input and potentially the output of the DI-MRCD model. The Texas studies [4–9] employed different approaches, and Oudhof's [10] preprocessing in previous theses also involved several decisions. Additionally, Engelberts [12] identified unrealistic behaviour in the initial model values possibly due to preprocessing issues in the data received from Slingerland [11]. Given this issue, along with the expanded dataset and the need to preprocess data for new patients, this chapter will re-evaluate the entire preprocessing process. It will explore the range of available options for each step and justify the specific choices made in this research.

3.1. Data Acquisition

The first step of the pipeline involves patient data acquisition, typically comprising DCE and DWI MRI scans, along with chemotherapy data.

3.1.1. Previous Studies

Both the Texas studies [4–9] and previous theses [10–12] used MRI scans from three time points denoted as t_i where $i = 0, 1, 2$. At t_0 , scans were acquired before NAT, t_1 scans were taken after at least one cycle of NAT, and t_2 scans were taken after multiple cycles of NAT.

In assessing the predictive performance of the model, the inclusion of a third scan (t_2) alongside the initial two scans used for initializing patient-specific parameters is crucial for evaluating outcome predictions. It is essential to note that for t_2 scans to validate the model effectively, visible tumour cells must be identifiable in the DCE MRI scans.

The initial studies by the Texas research group involved acquiring DCE-MRI, DW-MRI, and anatomical T_1 -weighted MR images at these three time points [4, 5]. Subsequent studies expanded the data acquisition to include five MRI data types per session: (1) precontrast T_1 map, (2) precontrast B_1 field

map for RF inhomogeneity correction, (3) DW-MRI data, (4) high-temporal resolution T_1 -weighted DCE-MRI data before, during, and after gadolinium-based contrast agent injection, and (5) high-resolution T_1 -weighted anatomical scan (post-contrast) [6–8]. Additionally, Jarrett et al. [9] incorporated a sixth scan using ^{64}Cu -DOTA-trastuzumab PET-CT at t_0 to detect tumour uptake of targeted therapy.

For previous theses, the EMC initially provided a cohort of four anonymised HER2+ patients. The limited number of patients was due to the positive response to chemotherapy, as subsequent t_2 scans of HER2+ patients often showed no detectable tumours. The EMC provided only DCE and DWI MRI scans, thus limiting the data types available for the studies in previous theses compared to the broader scope of the Texas studies.

3.1.2. Current Approach

In this research, the patient dataset is expanded to include the data of 24 anonymized patients denoted as p_i for $i = 1, \dots, 24$. Twelve patients have scans at two time points (t_0 and t_1), and the remaining twelve patients have scans at all three time points (t_0, t_1 and t_2), mirroring the protocols used in previous studies. However, some patients are excluded from the dataset due to the fact that some t_0 scans were taken at another hospital than the EMC, resulting in different intensities that could affect the results. Consequently, there are 7 patients with scans at three time points and 6 patients with scans at two time points. Other relevant patient information, such as chemotherapy doses, dates of t_i scans, age at diagnosis, pathological assessment (PA), BMI, and weight, was also collected. Tables 3.1 and 3.2 present this information, with chemotherapy schedules detailed in Appendix B.

	p_1	p_3	p_4		p_8	p_{10}	p_{11}	p_{12}
age at diagnosis	32	30	58	"	24	56	54	58
BMI [kg/m ²]	20.7	27.34	34.01	"	22.15	21.77	35.05	27.89
weight [kg]	61.4	79	96	"	64	60	84.2	67
tumour position	left	left	left	right	right	right	right	right
clinical start	cT2 (26mm)	cT2 (38mm)	cT4 (80mm)	cT2 (24mm)	cT2 (29mm)	cT2	cT2 (32mm)	cT4 (8cm)
lymph nodes	N2	pN0	N3	N0	N2	N3b/c	N3	N2
metastases	M0	M0	M0	M0	M0	M0	M0	M0
tumour type(s)	IC-NST gr.2	IC-NST gr.2 DCIS gr.3	IC-NST gr.2	IC-NST gr.1	IC-NST gr.2 DCIS gr.3	IC-NST gr.2	IC-NST gr.3	IC-NST gr.2
ER/PR/HER2	+/+	+/+	+/-	+/-	+/-	+/+	+/-	-/+
scan days	[0, 90, 169]	[0, 84, 174]	[0, 68, 184]	"	[0, 105, 206]	[0, 55, 83]	[0, 59, 136]	[0, 69, 111]
PA	ypT1aN1	ypT1cN0	ypT0N0	"	ypT1aN0	ypT0N0	ypTmiN0	ypTisN0
PA day	210	221	218	"	258	208	224	237

Table 3.1: Patient data for the group with scans at three time points. Note that p_4 has tumours in both breasts.

	p_6	p_{15}	p_{16}	p_{17}	p_{18}	p_{19}
age at diagnosis	39	49	63	43	75	58
BMI [kg/m ²]	21.85	27.64	22.55	19.59	29.71	22.31
weight [kg]	70	78	57	60	91	66
tumour position	left	left	right	right	left	left
clinical start	cT1a	cT2 (41mm)	cT1c (13mm)	cT2 (21mm)	cT2 (2.8cm)	cT2 (21mm)
lymph nodes	N2	N3b	pN1a	N0	N0	N2
metastases	M1	M1	M0	M0	M0	M0
tumour type(s)	IC NST gr. 3 DCIS gr. 3	IC-NST gr.2	IC-NST gr1	ICT-NST gr.3 DCIS gr.3	IC-NST gr.3 DCIS gr.2	IC-NST gr.3 DCIS gr.3
ER/PR/HER2	+/+/+	+/-/+	+/+/+	+/+/+	+(5%)/-/+	-/-/+
scan days	[0, 48]	[0, 89]	[0, 70]	[0, 117]	[0, 87]	[0, 63]
PA	ypT0N0	ypTisN0	ypT1c	ypT1cN0	ypTisN0	ypT0N0
PA day	194	229	235	175	230	196

Table 3.2: Patient data for the group with scans at two time points.

The MRI scans of the patient cohort in this research, similar to data from previous research, comprise DCE and DWI MRI scans for each time point t_i . The DCE scan includes 3D images at time points τ_n for $n = 1, \dots, 8$, where the first two scans ($n = 1, 2$) are pre-contrast, and the subsequent six are post-contrast. The DWI scan consists of two 3D images representing b-values of 50 and 800 s/mm², respectively. Additionally, an ADC map, calculated by the MRI scanner using the DWI images, is available. The use and explanation of the ADC map will be discussed in Section 3.5. The most common dimensions and corresponding voxel spacings of the images are detailed in Table 3.3. As shown in this table, the resolution of the two different image types, results in varying Fields of View (FOV). Therefore, the outermost voxels of the DWI images are removed to ensure the same centre and achieve a FOV consistent with that of the DCE images. It is also important to note that each scan is provided as a directory of DICOM files (.dcm). In this project, all DICOM files were converted to NIFTI format using the Python package `dicom2nifti` [30].

	dimensions	voxel spacing [mm]
DCE	$512 \times 512 \times 120$	$0.664 \times 0.664 \times 1.6$
	$512 \times 512 \times 86$	$0.664 \times 0.664 \times 2.2$
DWI	$256 \times 256 \times 32$	$1.406 \times 1.406 \times 6.5$

Table 3.3: General dimensions and voxel sizes of the different types of MRI scans provided by EMC.

3.2. Tumour Segmentation

To determine the number of tumour cells within the breast, it is essential to first locate the tumour. As discussed in Section 2.4, DCE-MRI scans can be used to detect a tumour region of interest (ROI).

3.2.1. Previous Studies

The Texas research group used various detecting algorithms to identify the tumour ROI. The first Texas studies [4–6] applied an 80% signal intensity increase threshold between pre- and post-contrast images within a manually outlined ROI. In contrast, the subsequent Texas study [7] calculated differences between pre-contrast and three consecutive post-contrast images using a standard deviation threshold for tumour inclusion. On the other hand, the last Texas studies [8, 9] used a fuzzy c-means (FCM)-based clustering algorithm for this purpose [31]. Although the rationale behind the selection of these specific methods is not detailed in every Texas study [4–9], each method contributes to the diversity of the Texas research pipeline. This variation demonstrates that the studies do not rely on a single general approach for tumour ROI detection. Notably, the FCM method offers advantages of automation, efficiency, and objectivity [32], and its adoption in recent Texas studies [8, 9] highlights its effectiveness in detecting the tumour ROI.

Since there were few patients in the previous theses [10–12], the tumours were manually segmented by a radiologist from the EMC. Radiologist Dr. A.I.M. Obdeijn used available pathological reports for accurate segmentation using ITK-Snap, a commonly used software for medical image segmentation and analysis.

3.2.2. Current Approach

As mentioned in Section 3.1, this research incorporates a larger patient dataset. However, focusing primarily on mathematical modelling rather than lesion-finding algorithms, manual segmentation of tumours using ITK-Snap was continued. Given the increased dataset, in collaboration with Dr. C. de Monyé, tumour segmentation was conducted to expedite the process. Similar to the approach taken by Dr. A.I.M. Obdeijn, Dr. C. de Monyé used pathological reports for precise tumour localization.

Figure 3.1 illustrates the process of tumour segmentation using ITK-Snap, focusing on the fourth scan out of eight timepoints in the DCE sequence at t_0 . Scan 4 is selected because tumours are generally most visible in the second post-contrast scan, which corresponds to the fourth scan in this case (since the first two scans are pre-contrast). However, it is important to note that for t_1 or t_2 , the tumour is typically best observed in the final DCE scan due to reduced contrast agent absorption post-chemotherapy. The segmentation process involves slicing through the scan, where each voxel containing tumour tissue is highlighted in red, generating a 3D binary mask with a value of 1 indicating the presence of tumour and 0 otherwise.

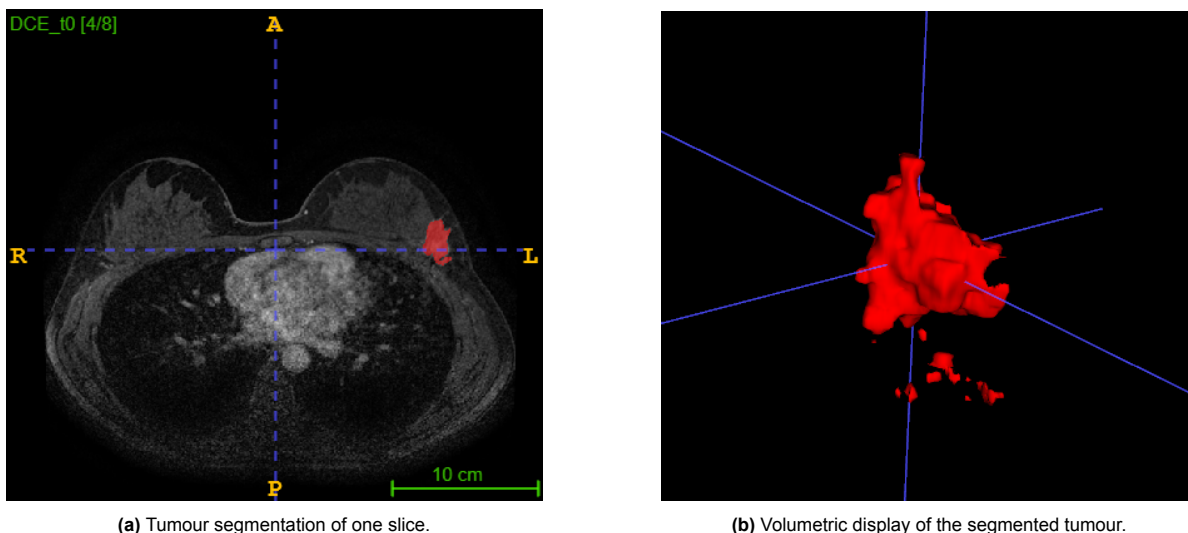


Figure 3.1: Segmentation of the tumours of p_1 at t_0 using ITK snap.

3.3. Registration

To accurately define the tumour and various tissues within the breast, all the images of a patient must first be aligned. The two types of MRI scans, DWI and DCE, are taken at three or two time points. This can result in differences in the positions of the breast within the various images. This variation is due to the patient lying slightly differently in the scanner at each time point, and possibly even moving between scans within the same time point, due to breathing or toilet visits.

Spatially aligning images, known as image registration, can involve various transformation models such as rigid, affine and non-rigid (or deformable) registration models. Rigid registration aligns images using translations and rotations, preserving the object's shape and size. Affine registration extends this by including scaling and shearing, enabling linear transformations that preserve collinearity. Collinearity means that points that are on the same line, will stay on the same line. These methods are preferred when preserving the original spatial relationships of the image is crucial. Non-rigid registration, which includes techniques like B-spline registration, enables handling complex deformations by using splines. Splines are mathematical functions that facilitate smooth and flexible transformations, allowing for adjustments in shape and size while preserving local image details [33].

Image registration is the process of aligning two images: a fixed image and a moving image [33]. The objective is to transform the moving image so that it aligns with the fixed image, resulting in a registered image and a corresponding set of transformation parameters. This process starts by sampling both the fixed and moving images, where samples represent a subset of voxels from the images, as it is often unnecessary to use all voxels. These samples are then compared using a metric that quantifies the similarity or difference between the images. An optimization technique is used to minimize the difference (or maximize the similarity) of this metric, which is dependent on the transformation parameters. The transformation parameters can be saved and applied to align other images with the fixed image. Optionally, a mask can be used to focus the registration process on specific regions of the image. In this case, samples are taken only from within the masked area, allowing for more precise alignment in regions of interest.

3.3.1. Previous Studies

The Texas studies [4–9] and Oudhof [10] categorise types of registration into two main categories. Intra-scan registration involves aligning scans acquired during a single scanning session. In this research, this refers to aligning the DCE and DWI scans with each other for a specific time point t_i . The other category is inter-scan registration, which aligns images acquired from different imaging sessions of the same patient. In this research, this involves aligning DCE and DWI scans across all time points.

The Texas studies [4–9] rigidly align intra-scans and used a non-rigid approach using an adaptive basis algorithm with a tumour volume-preserving constraint for inter-scans [34], yet they provide limited detail on the registration process.

In previous theses, Oudhof [10] also uses rigid registration for intra-scans and non-rigid registration for inter-scans. The decision to use rigid registration for intra-scans is grounded on the assumption that both DCE and DWI scans are conducted consecutively without interruptions, such as patient movement or breaks. Oudhof uses the ITKElastic package [35], which includes predefined parameter maps. Specifically, Oudhof applies the default 'rigid' and 'bspline' parameter maps. Additionally, Oudhof chooses to register all images based on the DCE scan from time point t_1 , due to the high resolution of the DCE scan, although the rationale for selecting t_1 is not elaborated upon.

Before applying the ITKElastic registration algorithm, Oudhof [10] used zero-padded Fast Fourier Transform (FFT) to upsample DWI images along the z -axis. This resampling is necessary because the resolutions of the DCE and DWI images are significantly different, making it difficult for the registration algorithm to match samples accurately. Therefore, Oudhof opted to upsample the DWI image in the z -direction. Additionally, to reduce the intensity discrepancies inherent to different MRI sequences, both the intensities of the DWI and DCE images were scaled by dividing each image by its maximum value.

3.3.2. Current Approach

Examining the scans of the current patient dataset and considering the ultimate objective has led to different choices compared to those made in the previous study by Oudhof [10]. This section elaborates on the choices and reasoning behind the approach used for this research.

Sequential Rigid and Affine Registration

While using non-rigid registration for inter-scan alignment can correct more complex distortions, it carries the risk of overfitting and may fail to preserve anatomical relationships accurately. Additionally, non-rigid registration involves a greater number of parameters and computational steps, leading to longer processing times. Consequently, non-rigid registration should be avoided when possible.

However, relying solely on a rigid approach for intra-scan registration is insufficient for accurately aligning all scans, particularly when patient movement has occurred. In such cases, it is necessary to consider not only translation and rotation but also scaling and shearing. Therefore, affine registration is a more suitable approach. The ITKElastic package, in particular, supports a sequential registration strategy. Initially, rigid registration, which addresses translations and rotations, ensures basic alignment based on prominent anatomical features shared between image types. This step reduces the computational complexity for subsequent affine registration, which incorporates additional transformations, such as scaling and shearing, to account for variations in resolution or image magnification between DCE and DWI scans. This sequential approach balances computational efficiency with the

flexibility needed to accurately align images while preserving essential anatomical relationships and spatial coherence.

Image Down-Sampling & Scaling

For the intra-scan registration, the DWI and DCE scans also have to be resampled and scaled. However, different choices are made: the DWI scans instead of the DCE scans are chosen to be the fixed images for several reasons. From the DWI scans, the most important information, the number of tumour cells per voxel, will be extracted (see Section 3.5). Moreover, the 3D model used to model the behaviour of the tumour has a high computational time, so the dimensions have to be downsampled. Therefore, it is more convenient to downsample the DCE image to the DWI image instead of upsampling the DWI image now and later downsampling it. On top of that, by upsampling data, data points are created, therefore with this approach reliable data is retained.

For the downsampling of the DCE images, this research, similar to Oudhof [22], employed FFT, using Python's `scipy.fft` functions (`rfft` and `irfft`). These functions were selected for their efficiency and compatibility with the real-valued data derived from the voxelized MRI images. While MRI data are typically complex-valued, the images used in this study were voxelized and converted to a real-valued format, making these FFT functions ideal for processing. This approach ensures accurate and efficient resampling. Although the default `AdvancedMattesMutualInformation` metric used for registration theoretically requires no scaling, scaling was necessary in practice. This need for scaling might be due to the reduction in the dynamic range of intensities, as the unscaled images had a range that could have been too wide. While Oudhof [10] used a method of normalizing by dividing by the maximum voxel value in the images, this approach was found to be sensitive to outliers, often leading to total misalignment. Therefore, an alternative method was adopted: scaling the intensities by dividing by the average voxel value across the entire image.

Registration Order

As a consequence of the previous steps, the DWI at t_1 will serve as the fixed image for the entire registration process. The selection of t_1 is justified by the need to calibrate the DI-MCRD model using t_0 and t_1 , followed by the estimation of tumour behaviour from t_1 to t_2 . Therefore, ensuring the reliability of data at t_1 is crucial. Consequently, the registration process will follow the structure outlined in Figure 3.2.

Moreover, since both DWI and DCE image sets comprise multiple images, a reference image must be chosen for the registration processes. Subsequently, parameter maps obtained from this reference image can be applied to register the remaining images. For the DWI scan the $b = 800$ s/mm², was selected due to its superior visibility of the boundary between the patient's thorax and the background. Even with this setting, the boundary remains somewhat indistinct. Conversely, for the DCE scans the boundary is much clearer. Therefore, the first DCE image (pre-contrast) is chosen, ensuring that the tumour does not receive additional intensity due to the CA (as it is not present yet) that could potentially impact the registration process. It should be noted that all visualizations of the registration process will be of these reference images.

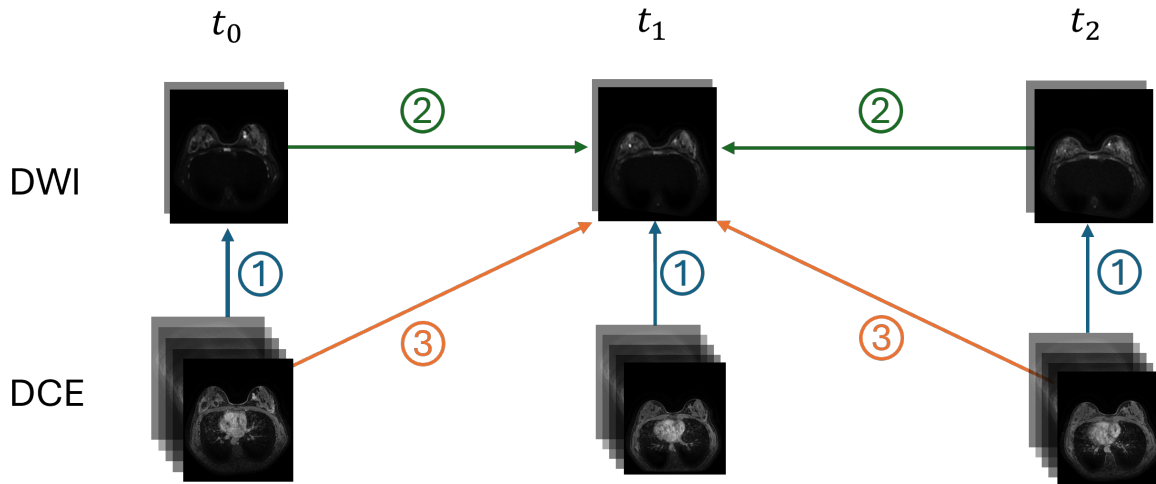


Figure 3.2: MRI image along with the registration structure for aligning all images to the DCE images at t_1 . The registration process involves three steps, step ①: DCE images are registered to the DWI images within the same time step t_i , step ②: DWI images at t_0 and t_2 are registered to the DWI image at t_1 , step ③: DCE images from t_0 and t_2 are registered to the DWI at t_1 using the parameter map derived from step ②.

All in all the registration of the images of one patient consists of the following steps:

1. Downsample all DCE images to the resolution of the DWI images using FFT.
2. Intra-scan registration for each t_i that is not yet aligned (see step ① Figure 3.2):
 - i. Scale the intensities of the DWI and DCE images by dividing them by their average value and save these average values.
 - ii. Using sequentially the default parameter maps 'rigid' and 'affine' register the DCE image at τ_1 on the DWI image from $b = 800 \text{ s/mm}^2$ image and save the parameter maps.
 - iii. Apply the parameter maps to the other DCE images τ_n for $n = 2, \dots, 8$ and the tumour segmentation.
 - iv. Scale the DCE images back using the saved average values.
3. Inter-scan registration (see step ② & ③ Figure 3.2):
 - i. Using sequentially the default parameter maps 'rigid' and 'affine' register the DWI images from t_0 and t_2 on DWI image from t_1 , all using the $b = 800 \text{ s/mm}^2$ image. Moreover, save the parameter maps.
 - ii. Apply the corresponding parameter maps to the DWI images with $b = 50 \text{ s/mm}^2$ from t_0 and t_2 .
 - iii. Apply the parameter maps to the corresponding DCE images and tumour segmentations at each timestep (step ③ Figure 3.2).

It should be noted that to generate the transformed moving image, the original grid of the moving image is resampled onto the deformed grid. Since this process may result in points being mapped to locations where there was no prior information, interpolation is necessary to estimate these values. In medical imaging, the BSpline interpolator is commonly used. However, to maintain the binary nature of tumour segmentations, the BSpline interpolator is configured to a linear mode by setting its order to zero during the registration of the tumour segmentations. For the other registrations, the interpolator's default settings are used.

3.3.3. Registration results

Once images are registered, the results can be effectively visualized using a checkerboard image, which alternates blocks of the fixed and registered images in a grid pattern. This method provides a

clear and intuitive display of the alignment and transformation achieved during the registration process, making it easier to assess the overlap and identify any remaining misalignments between the images.

The goal of this research is to align all images with the DWI image at t_1 , which serves as the overall fixed image for the registration process, with a particular focus on aligning the breast regions. In this subsection, the DCE scan at t_0 is specifically chosen to demonstrate the registration process due to its significant misalignment with the fixed image, requiring multiple iterations to achieve proper alignment. Consequently, in Figure 3.3, each sub-image presents a checkerboard representation of the overall fixed image (DWI t_1) and either the non-registered DCE t_0 image (Figure 3.3a) or the registered DCE t_0 images (Figures 3.3b–3.3d).

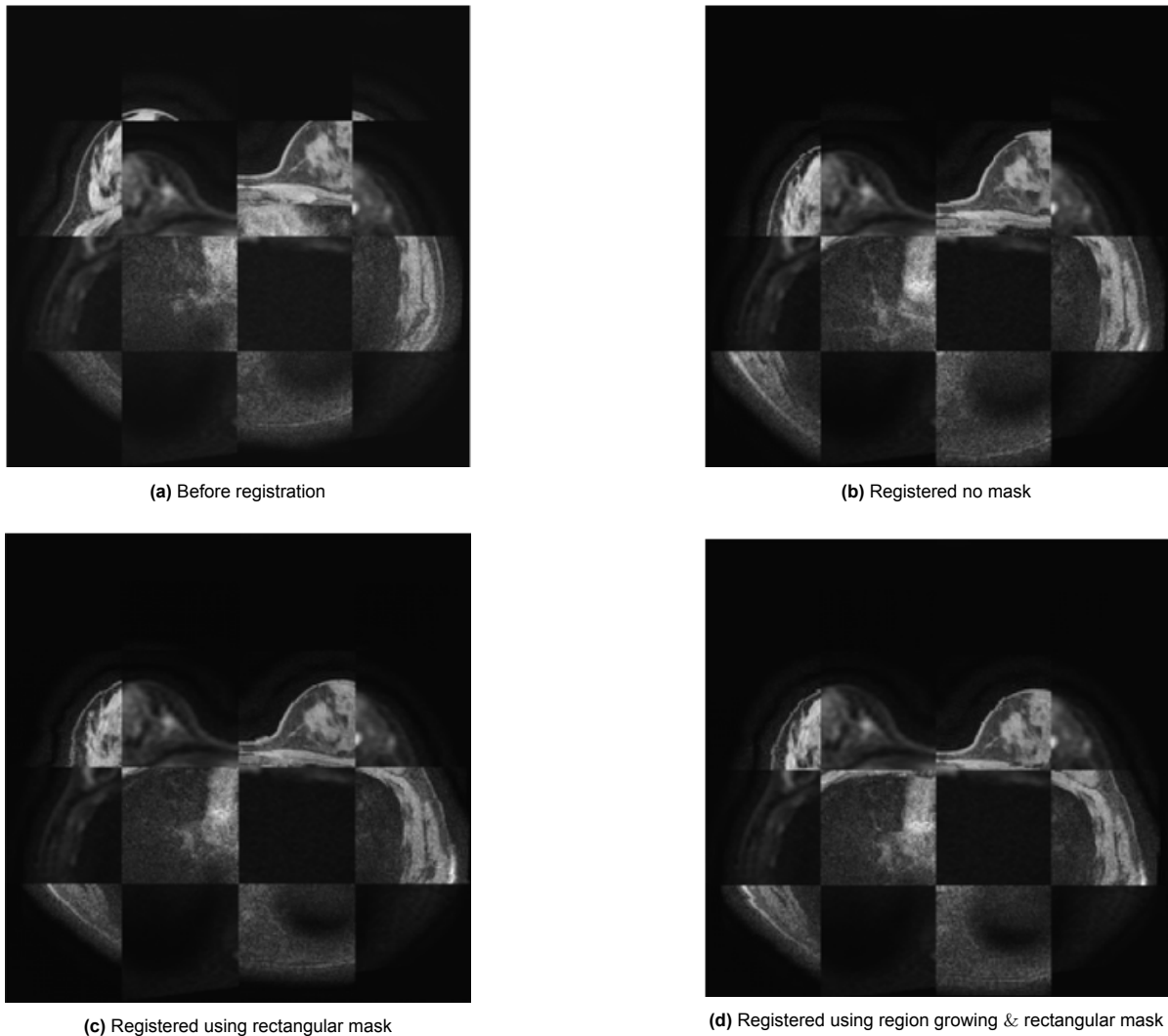


Figure 3.3: Checkerboard representation of DWI image at t_1 and DCE image at t_0 , before and after registration with and without different masks. These images correspond to p_1 and the middle slices are shown.

The non-registered DCE t_0 image shows significant misalignment with the fixed image in Figure 3.3a, indicating that considerable registration is necessary. The first iteration of the registration process, using the method described above, yielded the result shown in Figure 3.3b. The image remains poorly aligned with the fixed image, likely because the algorithm sampled points from areas outside the breast region, such as the background and thoracic regions. These irrelevant areas introduce noise into the alignment metric, leading to suboptimal registration results, especially in crucial regions like the breasts, where precise alignment is vital for accurate tumour modelling. To improve alignment accuracy, the algorithm should be directed to sample only within the breast region, using a masking technique.

Applying a rectangular mask to the upper two-thirds of all images produced the registration results shown in Figure 3.3c. The decision to mask the upper two-thirds, rather than the upper half, was based on the presence of breast tissue in the lower halves of some images. The mask applied to the DCE t_0 image is visualized in Figure 3.4a. Despite this masking approach, the registration result shows that the right breast and the sternum are still not perfectly aligned. Since these images form the basis for initial values in the mathematical model, improving alignment is crucial. Therefore, masks generated using region-growing techniques will be introduced on which subsection will elaborate.

Region Growing

Region growing is an image segmentation technique that begins with a seed point and includes neighbouring pixels based on a specified tolerance. The tolerance level determines how similar the pixel values need to be to the seed point for inclusion in the region, thus controlling the growth of the region from the seed point [36].

To improve the mask obtained from region growing, closing is often used. Closing is a morphological operation effective for filling small holes and gaps within the segmented region and smoothing the boundaries of the object. This is achieved by first performing dilation and then erosion [36].

Dilation is a morphological operation used to expand the boundaries of objects in a mask by adding pixels to their edges. It effectively closes small holes and gaps within the objects. Dilation operates using a structuring element, which defines the neighbourhood around each pixel and guides how the dilation affects the image. Larger structuring elements encompass more of the neighbourhood surrounding each pixel, influencing the extent to which dilation expands the objects. Erosion, on the other hand, is a morphological operation that removes pixels on the edges of objects in the mask, effectively shrinking the object. It is useful for eliminating small noise and separating connected objects [36]. After this process, the largest connected component is taken as the mask.

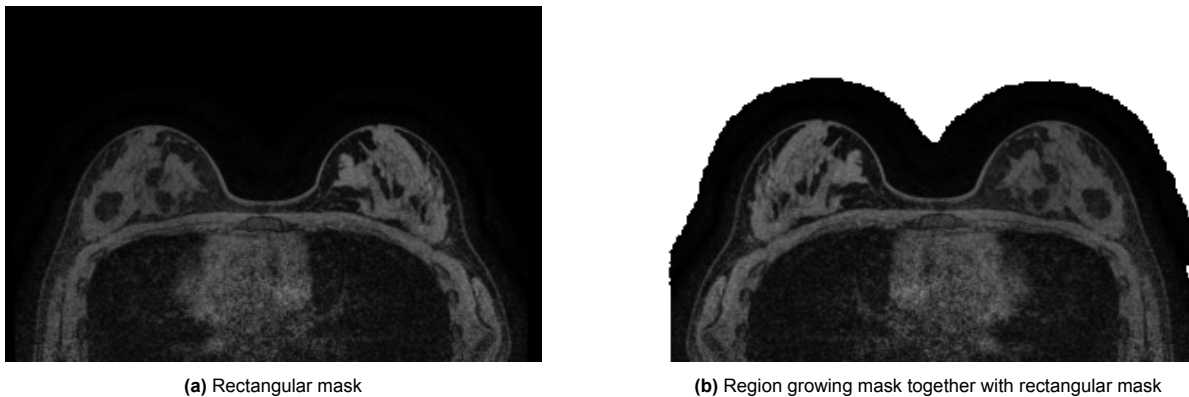


Figure 3.4: DCE image from t_0 of p_1 with masks applied, showing only the masked parts of the middle slices.

Using the region growing technique together with morphological operations, and combining this with the previously used mask, a new mask is obtained, an example of which is shown in Figure 3.4b. The structural element used for dilation is a 3-dimensional ball with radius 3. The aim is to obtain some background around the thorax's boundary, which is achieved with this structuring element and a relatively high tolerance that is scan-dependent. This extra background allows the registration algorithm to use the contrast between the background and the person's body to achieve better alignment of the images. Using this mask, the registration results shown in Figure 3.3d were achieved. These results demonstrate well-aligned images, indicating the successful completion of the registration step.

Note that the generation of the masks must be performed for every patient. This includes manually selecting a seed point for each image and tuning the region-growing algorithm by adjusting its threshold to obtain a good mask.

3.4. ROI

As seen in Figures 3.1 to 3.4, the images include extra information that is not relevant to modelling how breast cancer tumours grow. Therefore, it is essential to delineate the region of interest (ROI) that specifically includes the breast or breasts where the tumour is located.

3.4.1. Previous Studies

In the studies from Texas [4–9], no specific mention is made about excluding irrelevant information from the images. However, only the breast with the tumour is typically represented in the results. In Oudhof’s study [10], manual selection of the breast ROI is performed, followed by using region growing to create a mask delineating the breast area and distinguishing it from the background.

3.4.2. Current Approach

In this research, ROIs are manually selected by defining the x and y ranges based on the fixed reference scan (DWI at t_1). This ROI selection is then uniformly applied to all other aligned images. An example of ROI selection is shown in Figure 3.5a. After defining the ROI, the same region-growing algorithm as for the registration masks (including the same structuring element) is used to generate a binary mask for the breast area. Figure 3.5b illustrates the generated breast mask applied on the reference image.

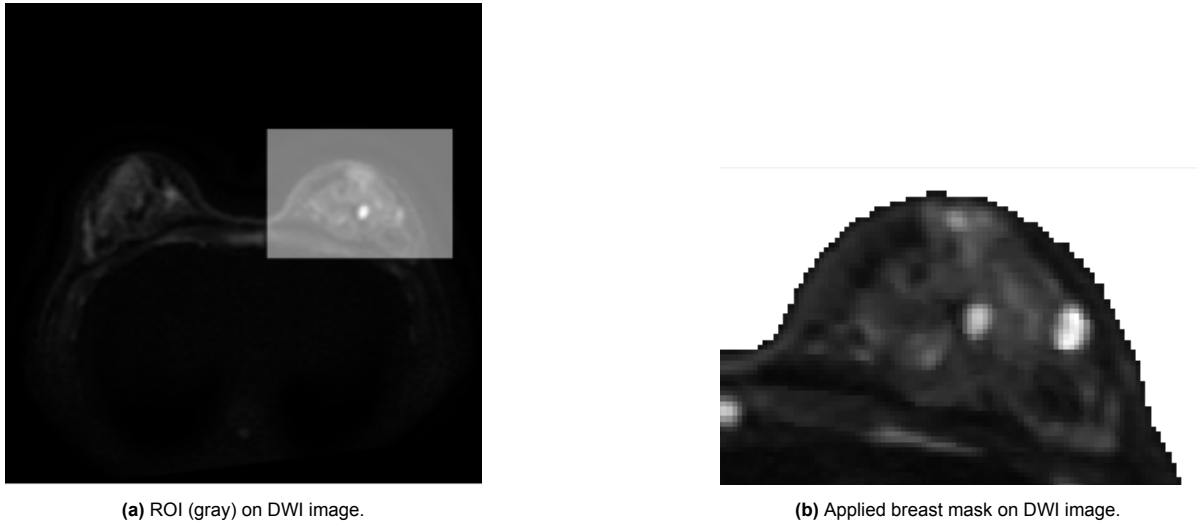


Figure 3.5: ROI and breast mask of patient p_1 displayed overlaid on the fixed reference image.

3.5. Number of Tumour Cells Calculation

Only knowing the location of the tumour is not enough for the initial values of the used mathematical model. Also, the number of tumour cells per voxel has to be known. As mentioned in Section 2.4.1 the DWI scans can be used to make an approximation of the number of tumour cells on a voxel-by-voxel basis.

3.5.1. Previous Studies

In the Texas studies [4–9], the ADC value is computed using the formula:

$$S_i = S_0 e^{-\text{ADC} \cdot b_i}, \quad (3.1)$$

where S_i is the signal intensity when the degree of diffusion weighting b_i equals i . To determine the ADC values, equation (3.1) is fitted to all b_i values for each voxel using nonlinear least squares optimization [37].

With the use of equation (3.2), the ADC value can be transformed for each voxel within the tumour ROI into an estimate of the tumour cell number, $N(\bar{x}, t)$ [4–9]:

$$N(\bar{x}, t) = \theta \left(\frac{\text{ADC}_w - \text{ADC}(\bar{x}, t)}{\text{ADC}_w - \text{ADC}_{\min}} \right). \quad (3.2)$$

Here, θ denotes the carrying capacity, representing the total number of tumour cells that fit into a voxel. θ is defined assuming a spherical packing density of 0.7405 and a nominal tumour cell radius of $10 \mu\text{m}$. ADC_w corresponds to the ADC of free water ($3 \times 10^{-3} \text{ mm}^2/\text{s}$), $\text{ADC}(\bar{x}, t)$ is the ADC value at voxel position \bar{x} and time t in image space, and ADC_{\min} is the minimum ADC value in a tumour voxel for the patient [4–9]. Moreover, the carrying capacity can be expressed as follows:

$$\theta = \frac{\text{voxel volume} \cdot \text{packing density}}{\text{tumour cell volume}} = \frac{\text{voxel volume} \cdot 0.7405}{4\pi/3 \cdot (0.01)^3} = 1.768 \cdot 10^5 \times [\text{voxel volume} (\text{mm}^3)]. \quad (3.3)$$

Oudhof [10] uses the ADC maps computed by the MRI scanners (See Section 3.1) rather than deriving them from the DWI scans. To estimate the number of tumour cells, Oudhof uses the same methodology as the Texas studies, using (3.2) along with identical parameter assumptions. However, ADC_{\min} is determined as the overall minimum ADC value of t_0 and t_1 for each patient since the third scan is used for verification and not calibration.

3.5.2. Current Approach

In this research, the DWI scans are used to compute the ADC map independently, rather than relying on the precomputed values from the MRI scanner. This approach is taken to avoid potential miscomputations from the MRI-generated ADC values and to ensure better transparency and explainability of the results. Subsequently, the ADC values are used following the methodology described by Oudhof [10]. Specifically, equation (3.2) is used along with identical parameter assumptions to compute the number of tumour cells within each voxel, defining ADC_{\min} as the overall minimum ADC value of t_0 and t_1 .

As mentioned in Section 3.1, the DWI scans provided by EMC include $b = 50 (= b_{50})$ and $b = 800 (= b_{800})$ s/mm^2 , so S_0 is unknown. b_0 scans are not required, since using a small but nonzero b -value like b_{50} , instead of b_0 , minimizes perfusion effects, resulting in more accurate diffusion measurements and fewer outliers.

To calculate the ADC value using these b -values, the following equation can be used [38]:

$$\text{ADC} = \frac{1}{b_{800} - b_{50}} \ln \left(\frac{S_{50}}{S_{800}} \right). \quad (3.4)$$

However, using (3.1) for b_{50} and b_{800} , one obtains a system of two equations:

$$\begin{cases} S_{50} &= S_0 e^{-\text{ADC} \cdot b_{50}}, \\ S_{800} &= S_0 e^{-\text{ADC} \cdot b_{800}}, \end{cases} \quad (3.5)$$

which involves two unknowns, S_0 and ADC, and leads to the same analytic solution as (3.4).

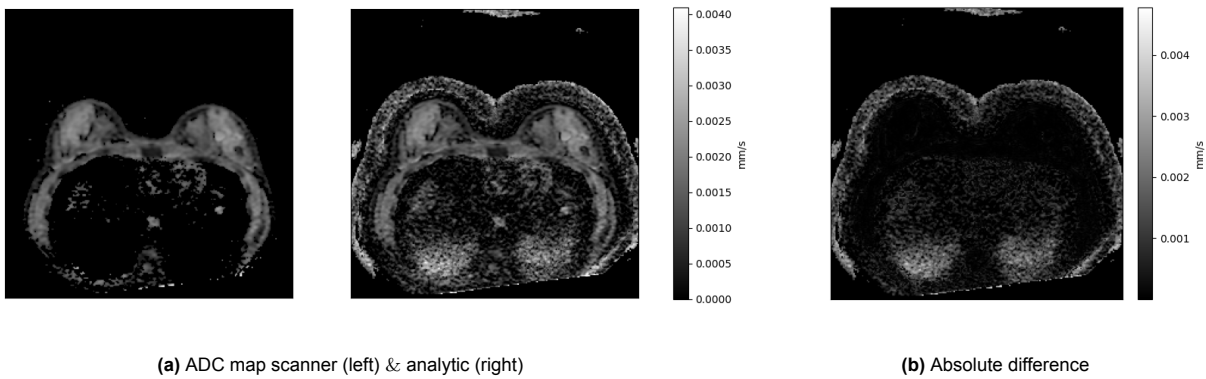


Figure 3.6: Computed ADC maps generated by the MRI scanner and analytically derived ADC values using (3.4) (a), along with the absolute error between the two maps (b). The results are of p_1 at t_1 , showing the middle slice in the z -direction.

Figure 3.6a shows the ADC maps, with the left map generated by the MRI scanner and the right map analytically computed using equation (3.4). In Figure 3.6b, the absolute difference between the two methods is illustrated. These figures show that the analytic computation assigns fewer values to zero, particularly outside the thoracic boundary. The maximum absolute difference observed is $5.2 \cdot 10^{-3}$ mm/s.

For this research, it is crucial to determine whether there are differences in ADC values within the breast, as these values will be used to estimate the number of tumour cells. Although not shown here, when zooming in on Figure 3.6b, a small error can be detected in the breast regions. To assess the actual impact, the number of tumour cells per voxel was computed using (3.2) for both ADC maps. These results are shown in Figure 3.7.

From this figure, it is immediately apparent that the self-computed ADC values result in a smoother distribution of tumour cells compared to the MRI-derived ADC map. Furthermore, the overall difference between the two methods is significant, with the maximum discrepancy reaching 2.91×10^4 tumour cells per voxel. This demonstrates that using a self-computed ADC map has a considerable impact on the estimated number of tumour cells. The MRI scanner tends to assign zero to values it cannot fit an ADC for, and the exact fitting process used by the scanner is not fully transparent. As a result, the self-computed ADC values are considered more reliable, especially since there is no ground truth for the number of tumour cells, which are approximated from the scans. Moreover, in Section 4.1.8, different results of the DI-MCRD model compared to Engelberts [12] are presented, due to these differences in the initial number of tumour cells differs from the distinct preprocessing pipelines.

On top of that, Engelberts [12] highlighted the unrealistic nature of the number of tumour cells per voxel in his discussion. He observed that the preprocessed EMC data provided by Oudhof [10] exhibited a binary pattern, where voxels containing the tumour consistently showed the maximum carrying capacity in all scans and zero where there were no tumour cells present. However, the current results and the regenerated results using the MRI ADC map do not show such binary behaviour.

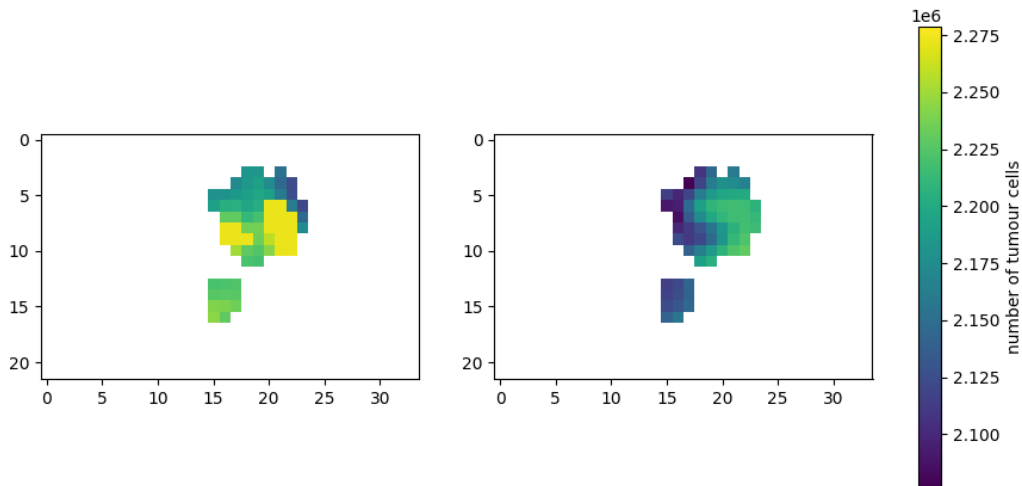


Figure 3.7: Number of tumour cells of p_1 at t_1 using different ADC maps: ADC computed by MRI (left) and analytic ADC (right). The middle slice in the z -direction is shown.

3.6. Segmentation Breast Tissue

For the DI-MCRD model, precise knowledge of the locations of different tissues within the breast is needed. While the tumour locations are identified, also the locations of fibroglandular and adipose tissues within the ROI have to be defined. As discussed in Section 2.4.2, DCE-MRI can effectively segment these breast tissues.

3.6.1. Previous Studies

In the Texas studies [4–9], various segmentation methods have been used. The first two studies [4, 5] used signal intensity-based segmentation to differentiate between adipose and fibroglandular tissues. In contrast, the subsequent study [6] applied an anatomical THRIVE method, which involved a high-resolution T_1 volume examination. The following study [7] did not specify the segmentation method used, while the final studies [8, 9] used a k -means clustering algorithm. Although these studies used different segmentation approaches, the rationale behind the selection of methods was not explicitly detailed.

Oudhof [10] explored three segmentation methods: simple thresholding, contrast-limited adaptive histogram equalization, and global histogram equalization. Global histogram equalization was identified as the most effective approach.

3.6.2. Current Approach

Building on Oudhof's [10] findings, her method for tissue segmentation will be adopted in this research. Hence, tissue segmentation in this study is performed using global histogram equalization followed by a simple thresholding technique. The algorithm is applied to the first DCE images, τ_1 , at scan time points t_0 and t_1 , considering only the voxels within the breast that do not correspond to tumour voxels. Multiple time points τ_i were tested, and they all gave similar results.

The results are validated against segmented DCE scans, resulting in a general threshold of 150, which is increased to 170 for p_4 due to tumours in both breasts. Figure 3.8 shows an example of a segmented breast alongside the original image.

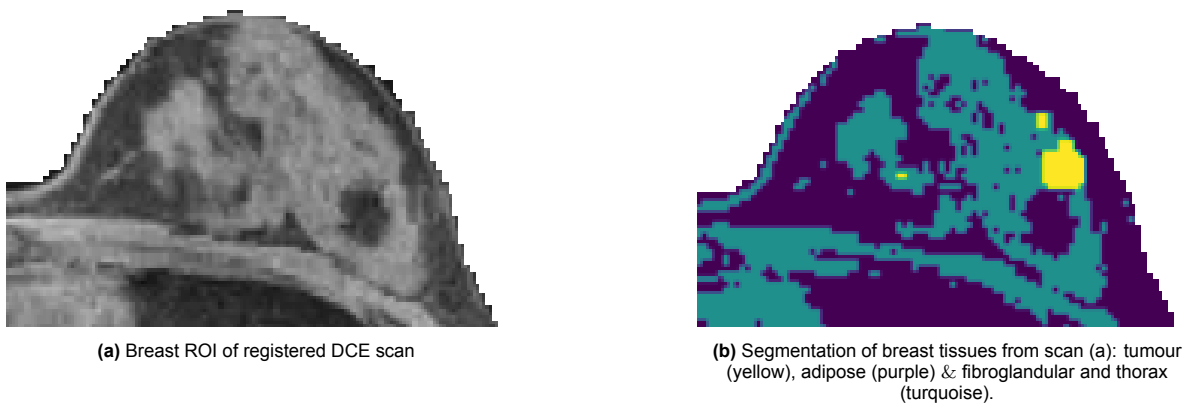


Figure 3.8: Tissue segmentation of p_1 at t_0 using global histogram equalization together with a simple threshold (=150). The middle z -slices are shown.

3.7. Concluding

The novel preprocessing process has been applied to the data of all 13 patients of whom the pre-processed data will be used in the subsequent chapters. This comprehensive preprocessing is crucial for ensuring the accuracy and reliability of the DI-MRCD model's input data. By addressing issues identified in previous studies and testing the pipeline on a larger dataset, the preprocessing pipeline has been optimized and made more generalizable. Consequently, this enhanced pipeline facilitates efficient preprocessing for patients, ensuring robustness and effectiveness when new patients are included in the research.

The manual steps required per patient include generating registration masks for each scan time point, manually selecting the ROI in which the breast with the tumours is located, and generating the corresponding breast ROI.

4

DI-MCRD Model

In this chapter, the DI-MCRD model and calibration algorithms from previous theses [10–12], which are based on the Texas studies [4–9], are introduced and explained. The expanded dataset, which includes patients with scans at two and three time points, is then processed through the model to establish baseline results and provide a more comprehensive evaluation of the model's performance with a larger sample. Following this, two modelling cycles with adaptations are conducted, and the preprocessed data of several patients from the expanded dataset is run through the updated model to assess the impact of these changes.

4.1. Current Model

The current 3-dimensional model including the mechanical coupling of tissue properties to tumour growth and the delivery of systemic therapy will be explained in the section. The governing equation of, a reaction-diffusion type partial differential equation for the spatial-temporal evolution of the number of tumour cells $N(\bar{x}, t)$ for time, t , and per voxel \bar{x} is given as follows [7, 8]:

$$\frac{\partial N(\bar{x}, t)}{\partial t} = \overbrace{\nabla \cdot (D(\bar{x}, t) \nabla N(\bar{x}, t))}^{\text{Diffusion}} + \underbrace{\mathbf{k}(\bar{x}) N(\bar{x}, t) \left(1 - \frac{N(\bar{x}, t)}{\theta} \right)}_{\text{Proliferation}} \underbrace{- \alpha C_{\text{tissue}}^{\text{drug}}(\bar{x}, t) N(\bar{x}, t)}_{\text{Reduction due to treatment}}, \quad (4.1)$$

where the diffusion term represents the effect of the tumour cell movement and the reaction term consists of the tumour cell proliferation and cell death in time. Note that the death due to treatment term is based on the first Texas study that included the chemotherapy term [7]. However, in Section 4.1.3, updated DI-models from other Texas studies [8, 9], the model used by Slingerland [11], and other potential approaches will be introduced and explored. In Tables 4.1 and 4.2 all model variables and parameters are described for a complete overview, the rationale behind the terms in detail will be described below.

4.1.1. Diffusion Term

The function $D(\bar{x}, t)$ represents the random movement or diffusion of tumour cells. In a previous study by the Texas research group [4], this diffusion was treated as a constant, leading to isotropic tumour growth. However, when compared with clinical observations, the same study found that incorporating the specific breast anatomy of each patient into the diffusion term significantly improved the accuracy of predicting the total number of tumour cells. Consequently, they used the von Mises stress $\sigma_{\text{vm}}(\bar{x}, t)$ to mechanically link $D(\bar{x}, t)$ to the material properties of breast tissue:

$$D(\bar{x}, t) = D_0 e^{-\gamma \sigma_{\text{vm}}(\bar{x}, t)}, \quad (4.2)$$

where γ is an empirical coupling constant, and D_0 is the diffusion coefficient in the absence of external forces, calibrated using MRI data. The exponential term reduces D_0 based on the von Mises stress,

which is calculated using a force equilibrium condition that accounts for pressure from the tumour cells and governs the mechanical coupling:

$$\nabla \cdot G(\bar{x})\nabla\vec{u} + \nabla \frac{G(\bar{x})}{1-2\nu} (\nabla \cdot \vec{u}) - \lambda \nabla N(\bar{x}, t) = 0, \quad (4.3)$$

where \vec{u} represents the displacement caused by tumour cell growth (spreading of the tumour), λ is another empirical coupling constant, and $G(\bar{x}) = E(\bar{x})/(2(1+\nu))$ represents the shear modulus [4–6]. Young's modulus E and Poisson's ratio ν describe the material properties.

Oudhof [10] found that using a 2D version with thick slices (6.55 mm) improved the model when a mechanically coupled approach was used compared to a non-coupled model. Similarly, Slingerland [11] observed a slight improvement with the coupled model when using thicker slices, suggesting potential benefits. However, as mentioned before their study was limited to a dataset of only three patients, so no definitive conclusions could be drawn. Given the success of the coupled model in the Texas studies [4–9] and its more realistic representation of tumour growth due to the inclusion of the effects of surrounding tissue forces, Engelberts [12] focused solely on the 3-dimensional mechanically coupled model in his thesis. Therefore, this research will also consider the 3D coupled model.

For a 3-dimensional model, equation (4.3) is used to obtain the von Mises stress as follows [12]: Firstly, denote the solution of (4.3) by $\vec{u} = (u, v, w)$ [mm], representing the local deformations in the x -, y -, and z -direction, respectively. The normal and shear strain on the tissue with this deformation, for small displacements, is given by:

$$\begin{pmatrix} \epsilon_{xx} \\ \epsilon_{yy} \\ \epsilon_{zz} \\ \epsilon_{xy} \\ \epsilon_{xz} \\ \epsilon_{yz} \end{pmatrix} = \begin{pmatrix} \partial u / \partial x \\ \partial v / \partial y \\ \partial w / \partial z \\ \partial u / \partial y \\ \partial u / \partial z \\ \partial v / \partial z \end{pmatrix}. \quad (4.4)$$

Here, the first three terms represent the normal strains, and the last three terms represent the shear strains. Using Hooke's Law in stiffness form for linear isotropic materials, the normal and shear stresses can be found:

$$\begin{pmatrix} \sigma_{xx} \\ \sigma_{yy} \\ \sigma_{zz} \\ \sigma_{xy} \\ \sigma_{xz} \\ \sigma_{yz} \end{pmatrix} = \frac{2G(\bar{x})}{1-2\nu} \begin{bmatrix} 1-\nu & \nu & \nu & 0 & 0 & 0 \\ \nu & 1-\nu & \nu & 0 & 0 & 0 \\ \nu & \nu & 1-\nu & 0 & 0 & 0 \\ 0 & 0 & 0 & 1-2\nu & 0 & 0 \\ 0 & 0 & 0 & 0 & 1-2\nu & 0 \\ 0 & 0 & 0 & 0 & 0 & 1-2\nu \end{bmatrix} \begin{pmatrix} \epsilon_{xx} \\ \epsilon_{yy} \\ \epsilon_{zz} \\ \epsilon_{xy} \\ \epsilon_{xz} \\ \epsilon_{yz} \end{pmatrix} \quad (4.5)$$

Here, again $G(\bar{x}) = \frac{E(\bar{x})}{2(1+\nu)}$, where the shear modulus $G(\bar{x})$ is spatially dependent for the three different types of tissue in the breast. Poisson's ratio and Young's modulus remain consistent as given in Table 4.2. Then, the von Mises stress at each voxel can be computed as follows [12]:

$$\sigma_{\text{vm}} = \sqrt{\frac{1}{2} [(\sigma_{xx} - \sigma_{yy})^2 + (\sigma_{xx} - \sigma_{zz})^2 + (\sigma_{zz} - \sigma_{yy})^2 + 6(\sigma_{xy}^2 + \sigma_{xz}^2 + \sigma_{yz}^2)]}. \quad (4.6)$$

4.1.2. The First Reaction Term

The proliferation of tumour cells is represented by the first reaction term in equation (4.1). This term accounts for logistic growth, which is determined per voxel. The carrying capacity θ is the same as mentioned in Section 3.5, the maximum number of tumour cells that fit in one voxel. The logistic term, which has been shown to accurately model tumour growth (see Section 2.2), represents the limitation on tumour growth when a voxel is 'full'. This limitation arises from constraints such as nutritional, immunological, or spatial factors. Additionally, MRI data is used to calibrate the spatially resolved proliferation rate, denoted as $k(\bar{x})$.

4.1.3. The Second Reaction Term

The second reaction term in equation (4.1) characterizes the reduction of tumour cells due to therapy. The drug-induced term varies across studies, and the different DI models are explained in this subsection.

Extended Kety Tofts

Initially, the first approach from the Texas studies [7] is considered, as expressed in (4.1). The parameter α signifies the therapy's efficacy, and $C_{\text{tissue}}^{\text{drug}}(\bar{x}, t)$ represents the drug concentration in the tumour tissue at position \bar{x} and time t , approximated from the extended Kety–Tofts (EKT) model and DCE-MRI data [7]. Before applying the EKT model, the contrast agent (CA) concentration in the tissue must be derived from the DCE scans, as the MRI signal does not directly correlate linearly with CA concentration. A calibration sequence (e.g., with specific flip angles) is required to accurately estimate this concentration. However, [7] does not specify the calibration techniques used. The EKT model, a two-compartment model, describes the temporal variations in the concentration of CA between the tissue and blood plasma spaces [39].

$$C_{\text{tissue}}^{\text{CA}}(t) = K^{\text{trans}} \int_0^t \left(C_{\text{plasma}}^{\text{CA}}(u) \cdot \exp\left(-\frac{K^{\text{trans}}}{v_e}(t-u)\right) \right) du + v_p C_{\text{plasma}}^{\text{CA}}(t), \quad (4.7)$$

where $C_{\text{tissue}}^{\text{CA}}(t)$ and $C_{\text{plasma}}^{\text{CA}}(t)$ denote the concentrations of the CA in tissue and plasma, respectively. K^{trans} [d^{-1}] represents the volume transfer constant of the CA from the plasma space to the tissue space. Moreover, the volume fractions of the extravascular extracellular space and the plasma space are denoted by v_e and v_p , respectively. When $v_p = 0$ the model is known as the Kety-Tofts model (KT). The concentration of the CA in the tissue as mentioned before is derived from the DCE-MRI scans, while the concentration of the CA in the plasma is based on a literature function, known as the arterial input function (AIF), chosen to be population-averaged [40]. Using these concentrations, Equation (4.7) can be fitted to estimate K^{trans} , v_e , and v_p on a voxel-by-voxel basis: $K^{\text{trans}}(\bar{x})$, $v_e(\bar{x})$, and $v_p(\bar{x})$. Assuming that the drug distribution behaves similarly to that of the CA, the EKT model, together with the estimated variables, the drug concentration for each voxel \bar{x} at time t can be obtained:

$$C_{\text{tissue}}^{\text{drug}}(\bar{x}, t) = K^{\text{trans}}(\bar{x}) \int_0^t \left(C_{\text{plasma}}^{\text{drug}}(u) \cdot \exp\left(-\frac{K^{\text{trans}}(\bar{x})}{v_e(\bar{x})}(t-u)\right) \right) du + v_p(\bar{x}) C_{\text{plasma}}^{\text{drug}}(t), \quad (4.8)$$

where $C_{\text{plasma}}^{\text{drug}}(t)$ denotes the drug concentration in plasma, a literature-based function specific to the drug. Specifically, the measured population curves for drug concentration in the plasma for specific therapies are used [7].

Nomarlized Blood Volume Map with Kety Tofts

Moving on to the subsequent Texas study [8], which extends the DI-model to incorporate multiple chemotherapy regimens, the governing equation becomes:

$$\frac{\partial N(\bar{x}, t)}{\partial t} = \nabla \cdot (D \nabla N(\bar{x}, t)) + \mathbf{k}(\bar{x}) N(\bar{x}, t) \left(1 - \frac{N(\bar{x}, t)}{\theta} \right) - C_{\text{drug}}(\bar{x}, t) N(\bar{x}, t), \quad (4.9)$$

where,

$$C_{\text{drug}}(\bar{x}, t) = \underbrace{\alpha_1 C_{\text{drug}1}(\bar{x}, t^*)}_{\text{chemotherapy 1}} \exp(-\beta_1 t) + \underbrace{\alpha_2 C_{\text{drug}2}(\bar{x}, t^*)}_{\text{chemotherapy 2}} \exp(-\beta_2 t). \quad (4.10)$$

Here, α_i represents the efficacy of each drug, and $C_{\text{drug}i}(\bar{x}, t^*)$ denotes the initial concentration of each drug. The term t^* refers to the day of the scan— $t^* = t_0$ during the calibration phase and $t^* = t_1$ during the prediction phase. The parameter β_i governs the exponential decay of the drug. Calibration of α_i and β_i is patient-specific, with β_i constrained within literature-defined [41–45] ranges corresponding to the terminal elimination half-lives of each drug.

The term $C_{\text{drug}i}(\bar{x}, t^*)$ is defined using DCE-MRI scans in conjunction with both the normalized blood volume method (NBVM) and the Kety-Tofts (KT) model. First, $C_{\text{drug}}(\bar{x}, t^*)$ is determined by computing a normalized blood volume map (NBVM). This is achieved by calculating the area under the dynamic curve (AUC) of the baseline-subtracted time courses for each voxel, and then normalizing it by the maximum AUC value from the entire tumour ROI [8]. To explain this process more clearly, it is assumed that the DCE-MRI scans are such that $S(\bar{x}, \tau_n, t^*)$ represents the DCE signal value at voxel \bar{x} for scan time-point τ_n , with $n = 1, \dots, 8$ (pre-contrast for $n = 1, 2$, post-contrast for the remaining time points), and for scan days t^* . The $C_{\text{drug}}(\bar{x}, t^*)$ is then derived by the NBVM method through the following steps [11]:

1. Subtracting the baseline signal: The average baseline signal is subtracted from the pre-contrast dynamic, yielding the baseline-subtracted time course for $n = 3, \dots, 8$:

$$S_b(\bar{x}, \tau_n, t^*) = S(\bar{x}, \tau_n, t^*) - \frac{1}{2} (S(\bar{x}, \tau_1, t^*) + S(\bar{x}, \tau_2, t^*)) \quad (4.11)$$

2. Computing the area under the curve (AUC): The AUC is calculated for each voxel after the contrast injection:

$$\text{AUC}(\bar{x}, t^*) = \int_{\tau_2}^{\tau_8} S_b(\bar{x}, \tau_n, t^*) dt \quad (4.12)$$

3. Normalizing the AUC: The AUC is divided by the maximum AUC across the entire tumour region of interest (ROI):

$$C_{\text{drug}}(\bar{x}, t^*) = \frac{\text{AUC}(\bar{x}, t^*)}{\max_{\bar{x}^* \in \bar{x}_{\text{tum}}} \text{AUC}(\bar{x}^*, t^*)} \quad (4.13)$$

Next, the Texas study [8] briefly mentions that the NBVM $C_{\text{drug}}(\bar{x}, t^*)$ is scaled by the peak concentration of the drug, estimated using the KT model, to define the initial drug distribution throughout the domain at the time of each dose of therapy. Since this is the only explanation provided, the following interpretation is assumed. The peak concentration is obtained by maximizing the drug-specific tissue concentration calculated using the Kety-Tofts model (with $v_p = 0$) for each drug, based on different plasma concentrations $C_{\text{plasma}}^{\text{drug}_i}(t)$. The maximized tissue concentrations, $\max_t C_{\text{tissue}}^{\text{drug}_i}(t)$, are then used to scale $C_{\text{drug}}(\bar{x}, t^*)$ to obtain the following assumed final drug concentration $C_{\text{drug}_i}(\bar{x}, t^*)$:

$$C_{\text{drug}_i}(\bar{x}, t^*) = \frac{C_{\text{drug}}(\bar{x}, t^*)}{\max_t C_{\text{tissue}}^{\text{drug}_i}(t)} \quad (4.14)$$

It should be noted that this Texas study [8] also does not provide details on how the concentration of CA in the tissue is derived using DCE scans. Furthermore, they do not specify how the timing of chemotherapy days is incorporated into their models.

Normalized Blood Volume Method with PET-scan

In the latest Texas study [9], a governing equation similar to (4.9) and a drug expression similar to (4.10) from the previous Texas study [8] are used. However, due to data limitations in temporal resolution, the Kety-Tofts model could not be applied. As a result, only the NBVM, as described above, is used without scaling it by the peak concentration of each drug. This leads to a similar chemotherapy distribution for drug 1 and drug 2, as the study does not provide a methodology for determining two drug-specific concentrations, C_{drug_i} , from a single scan. Consequently, this remains an unresolved issue.

Moreover, the results from the previous Texas study [8] show limitations in predicting the correct outcomes for HER2+ patients. As mentioned earlier, HER2+ patients receive both standard chemotherapies and targeted therapies, such as trastuzumab and pertuzumab, which work differently from standard treatments. The targeted therapies slow down the growth instead of killing the tumour cells. This difference likely contributes to the model's reduced accuracy. To address this, the model was modified in the latest study [9] to incorporate the effects of targeted therapies. This extension introduced more free parameters, necessitating the inclusion of PET scans alongside MRI data, specifically ^{64}Cu -DOTA-trastuzumab PET-CT. With this targeted therapy incorporated, the governing equation becomes:

$$\frac{\partial N(\bar{x}, t)}{\partial t} = \nabla \cdot (D \nabla N(\bar{x}, t)) + \mathbf{k}_H(\bar{x}) N(\bar{x}, t) \left(1 - \frac{N(\bar{x}, t)}{\theta} \right) - C_{\text{drug}}(\bar{x}, t) N(\bar{x}, t), \quad (4.15)$$

Here, \mathbf{k}_H depends on the concentration of the targeted therapies and $\mathbf{k}(\bar{x})$, such that proliferation is inhibited by the targeted therapies. For the explicit formulation of \mathbf{k}_H , please refer to [9].

Previous Theses Drug Inclusion Models

Slingerland [11] investigated the inclusion of chemotherapy in her research. Due to data limitations, using an improved model with a PET scan, similar to the latest Texas study, was not feasible. She compared the Kety-Tofts (KT) model with the Normalized Blood Volume Map (NBVM). For the KT

model, the Extended Kety-Tofts (EKT) model with $v_p = 0$ was used, as described in the first DI-model in this section. However, the application of the NBVM in the DI-model was slightly adapted compared to previous models [8, 9]. She explicitly incorporated the days of chemotherapy treatments and assumed overall drug parameters instead of drug-specific ones. The drug concentration for the NBVM in her case, as used in the governing equation (4.9), was given by:

$$C_{\text{drug}}(\bar{x}, t) = \alpha C_{\text{drug}}(\bar{x}, t_0) e^{-\beta(t-\bar{t})}. \quad (4.16)$$

Slingerland's model uses a single drug efficiency parameter α , a single drug decay parameter β , and a single initial drug distribution $C_{\text{drug}}(\bar{x}, t_0)$, calculated using the NBVM as described in the previous sections [8, 9]. However, it is important to note that C_{drug} is fixed at t_0 , meaning that C_{drug} will not be updated during the prediction phase. Additionally, \bar{t} represents the closest first day of a chemotherapy cycle to t . It should be noted that the specific dosages, as outlined in the chemotherapy schemes in Appendix B, for the different drugs within the cycles are not accounted for. Furthermore, only the first day of each cycle is used for \bar{t} , meaning that the second week of each therapy cycle—when only paclitaxel is administered—is not included in the model.

Both Engelberts and Slingerland [11, 12] discuss the co-dependence between α and β , which led to the decision to include only α in the calibration phase, differing from the approach in [9]. The choice of the drug decay parameter $\beta = 0.5$ is made based on observed behaviour, as the literature is not fully conclusive on its specific value. However, upon examining the found co-dependence, it seems not that clear since α represents the overall drug efficiency, affecting the amplitude of the drug concentration, while β represents the rate of decay of the drug concentration over time. Hence, these parameters serve distinct purposes within (4.16): α affects the magnitude, and β affects the rate of change. Moreover, conducting a dimensional analysis on (4.9) results in $[\alpha] = L^3 M^{-1} T^{-1}$ and $[\beta] = T^{-1}$, which also does not suggest co-dependence. Therefore, reevaluating this choice and including both α and β in the calibration process could improve the model's predictive performance.

Comparing both methods, which are based on numerous assumptions and do not entirely yield the desired results as observed in the literature, Slingerland [11] ultimately chooses the NBVM. This decision is motivated by the NBVM's provision of more realistic outcomes, better suitability for the project's data, and higher efficiency. However, given that neither model achieves the desired behaviour of the drug inclusion and the preference for the EKT model, as highlighted in Texas studies [7, 8], the use of the NBVM remains questionable by Slingerland.

Given these conclusions, re-considering the EKT model is a logical option due to its effectiveness demonstrated in the Texas studies [7, 8]. However, the EKT model is an explicit method that requires more detailed information from the DCE scans than is available in the EMC patient data set. This includes the previously mentioned calibration sequence with specific flip angles to accurately estimate $C_{\text{tissue}}^{\text{drug}}$. Additionally, the arterial input function (AIF) should ideally be patient-specific; however, Oudhof [11] used a general AIF. Given these limitations, applying the EKT model under these conditions would require numerous assumptions, diminishing the method's precision and explicitness. Therefore, in this research, similar to Engelberts [12], the NBVM with single drug parameters will be used.

4.1.4. Baseline Model

To ensure a comprehensive overview in this chapter, the DI-MCRD model used to create baseline results is given:

$$\frac{\partial N(\bar{x}, t)}{\partial t} = \nabla \cdot (D \nabla N(\bar{x}, t)) + \mathbf{k}(\bar{x}) N(\bar{x}, t) \left(1 - \frac{N(\bar{x}, t)}{\theta} \right) - \alpha C_{\text{drug}}(\bar{x}, t_0) N(\bar{x}, t) e^{-\beta(t-\bar{t})}, \quad (4.17)$$

$$D = D_0 e^{-\gamma \sigma_{\text{vm}}(\bar{x}, t)}, \quad (4.18)$$

$$\nabla \cdot G \nabla \vec{u} + \nabla \frac{G}{1-2\nu} (\nabla \cdot \vec{u}) - \lambda \nabla N(\bar{x}, t) = 0. \quad (4.19)$$

To model the change in the number of tumour cells over time the total system of three PDEs equations (4.17)–(4.19) is numerically evaluated forward in time using the following steps for each voxel, given an initial value $N(\bar{x}, t)$ and a set of parameters:

1. Compute gradient $\nabla N(\bar{x}, t)$ using central differences
2. Solve (4.19) for $\vec{u}(\bar{x}, t)$
3. Calculate $\sigma_{vm}(\bar{x}, t)$
4. Update $D(\bar{x}, t)$ using (4.18)
5. Calculate $N(\bar{x}, t + \Delta t)$ using (4.17)
6. Update time parameter $t := t + \Delta t$

These steps are repeated until the desired end time is reached.

It must be noted that in the DI-MCRD model, all calibration parameters— $\mathbf{k}(\bar{x})$, D_0 , and α —must be positive due to the nature of the model equations. However, negative values for $\mathbf{k}(\bar{x})$ have been observed in the calibration results of both the Texas studies [7] and Engelberts' study [12]. This is problematic because, in the context of logistic growth, a negative $\mathbf{k}(\bar{x})$ would lead to excessive cell death when the number of tumour cells is low, and insufficient tumour cell death when N is large. Such behaviour is unrealistic.

The chemotherapy term in the model is intended to account for cell death. Alternatively, a simple death term $-\gamma N$ could be added to explicitly model cell death, ensuring that the dynamics remain realistic.

4.1.5. Discretization & Numerical Methods

To numerically solve the 3D system of PDEs of the DI-MCRD model, the equations are discretized using central differences on a voxel grid derived from an $n_x \times n_y \times n_z$ MRI image. The relevant details for this research are outlined based on Engelberts [12]. Each voxel is denoted as $\bar{x} = (x_i, y_j, z_k)$, where i , j , and k index the spatial dimensions. The time-stepping is defined by $t_m := m\Delta t$. Following Engelberts [12], the key variables are represented as $N_{i,j,k}^m$, $D_{i,j,k}^m$, $k_{i,j,k}$, and $C_{i,j,k}^m$, leading to the following discretization of (4.17):

$$\begin{aligned} \frac{\partial N_{i,j,k}^m}{\partial t} \approx & \frac{1}{2\Delta x^2} \left((D_{i-1,j,k}^m + D_{i,j,k}^m) N_{i-1,j,k}^m - (D_{i-1,j,k}^m + 2D_{i,j,k}^m + D_{i+1,j,k}^m) N_{i,j,k}^m + (D_{i,j,k}^m + D_{i+1,j,k}^m) N_{i+1,j,k}^m \right) \\ & + \frac{1}{2\Delta y^2} \left((D_{i,j-1,k}^m + D_{i,j,k}^m) N_{i,j-1,k}^m - (D_{i,j-1,k}^m + 2D_{i,j,k}^m + D_{i,j+1,k}^m) N_{i,j,k}^m + (D_{i,j,k}^m + D_{i,j+1,k}^m) N_{i,j+1,k}^m \right) \\ & + \frac{1}{2\Delta z^2} \left((D_{i,j,k-1}^m + D_{i,j,k}^m) N_{i,j,k-1}^m - (D_{i,j,k-1}^m + 2D_{i,j,k}^m + D_{i,j,k+1}^m) N_{i,j,k}^m + (D_{i,j,k}^m + D_{i,j,k+1}^m) N_{i,j,k+1}^m \right) \\ & + k_{i,j,k} N_{i,j,k}^m \left(1 - \frac{N_{i,j,k}^m}{\theta} \right) - \alpha C_{i,j,k}^m \end{aligned} \quad (4.20)$$

Using lexicographic ordering the elements of $N_{i,j,k}^m$, $D_{i,j,k}^m$, $k_{i,j,k}$ and $C_{i,j,k}^m$ can be conglomerated into vectors \mathbf{N}^m , \mathbf{D}^m , \mathbf{k}^m and \mathbf{C}^m , respectively. Thus (4.20) can be rewritten in the matrix-vector system as follows:

$$\frac{\partial \mathbf{N}^m}{\partial t} = \mathbf{A} \mathbf{N}^m + \mathbf{f}(\mathbf{N}^m) \quad (4.21)$$

with

$$\mathbf{f}(\mathbf{N}^m) = \mathbf{k} \cdot \mathbf{N}^m \cdot \left(1 - \frac{\mathbf{N}^m}{\theta} \right) - \alpha \mathbf{C}^m \cdot \mathbf{N}^m \quad (4.22)$$

where the symmetric positive definite matrix \mathbf{A} and vector \mathbf{C}^m , are defined precisely in [12]. For the linear elastic equation (4.3) is discretized similarly, resulting in the following system:

$$\mathbf{B} \vec{\mathbf{u}} = \mathbf{g}(\mathbf{N}^m). \quad (4.23)$$

Here, \mathbf{B} is a sparse symmetric negative definite matrix, and the specifics of \mathbf{B} and \mathbf{g} are described in [12].

As previously mentioned, Engelberts [12] focused on improving the numerical efficiency of the DI-MCRD model, exploring various numerical methods. For the linear-elastic equation (4.23), the Conjugate Gradient (CG) method, a Krylov method using conjugate directions [46], was identified as the

most optimal in terms of numerical efficiency and precision and was further accelerated using a novel preconditioner developed by Engelberts, incorporating FFTs and a tridiagonal solver.

The optimal temporal integration for solving (4.22) was achieved through a Parareal implementation using Runge-Kutta 4 (RK4) and Crank-Nicolson (CN) as the fine and coarse solvers, respectively. The RK4 method, a fourth-order accurate explicit method, balances accuracy and computational cost but can be relatively expensive. In contrast, the CN method, a second-order accurate implicit method, offers lower computational cost and good stability. The parallelized model of Engelberts was executed on the BGR group's EMC cluster, consisting of CPUs running at 2.9 GHz with 512 GB of RAM. For this research, the same methods will be used as well as the EMC cluster to establish the results.

4.1.6. Parameter Calibration

To determine patient-specific parameters, the DI-MCRD model must be calibrated using the number of tumour cells at t_0 and t_1 , which have been obtained through the preprocessing pipeline (see Chapter 3). All the studies from the Texas research group [4–9] and the previous theses [10–12] follow similar cycles to calibrate their system. They begin by selecting initial parameters, running the model from t_0 to t_1 , and comparing the number of simulated tumour cells with the number of tumour cells obtained from the preprocessing pipeline at t_1 . Through an optimization process, the parameters are iteratively updated, and the cycle is repeated until the difference between the model's output and the preprocessed data is minimized or the selected stopping criteria are met.

In previous theses [11, 12], the calibrated parameters, denoted by the vector \mathbf{P} , were $\mathbf{P} = (\mathbf{k}(\bar{x}), D_0, \alpha)$. The chemotherapy parameter differed from the Texas studies [7–9], which included additional chemotherapy parameters. Additional parameters that could be optimized include the carrying capacity θ , which may vary spatially, the coupling constant for von Mises stress σ , the material property ν , the coupling constant for the displacement vector λ , the stiffness parameter $E(\bar{x})$, which can be tissue-dependent, and the drug inclusion parameter β .

Mathematically, the non-linear optimization problem can be formulated as follows. Let $N_{\text{data}}(t)$ denote the number of tumour cells at times t_0 , t_1 , and t_2 obtained from the preprocessing, and let $N_{\text{model}}(t; \mathbf{P})$ represents the predicted number of tumour cells at time t with the parameter set \mathbf{P} from the DI-MCRD model. Note that $N_{\text{model}}(t; \mathbf{P})$ depends on the initial value $N_{\text{data}}(t_0)$, and that an initial parameter set \mathbf{P}_0 is required for the iterative optimization process. The objective is to find the parameter set \mathbf{P} that minimizes the L^2 -norm between the preprocessed and predicted number of tumour cells at t_1 :

$$\mathbf{P}^* = \arg \min_{\mathbf{P}} \|N_{\text{data}}(t_1) - N_{\text{model}}(t_1; \mathbf{P})\|_2^2. \quad (4.24)$$

Since the proliferation rate $\mathbf{k}(\bar{x})$ is defined for each voxel, for a voxel grid of total size n , the parameter set $\mathbf{P} = (\mathbf{k}(\bar{x}), D_0, \alpha)$ includes n parameters for k , one for D_0 , and one for α , resulting in $n + 2$ parameters in total. This leads to an underdetermined system, which requires minimization. To address this, regularization is applied to constrain the parameter space and guide the optimization toward realistic values. Regularization not only provides additional constraints to guide the solution in an underdetermined system, but it also smooths the optimization process, reducing the risk of overfitting and avoiding local minima, ultimately enhancing the stability and realism of the solution [47].

Non-linear Optimization & regularization

To find \mathbf{P} Engelberts [12] compared four nonlinear optimization methods: Levenberg-Marquardt (LM), Trust Region Reflective (TRF), Powell's Dog-Leg (DL), and the Adjoint State Method (AD). The LM method [48], frequently used by the Texas research group [4, 7–9], combines gradient descent and Gauss-Newton techniques, with a damping factor that adjusts to improve convergence. TRF [49] builds upon LM by introducing a trust region to constrain the step size, which enhances robustness and accuracy. Powell's Dog-Leg [50–52], another trust region method, merges steepest descent and Gauss-Newton directions, offering flexibility by applying non-strict bounds, which makes it particularly effective for complex optimization problems. The Adjoint State Method (AD) [6, 53], used in other Texas studies [5, 6], relies on adjoint sensitivity analysis to optimize large-scale systems efficiently.

In addition to optimization methods, Engelberts also compared different regularization techniques, including Tikhonov, Total Variation (TV), and Laplacian regularization, as detailed in [12]. His final com-

parison concluded that Powell's Dog-Leg, combined with Total Variation regularization using a hyperparameter value of 10^5 , was the most effective approach [12]. Therefore, this research will adopt this approach to establish the baseline results.

Approximating Jacobians

For the LM, TRF, and DL methods, the Jacobian of the DI-MCRD model is required. Due to the number of parameters and the size of the system, a naive calculation is unfeasible. Therefore, Engelberts [12] developed a novel approach using a more analytical method to find the Jacobians.

Since the expressions and reasoning behind this novel Jacobian method will be needed later, they are explained below. For further details, please refer to Engelberts' work [12]. To find \mathbf{N}^{m+1} , a set of parameters \mathbf{P} and the previous step \mathbf{N}^m are required. Let $\mathbf{N}^{m+1} = \mathcal{S}(\mathbf{N}^m, \mathbf{P})$ represent the scheme to find the next iterate of \mathbf{N}^m . Then, its derivative with respect to \mathbf{P} is given by:

$$\frac{d\mathbf{N}^{m+1}}{d\mathbf{P}} = \frac{\partial \mathcal{S}(\mathbf{N}^m, \mathbf{P})}{\partial \mathbf{P}} + \frac{\partial \mathcal{S}(\mathbf{N}^m, \mathbf{P})}{\partial \mathbf{N}^m} \cdot \frac{d\mathbf{N}^m}{d\mathbf{P}}. \quad (4.25)$$

Since $\frac{d\mathbf{N}^0}{d\mathbf{P}} = 0$, it is possible to find the Jacobian alongside the parallel time-stepping of the temporal integration in the DI-MCRD model. This can be achieved using a simple Forward Euler (FE) scheme, denoted by $\mathcal{F}^{\mathcal{E}}(\mathbf{N}^m, \mathbf{P})$. Using the FE scheme for the temporal integration of (4.21) gives:

$$\mathbf{N}^{m+1} = \mathcal{F}^{\mathcal{E}}(\mathbf{N}^m, \mathbf{P}) = \mathbf{N}^m + \Delta t \left(A(\mathbf{N}^m) \mathbf{N}^m + \mathbf{k} \mathbf{N}^m \left(1 - \frac{\mathbf{N}^m}{\theta} \right) - \mathbf{C}^m \mathbf{N}^m \right) \quad (4.26)$$

Using this scheme the derivatives for the parameters in the optimisation set $\mathbf{P} = (\mathbf{k}(\bar{x}), D_0, \alpha)$ are given as follows:

$$\frac{d\mathbf{N}^{m+1}}{d\mathbf{k}} = \Delta t \left(\mathbf{N}^m \left(1 - \frac{\mathbf{N}^m}{\theta} \right) + \left(\frac{I}{\Delta t} + A(\mathbf{N}^m) + \mathbf{k} \left(1 - \frac{2\mathbf{N}^m}{\theta} \right) - \alpha \mathbf{C}^m \right) \frac{d\mathbf{N}^m}{d\mathbf{k}} + \frac{\partial A(\mathbf{N}^m)}{\partial \mathbf{N}^m} \mathbf{N}^m \frac{d\mathbf{N}^m}{d\mathbf{k}} \right) \quad (4.27)$$

$$\frac{d\mathbf{N}^{m+1}}{dD_0} = \Delta t \left(\frac{A(\mathbf{N}^m)}{D_0} \mathbf{N}^m + \left(\frac{I}{\Delta t} + A(\mathbf{N}^m) + \mathbf{k} \left(1 - \frac{2\mathbf{N}^m}{\theta} \right) - \alpha \mathbf{C}^m \right) \frac{d\mathbf{N}^m}{dD_0} + \frac{\partial A(\mathbf{N}^m)}{\partial \mathbf{N}^m} \mathbf{N}^m \frac{d\mathbf{N}^m}{dD_0} \right) \quad (4.28)$$

$$\frac{d\mathbf{N}^{m+1}}{d\alpha} = \Delta t \left(-\mathbf{C}^m \mathbf{N}^m + \left(\frac{I}{\Delta t} + A(\mathbf{N}^m) + \mathbf{k} \left(1 - \frac{2\mathbf{N}^m}{\theta} \right) - \alpha \mathbf{C}^m \right) \frac{d\mathbf{N}^m}{d\alpha} + \frac{\partial A(\mathbf{N}^m)}{\partial \mathbf{N}^m} \mathbf{N}^m \frac{d\mathbf{N}^m}{d\alpha} \right) \quad (4.29)$$

It can be observed that the first term in each derivative corresponds to the contributions of the proliferation, diffusion, and chemotherapy terms, as they are linearly dependent on their respective parameters. This implies that no additional calculations are needed for these terms. The second term in each derivative shares the same pre-factor, hence it only needs to be computed once. The third and final term is more complex to compute; however, Engelberts [12] points out that the derivative of matrix A with respect to \mathbf{N}^m is negligibly small.

Engelberts [12] also investigated the use of the more accurate RK4 method for Jacobian calculation. However, he observed that this method substantially increases computational time relative to the Forward Euler (FE) approach. Despite its lower accuracy, Engelberts demonstrated that the FE method provides a sufficiently precise approximation of the Jacobian for parameter optimization. Consequently, the FE method was adopted in the latest implementation of his code.

4.1.7. Variables & Parameters

In this section, tables containing the variables and parameters from the DI-MCRD model systems equations (4.17)–(4.19) are provided.

Variable	Description
$N(\bar{x}, t)$	Number of tumour cells in the voxel at position \bar{x} at time t
D	Diffusion coefficient of tumour cells [mm^2/d]
σ_{vm}	von Mises stress [N/m^2]
\vec{u}	Displacement vector due to tumour cell growth [mm]
G	Shear modulus due to breast tissue properties [kPa]
$C_{\text{tissue}}^{\text{drug}}(\bar{x}, t)$	Concentration of drug in the tissue in the voxel at position \bar{x} at time t [μM]

Table 4.1: Description of the variables of the DI-MCRD model system equations (4.17)–(4.19).

Parameter	Description	Value
D_0	Diffusion coefficient of tumour cells without stress	Calibrated [mm^2/d]
γ	Mechanical coupling coefficient for stress	Assigned at $2.0 \times 10^{-3} \text{ m}^2/\text{N}$
ν	Poisson's ratio	Assigned at 0.45
E	Young's modulus for adipose, fibroglandular and tumour tissue	Assigned at 2, 4, and 20 kPa, respectively
λ	Coupling constant for the displacement of tumour cells	Assigned at $2.5 \times 10^{-3} \text{ kPa}/\text{cell}$
$\mathbf{k}(\bar{x})$	Proliferation rate of tumour cells in the voxel at position \bar{x}	Calibrated [$1/\text{d}$]
θ	carrying capacity of tumour cells per voxel	Defined [cells]
α	Efficacy of the drug against tumour cells	Calibrated [$1/(\mu\text{M} \cdot \text{d})$]
β	Decay of the drug	Assigned at 0.25 [$1/\text{d}$]

Table 4.2: Description of the parameters of the DI-MCRD model system described in equations (4.17)–(4.19). These values correspond to those used by Engelberts [12] in the most recent version of his code.

4.1.8. Baseline Results

The numerically efficient algorithm of the DI-MCRD model equations (4.17)–(4.19), designed by Engelberts [12], along with the parameter settings from his most recent version, is applied to the newly expanded and preprocessed dataset, which includes 13 patients. The model parameters are fixed as shown in Table 4.2, and the initial parameter set \mathbf{P}_0 for calibration consists of $\mathbf{k}(\bar{x})$, with random values uniformly distributed between 0.0 and 0.10, $D_0 = 2 \cdot 10^{-2}$, and $\alpha = 0.5$. The trust region bounds for the DL method are set as $\mathbf{k}(\bar{x}) \in [-0.5, 0.8]^n$, $D_0, \alpha \in [0, 1]$ for a system of total grid size n . The regularization parameter for the regularization terms is set to 10^5 . The maximum calibration time t_{max} is set to 12 hours. If the objective does not fall below 10^{-5} within this time frame, the calibration process is cut off. Additionally, the voxel grid is downsized to $33 \times 33 \times 33$, a size also used by Engelberts [12].

The results of this baseline run are presented in Table 4.3. The first three columns show the calibrated patient-specific parameters, where the range of calibrated values for $\mathbf{k}(\bar{x})$ is displayed, as it is defined for each voxel. The remaining four columns represent the errors and relative errors at times t_1 and t_2 . The error $e(t)$ is calculated as the L^2 -norm between the data and the model prediction:

$$e(t) = \|N_{\text{data}}(t) - N_{\text{model}}(t, \mathbf{P})\|_2 \quad (4.30)$$

The relative error $e_r(t)$ is defined as the ratio of this error to the initial data norm:

$$e_r(t) = \frac{\|N_{\text{data}}(t) - N_{\text{model}}(t, \mathbf{P})\|_2}{\|N_{\text{data}}(t_0)\|_2} \quad (4.31)$$

Using the L^2 -norm, the voxel position of the tumours is taken into account, which is crucial for an evaluation of the results. Since this metric evaluates whether the model accurately predicts tumour locations.

For the error calculations at t_2 in the 2-scan patient group, it is assumed that patients have zero tumour cells at each voxel on their day of the pathological check (see PA day Tables 3.1 and 3.2). Therefore, t_2 is set as the PA date, and $N_{\text{data}}(t_2) = 0$. Notably, only patients p_6 and p_{19} achieve pCR, meaning they have no remaining tumours. For the other 2-scan patients who do not achieve pCR, the interpretation of their results differs, and hence patients p_{15} , p_{16} , p_{17} , and p_{18} are italicized in Table 4.3 to denote this difference. While the errors for these non-pCR patients are not irrelevant, they must be interpreted differently. The relative errors indicate how many tumour cells are still present in each voxel at t_2 relative to the initial tumour cells per voxel. Whereas the error in t_2 indicates how many tumour cells are predicted to be present at t_2 .

	$[k_{\min}, k_{\max}]$	D_0	α	$e_r(t_1)$	$e_r(t_2)$	$e(t_1)$	$e(t_2)$
p_1	$[-0.2476, 0.7070]$	0.0190	1.0001	0.0884	0.4547	$1.1867 \cdot 10^7$	$6.1035 \cdot 10^7$
p_3	$[-0.1095, 0.8776]$	0.0089	0.2979	0.0621	0.9592	$2.4594 \cdot 10^7$	$3.7989 \cdot 10^8$
p_4	$[-0.7782, 0.7720]$	0.0172	0.7606	0.0635	0.5286	$6.8885 \cdot 10^7$	$5.7364 \cdot 10^8$
p_6	$[-0.1585, 0.1865]$	0.0103	0.6745	0.0004	0.1820	$1.0473 \cdot 10^5$	$4.9567 \cdot 10^7$
p_8	$[-0.1241, 0.4092]$	0.0168	0.5404	0.0166	0.2322	$2.8244 \cdot 10^6$	$3.9525 \cdot 10^7$
p_{10}	$[-0.0911, 0.7614]$	0.0059	0.5675	0.0215	0.5900	$2.7244 \cdot 10^6$	$7.4766 \cdot 10^7$
p_{11}	$[-0.3581, 0.8971]$	0.1572	0.3631	0.1095	0.6992	$2.8829 \cdot 10^7$	$1.8412 \cdot 10^8$
p_{12}	$[-0.1791, 0.9778]$	0.0198	0.6567	0.0382	0.4877	$1.3752 \cdot 10^7$	$1.7537 \cdot 10^8$
p_{15}	$[-0.1401, 0.5848]$	0.0090	1.0418	0.0882	<i>0.7269</i>	$2.8652 \cdot 10^7$	<i>$2.3605 \cdot 10^8$</i>
p_{16}	$[-0.0652, 0.3694]$	0.0075	0.5570	0.0335	<i>1.3802</i>	$1.2774 \cdot 10^6$	<i>$5.2633 \cdot 10^7$</i>
p_{17}	$[-0.0830, 0.7184]$	0.0001	0.0913	0.0017	<i>0.3379</i>	$1.8293 \cdot 10^5$	<i>$3.5985 \cdot 10^7$</i>
p_{18}	$[-0.1985, 0.2069]$	0.0201	1.0000	0.0502	<i>0.2105</i>	$1.0650 \cdot 10^7$	<i>$4.4678 \cdot 10^7$</i>
p_{19}	$[-0.1995, 0.2784]$	0.0572	0.9888	0.0021	0.5829	$2.2148 \cdot 10^5$	$6.1135 \cdot 10^7$

Table 4.3: Baseline results of the DI-MCRD model applied to the entire dataset.

In addition to the table, visualizing the results is crucial for evaluating the model's performance. For each patient, several types of plots are generated to provide a comprehensive analysis. First, the total number of tumour cells over time is plotted alongside the actual number of tumour cells at t_1 , t_2 , and t_3 , offering a global comparison between the model predictions and observed data, as demonstrated in Figure 4.1. To evaluate the spatial alignment of the predictions, another visualization involves plotting a slice of the breast to display both N_{data} and N_{model} at t_1 and t_2 , giving a spatial perspective of the tumour distribution. Alongside this, the error of slice of both time points, the proliferation rate $k(\bar{x})$ and the shear modulus $G(\bar{x})$ are plotted (see Figures 4.2–4.4 for examples). Additionally, a 3D plot can be used to further illustrate the spatial correspondence between N_{data} and N_{model} at these same time points. In these 3D plots, all values below N_{\min} , defined as:

$$N_{\min} = \min_{\bar{x}, t=t_0, t_1} N_{\text{data}}(\bar{x}, t). \quad (4.32)$$

are removed to focus on the regions where tumour cells are detectable by MRI. This approach ensures that the visualized model results correspond to observable tumour masses, even though the model has the precision to simulate values below the MRI detection threshold (see Figures 4.5 and 4.6 for examples). Finally, a slice of $k(\bar{x})$ can be plotted to illustrate the distribution of the proliferation rate.

The most important observation from Table 4.3 is that the k_{\min} values are consistently negative. However, as previously mentioned, this is unrealistic since $k(\bar{x})$ represents tumour growth, while α is intended to represent the decay of tumour cells. Looking at Figures 4.2c and 4.4b, it can be seen that for p_8 and p_{17} , the negative k_{\min} values are not present around the tumour's location. In this case, the negative values of $k(\bar{x})$ seem inconsequential because, when no tumour cells are present in a voxel, equation (4.17) equals zero, meaning the parameters have no influence. However, when diffusing tumour cells arrive at these voxels they will die in the upcoming time iterations due to this negative

proliferation. Moreover, in the case of p_{12} in Figure 4.3c, negative values of $k(\bar{x})$ are found around the tumour location, which is unrealistic. This highlights that negative values for $k(\bar{x})$ are present in unrealistic regions and indicate potential issues the patient-specific calibration of Engelbert's model. However, it should be noted that the high positive proliferation rates for each patient are concentrated within the cores of the tumours.

Evaluating the results by examining the plots that display the total number of tumour cells over time, it appears that the model predicts the tumour progression relatively well for patients p_{12} , p_{17} , and to some extent, p_8 . These cases are illustrated in Figure 4.1, with all plots available in the Appendix (Figures C.1 and C.2). However, for the remaining patients, the total number of tumour cells unexpectedly increases after t_1 , contrary to the anticipated decrease due to chemotherapy. This is most likely due to the proliferation rates within the tumours' cores being too high combined with an insufficient chemotherapy parameter, leading to inadequate cell death and subsequent tumour growth. The most promising results from the baseline will be further investigated.

p_8

Looking at p_8 , while Figure 4.1a is not perfect, it does appear realistic, as there is a small decay after t_1 . Additionally, the relative error from Table 4.3 at t_2 is very promising. However, when examining the slices from Figure 4.3a, it becomes evident that the visual results are less convincing. The model predicts no diffusion, whereas the actual data shows upward tumour diffusion. The calibrated diffusion D_0 should allow for some diffusion, but the high-stiffness area at t_1 , as shown in Figure 4.2d, restricts diffusion due to the mechanical coupling in the DI-MCRD model. In the 3D representation in Figure 4.5a, it can also be seen that while the tumour diffuses from t_1 to t_2 in the actual data, the model predicts no diffusion of the large tumour, though it does predict some minor diffusion.

p_{12}

For p_{12} , comparing Figure 4.1b with the high relative error $e_r(t_2)$ from Table 4.3 suggests that the tumour location is not accurately predicted. This misprediction is evident in Figure 4.3a at t_2 . The model assumes the tumour location remains unchanged, leading to no diffusion, whereas the actual data shows upward tumour diffusion. This situation is similar to p_8 , as the calibrated diffusion D_0 should allow for some diffusion. Additionally, Figure 4.3d shows that this tumour also lies in a high-stiffness area, which likely restricts its diffusion.

However, Figure 4.3a only shows a slice. When examining the overall prediction using the 3D representation in Figure 4.5b, the alignment of tumours at t_2 appears reasonable. At first glance, this might not seem the case due to the presence of multiple purple dots, but it should be noted that these dots correspond to a low number of tumour cells. The important factor is the similar position and shape visible behind these dots. Therefore, the high relative error could also be attributed to a misprediction in the number of tumour cells at certain voxel locations, including the purple voxels with a lower number of tumour cells.

Looking at the proliferation rate $k(\bar{x})$ in Figure 4.3c, some voxels have negative values. When examining the shear modulus, where the yellow regions represent the tumour's location from t_0 , it can be seen that these negative values of k correspond to areas where the tumour was present at t_0 but not at t_1 . Hence, in this case, the proliferation term functions more like a death term. Additionally, this negative proliferation rate can hinder tumour cell diffusion, as tumour cells that diffuse into voxels with negative k will die in subsequent time steps.

p_{17}

For p_{17} , both the clinical staging (cT2) and pathological assessment (ypTis) (see Table 3.2) suggest a decrease in the number of tumour cells. This trend is observed for nearly the entire course, as shown in Figure 4.1c. However, the slight increase towards the end raises concerns. This increase towards the end is especially a concern since the ultimate goal is to simulate the model until the tumour cell count reaches the lowest level detectable by MRI scanners, to estimate the required number of chemotherapy rounds. Hence, an increase at the end means never-ending simulation since the lowest level of tumour cells detectable by MRI scanners will never be reached.

Examining the other visual results for p_{17} shown in Figures 4.4 and 4.6, it is immediately evident that at t_2 , the model predicts far too many tumour cells, indicating that the increase observed in Figure 4.1c

is also visually unrealistic. Additionally, where $k(\bar{x})$ is highest, the number of tumour cells noticeably increases from t_1 to t_2 in the N_{model} results. Notably, there is no visible diffusion, primarily due to the very low D_0 .

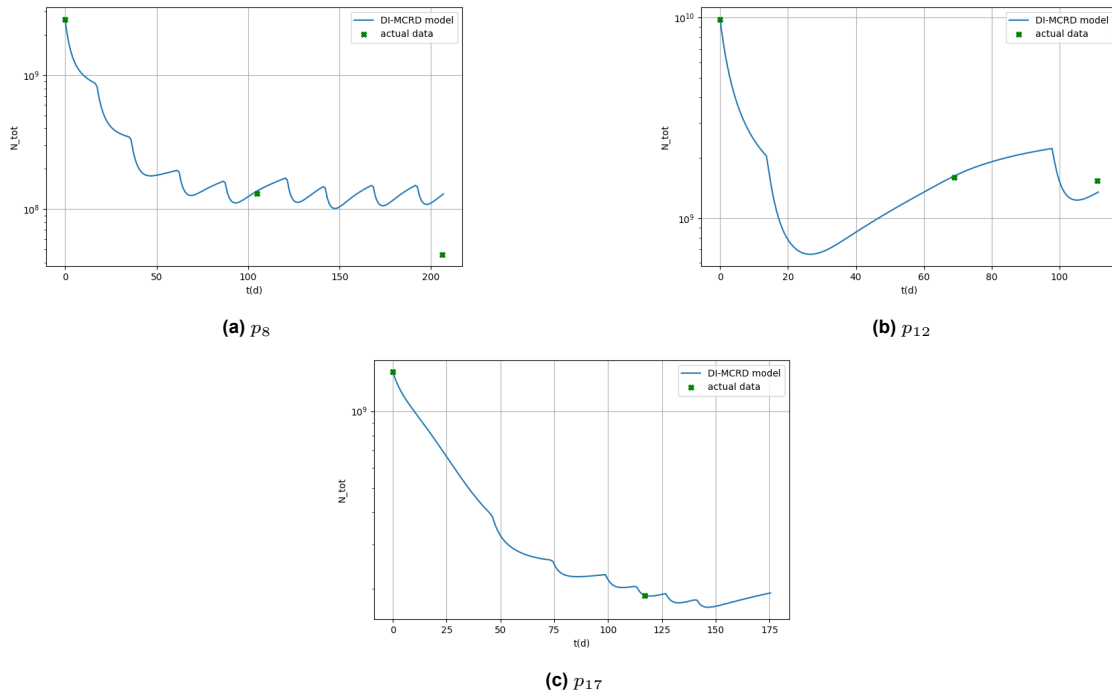


Figure 4.1: Total amount of tumour cells over time for three different patients obtained using baseline model.

Overall, considering the results from Engelberts' model with the expanded patient dataset, it can be concluded that the DI-MCRD model does not yet perform as expected. The calibrated parameters for $k(\bar{x})$ are unrealistic, and the predictions at t_2 are often inaccurate, with tumour cell counts increasing after t_1 , which contradicts the expected behavior following chemotherapy. The tumour growth observed after t_1 is likely due to the too high calibrated values of k within the tumour cores, combined with insufficient chemotherapy parameters.

When comparing these results with those from Engelberts' original work [12], which included the same patients p_1 and p_3 , both sets of results are unsatisfactory. However, Engelberts' results appear more realistic in comparison.

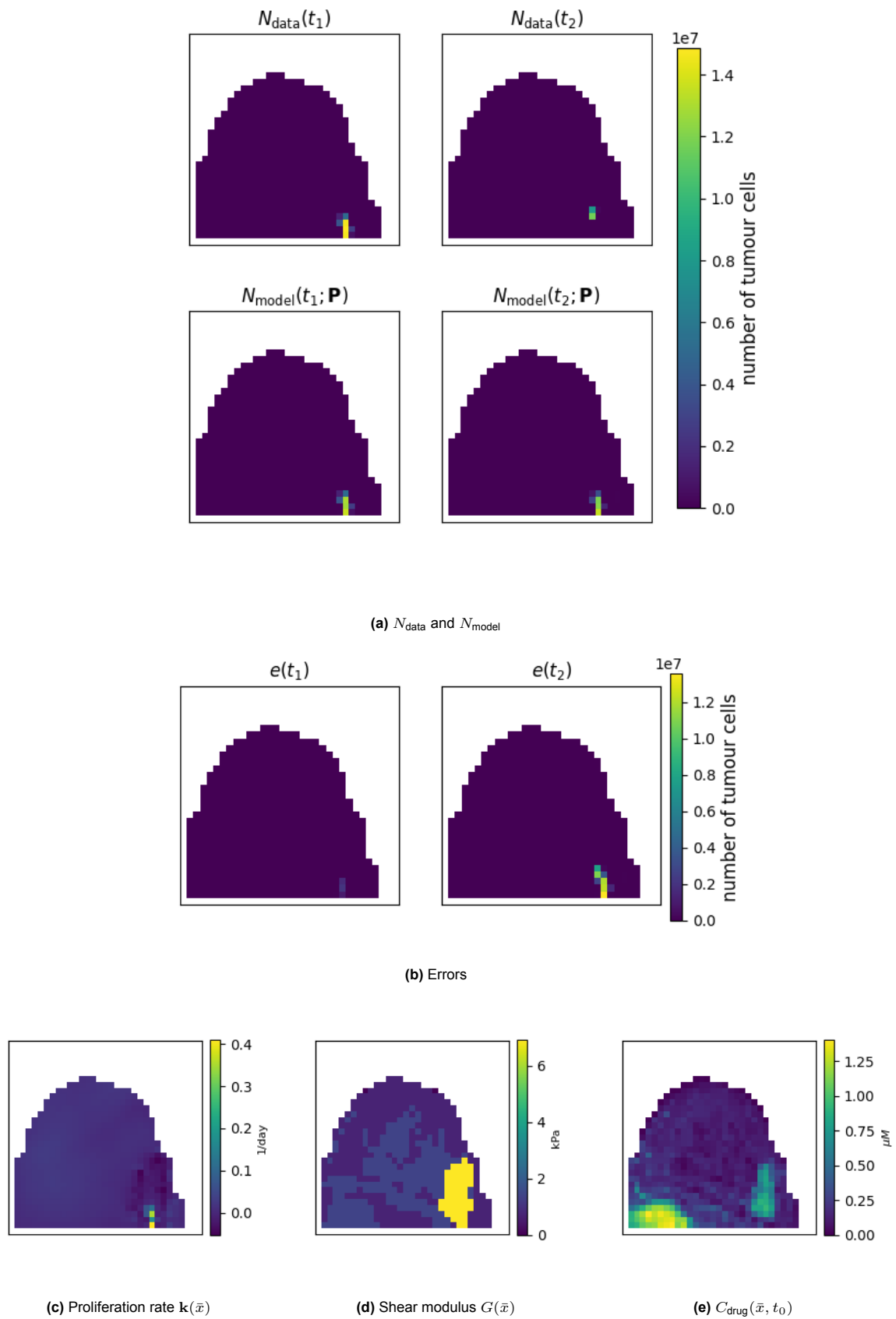
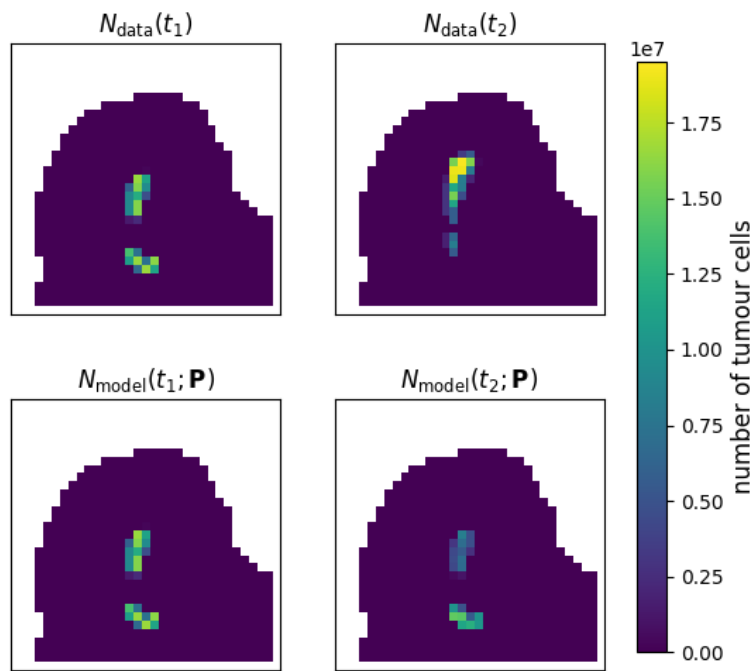
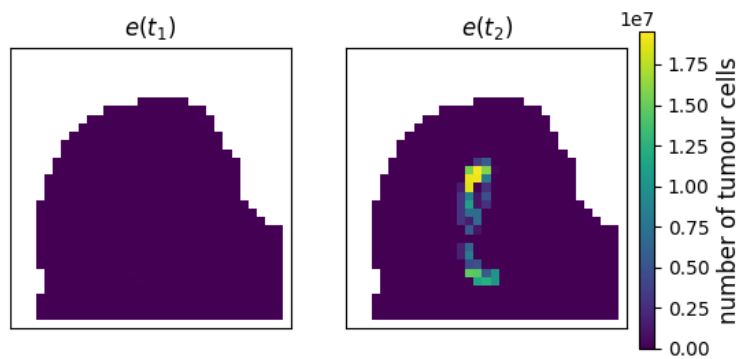


Figure 4.2: Baseline results for p_8 visualized using slices. (a) shows the N_{data} representation at t_1 and t_2 , along with $N_{\text{model}}(t_1)$, the calibrated number of tumour cells at t_1 , and $N_{\text{model}}(t_2)$, the prediction made by the DI-MCRD model at t_2 . (b) presents the errors between N_{data} and N_{model} at t_1 and t_2 . (c) visualizes the proliferation rate $k(\bar{x})$, (d) displays the shear modulus $G(\bar{x})$, and (e) displays the drug distribution $C_{\text{drug}}(\bar{x}, t_0)$.

(a) N_{data} and N_{model} 

(b) Errors

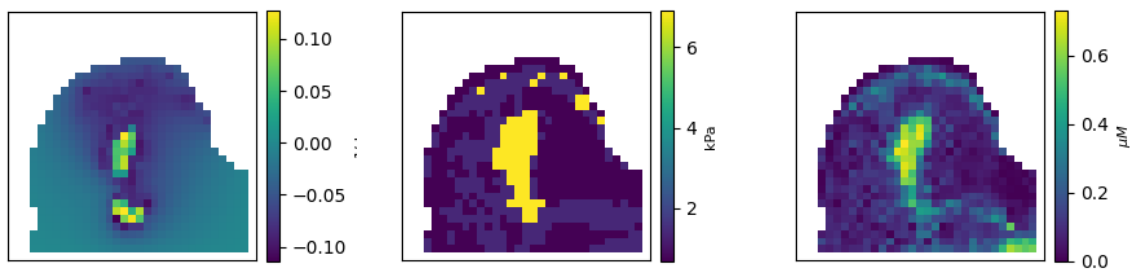
(c) Proliferation rate $k(\bar{x})$ (d) Shear modulus $G(\bar{x})$ (e) $C_{drug}(\bar{x}, t_0)$

Figure 4.3: Baseline results for p_{12} visualized using slices. (a) shows the N_{data} representation at t_1 and t_2 , along with $N_{model}(t_1)$, the calibrated number of tumour cells at t_1 , and $N_{model}(t_2)$, the prediction made by the DI-MCRD model at t_2 . (b) presents the errors between N_{data} and N_{model} at t_1 and t_2 . (c) visualizes the proliferation rate $k(\bar{x})$, (d) displays the shear modulus $G(\bar{x})$, and (e) displays the drug distribution $C_{drug}(\bar{x}, t_0)$.

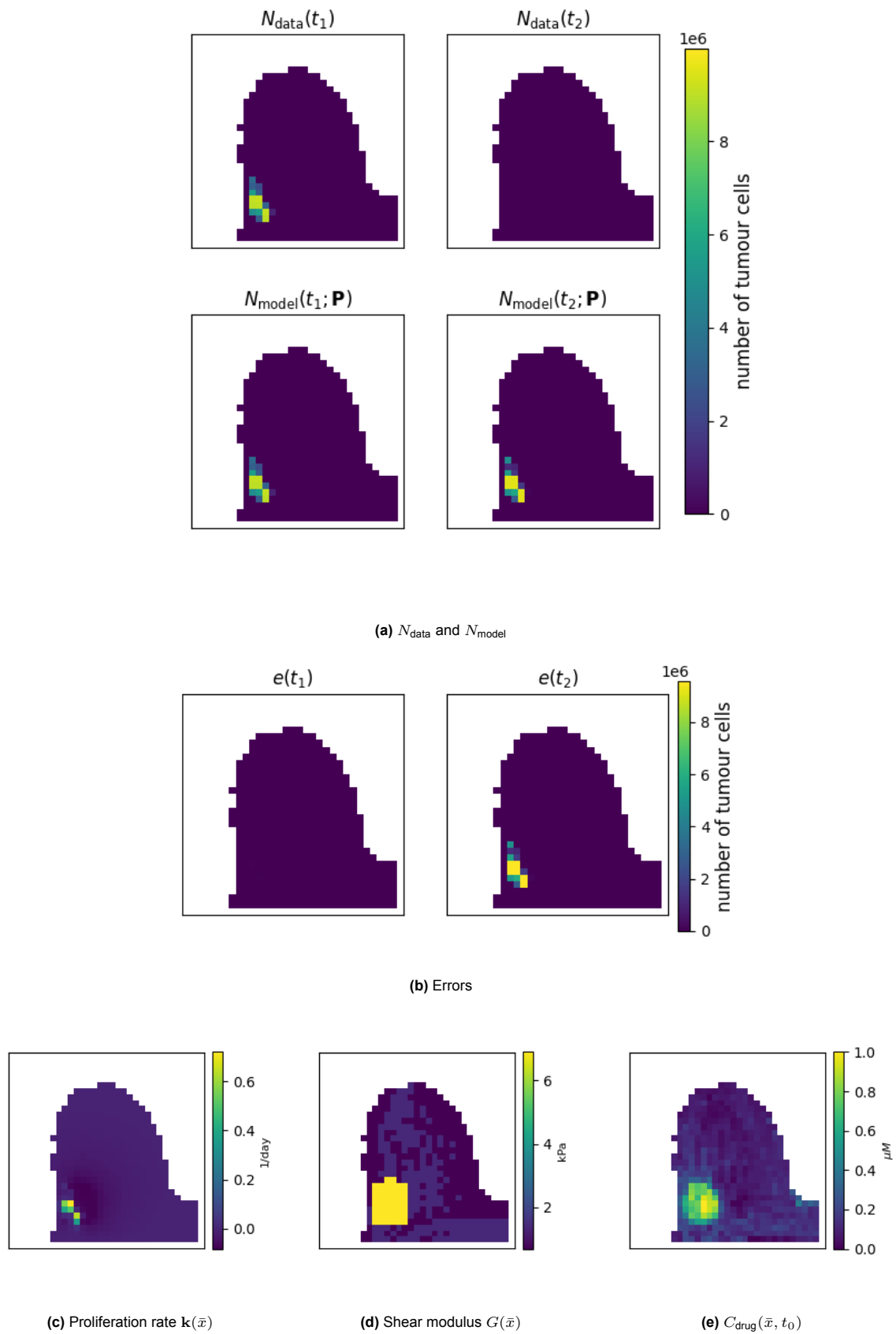


Figure 4.4: Baseline results for p_{17} visualized using slices. (a) shows the N_{data} representation at t_1 and t_2 , along with $N_{\text{model}}(t_1)$, the calibrated number of tumour cells at t_1 , and $N_{\text{model}}(t_2)$, the prediction made by the DI-MCRD model at t_2 . (b) presents the errors between N_{data} and N_{model} at t_1 and t_2 . (c) visualizes the proliferation rate $k(\bar{x})$, (d) displays the shear modulus $G(\bar{x})$, and (e) displays the drug distribution $C_{\text{drug}}(\bar{x}, t_0)$.

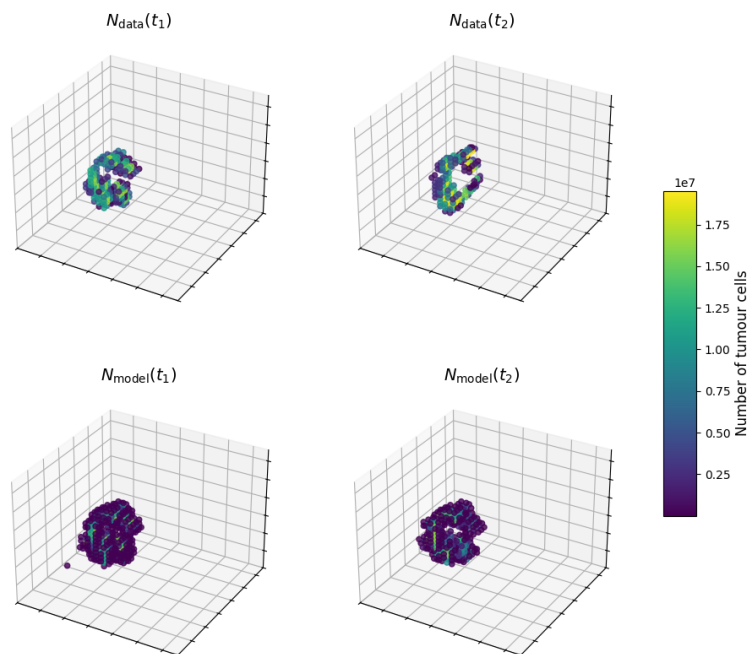
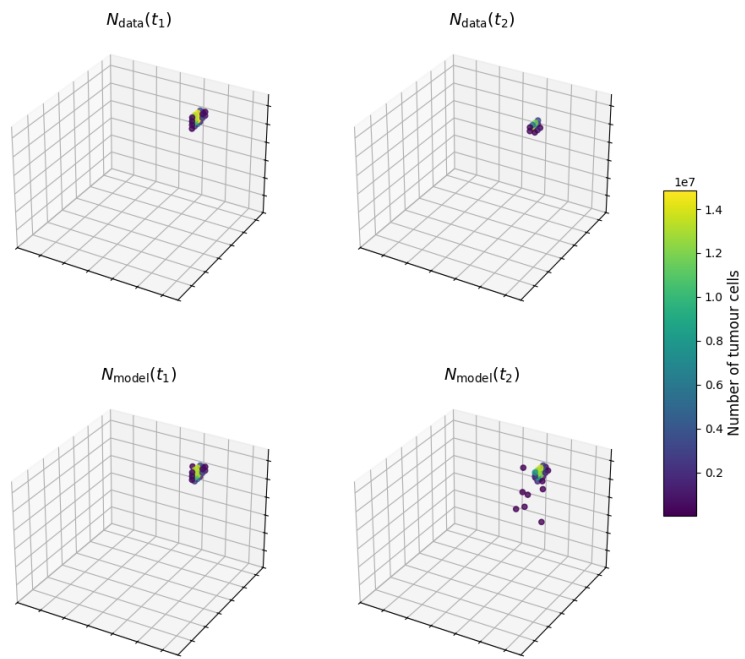


Figure 4.5: 3D representation of the number of tumour cells for patients p_8 and p_{12} obtained using the baseline model. Within each subfigure, the top row shows the N_{data} representation at t_1 and t_2 , while the bottom row displays $N_{\text{model}}(t_1)$, the calibrated number of tumour cells at t_1 , and $N_{\text{model}}(t_2)$, the prediction made by the DI-MCRD model at t_2 . In the bottom row, all voxels with a tumour cell count less than N_{min} are removed.

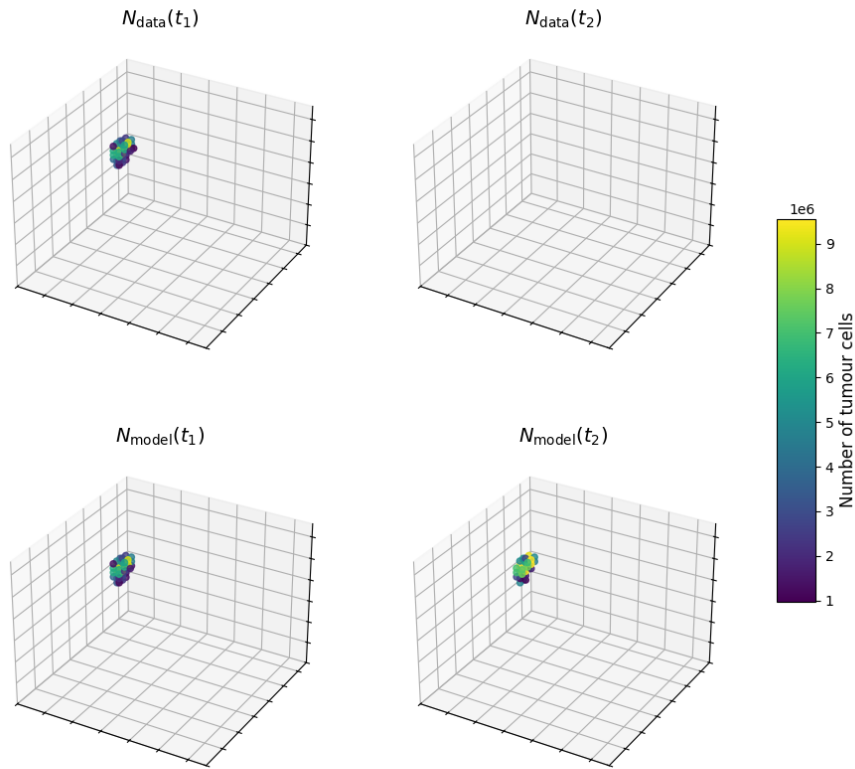


Figure 4.6: 3D representation of the number of tumour cells for patient p_{17} obtained using the baseline model. The top row shows the N_{data} representation at t_1 and t_2 , while the bottom row displays $N_{\text{model}}(t_1)$, the calibrated number of tumour cells at t_1 , and $N_{\text{model}}(t_2)$, the prediction made by the DI-MCRD model at t_2 . In the bottom row, all voxels with a tumour cell count less than N_{min} are removed.

4.2. Model Cycle I: Positive Parameters

To address the limitations of the baseline results, model refinement cycles will be conducted in the following sections. After each (sub)cycle, the improved model will be tested on a subset of the dataset, comprising three patients: p_3 , p_8 , and p_{10} . These patients have scans at three time points and demonstrated satisfactory convergence in the baseline results. This subset is assumed to be sufficient for evaluating whether model cycles lead to improvements, while also reducing the computational run-times required for each (sub)cycle. An overview of the different (sub)cycles is given in Section 4.5.

This section describes the first cycle, which consists of two sub-cycles. First, some general issues found in Engelberts' [12] model will be mentioned, along with corresponding improvements, after which the negative calibrated parameters will be addressed.

4.2.1. Model Cycle Ia: Updated Prediction Parameters & DL with Positive Bounds

The values of $C_{\text{drug}}(\bar{x}, t_0)$ in (4.16) and the tissue distribution used for shear modulus $G(\bar{x})$ in (4.19) are obtained using MRI-DCE scans from t_0 . Engelberts uses the same terms for predictions from t_1 to t_2 . However, at t_1 , a DCE-MRI scan is also available, allowing for an updated $C_{\text{drug}}(\bar{x}, t_1)$ and tissue distribution. The Texas studies [7–9] already use updated parameters for the prediction step. However, they note that both the concentration of the drug in tumour tissue and G are discontinuous over time. Specifically, both remain constant from t_0 to t_1 , with a jump at t_1 due to the update of parameters, after

which they remain constant again.

Thus, an improvement to the DI-MCRD model could involve updating these terms. For the inclusion of chemotherapy, the term becomes:

$$C_{\text{drug}}(\bar{x}, t) = \alpha C_{\text{drug}}(\bar{x}, t^*) e^{-\beta(t-\bar{t})}. \quad (4.33)$$

where t^* represents t_0 during the calibration phase and t_1 during the prediction phase. Additionally, the shear modulus is updated to $G(\bar{x}, t^*)$.

To address the issue of negative values for $\mathbf{k}(\bar{x})$, the first option is to set the trust region bounds for the DL method as $\mathbf{k}(\bar{x}) \in [0, 0.8]^n$, instead of allowing negative values as in the previous section. Additionally, increasing the initial value of α to 1, instead of 0.5, aims to stimulate the chemotherapy term to more effectively reduce the number of tumour cells. Therefore the trust region bounds of α are now $\alpha \in [0, 2]$.

Results

These two adaptations to Engelberts' DI-MCRD model were implemented, and the preprocessed data from three patients was used to evaluate the potential improvements brought by these changes. The results can be found in Table 4.4 and the visualizations of the results can be found in Appendix C.2.1. Comparing this table to the baseline results (Table 4.3), the following observations can be made.

	$[k_{\min}, k_{\max}]$	D_0	α	$e_r(t_1)$	$e_r(t_2)$	$e(t_1)$	$e(t_2)$
p_3	$[-0.1063, 1.4400]$	0.0035	1.0873	0.1266	1.0103	$5.0135 \cdot 10^7$	$4.0013 \cdot 10^8$
p_8	$[-0.1343, 0.7999]$	0.0473	1.7442	0.0135	0.2358	$2.3030 \cdot 10^6$	$4.0140 \cdot 10^7$
p_{10}	$[-0.1169, 0.8676]$	0.0195	1.0802	0.1093	0.5412	$1.3856 \cdot 10^7$	$6.8572 \cdot 10^7$

Table 4.4: Cycle Ia results of the DI-MCRD model applied for three patients.

First, the application of positive lower non-strict bounds only reduced the negativity of k_{\min} for p_3 , while for the other patients, k_{\min} became even more negative. When examining the $\mathbf{k}(\bar{x})$ plots (see Appendix C.2.1), none of the patients show negative values in the slices provided. While this seems promising, it remains unclear whether other slices contain negative values in unrealistic locations. In conclusion, the adjustment to the non-strict bounds did not fully resolve the issue of negative $\mathbf{k}(\bar{x})$ values.

Second, the calibration for p_3 and p_{10} are significantly worse than in the baseline model. However, the prediction errors are quite similar to those in the baseline case, and this holds true for all patients. Third, the diffusion parameter D_0 decreased for p_3 and increased for the other two patients. Finally, the chemotherapy term α increased substantially, likely due to the higher initial setting.

Visually examining the results, starting with the total number of tumour cells over time in Figure 4.7, a noticeable jump is observed at t_1 for all patients. This jump reflects the aforementioned discontinuity caused by the updated parameters during the prediction phase. The likely cause of this is the update of the chemotherapy term, as $G(\bar{x}, t^*)$ mainly influences tumour diffusion, not the reduction or apparent growth in the number of tumour cells, where chemotherapy has a more direct effect. Comparing the plots of $C_{\text{drug}}(\bar{x}, t^*)$ for $t^* = t_0$ and $t^* = t_1$ in Appendix C.2.1, it is particularly evident for patients p_3 and p_8 that C_{drug} is higher at t_0 at the tumour's location. This difference confirms the assumption that C_{drug} is the main contributor to the jump observed at t_1 . As a result, the number of tumour cells increases unrealistically, which should not occur so abruptly. Thus, the approach of updating parameters for the prediction phase seems ineffective. However, compared to the baseline results, the more pronounced decreasing trend after t_1 is likely due to the higher α values. These results could indicate good predictive performance if the prediction phase had been run using the same parameters as the calibration phase.

The other visual results (see Appendix C.2.1) show nothing particularly noteworthy, except that p_8 has an accurate prediction of the tumour's position at t_2 , which is likely reflected in its lowest relative error among the three patients in Table 4.4. Additionally, when compared to the baseline results for p_8 , the tumour has diffused better than in the baseline model. This is likely due to the higher number of tumour

cells resulting from the jump and the increased D_0 , leading to a slight improvement in the relative error at t_2 compared to the baseline.

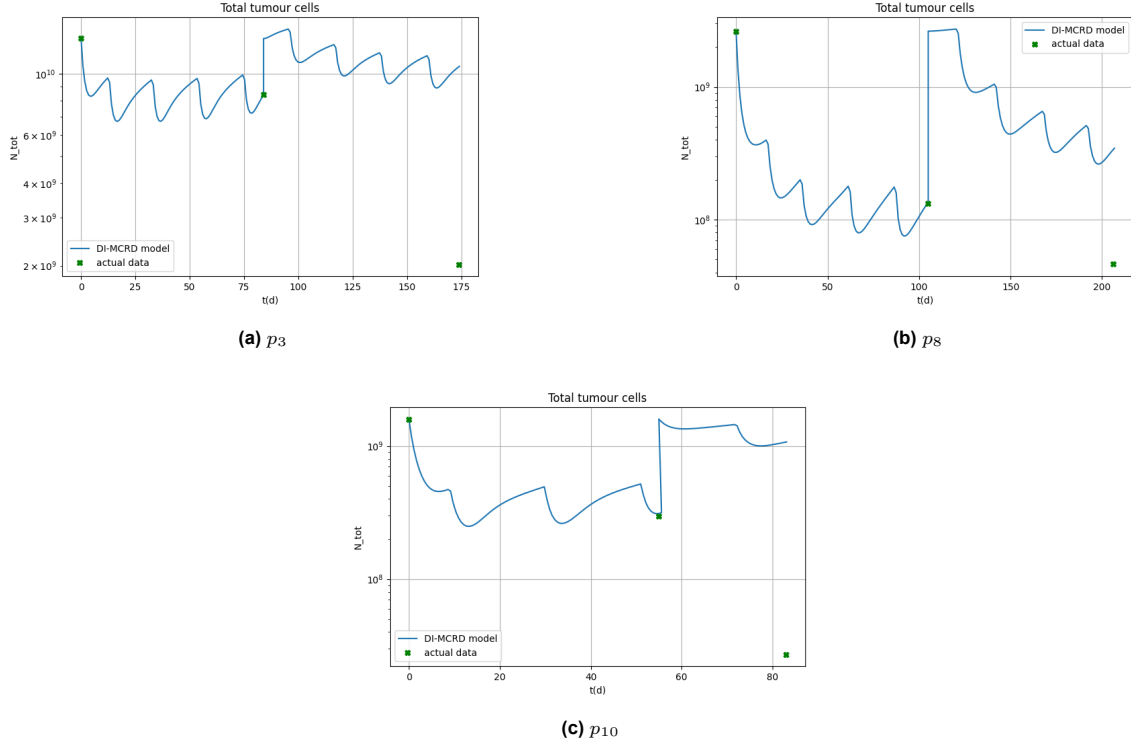


Figure 4.7: Total amount of tumour cells over time for three different patients obtained using model cycle Ia model.

4.2.2. Model Cycle Ib: TRF

Following the conclusion of the previous subcycle Ia, the parameters are no longer updated during the prediction phase. Moreover, as the non-strict bounds of the DL method do not resolve the negative proliferation rate $k(\bar{x})$ the TRF method will be used within this subcycle. As mentioned in Section 4.1.6 the TRF method is an optimization method with a strict trust region.

Results

To be able to compare the TRF with the DL method both methods are run for the same set of three patients as in the previous sub-cycle, both have similar trust region bounds as in the previous subcycle $k(\bar{x}) \in [0, 0.8]^n$ and $\alpha = 1$ with $\alpha \in [0, 2]$. The results can be found in Table 4.5.

	method	$[k_{\min}, k_{\max}]$	D_0	α	$e_r(t_1)$	$e_r(t_2)$	$e(t_1)$	$e(t_2)$
p_3	DL	$[-0.1418, 1.8918]$	0.0009	1.0783	0.1309	1.2173	$5.1824 \cdot 10^7$	$4.8210 \cdot 10^8$
	TRF	$[-0.1002, 0.8739]$	0.0098	1.0181	0.3899	0.9512	$1.5443 \cdot 10^8$	$3.7672 \cdot 10^8$
p_8	DL	$[-0.1402, 0.8001]$	0.0519	1.7436	0.0131	0.2215	$2.2269 \cdot 10^6$	$3.7703 \cdot 10^7$
	TRF	$[-0.1447, 0.7437]$	0.0583	1.6488	0.0186	0.2211	$3.1718 \cdot 10^6$	$3.7639 \cdot 10^7$
p_{10}	DL	$[-0.1169, 0.8676]$	0.0195	1.0802	0.1093	0.5714	$1.3856 \cdot 10^7$	$7.2405 \cdot 10^7$
	TRF	$[-0.1890, 0.6226]$	0.0293	1.1266	0.1055	0.5303	$1.3373 \cdot 10^7$	$6.7202 \cdot 10^7$

Table 4.5: Cycle Ib results of the DI-MCRD model applied for three patients.

From Table 4.5, it is immediately apparent that negative k_{\min} values are present for both optimization methods. This is not surprising for the DL method, as it was also observed in the previous subcycle

due to the non-strict bounds of the method. However, this is unexpected for the TRF method, which uses a strict trust region.

An explanation for this behavior lies in the fact that TRF uses the Conjugate Gradient Steihaug method [54] at each iteration to approximate the solution to the trust region subproblem, which determines the new set of parameters for the next iteration. Since this is an approximation, it can sometimes yield negative parameters. The difficulty in obtaining positive values for $k(\bar{x})$ suggests that the problem being solved may reflect a conflict between the model and the patient data.

Other observations from the table, when compared to the baseline results (see Table 4.3), are consistent with the previous cycle. In most cases, k_{\min} became even more negative, and the calibration for p_3 and p_{10} worsened significantly compared to the baseline model. However, the prediction errors for all patients remain similar to the baseline.

When considering Table 4.5 alongside the total number of tumour cells for both methods shown in Figure 4.8, several points can be noted. The calibration error is better for DL in patients p_3 and p_8 , whereas the TRF method performs better for p_{10} . However, in terms of prediction errors, the TRF method outperforms DL for all patients. This can also be seen in Figure 4.8, where the TRF plots show a smaller increase after t_1 than those for the DL method, making them more realistic. Nonetheless, in all cases, the model still overpredicts the number of tumour cells at t_2 .

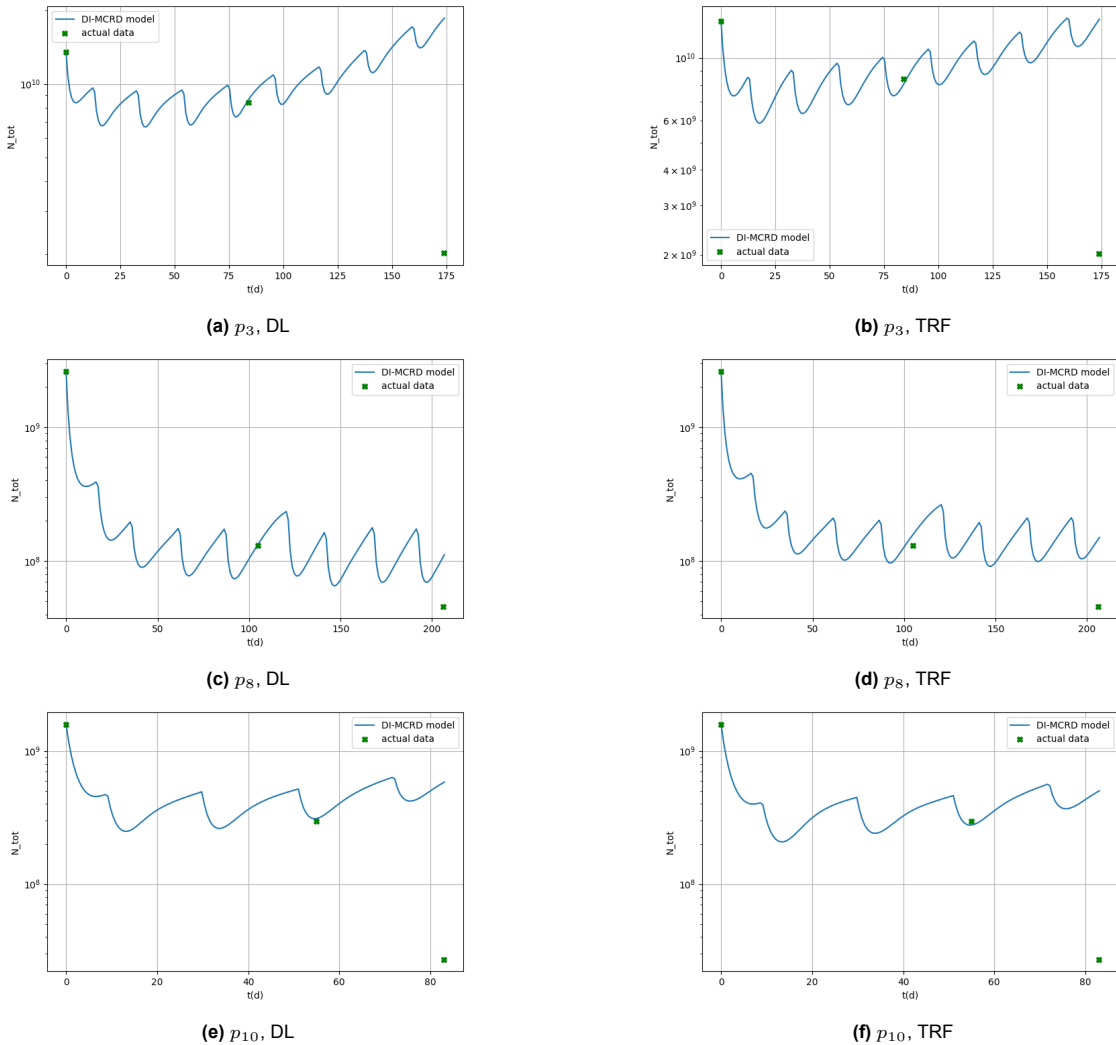


Figure 4.8: Total number of tumour cells over for three different patients using both DL and TRF optimization using the model from cycle Ib. The results are obtained using model cycle Ib model.

Examining the other visual results, which are provided in Appendix C.2.2, the main observation is that, similar to the previous cycle, all methods and patients show positive k values in the provided slices. While this appears promising, it remains uncertain whether other slices contain negative values in unrealistic locations.

It should be noted that the calibrated parameters and errors at t_1 for the DL method are not exactly the same as those in Table 4.4, particularly for the parameters of p_3 . These were expected to be identical due to the same initial conditions, a fixed random seed was used to ensure consistency in the randomly distributed $\mathbf{k}(\bar{x})$. The likely reason for this discrepancy is the use of a shared computing cluster, where multiple jobs from this research and other users may impact performance, leading to variations in the number of iterations completed within the calibration process before reaching t_{\max} .

To conclude this first model cycle, the most important findings are summarized. First, while updating the chemotherapy parameters and the shear modulus at t_1 provides a more realistic representation, the results show an unrealistic jump at t_1 . Therefore, this improvement is not considered satisfactory. Addressing the negative values of k by increasing α and using the TRF optimization method instead of DL did not yield the desired improvements. Both methods still show an increase in tumour cells after t_1 , and the calibration error has increased compared to the baseline results, although the prediction errors remain of the same order. Furthermore, k_{\min} remains negative in all cases.

4.3. Model Cycle II: Tissue-Specific Parameters

Since the previous cycle yielded suboptimal results with only minor adjustments to the baseline model, this cycle introduces more substantial changes. The primary objective is to gain better control over the proliferation rate and address the underdetermined nature of the system. To achieve this, the proliferation rate will now be made tissue-specific rather than defined on a per-voxel basis. More specifically, $\mathbf{k}(\bar{x})$ will be defined as follows:

$$\mathbf{k}(\bar{x}) = \begin{cases} k_{\text{tum}} & \text{if } \bar{x} \text{ is tumour tissue,} \\ k_{\text{adip}} & \text{if } \bar{x} \text{ is adipose tissue,} \\ k_{\text{fib}} & \text{if } \bar{x} \text{ is fibroglandular tissue.} \end{cases} \quad (4.34)$$

The voxels will be classified using tissue segmentation based on the DCE scans from the preprocessing pipeline (see Section 3.2). There are tissue segmentations available at both t_0 and t_1 . It is important to reiterate that if a voxel does not contain tumour cells, equation (4.17) becomes zero. In these voxels with zero tumour cells, k may be positive, this allows diffusing tumour cells that enter this voxel to continue proliferating.

To maintain spatial consistency and simplicity, the tissue classification will remain fixed, requiring a choice between the segmentation from t_0 or t_1 . If the t_0 classification is used, voxels identified as tumour at that time may remain tumour tissue or transition to adipose or fibroglandular tissue by t_1 , with the assumption that chemotherapy will cause most tumour cells to die, leaving only a small fraction to diffuse into other voxels. Consequently, the relevant voxels in $\mathbf{k}(\bar{x})$ would primarily consist of k_{tum} . Alternatively, using the classification from t_1 captures voxels that were tumour cells at t_0 but have since transitioned to fibroglandular or adipose tissue, represented by k_{fib} and k_{adip} , leading to a more diverse $\mathbf{k}(\bar{x})$. Given this, the tissue classification from t_1 is chosen.

Initializing $\mathbf{k}(\bar{x})$ involves two options: maintaining uniform values or assigning different initial proliferation rates for each tissue type. Generally, the tissues k_{fib} and k_{adip} were initially classified as tumour but have since transitioned to non-tumour states. As a result, they are expected to exhibit lower proliferation rates than k_{tum} , as the tumour cells in these regions have died. However, if tumour cells diffuse into these regions, some proliferation should occur, as otherwise, the tumour cells would die immediately.

Moreover, note that due to the reduction from $n + 2$ parameters to only 5, the system is no longer underdetermined. As a result, regularization is no longer necessary since the optimization process no longer requires constraints or smoothing to navigate the parameter space.

This reduction in parameters also leads to a smaller Jacobian. While the derivatives in equations (4.27)–(4.29) remain unchanged, the implementation of $\frac{d\mathbf{N}^m}{d\mathbf{k}}$ has been modified. Additionally, the overall im-

plementation of the model, including the Jacobian, had to be adapted to handle the reduced parameter set effectively.

Results

The tissue-specific version of the DI-MRCD model is run for the same set of patients as in the previous cycle. To determine the most appropriate calibration method, both TRF and DL are applied again for each patient. Both methods are reconsidered because they produced mixed results in the previous cycle, leaving uncertainty about which one yields the best and most realistic results. Uniform initial parameters are used for the proliferation rates, with $k_{\text{tum}} = k_{\text{adip}} = k_{\text{fib}} = 0.05$. The trust regions, $\mathbf{k}(\bar{x}) \in [0, 0.8]^3$, and the chemotherapy parameter $\alpha = 1$ (with $\alpha \in [0, 2]$), remain consistent with the previous cycle.

	method	$[k_{\text{adip}}, k_{\text{fib}}, k_{\text{tum}}]$	D_0	α	$e_r(t_1)$	$e_r(t_2)$	$e(t_1)$	$e(t_2)$
p_3	DL	[0.0088, 0.0072, 0.0546]	0.0524	1.0282	0.6589	0.6183	$2.6097 \cdot 10^8$	$2.4488 \cdot 10^8$
	TRF	[0.0124, 0.0109, 0.0544]	0.0567	1.0365	0.6620	0.6198	$2.6216 \cdot 10^8$	$2.4546 \cdot 10^8$
p_8	DL	[-0.0099, -0.0175, 0.1067]	0.2220	0.5231	0.1090	0.2143	$1.8553 \cdot 10^7$	$3.6484 \cdot 10^7$
	TRF	[0.0000, 0.0000, 0.1320]	0.1705	0.6810	0.1141	0.2165	$1.9419 \cdot 10^7$	$3.6861 \cdot 10^7$
p_{10}	DL	[-0.0879, -0.1195, 0.1358]	0.3146	0.4798	0.2026	0.4517	$2.5671 \cdot 10^7$	$5.7236 \cdot 10^7$
	TRF	[0.0000, 0.0001, 0.1229]	0.2847	0.4826	0.2219	0.4456	$2.8113 \cdot 10^7$	$5.6470 \cdot 10^7$

Table 4.6: Cycle II results of the DI-MCRD model applied for three patients.

From Table 4.6 and Figure 4.9, it is evident that the calibration errors are significantly worse compared to both the previous cycle and the baseline results. Analysis of the optimization process for all patients and both models reveals that after a certain number of iterations, the parameter set stagnates, and further iterations degrade the results. This indicates a failure to converge to a lower calibration error. The most likely cause is a conflict between the model and the patient data, which probably stems from the system being overdetermined—there are more equations than unknowns. In such cases, finding a consistent solution is difficult, as it is unlikely all equations will align perfectly. This inconsistency may cause the optimization process to get stuck in a local minimum, preventing further improvement.

Despite the poor calibration results, an improvement in prediction errors is observed compared to the baseline. It should be noted, however, that these improved predictions are not entirely reliable due to the suboptimal calibration. Nonetheless, a realistic decrease in the number of tumour cells is observed for p_8 in figures 4.9c and 4.9d, while the other two patients still show an increase in tumour cells. This contradiction between better prediction and worse calibration suggests that further adjustments to the model might be necessary to achieve more consistent results.

An important observation from Table 4.6 is that the DL method still produces negative values for k_{fib} and k_{adip} , whereas the TRF method yields only positive values for these parameters. Given that all proliferation rates should be positive, TRF appears to provide more biologically realistic results. However, it is worth noting that DL achieves a better calibration error than TRF, indicating a trade-off between calibration performance and realistic parameter values.

Further analysis from Table 4.6 reveals two notable trends. First, the proliferation rate k_{tum} is consistently higher than k_{fib} and k_{adip} , as expected. Voxels that still contain tumour cells at t_1 naturally exhibit higher proliferation rates than those that no longer contain tumour cells. Second, the diffusion parameter D_0 is significantly larger than in both the baseline and previous cycle results. This increase is likely due to the use of non-voxel-specific proliferation rates. When a voxel exhibits an increased number of tumour cells at t_1 but is not classified as tumour, diffusion to a neighbouring tumour-classified voxel likely occurs, to proliferate as expected.

In Appendix C.3, additional visualizations of the results are presented. In the 3D plots for p_3 and p_{10} , it can be observed that there are many voxels surrounding the tumour, as expected from the data, that contain a small number of tumour cells. It appears that the tumour shape from t_0 is still present, which

could indicate that the chemotherapy term did not work effectively, or, due to the previously mentioned higher diffusion parameter D_0 , the tumour cells have diffused more extensively.

Beyond these result-related insights, the tissue-specific adaptation of the model has led to a significant reduction in the time required per iteration. This improvement is due to the fact that the Jacobian now only needs to be generated for five parameters instead of $n + 2$. Comparing the average number of iterations within t_{\max} , cycle II completes approximately 31 iterations on average, compared to 26 for cycle Ib. Thus, this adaptation improves the computational performance and therefore accelerates the optimization process.

Concluding this second model cycle, the more substantial change to the model, making it tissue-specific, unfortunately, did not yield the desired results. The model's calibration worsened, and the optimization did not converge to an acceptable error, likely getting stuck in a local minimum. Only p_8 produced realistic results. However, the combination of the tissue-specific model with TRF optimization resulted in only positive proliferation rates, which is a more realistic outcome. Therefore, TRF optimization will be used going forward. Additionally, this model adaptation improved computational performance.

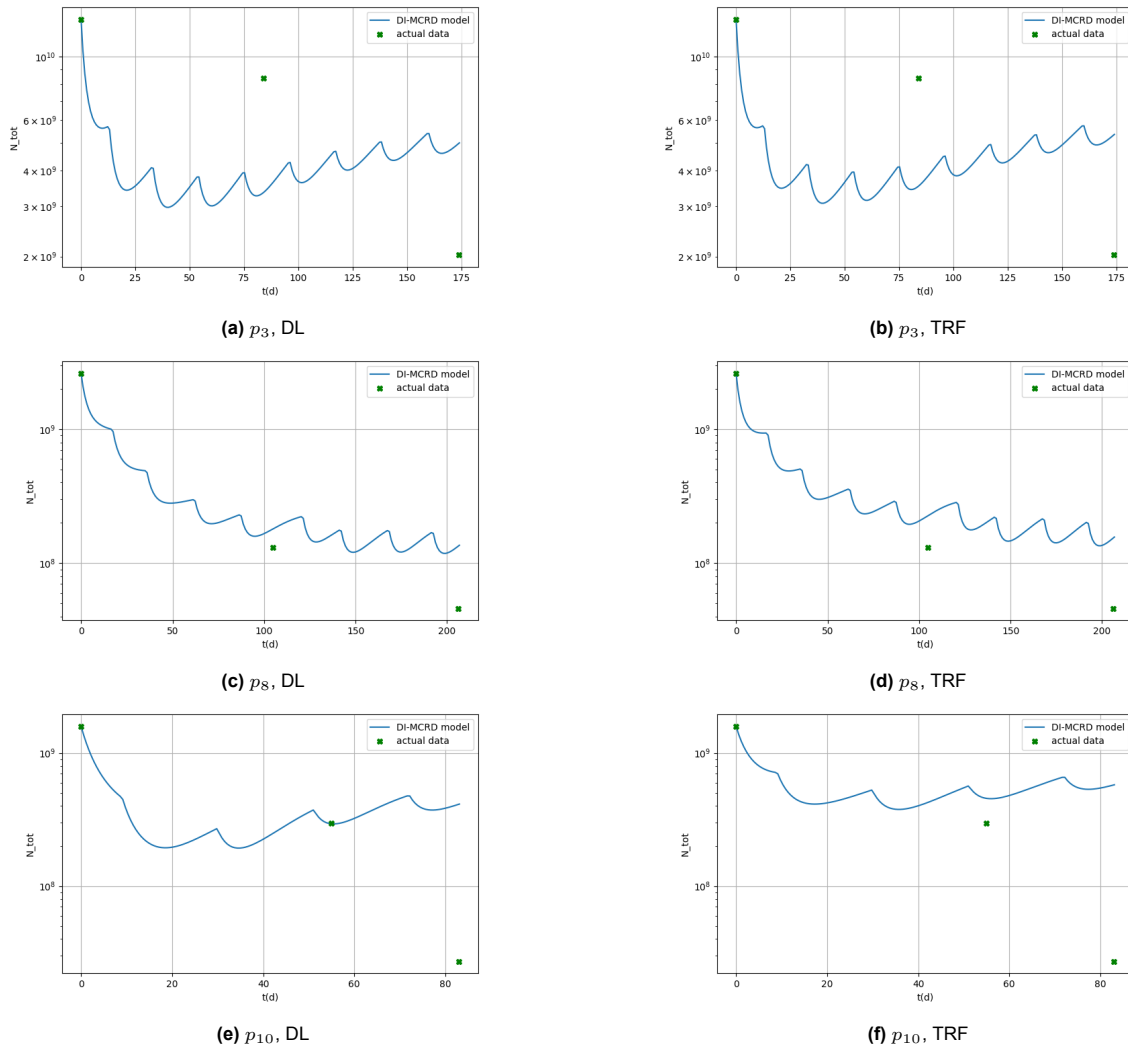


Figure 4.9: Total number of tumour cells over for three different patients using both DL and TRF optimization using the model from cycle IIa.

4.4. Model Cycle III: Inclusion of Death Term

Since the model in the previous cycle struggled to calibrate properly, likely due to a conflict between the model and the patient data, a new term will be introduced in this cycle: a 'death' term. This term is

designed to assist the chemotherapy term in reducing the number of tumour cells, also preventing $k(\bar{x})$ from becoming negative. Moreover, this new term aims to produce a decaying trajectory in the number of tumour cells over time, rather than an increasing one. Additionally, the death term is biologically realistic, as tumour cells undergo natural cell death even in the absence of chemotherapy. The updated model equation is as follows:

$$\frac{\partial N(\bar{x}, t)}{\partial t} = \nabla \cdot (D\nabla N(\bar{x}, t)) + \mathbf{k}(\bar{x})N(\bar{x}, t) \left(1 - \frac{N(\bar{x}, t)}{\theta}\right) - \alpha C_{\text{drug}}(\bar{x}, t_0)N(\bar{x}, t)e^{-\beta(t-\tilde{t})} - \gamma N(\bar{x}, t). \quad (4.35)$$

Here, γ is the death term parameter, which also needs to be calibrated and is therefore included in the parameter set \mathbf{P} , such that $\mathbf{P} = (\mathbf{k}(\bar{x}), D_0, \alpha, \gamma)$. To avoid an underdetermined system, $\mathbf{k}(\bar{x})$ remains tissue-specific, resulting in six parameters that need to be calibrated. However, with the inclusion of γ , the derivatives of the Jacobian presented in equations (4.27)–(4.29) have changed. Specifically, the prefactor has been modified, and an additional derivative has been introduced, resulting in the following updated derivatives:

$$\frac{d\mathbf{N}^{m+1}}{d\mathbf{k}} = \Delta t \left(\mathbf{N}^m \left(1 - \frac{\mathbf{N}^m}{\theta}\right) + \left(\frac{I}{\Delta t} + A(\mathbf{N}^m) + \mathbf{k} \left(1 - \frac{2\mathbf{N}^m}{\theta}\right) - \alpha \mathbf{C}^m - \gamma\right) \frac{d\mathbf{N}^m}{d\mathbf{k}} + \frac{\partial A(\mathbf{N}^m)}{\partial \mathbf{N}^m} \mathbf{N}^m \frac{d\mathbf{N}^m}{d\mathbf{k}} \right) \quad (4.36)$$

$$\frac{d\mathbf{N}^{m+1}}{dD_0} = \Delta t \left(\frac{A(\mathbf{N}^m)}{D_0} \mathbf{N}^m + \left(\frac{I}{\Delta t} + A(\mathbf{N}^m) + \mathbf{k} \left(1 - \frac{2\mathbf{N}^m}{\theta}\right) - \alpha \mathbf{C}^m - \gamma\right) \frac{d\mathbf{N}^m}{dD_0} + \frac{\partial A(\mathbf{N}^m)}{\partial \mathbf{N}^m} \mathbf{N}^m \frac{d\mathbf{N}^m}{dD_0} \right) \quad (4.37)$$

$$\frac{d\mathbf{N}^{m+1}}{d\alpha} = \Delta t \left(-\mathbf{C}^m \mathbf{N}^m + \left(\frac{I}{\Delta t} + A(\mathbf{N}^m) + \mathbf{k} \left(1 - \frac{2\mathbf{N}^m}{\theta}\right) - \alpha \mathbf{C}^m - \gamma\right) \frac{d\mathbf{N}^m}{d\alpha} + \frac{\partial A(\mathbf{N}^m)}{\partial \mathbf{N}^m} \mathbf{N}^m \frac{d\mathbf{N}^m}{d\alpha} \right) \quad (4.38)$$

$$\frac{d\mathbf{N}^{m+1}}{d\gamma} = \Delta t \left(-\mathbf{N}^m + \left(\frac{I}{\Delta t} + A(\mathbf{N}^m) + \mathbf{k} \left(1 - \frac{2\mathbf{N}^m}{\theta}\right) - \alpha \mathbf{C}^m - \gamma\right) \frac{d\mathbf{N}^m}{d\gamma} + \frac{\partial A(\mathbf{N}^m)}{\partial \mathbf{N}^m} \mathbf{N}^m \frac{d\mathbf{N}^m}{d\gamma} \right) \quad (4.39)$$

The inclusion of the parameter γ is implemented in the model. However, the initial value and the parameter bounds for γ are still unknown and must be tuned. To estimate a reasonable initial value for γ , the following reasoning is applied.

First, if we assume that the death term is primarily intended to prevent $\mathbf{k}(\bar{x})$ from becoming negative, the following relationship would be desired:

$$-\gamma N(\bar{x}, t) = \mathbf{k}(\bar{x})N(\bar{x}, t) \left(1 - \frac{N(\bar{x}, t)}{\theta}\right) \quad (4.40)$$

for cases where the proliferation rate was negative. Assuming that $N = \frac{\theta}{2}$ and solving equation (4.40), it is found that the initial γ should be approximately $-\mathbf{k}(\bar{x})/2$. Using the average of the previously observed negative values of $\mathbf{k}(\bar{x})$, this suggests that the initial γ should be around 0.08.

Second, it should be noted that the death term does not replace the chemotherapy term but rather reduces the number of tumour cells that are not affected by the chemotherapy term. Therefore, the following relationship should hold:

$$\gamma N(\bar{x}, t) < \alpha C_{\text{drug}}(\bar{x}, t_0)N(\bar{x}, t)e^{-\beta(t-\tilde{t})} \quad (4.41)$$

Using that the exponent equals 1 at $t = \tilde{t}$, it follows that $\gamma < \alpha C_{\text{drug}}(\bar{x}, t_0)$. For all patients, the maximum value of $C_{\text{drug}}(\bar{x}, t_0)$ is 2.59, and the maximum value of α observed in the cycles is 1.74. Therefore, the upper bound for γ is approximately 4.5. However, it is important to note that the death term reduces the number of tumour cells in each voxel at the same rate, while the chemotherapy term is dependent on the chemotherapy cycles. Thus, the initial value of γ should not be set too high.

Results

To evaluate the new model adaptation, different initial values of $\gamma_0 = 0.05, 0.005, 0.0005$ are tested, using the same trust region bound $\gamma \in [0, 4.5]$. All other parameter settings remain consistent with the

previous cycle. Since TRF calibration provided the most realistic results in the prior cycle, it is the only method used here. This cycle is again run for the same set of three patients, with the results presented in Table 4.7.

	γ_0	$[k_{\text{adip}}, k_{\text{fib}}, k_{\text{tum}}]$	D_0	α	γ	$e_r(t_1)$	$e_r(t_2)$	$e(t_1)$	$e(t_2)$
p_3	0.05	[0.0500, 0.0500, 0.0500]	0.0200	1.0000	0.0500	0.7722	0.3759	$3.0584 \cdot 10^8$	$1.4887 \cdot 10^8$
	0.005	[0.0467, 0.0457, 0.0734]	0.0238	1.0322	0.0119	0.7101	0.6113	$2.8123 \cdot 10^8$	$2.4209 \cdot 10^8$
	0.0005	[0.0365, 0.0359, 0.0636]	0.0220	1.0047	0.0179	0.7155	0.4559	$2.8336 \cdot 10^8$	$1.8053 \cdot 10^8$
p_8	0.05	[0.0402, 0.0411, 0.2305]	-0.0510	0.9727	0.0423	0.1539	0.1826	$2.6207 \cdot 10^7$	$3.1092 \cdot 10^7$
	0.005	[0.0404, 0.0404, 0.1195]	0.0347	0.9924	0.9528	0.2201	0.1215	$3.7476 \cdot 10^7$	$2.0684 \cdot 10^7$
	0.0005	[0.0006, 0.0382, 0.2434]	0.9421	0.7581	0.0547	0.1073	0.1978	$1.8268 \cdot 10^7$	$3.3680 \cdot 10^7$
p_{10}	0.05	[0.1525, 0.1155, 0.5809]	0.7285	0.5791	0.1782	0.2241	0.4326	$2.8397 \cdot 10^7$	$5.4821 \cdot 10^7$
	0.005	[0.0434, 0.0397, 0.2262]	0.0687	1.0346	0.9133	0.3701	0.1480	$4.6896 \cdot 10^7$	$1.8755 \cdot 10^7$
	0.0005	[0.0149, 0.0121, 0.2717]	0.0109	0.7068	0.0303	0.2353	0.4853	$2.9811 \cdot 10^7$	$6.1488 \cdot 10^7$

Table 4.7: Cycle III results of the DI-MCRD model applied for three patients for different initial values of γ .

Analyzing the table in comparison with Figure 4.10, which shows the number of tumour cells over time for all cases, the following observations can be made. The calibration error worsened compared to the previous cycle, while the prediction improved. This improvement is likely due to the inclusion of an additional tumour cell decay term in the model, resulting in better tumour decay compared to the previous cycle, as seen in Figures 4.10d and 4.10f. However, some unexpected and unrealistic results emerged. For p_8 with $\gamma_0 = 0.05$, a negative diffusion parameter was observed, and for p_8 with $\gamma_0 = 0.005$, Figure 4.10e shows a spiky, oscillatory pattern. Additionally, p_{10} with $\gamma_0 = 0.005$ exhibited an exponential decay in the number of tumour cells, likely due to the high calibrated value of γ . Furthermore, examining the iterations within the optimization process revealed that, in almost all cases, parameters were updated only once, after which no further improvement was achieved, leading to a lack of convergence. Notably, p_3 with $\gamma_0 = 0.05$ did not update the initial parameters at all.

Concluding this third cycle, the promising inclusion of the death term parameter did not yet deliver the expected results. However, due to time constraints, this method could not be further investigated. For future research, it is recommended to address the poor convergence observed in this cycle, potentially by tuning the parameters or considering alternative optimization methods. The other visual results can be found in Appendix C.4.

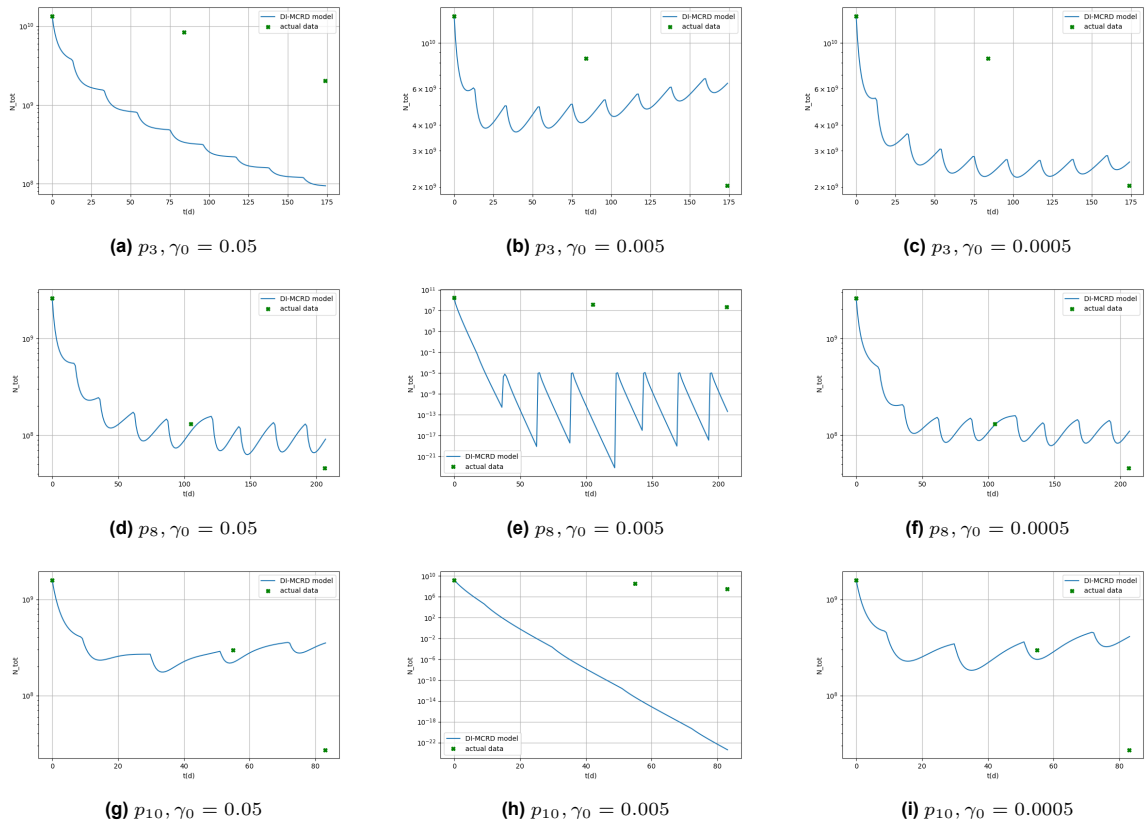


Figure 4.10: Total number of tumour cells over for three different patients for different initial values γ_0 using the model from cycle III.

4.5. Overview of the Modelling Cycles

In this section, a table is provided to give a clear overview of the different model cycles discussed in this chapter, highlighting the specific choices made in each cycle.

	method(s)	α_0	$\alpha \in$	$\mathbf{k}(\bar{x}) \in$	t^*	#params
baseline model	DL	0.5	$[0, 1]$	$[-0.5, 0.8]^n$	t_0	$n + 2$
cycle Ia: positive & updated parameters	DL	1	$[0, 2]$	$[0, 0.8]^n$	t_0, t_1	$n + 2$
cycle Ib: positive parameters	DL, TRF	1	$[0, 2]$	$[0, 0.8]^n$	t_0	$n + 2$
cycle II: tissue-specific	DL, TRF	1	$[0, 2]$	$[0, 0.8]^3$	t_0	5
cycle III: death term inclusion	TRF	1	$[0, 2]$	$[0, 0.8]^3$	t_0	6

Table 4.8: This table shows the differences between the models cycles taken within this chapter. Here method(s) refers to the optimization methods used/compared, α_0 refers to the initial value of α , $\alpha \in$ and $\mathbf{k}(\bar{x}) \in$ refer to the trust region bounds of the optimization methods, t^* refers to the time points where the parameters $C_{drug}(\bar{x}, t^*)$ and $G(\bar{x}, t^*)$ are updated, # params refers to the number of patient-specific parameters that need to be fitted.

5

Conclusion & Discussion

Building on three previous master's theses [10–12], this research aimed to improve the predictive capacity of the Drug-Induced Mechanically Coupled Reaction-Diffusion (DI-MRCD) model in simulating the chemotherapy response of human epidermal growth factor receptor 2 positive (HER2+) breast cancer patients. The model uses dynamic contrast-enhanced (DCE) and diffusion-weighted imaging (DWI) magnetic resonance imaging (MRI) data from two or three time points. These scans are preprocessed using a pipeline to estimate the number of tumour cells per voxel. Using the number of tumour cells from the first two time points, the DI-MRCD model is calibrated to determine patient-specific parameters, allowing for the prediction of tumour cell evolution over time, which can be verified with a third scan, if available.

The improvements to the model's predictive capacity in this thesis focused on two main areas. First, the preprocessing pipeline was reevaluated, as the previous pipeline was neither tailored to patient-specific data nor generally applicable across a broader patient cohort. The dataset was expanded from the three patients used in previous studies to thirteen patients, necessitating the development of a novel, generalized preprocessing approach suitable for all patients. This reevaluation led to several key improvements in the preprocessing pipeline. Second, the DI-MRCD model itself, along with the optimization techniques used for calibration, underwent several refinements. Multiple iterations were performed aiming at enhancing the model's predictive accuracy.

In this chapter, both main areas of the research will be discussed separately in two sections. Within each section, a brief evaluation of the results will be followed by a discussion of key points. The chapter will conclude with a summary of future research opportunities.

5.1. Pre-Processing Pipeline

The preprocessing pipeline consists of six steps, each of which will be summarised and discussed separately. The first step is data acquisition, where MRI scans, chemotherapy data, and other patient specifics are collected. The Erasmus Medical Centre (EMC) provided a dataset consisting of 24 patients. However, several initial time point scans were not taken at the EMC, resulting in varying intensities and file formats, and thus were excluded from the dataset. This resulted in a final dataset of thirteen patients. For extensive evaluation of the predictive performance of the DI-MRCD model, a larger dataset would be preferable. Therefore, finding a way to realistically incorporate the scans from the excluded patients would be beneficial.

The second step involved segmenting the tumours using the DCE-MRI scans, in close collaboration with Radiologist Dr. C. de Monyé. We reviewed the scans together, discussing each patient and outlining the lesions around the tumours. While I completed some of the segmentations independently at home, every step was subsequently reviewed and verified by Dr. de Monyé, ensuring consistency and reducing the likelihood of significant errors. Despite her expertise, human error is always a possibility, particularly when working with challenging cases. Many patients had DCIS tumours, and the scans from the later time points often revealed only very small tumours, which were difficult to detect, even

for Dr. de Monyé. In such cases, it was sometimes challenging to definitively classify some voxels as tumour or non-tumour. To further improve the precision and reliability of the segmentations, an additional review by another radiologist could be beneficial. Alternatively, a fuzzy c-means algorithm can be used alongside the radiologist's segmentation to refine the boundaries of the tumours, as seen in studies from the Texas research group [8, 9].

The third step involved registering the MRI images and tumour segmentations with each other. A sequential registration process, combining rigid and affine methods, was used to balance computational efficiency with the flexibility required to accurately align images while preserving essential anatomical relationships and spatial coherence. Before registration, the DCE images were downsampled to match the resolution of the DWI images and had to be scaled. Although, in theory, scaling should not be necessary when using the default AdvancedMattesMutualInformation metric, further investigation into this unexpected requirement is warranted. Additionally, registration masks were essential for proper alignment. A rectangular mask on the breast, combined with a region-growing algorithm, was found to be the most effective approach. The registration order was adapted from Oudhof's version [10], with the DWI image from the second time point selected as the fixed image. This choice prevented unnecessary upsampling and the generation of artificial information and ensured optimal reliability for the predictive step of the DI-MRCD model. In conclusion, this step developed a generally applicable registration process that effectively aligns the images, requiring only the manual selection of seed points and thresholds for region growing in the registration masks.

The fourth step involves selecting the region of interest (ROI), specifically the breast or breasts where the tumour is located, and obtaining a corresponding breast mask. For this step, the same approach as Oudhof [10] was followed. The ROI is manually selected, after which the seed point and threshold for the region-growing method are manually adjusted to obtain the breast mask. An automatic algorithm could be developed that uses the tumour segmentation to select the ROI and generate the breast mask more efficiently.

In the fifth step, the number of tumour cells per voxel is determined using DWI-MRI scans, with the apparent diffusion coefficient (ADC) used for this calculation. Previous theses [10–12] relied on ADC values computed by the MRI scanner. However, to avoid potential errors in the MRI-generated ADC values and to enhance transparency and reliability in this research, the ADC values were computed using a literature-based formula [38], which is also used in the Texas studies [4–9]. The use of self-computed ADC values resulted in significant differences in the number of tumour cells per voxel and a smoother distribution of tumour cells compared to the MRI-generated ADC values. However, a general remark on the use of ADC values is that, in addition to cellularity, factors such as cell size and cell membrane permeability also influence changes in ADC values, meaning the estimated tumour densities are only an approximation of the actual tumour densities. Moreover, while all the Texas studies [4–9] also use this ADC value, they consistently note the ambiguity of its interpretation and recommend finding a more precise method for estimating tumour densities.

The final preprocessing step involved segmenting the different tissues within the breast. This was achieved using global histogram equalization and a simple thresholding technique, similar to the approach of Oudhof [10]. It is important to note that in this segmentation process, each voxel is assumed to be classified as either fibroglandular, adipose, or tumourous tissue. This is, of course, a simplification of reality, as is the assumption that a tumourous voxel consists solely of tumour cells.

5.2. DI-MRCD Model

In this study, a system of partial differential equations (PDEs) is used to model the spatiotemporal evolution of tumour cells per voxel. The patient-specific parameters that need to be fitted include D_0 the diffusion parameter, $k(\bar{x})$ the proliferation rate defined per voxel, and α the efficacy parameter of the chemotherapy. These parameters must be calibrated by fitting the model to MRI-derived data from the first two time points, allowing for patient-specific parameterization. The derived data is the amount of tumour cells per voxel as described in the previous section.

Baseline Results

Initially, the latest version of the model, created by Engelberts [12], was used to establish baseline results. Engelberts used the non-linear Dog-Leg (DL) optimization method, which uses non-strict bounds,

with a negative lower bound. Additionally, since the optimization problem is underdetermined, regularization terms are incorporated to stabilize the solution. While the DL method calibrated well, after the second time point, the total number of tumour cells almost always increased, which is unrealistic, as the tumour cell count is expected to decrease due to chemotherapy. The MRI scans, including scans at three time points, did not reflect this predicted behaviour. Additionally, another issue observed in the results was that the minimum proliferation rate for all patients was negative, which is highly unrealistic given that the proliferation term is defined by a logistic growth model. Furthermore, it was found that the mechanical coupling led to insufficient tumour diffusion in regions of high stiffness at the second time point, which did not match the expected diffusion patterns based on the data.

First Modelling Cycle

The first model cycle consisted of two subcycles. In the first subcycle, the model was updated by updating the chemotherapy parameters and the shear modulus at the second time point to make the model more realistic, following a similar approach used in the Texas studies [4–9]. Additionally, the Dog-leg (DL) method was used with a positive lower bound and the initial value of α was increased. However, the updating of the parameters for the prediction phase led to an unrealistic jump in the number of tumour cells at the second time point, likely due to the chemotherapy parameter updates. Moreover, the minimum proliferation rates were still calibrated to negative values.

In the second subcycle, the parameter updating was cancelled, and a different optimization method, the Trust-Region Reflective (TRF) method, was used, which enforces strict parameter bounds. The TRF method was used with similar positive bounds as in the previous subcycle and the same increase in initial α was used. However, even with the TRF method, the results still showed negative minimum values for k . Despite this, a visual examination of the proliferation rate through a slice revealed no negative values around the tumour's location, which is promising.

The cancellation of parameter updating reduced the model's realism. Therefore, alternative approaches could have been explored to incorporate the additional available patient information into the model. For example, instead of performing a discrete parameter update at the second time step, a smoother transition between the parameters at the first and second time points could be implemented.

Second Modelling Cycle

The second modelling cycle involved a more substantial change to the model to gain better control over the system and address its underdetermined nature. To achieve this, the proliferation rate was made tissue-specific. The tissue classification was based on the segmentation from the second time point to introduce more diversity in $k(\bar{x})$. With this reduction in the number of parameters, the system became overdetermined rather than underdetermined, eliminating the need for regularisation terms. Uniform initial values for the different tissues were chosen, and both DL and TRF optimization methods were tested, as the TRF method had not produced more realistic results in the previous subcycle.

The results showed that the calibration errors were significantly worse compared to previous cycles, likely due to a lack of convergence, suggesting that the system may have been stuck in a local minimum. Given the highly overdetermined nature of the system, it is likely that the model conflicted with the data, making it difficult to find a consistent solution. Moreover, it still overpredicts the amount of tumour cells. Nevertheless, the TRF optimization produced only positive proliferation rates, unlike the DL method, making TRF the more realistic option. Although the model did not yield the desired results, it improved computational performance due to the smaller parameter set, which resulted in a smaller Jacobian for optimization.

The fact that the chemotherapy term and the shear modulus configurations are taken from the first time point, while the tissue classification is based on the segmentation from the second time point, creates an inconsistency in the model. Therefore, reassessing this choice or incorporating a smooth transition between the updates of the shear modulus and chemotherapy term is necessary. Additionally, the tissue-specific model could have considered tumourous versus non-tumourous instead of the three different tissue types. Moreover, the carrying capacity could have been used to calculate how much space remains for other tissues within a voxel, which could then provide a weighted average of the tissue-specific proliferation rates for each voxel. This approach would enhance the biological interpretation of tissue composition, as a voxel is unlikely to consist solely of tumourous tissue but rather a mixture of various tissue types.

Third modelling Cycle

The third and final model cycle introduced a biologically realistic death term, with the parameter γ , to account for natural cell death in addition to the chemotherapy effect. This term was intended to support the chemotherapy term in reducing tumour cell numbers and preventing negative proliferation rates. However, despite its potential, this modification led to unrealistic results, likely due to convergence issues that could not be further investigated due to time constraints.

Exploring a wider range of initial values could improve convergence and provide better insight into the model's behaviour. Additionally, to prevent the death term from overshadowing the chemotherapy effect, a dependency could be introduced to ensure the death term remains smaller. While these experiments were limited, this model holds promise for future research given its biological relevance.

5.3. Concluding & Future Research

In conclusion, the newly developed pre-processing pipeline has significantly enhanced the reliability and generalizability of the input data for the DI-MRCD model, particularly when new patients are included in future research. The DI-MRCD model has undergone several modelling cycles, providing more insight and control, and making it biologically more accurate. However, the results are not yet fully satisfactory. It is important to note that fitting patient-specific parameters using only two time points is challenging. Ideally, a clinical study involving multiple patients and multiple scans throughout their chemotherapy treatment would provide better insights into whether the DI-MRCD model accurately represents the response of a HER2+ breast cancer tumour to treatment.

In addition to this, several other areas of future research are outlined below. First, currently, only the parameters D_0 , k_{adip} , k_{fib} , k_{tum} , α , and γ are calibrated using patient data. However, other parameters are also likely to be patient-specific. For example, Young's modulus, E , which contributes to the shear modulus, is currently based on literature values for each tissue type. However, the stiffness of a tissue is certainly tissue-specific. Additionally, while the chemotherapy effectiveness parameter α is included, the drug decay rate β could also be considered for calibration. It is important to note, however, that including more parameters increases the complexity of the model, requiring more tuning of parameter ranges and initial values. This, in turn, raises the risk of getting trapped in local minima during optimization and increases the likelihood of overfitting.

Second, currently, when a voxel does not contain tumour cells, $k(\bar{x})$ is likely to be set to zero or a negative value by the DI-MRCD model. However, when a tumour cell diffuses into such a voxel, it will die in subsequent iterations due to the low proliferation rate of that voxel. A more realistic approach would be to allow $k(\bar{x})$ to change over time ($k(\bar{x}, t)$), enabling the proliferation rate to diffuse along with the tumour cells, reflecting changes in the local environment of each voxel.

Third, currently, the chemotherapy term only accounts for the first day of each treatment cycle and does not consider the varying dosages administered across therapies. Furthermore, the second week of each cycle, during which paclitaxel is typically administered again, is not included in the model. To improve the accuracy of the model, incorporating this additional treatment data could be beneficial, allowing for a more comprehensive use of the available patient data.

Fourth, to gain better insight into the optimization process and the calibration of patient-specific parameters, the Bayesian method can be employed. By using Bayesian optimization instead of the TRF method, it not only provides parameter estimates but also valuable insight into the uncertainty of the parameter set. Bayesian optimization incorporates a probabilistic model that quantifies the confidence in each parameter, enabling a more informed exploration of the solution space. This optimization method has already been applied to cancer modelling in studies by Laura Scarabosio [55, 56], particularly for the tumour microenvironment, where a similar model equation is used as in the DI-MRCD model.

Last, once several model adaptations result in a robust working model that can predict chemotherapy responses for some patients, additional available data—such as BMI, weight, tumour receptors, scan days, tumour type, and clinical start—can be analyzed to identify correlations. The goal would be to enhance the explanatory power of the model by determining for which patient subgroups the model provides accurate predictions.

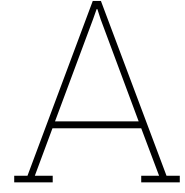
References

- [1] Hyuna Sung, Jacques Ferlay, Rebecca L Siegel, Mathieu Laversanne, Isabelle Soerjomataram, Ahmedin Jemal, and Freddie Bray. Global cancer statistics 2020: Globocan estimates of incidence and mortality worldwide for 36 cancers in 185 countries. *CA: a Cancer Journal for Clinicians*, 71(3):209–249, 2021.
- [2] Emily Heer, Andrew Harper, Noah Escandor, Hyuna Sung, Valerie McCormack, and Miranda M Fidler-Benaoudia. Global burden and trends in premenopausal and postmenopausal breast cancer: a population-based study. *The Lancet Global Health*, 8(8):e1027–e1037, 2020.
- [3] IKNL. Incidentie borstkanker. URL <https://iknl.nl/kankersoorten/borstkanker/registratie/incidentie>. Accessed: 21-12-2023.
- [4] Jared A Weis, Michael I Miga, Lori R Arlinghaus, Xia Li, A Bapsi Chakravarthy, Vandana Abramson, Jaime Farley, and Thomas E Yankeelov. A mechanically coupled reaction-diffusion model for predicting the response of breast tumors to neoadjuvant chemotherapy. *Physics in Medicine & Biology*, 58(17):5851, 2013.
- [5] Jared A Weis, Michael I Miga, Lori R Arlinghaus, Xia Li, Vandana Abramson, A Bapsi Chakravarthy, Praveen Pendyala, and Thomas E Yankeelov. Predicting the response of breast cancer to neoadjuvant therapy using a mechanically coupled reaction-diffusion model. *Cancer Research*, 75(22):4697–4707, 2015.
- [6] Jared A Weis, Michael I Miga, and Thomas E Yankeelov. Three-dimensional image-based mechanical modeling for predicting the response of breast cancer to neoadjuvant therapy. *Computer Methods in Applied Mechanics and Engineering*, 314:494–512, 2017.
- [7] Angela M Jarrett, David A Hormuth, Stephanie L Barnes, Xinzeng Feng, Wei Huang, and Thomas E Yankeelov. Incorporating drug delivery into an imaging-driven, mechanics-coupled reaction-diffusion model for predicting the response of breast cancer to neoadjuvant chemotherapy: Theory and preliminary clinical results. *Physics in Medicine & Biology*, 63(10):105015, 2018.
- [8] Angela M Jarrett, David A Hormuth II, Chengyue Wu, Anum S Kazerouni, David A Ekrut, John Virostko, Anna G Sorace, Julie C DiCarlo, Jeanne Kowalski, Debra Patt, et al. Evaluating patient-specific neoadjuvant regimens for breast cancer via a mathematical model constrained by quantitative magnetic resonance imaging data. *Neoplasia*, 22(12):820–830, 2020.
- [9] Angela M Jarrett, David A Hormuth, Vikram Adhikarla, Prativa Sahoo, Daniel Abler, Lusine Tumyan, Daniel Schmolze, Joanne Mortimer, Russell C Rockne, and Thomas E Yankeelov. Towards integration of ⁶⁴cu-dota-trastuzumab pet-ct and MRI with mathematical modeling to predict response to neoadjuvant therapy in HER2+ breast cancer. *Scientific Reports*, 10(1):20518, 2020.
- [10] Nathalie L. Oudhof. Predicting tumour response. Master’s thesis, Delft University of Technology, 2022.
- [11] Eva Slingerland. Modelling breast cancer treatment. Master’s thesis, Delft University of Technology, 2022.
- [12] Rutger Q. Engelberts. A numerically efficient implementation of the di-mcrd model in 3d. Master’s thesis, Delft University of Technology, 2023.
- [13] Britta Weigelt, Felipe C Geyer, and Jorge S Reis-Filho. Histological types of breast cancer: How special are they? *Molecular Oncology*, 4(3):192–208, 2010.

- [14] Richtlijndatabase.nl. TNM 8 - Borstkanker - Richtlijndatabase, 2024. URL https://richtlijndatabase.nl/richtlijn/borstkanker/tnm_8.html. Accessed: 14-07-2024.
- [15] S Dawood, K Broglio, FJ Esteva, NK Ibrahim, S-W Kau, R Islam, KD Aldape, T-K Yu, GN Hortobagyi, and AM Gonzalez-Angulo. Defining prognosis for women with breast cancer and cns metastases by HER2 status. *Annals of Oncology*, 19(7):1242–1248, 2008.
- [16] Ashis K Basu. DNA damage, mutagenesis, and cancer. *International Journal of Molecular Sciences*, 19(4):970, 2018.
- [17] Alexia L McKnight, Jennifer L Kugel, Phillip J Rossman, Armando Manduca, Lynn C Hartmann, and Richard L Ehman. MR Elastography of breast cancer: Preliminary results. *American Journal of Roentgenology*, 178(6):1411–1417, 2002.
- [18] David A Hormuth, Jared A Weis, Stephanie L Barnes, Michael I Miga, Erin C Rericha, Vito Quaranta, and Thomas E Yankeelov. A mechanically coupled reaction-diffusion model that incorporates intra-tumoural heterogeneity to predict in vivo glioma growth. *Journal of The Royal Society Interface*, 14(128):20161010, 2017.
- [19] Narmin Ghaffari Laleh, Chiara Maria Lavinia Loeffler, Julia Grajek, Kateřina Staňková, Alexander T Pearson, Hannah Sophie Muti, Christian Trautwein, Heiko Enderling, Jan Poleszczuk, and Jakob Nikolas Kather. Classical mathematical models for prediction of response to chemotherapy and immunotherapy. *PLoS Computational Biology*, 18(2):e1009822, 2022.
- [20] Angela M Jarrett, Ernesto ABF Lima, David A Hormuth, Matthew T McKenna, Xinzeng Feng, David A Ekrut, Anna Claudia M Resende, Amy Brock, and Thomas E Yankeelov. Mathematical models of tumor cell proliferation: A review of the literature. *Expert Review of Anticancer Therapy*, 18(12):1271–1286, 2018.
- [21] EO Alzahrani, Asim Asiri, MM El-Dessoky, and Yang Kuang. Quiescence as an explanation of gompertzian tumor growth revisited. *Mathematical Biosciences*, 254:76–82, 2014.
- [22] Antonio C Wolff, Donald Berry, Lisa A Carey, Marco Colleoni, Mitchell Dowsett, Matthew Ellis, Judy E Garber, David Mankoff, Soonmyung Paik, Lajos Pusztai, et al. Research issues affecting preoperative systemic therapy for operable breast cancer. *Journal of Clinical Oncology*, 26(5):806–813, 2008.
- [23] Mette S van Ramshorst, Claudette E Loo, Emilie J Groen, Gonneke H Winter-Warnars, Jelle Wesseling, Frederieke van Duijnhoven, Marie-Jeanne T Vrancken Peeters, and Gabe S Sonke. MRI predicts pathologic complete response in HER2-positive breast cancer after neoadjuvant chemotherapy. *Breast Cancer Research and Treatment*, 164:99–106, 2017.
- [24] Vishwa S Parekh and Michael A Jacobs. Multiparametric radiomics methods for breast cancer tissue characterization using radiological imaging. *Breast Cancer Research and Treatment*, 180:407–421, 2020.
- [25] Mette S van Ramshorst, Anna van der Voort, Erik D van Werkhoven, Ingrid A Mandjes, Inge Kemper, Vincent O Dezentjé, Irma M Oving, Aafke H Honkoop, Lidwine W Tick, Agnes J van de Wouw, et al. Neoadjuvant chemotherapy with or without anthracyclines in the presence of dual HER2 blockade for HER2-positive breast cancer (TRAIN-2): a multicentre, open-label, randomised, phase 3 trial. *The Lancet Oncology*, 19(12):1630–1640, 2018.
- [26] Balaraman Kalyanaraman. Teaching the basics of cancer metabolism: Developing antitumor strategies by exploiting the differences between normal and cancer cell metabolism. *Redox Biology*, 12:833–842, 2017.
- [27] Rahul P Kotian and Prakashini Koteswar. Dwi physics and imaging techniques. In *Diffusion Tensor Imaging and Fractional Anisotropy: Imaging Biomarkers in Early Parkinson's Disease*, pages 31–46. Springer, 2022.

- [28] Nkiruka C Atuegwu, Lori R Arlinghaus, Xia Li, A Bapsi Chakravarthy, Vandana G Abramson, Melinda E Sanders, and Thomas E Yankeelov. Parameterizing the logistic model of tumor growth by DW-MRI and DCE-MRI data to predict treatment response and changes in breast cancer cellularity during neoadjuvant chemotherapy. *Translational Oncology*, 6(3):256–264, 2013.
- [29] Xia Li, Hakmook Kang, Lori R Arlinghaus, Richard G Abramson, A Bapsi Chakravarthy, Vandana G Abramson, Jaime Farley, Melinda Sanders, and Thomas E Yankeelov. Analyzing spatial heterogeneity in DCE- and DW-MRI parametric maps to optimize prediction of pathologic response to neoadjuvant chemotherapy in breast cancer. *Translational Oncology*, 7(1):14–22, 2014.
- [30] Icometrix. Dicom2nifti, 2024. URL <https://icometrix.github.io/dicom2nifti/>. Accessed: 2024-09-03.
- [31] Chengyue Wu, Federico Pineda, David A Hormuth, Gregory S Karczmar, and Thomas E Yankeelov. Quantitative analysis of vascular properties derived from ultrafast DCE-MRI to discriminate malignant and benign breast tumors. *Magnetic Resonance in Medicine*, 81(3):2147–2160, 2019.
- [32] Weijie Chen, Maryellen L Giger, and Ulrich Bick. A fuzzy c-means (fcm)-based approach for computerized segmentation of breast lesions in dynamic contrast-enhanced MR Images. *Academic Radiology*, 13(1):63–72, 2006.
- [33] Barbara Zitova and Jan Flusser. Image registration methods: A survey. *Image and Vision Computing*, 21(11):977–1000, 2003.
- [34] Xia Li, Benoit M Dawant, E Brian Welch, A Bapsi Chakravarthy, Darla Freehardt, Ingrid Mayer, Mark Kelley, Ingrid Meszoely, John C Gore, and Thomas E Yankeelov. A nonrigid registration algorithm for longitudinal breast MR Images and the analysis of breast tumor response. *Magnetic Resonance Imaging*, 27(9):1258–1270, 2009.
- [35] Stefan Klein, Marius Staring, Keelin Murphy, Max A Viergever, and Josien PW Pluim. Elastix: A toolbox for intensity-based medical image registration. *IEEE Transactions on Medical Imaging*, 29(1):196–205, 2009.
- [36] Yoshitaka Masutani, Thomas Schiemann, and Karl-Heinz Höhne. Vascular shape segmentation and structure extraction using a shape-based region-growing model. In *Medical Image Computing and Computer-Assisted Intervention—MICCAI’98: First International Conference Cambridge, MA, USA, October 11–13, 1998 Proceedings 1*, pages 1242–1249. Springer, 1998.
- [37] Jennifer G Whisenant, Gregory D Ayers, Mary E Loveless, Stephanie L Barnes, Daniel C Colvin, and Thomas E Yankeelov. Assessing reproducibility of diffusion-weighted magnetic resonance imaging studies in a murine model of HER2+ breast cancer. *Magnetic Resonance Imaging*, 32(3):245–249, 2014.
- [38] Luisa Nogueira, S Brandão, E Matos, RG Nunes, J Loureiro, HA Ferreira, and I Ramos. Diffusion-weighted imaging: Determination of the best pair of b-values to discriminate breast lesions. *The British Journal of Radiology*, 87(1039):20130807, 2014.
- [39] Thomas E Yankeelov and John C Gore. Dynamic contrast-enhanced magnetic resonance imaging in oncology: Theory, data acquisition, analysis, and examples. *Current Medical Imaging*, 3(2):91–107, 2007.
- [40] Wei Huang, Luminita A Tudorica, Xin Li, Sunitha B Thakur, Yiyi Chen, Elizabeth A Morris, Ian J Tagge, Maayan E Korenblit, William D Rooney, Jason A Koutcher, et al. Discrimination of benign and malignant breast lesions by using shutter-speed dynamic contrast-enhanced MR Imaging. *Radiology*, 261(2):394–403, 2011.
- [41] DR Barpe, DD Rosa, and PE Froehlich. Pharmacokinetic evaluation of doxorubicin plasma levels in normal and overweight patients with breast cancer and simulation of dose adjustment by different indexes of body mass. *European Journal of Pharmaceutical Sciences*, 41(3-4):458–463, 2010.

- [42] WJ van der Vijgh. Clinical pharmacokinetics of carboplatin. *Clinical Pharmacokinetics*, 21(4): 242–261, 1991.
- [43] T Mori, Y Kinoshita, A Watanabe, T Yamaguchi, K Hosokawa, and H Honjo. Retention of paclitaxel in cancer cells for 1 week in vivo and in vitro. *Cancer Chemotherapy and Pharmacology*, 58(5): 665–672, 2006.
- [44] KD Tew. Paclitaxel. *Reference Module in Biomedical Sciences*, 2016. URL <https://www.sciencedirect.com/science/article/pii/B9780128012383993930?via%3Dihub>.
- [45] L Yang, XC Zhang, SF Yu, HQ Zhu, AP Hu, J Chen, and P Shen. Pharmacokinetics and safety of cyclophosphamide and docetaxel in a hemodialysis patient with early stage breast cancer: a case report. *BMC Cancer*, 15:917, 2015.
- [46] C. Vuik and D.J.P. Lahaye. Scientific computing (wi4201). Lecture Notes for WI4201, 2012.
- [47] Ahmed El-Koka, Kyung-Hwan Cha, and Dae-Ki Kang. Regularization parameter tuning optimization approach in logistic regression. In *2013 15th International Conference on Advanced Communications Technology (ICACT)*, pages 13–18. IEEE, 2013.
- [48] Donald W Marquardt. An algorithm for least-squares estimation of nonlinear parameters. *Journal of the Society for Industrial and Applied Mathematics*, 11(2):431–441, 1963.
- [49] Thomas F Coleman and Yuying Li. An interior trust region approach for nonlinear minimization subject to bounds. *SIAM Journal on Optimization*, 6(2):418–445, 1996.
- [50] Michael JD Powell. A hybrid method for nonlinear equations. *Numerical Methods for Nonlinear Algebraic Equations*, pages 87–161, 1970.
- [51] Michael JD Powell. A new algorithm for unconstrained optimization. In *Nonlinear programming*, pages 31–65. Elsevier, 1970.
- [52] Manolis LA Lourakis and Antonis A Argyros. Is levenberg-marquardt the most efficient optimization algorithm for implementing bundle adjustment? In *Tenth IEEE International Conference on Computer Vision (ICCV'05) Volume 1*, volume 2, pages 1526–1531. IEEE, 2005.
- [53] Andrew M. Bradley. Pde-constrained optimization and the adjoint method. Technical report, Stanford University, 2013. URL <https://cs.stanford.edu/~ambrad/>. Technical Report.
- [54] Trond Steihaug. The conjugate gradient method and trust regions in large scale optimization. *SIAM Journal on Numerical Analysis*, 20(3):626–637, 1983.
- [55] Sabrina Schönfeld, Laura Scarabosio, Alican Ozkan, Marissa Nichole Rylander, and Christina Kuttler. Using systemic modeling and bayesian calibration to investigate the role of the tumor microenvironment on chemoresistance. *arXiv preprint arXiv:2310.19688*, 2023.
- [56] Sabrina Schönfeld, Alican Ozkan, Laura Scarabosio, Marissa Nichole Rylander, and Christina Kuttler. Environmental stress level to model tumor cell growth and survival. *arXiv preprint arXiv:2201.06985*, 2022.



Exponential and Gompertz Model for Tumour Growth

In this chapter, both models will first be explained, followed by their application to existing data to evaluate whether they can approximate tumour predict tumour decay.

A.1. Exponential model

The exponential model is the initial model that is used for tumour growth. It is given by the following differential equation [19]:

$$\frac{dN}{dt} = (\alpha - \beta)N, \quad (\text{A.1})$$

where α [time⁻¹] represent the growth and β [time⁻¹] the death rate. This differential equation can easily be solved:

$$N(t) = N_0 e^{(\alpha - \beta)t}, \quad (\text{A.2})$$

with initial condition $N(0) = N_0$. [19]

A.2. Gompertz model

The Gompertz model stands as perhaps the most significant and applicable tumour model in practical terms [21]. Its fundamental assumption lies in the exponential decrease of cell growth rate over time. Mathematically, the Gompertz model is represented by the system:

$$\begin{cases} \frac{dN}{dt} = r(t)N(t) \\ \frac{dr}{dt} = -ar(t). \end{cases} \quad (\text{A.3})$$

Here, N denotes the size of the tumour, a represents a constant, and r stands for the growth rate. Through certain substitutions, the model can be simplified to a more widely recognized version of the Gompertz model. Moreover, an analytic solution can be derived using an initial condition $N(0) = N_0$.

Firstly, observe that

$$\frac{d(\ln N)}{dt} = \frac{1}{N} \frac{dN}{dt} = r = -\frac{1}{a} \frac{dr}{dt}. \quad (\text{A.4})$$

Consequently, for some constant b , the following relation can be established:

$$\ln N = \frac{1}{a} (-r(t) + b), \quad (\text{A.5})$$

yielding $r(t) = b - a \ln N$ and leading to the more commonly recognized form of the Gompertz model:

$$\frac{dN}{dt} = N(b - a \ln N). \quad (\text{A.6})$$

Note that this model is not defined for $N = 0$. Hence, for a growing tumour, it must be assumed that the initial tumour has a certain size.

The tumour size is an increasing function that converges to the carrying capacity defined by $K = e^{b/a}$. To derive the analytic solution, the substitution $u = \ln(N/K)$ is used, leading to:

$$N(t) = \exp \left[ce^{-at} + \frac{b}{a} \right], \quad c \in \mathbb{R}. \quad (\text{A.7})$$

Applying the initial condition yields the final solution:

$$N(t) = \exp \left[\frac{b}{a} + \ln(N_0/K)e^{-at} \right] \quad (\text{A.8})$$

A.3. Results of Simple Experiments

Since new patient data was not available at the start of this research, the patient data from Oudhof [10] is used for preliminary experiments. The primary objective was to evaluate whether simpler models for tumour cell decay over time could offer an effective alternative to the more complex DI-MRCD model. These initial experiments analyzed the total number of tumour cells at each time step, without taking into account individual voxel-level data. The model parameters were calibrated using the first two time points, and predictions were made for the last time point. To assess the model's accuracy, the predicted trajectory was compared against the actual number of tumour cells at the final time point, with the goal of achieving close alignment. This approach mirrors that of the DI-MRCD model, though without the voxel-level specificity. The results of this experiment are shown in Figure A.1. It is immediately evident

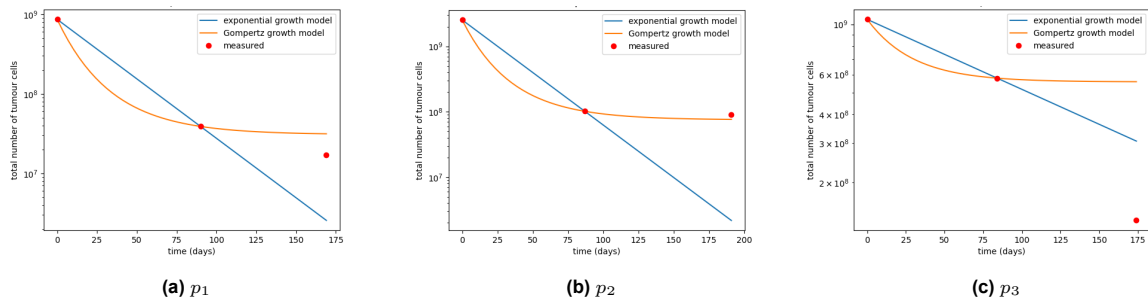


Figure A.1: Evaluation of exponential and Gompertz models for three patients. The models were calibrated on the first two time points to predict tumour cell from the second point to the third time point.

that the exponential model is not suitable for modeling tumor decay, as its steep decline prevents it from even getting close to the third data point. In contrast, after manually adjusting the initial parameters, the Gompertz model demonstrated a better fit for the third point. However, this parameter tuning was patient-specific, raising concerns about the model's reliability. Nonetheless, when the third time point was also used for calibration, the Gompertz model could fit all data points perfectly, suggesting some potential when having more datapoints to fit. Despite this, the Gompertz model only captures tumour growth and does not account for decay due to chemotherapy or metastasis, limiting its broader applicability.

B

Chemotherapy schedules

	Cycle 1					Cycle 2					Cycle 3					
	D1				D8	D1				D8	D1				D8	
	C	Pa	Pe	T	Pa	C	Pa	Pe	T	Pa	C	Pa	Pe	T	C	Pa
p_1	900	150	840	420	150	977	150	420	300	150	830	150	420	300	0	150
p_3	900	150	840	600	150	900	150	420	450	150	900	150	420	450	0	155
p_4	750	150	840	750	150	750	150	420	600	150	720	150	420	600	0	170
p_6	820	150	840	600	150	900	150	420	450	150	900	150	420	450	0	150
p_8	900	150	840	600	150	900	150	420	450	0	750	150	420	450	0	0
p_{10}	600	130	840	450	130	600	130	420	300	130	600	130	420	300	0	130
p_{11}	990	150	840	600	150	900	150	420	450	150	900	150	420	600	0	150
p_{12}	650	130	1200*	600*	130	600	130	600*	600*	130	660	130	600*	600*	0	130
p_{15}	750	150	840	600	150	900	150	420	450	150	820	150	420	450	0	150
p_{16}	750	130	420	300	130	750	130	420	300	130	750	130	420	300	0	130
p_{17}	680	150	840	450	150	670	110	420	300	110	0	150	0	300	0	150
p_{18}	0	170	840	750	170	0	170	420	600	170	0	170	420	600	0	170
p_{19}	720	150	840	600	150	810	150	420	450	150	330	150	420	450	300	110

	Cycle 4						Cycle 5						Cycle 6					
	D1				D8		D1				D8		D1				D8	
	C	Pa	Pe	T	C	Pa	C	Pa	Pe	T	Pa	C	Pa	Pe	T	C	Pa	
<i>p</i> ₁	900	150	420	300	0	140	900	150	420	300	150	810	110	420	300	0	110	
<i>p</i> ₃	900	150	420	450	0	150	900	150	420	450	150	900	150	420	450	0	150	
<i>p</i> ₄	720	150	420	60	0	170	720	150	420	600	170	680	150	420	600	0	170	
<i>p</i> ₆	900	150	420	450	0	150	900	150	420	450	150	900	150	420	450	0	150	
<i>p</i> ₈	900	150	420	450	0	150	900	150	420	450	150	900	150	420	450	0	150	
<i>p</i> ₁₀	600	130	420	300	0	130	600	130	600*	600*	130	600	130	600*	600*	0	130	
<i>p</i> ₁₁	990	150	600*	600*	0	150	990	150	600*	600*	150	900	150	420	600	0	150	
<i>p</i> ₁₂	600	130	600*	600*	0	130	600	130	600*	600*	130	530	130	600*	600*	0	130	
<i>p</i> ₁₅	900	150	420	450	0	150	900	150	420	450	150	900	150	420	450	0	150	
<i>p</i> ₁₆	700	130	420	300	0	130	750	130	420	300	130	0	130	420	300	0	130	
<i>p</i> ₁₇	0	150	0	300	0	150	0	150	0	0	150	0	150	0	300	0	150	
<i>p</i> ₁₈	0	170	420	600	0	170	0	170	420	600	170	0	170	420	600	0	170	
<i>p</i> ₁₉	330	120	420	450	340	110	300	120	420	450	110	340	120	420	450	340	130	

	Cycle 7					Cycle 8					Cycle 9				
	D1				D8	D1				D8	D1				D8
	C	Pa	Pe	T	Pa	C	Pa	Pe	T	Pa	C	Pa	Pe	T	Pa
<i>p</i> ₁	900	110	420	300	110	900	110	420	300	110	900	110	420	300	110
<i>p</i> ₃	900	150	420	450	150	900	150	420	450	150	900	150	420	450	150
<i>p</i> ₄	660	150	420	600	150	600	150	420	600	150	660	150	420	600	0
<i>p</i> ₆	0	150	420	450	150	0	150	420	450	150	0	150	420	450	150
<i>p</i> ₈	900	150	420	450	150	900	150	420	450	150	900	150	420	450	150
<i>p</i> ₁₀	600	130	420	300	130	600	130	600*	600*	130	600	130	600*	600*	130
<i>p</i> ₁₁	900	120	420	600	120	990	120	420	600	120	900	120	420	600	120
<i>p</i> ₁₂	450	130	600*	600*	130	450	130	600*	600*	130	450	130	600*	600*	130
<i>p</i> ₁₅	830	150	420	450	150	820	150	420	450	150	820	150	420	450	150
<i>p</i> ₁₆	0	130	420	300	130	0	130	420	300	130	0	130	420	300	130
<i>p</i> ₁₇	0	0	0	0	0	0	0	0	0	0	0	0	0	0	0
<i>p</i> ₁₈	0	170	420	600	170	0	170	420	600	170	0	170	420	600	170
<i>p</i> ₁₉	0	0	0	450	0	0	0	0	0	0	0	0	0	0	0

Table B.1: Chemotherapy schedules for each patient, detailing the 9-cycle regimen with dosages (in mg) of carboplatin (C), paclitaxel (Pa), pertuzumab (Pe), and trastuzumab (T) administered on Day 1 (D1) and Day 8 (D8) of each cycle. An asterisk (*) indicates subcutaneous administration.

C

Full DI-MCRD Model Results

This chapter presents all the plots not included in Chapter 4.

C.1. Baseline Results

These results correspond to the baseline model described in Section 4.1.8.

C.1.1. Total Number of Tumour Cells Over Time

The following plots represent the total number of tumour cells over time for the patients not shown in Section 4.1.8.

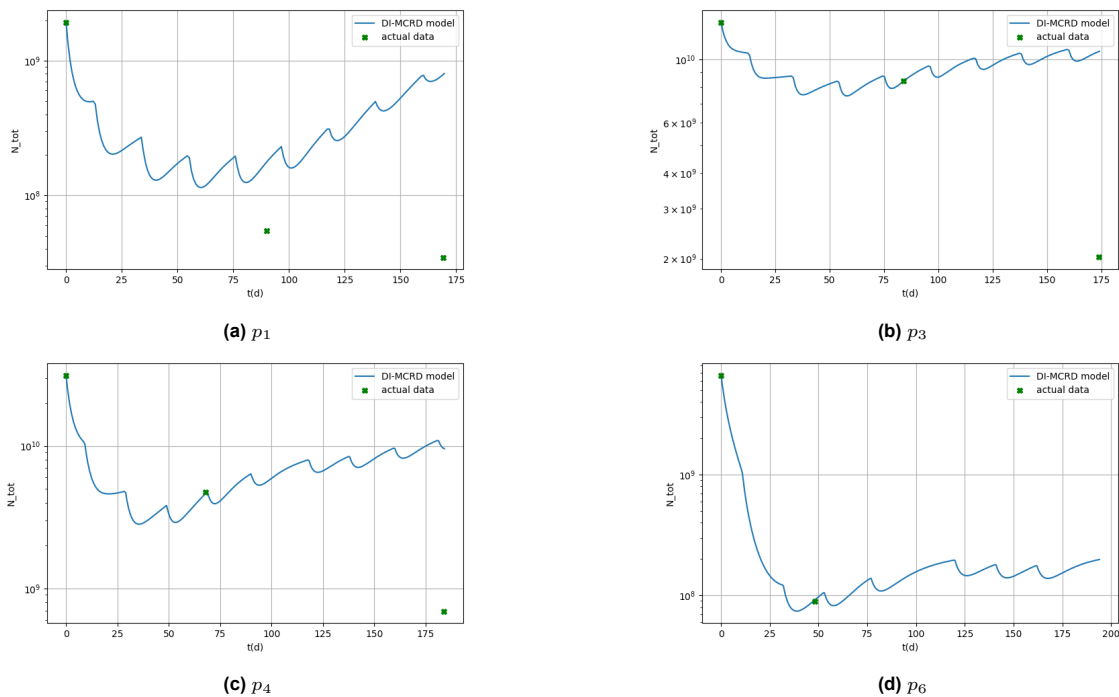


Figure C.1: Total number of tumour cells over time for the first subset of the dataset.

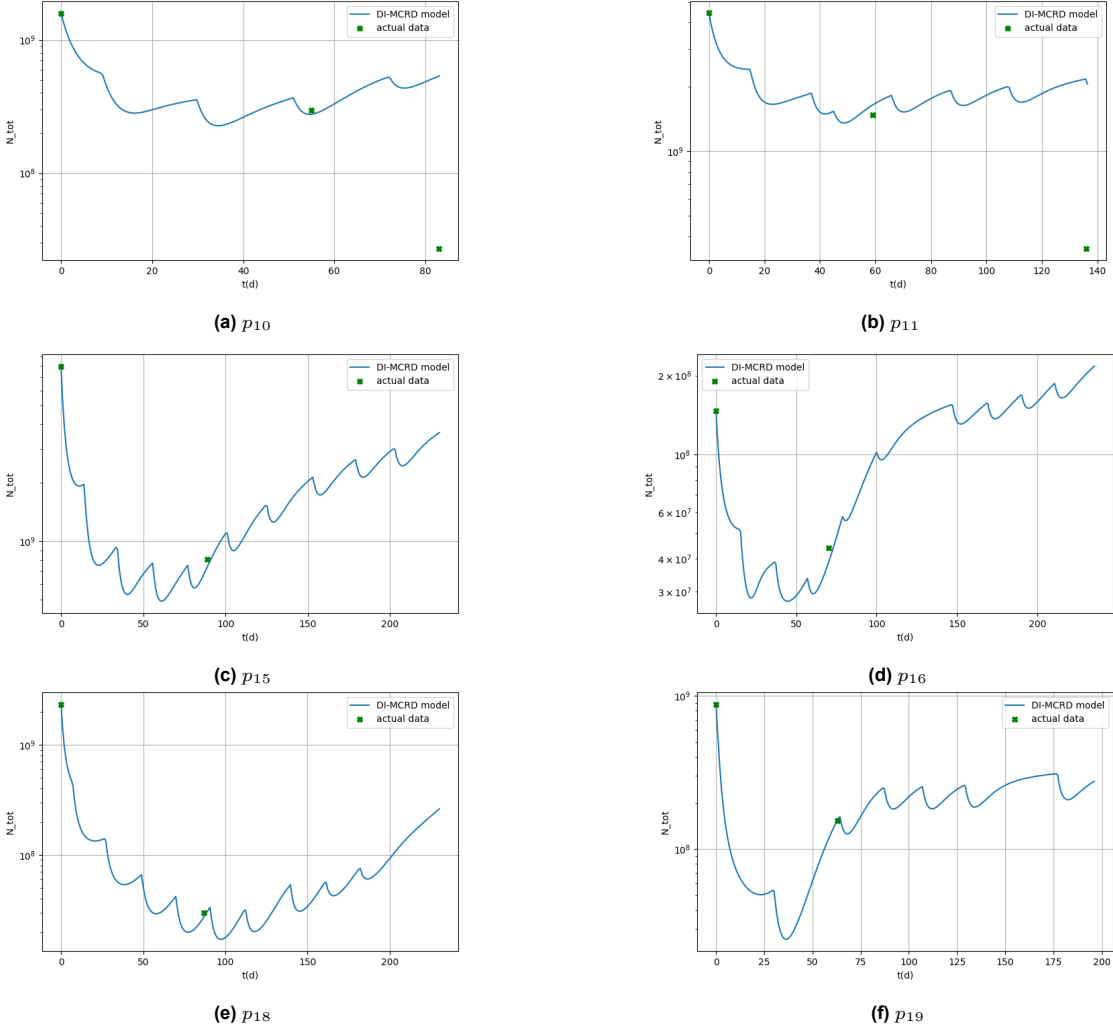


Figure C.2: Total number of tumour cells over time for the second and final subset of the dataset.

C.1.2. Slices Visualization

This section presents the slice results for the patients not shown in Section 4.1.8.

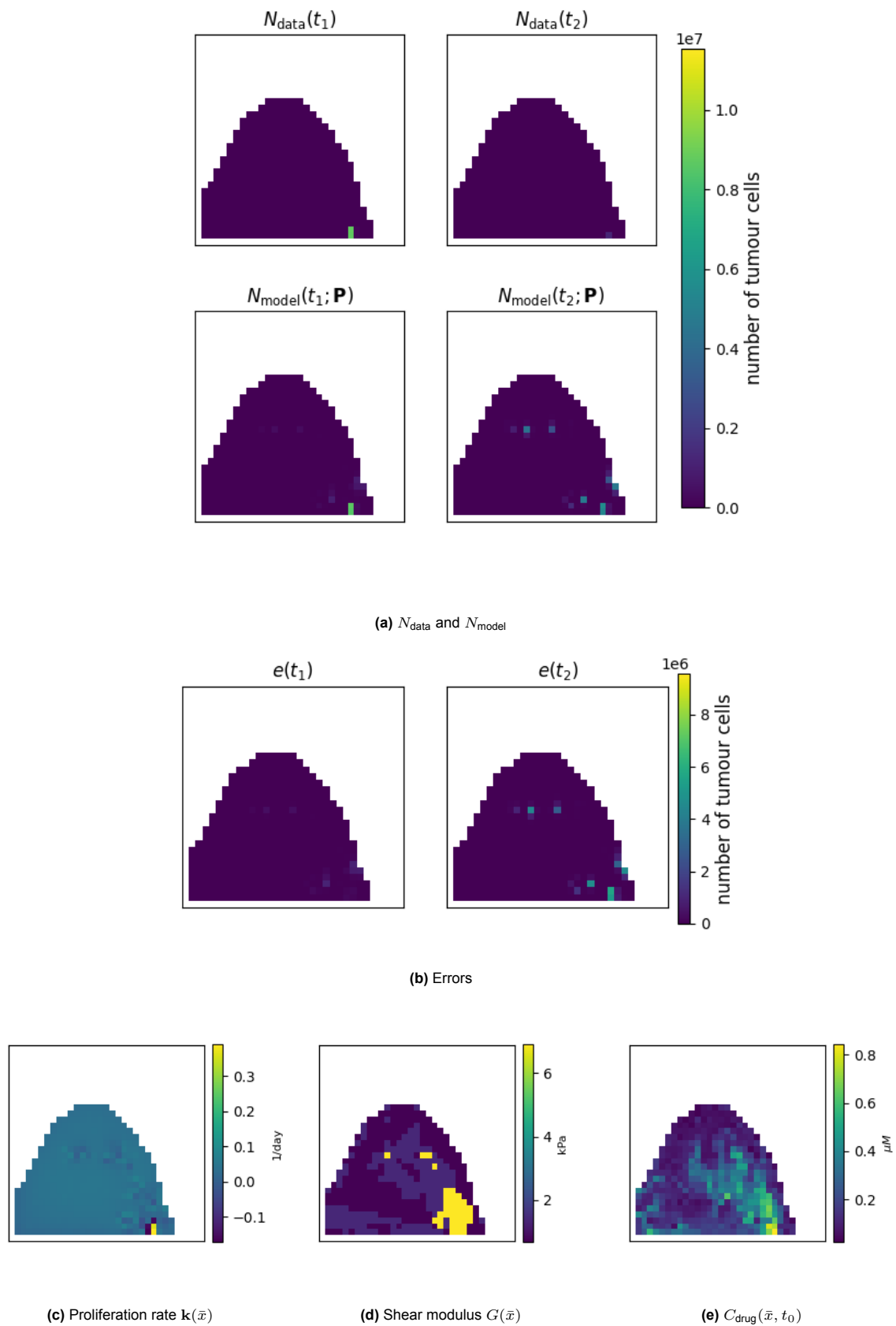
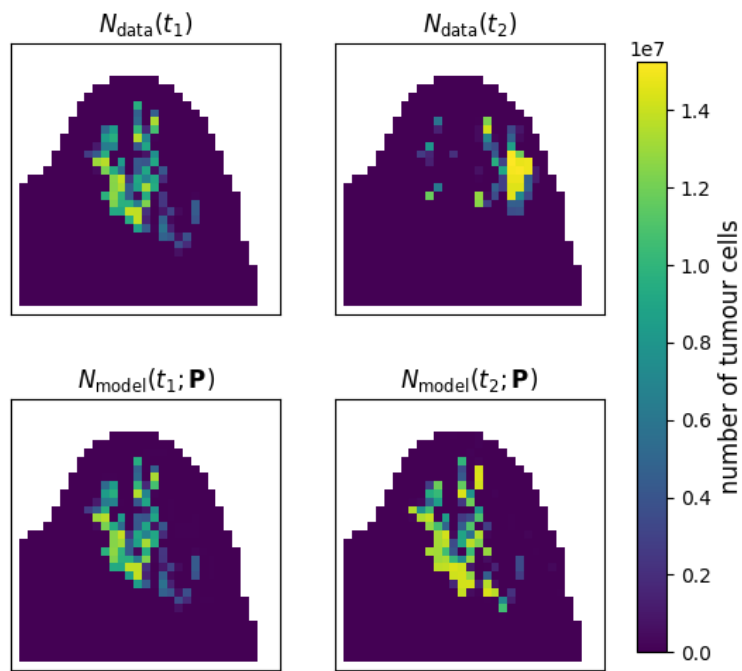
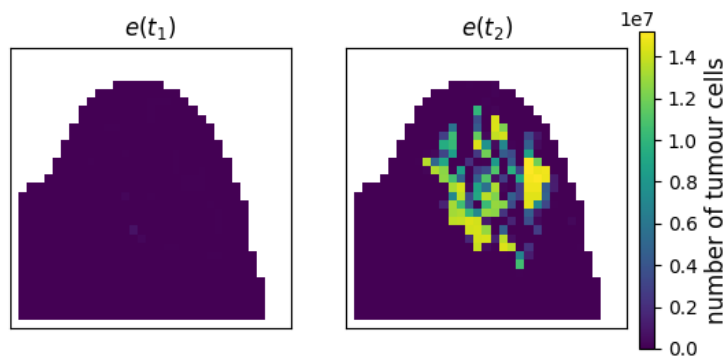


Figure C.3: Baseline results for p_1 visualized using slices. (a) shows the N_{data} representation at t_1 and t_2 , along with $N_{\text{model}}(t_1)$, the calibrated number of tumour cells at t_1 , and $N_{\text{model}}(t_2)$, the prediction made by the DI-MCRD model at t_2 . (b) presents the errors between N_{data} and N_{model} at t_1 and t_2 . (c) visualizes the proliferation rate $k(\bar{x})$, (d) displays the shear modulus $G(\bar{x})$, and (e) displays the drug distribution $C_{\text{drug}}(\bar{x}, t_0)$.

(a) N_{data} and N_{model} 

(b) Errors

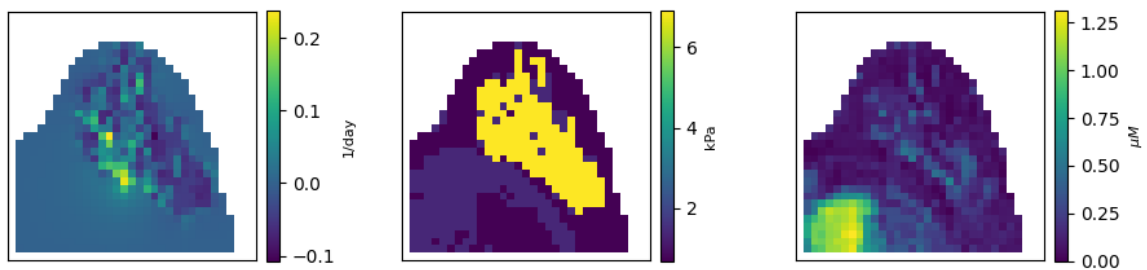
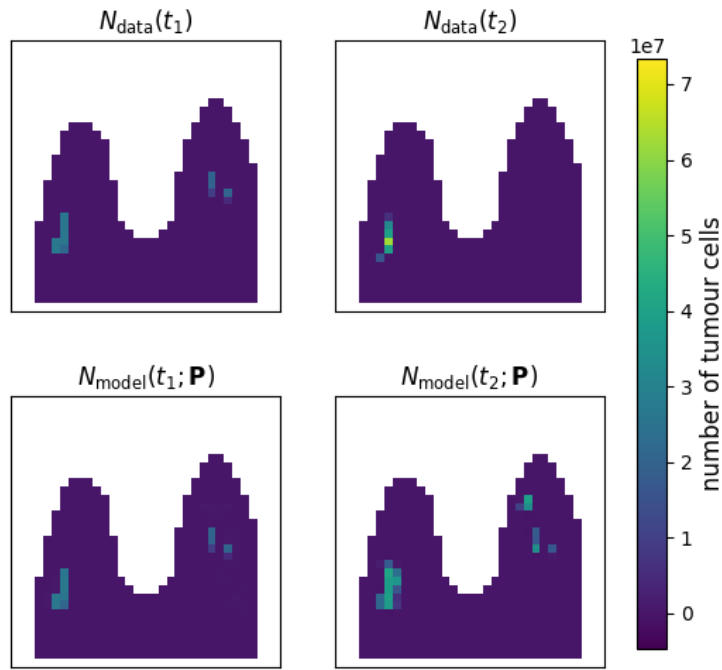
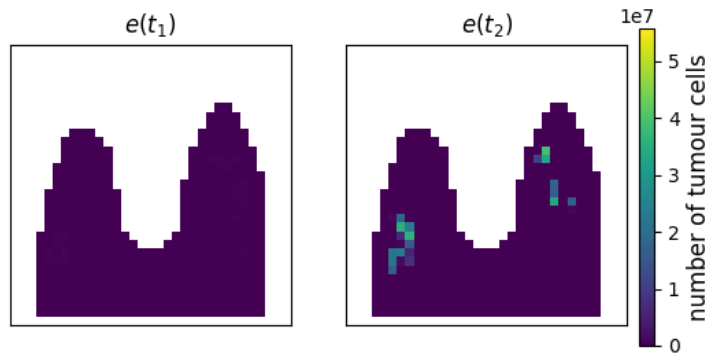
(c) Proliferation rate $k(\bar{x})$ (d) Shear modulus $G(\bar{x})$ (e) $C_{drug}(\bar{x}, t_0)$

Figure C.4: Baseline results for p_3 visualized using slices. (a) shows the N_{data} representation at t_1 and t_2 , along with $N_{model}(t_1)$, the calibrated number of tumour cells at t_1 , and $N_{model}(t_2)$, the prediction made by the DI-MCRD model at t_2 . (b) presents the errors between N_{data} and N_{model} at t_1 and t_2 . (c) visualizes the proliferation rate $k(\bar{x})$, (d) displays the shear modulus $G(\bar{x})$, and (e) displays the drug distribution $C_{drug}(\bar{x}, t_0)$.

(a) N_{data} and N_{model} 

(b) Errors

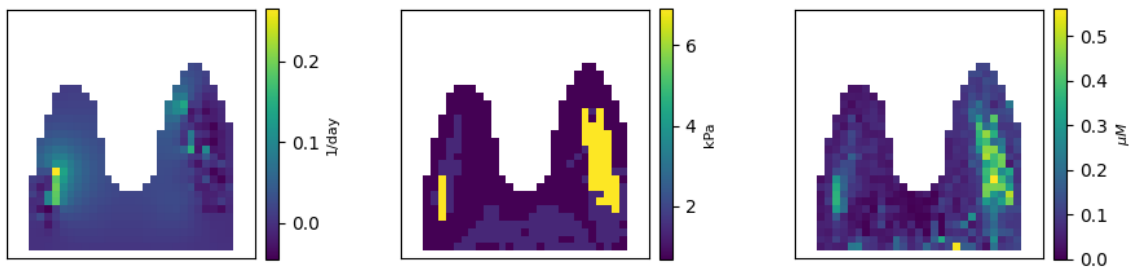
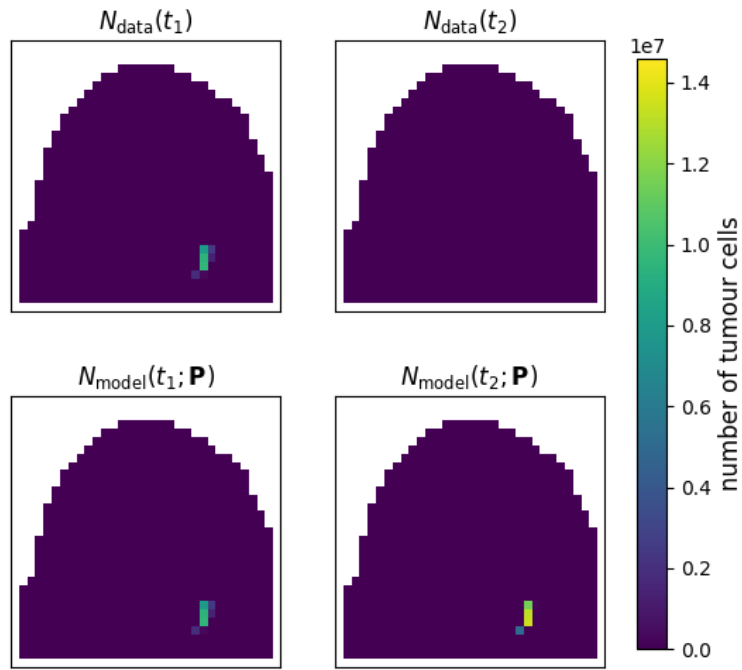
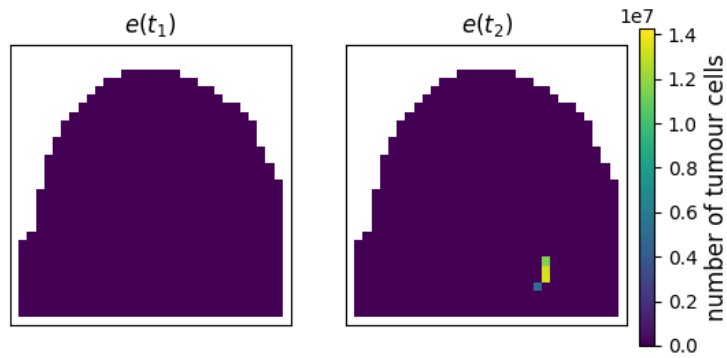
(c) Proliferation rate $k(\bar{x})$ (d) Shear modulus $G(\bar{x})$ (e) $C_{drug}(\bar{x}, t_0)$

Figure C.5: Baseline results for p_4 visualized using slices. (a) shows the N_{data} representation at t_1 and t_2 , along with $N_{model}(t_1)$, the calibrated number of tumour cells at t_1 , and $N_{model}(t_2)$, the prediction made by the DI-MCRD model at t_2 . (b) presents the errors between N_{data} and N_{model} at t_1 and t_2 . (c) visualizes the proliferation rate $k(\bar{x})$, (d) displays the shear modulus $G(\bar{x})$, and (e) displays the drug distribution $C_{drug}(\bar{x}, t_0)$.

(a) N_{data} and N_{model} 

(b) Errors

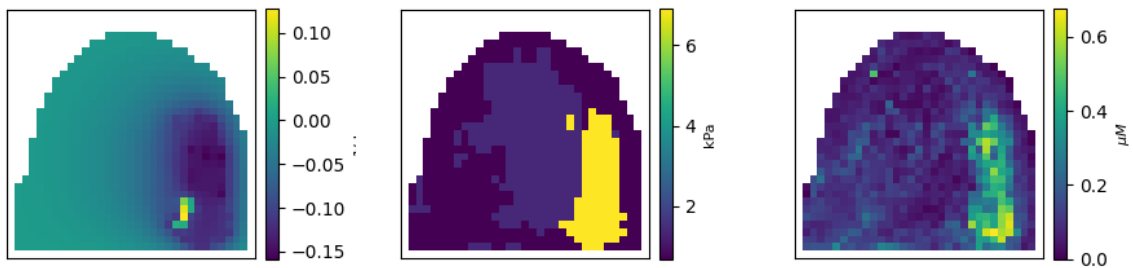
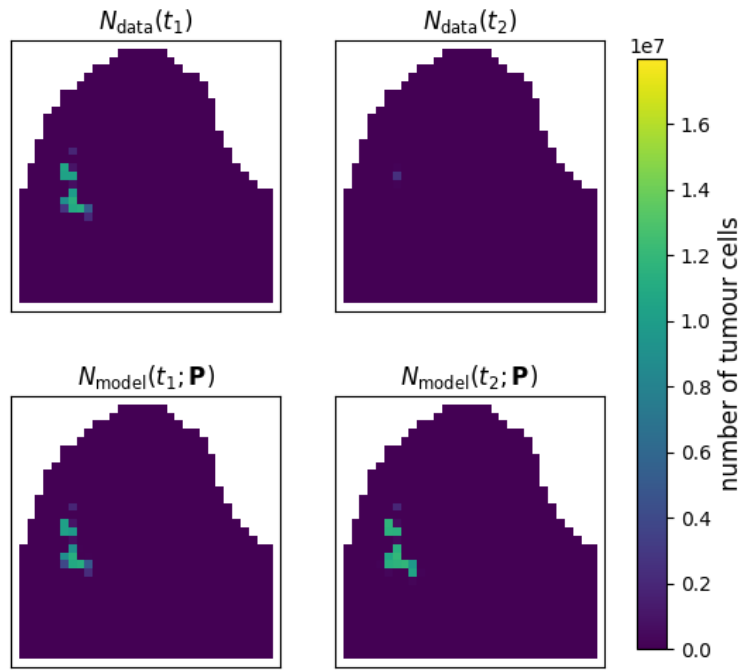
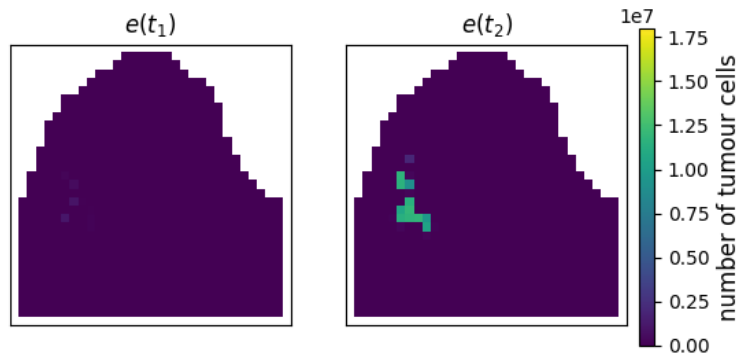
(c) Proliferation rate $k(\bar{x})$ (d) Shear modulus $G(\bar{x})$ (e) $C_{drug}(\bar{x}, t_0)$

Figure C.6: Baseline results for p_6 visualized using slices. (a) shows the N_{data} representation at t_1 and t_2 , along with $N_{model}(t_1)$, the calibrated number of tumour cells at t_1 , and $N_{model}(t_2)$, the prediction made by the DI-MCRD model at t_2 . (b) presents the errors between N_{data} and N_{model} at t_1 and t_2 . (c) visualizes the proliferation rate $k(\bar{x})$, (d) displays the shear modulus $G(\bar{x})$, and (e) displays the drug distribution $C_{drug}(\bar{x}, t_0)$.

(a) N_{data} and N_{model} 

(b) Errors

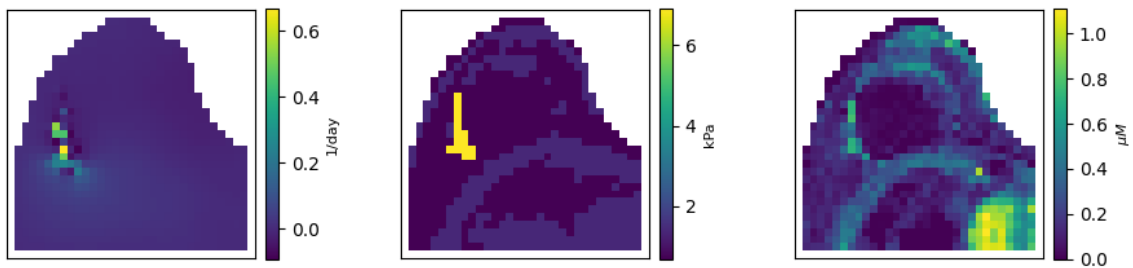
(c) Proliferation rate $k(\bar{x})$ (d) Shear modulus $G(\bar{x})$ (e) $C_{\text{drug}}(\bar{x}, t_0)$

Figure C.7: Baseline results for p_{10} visualized using slices. (a) shows the N_{data} representation at t_1 and t_2 , along with $N_{\text{model}}(t_1)$, the calibrated number of tumour cells at t_1 , and $N_{\text{model}}(t_2)$, the prediction made by the DI-MCRD model at t_2 . (b) presents the errors between N_{data} and N_{model} at t_1 and t_2 . (c) visualizes the proliferation rate $k(\bar{x})$, (d) displays the shear modulus $G(\bar{x})$, and (e) displays the drug distribution $C_{\text{drug}}(\bar{x}, t_0)$.

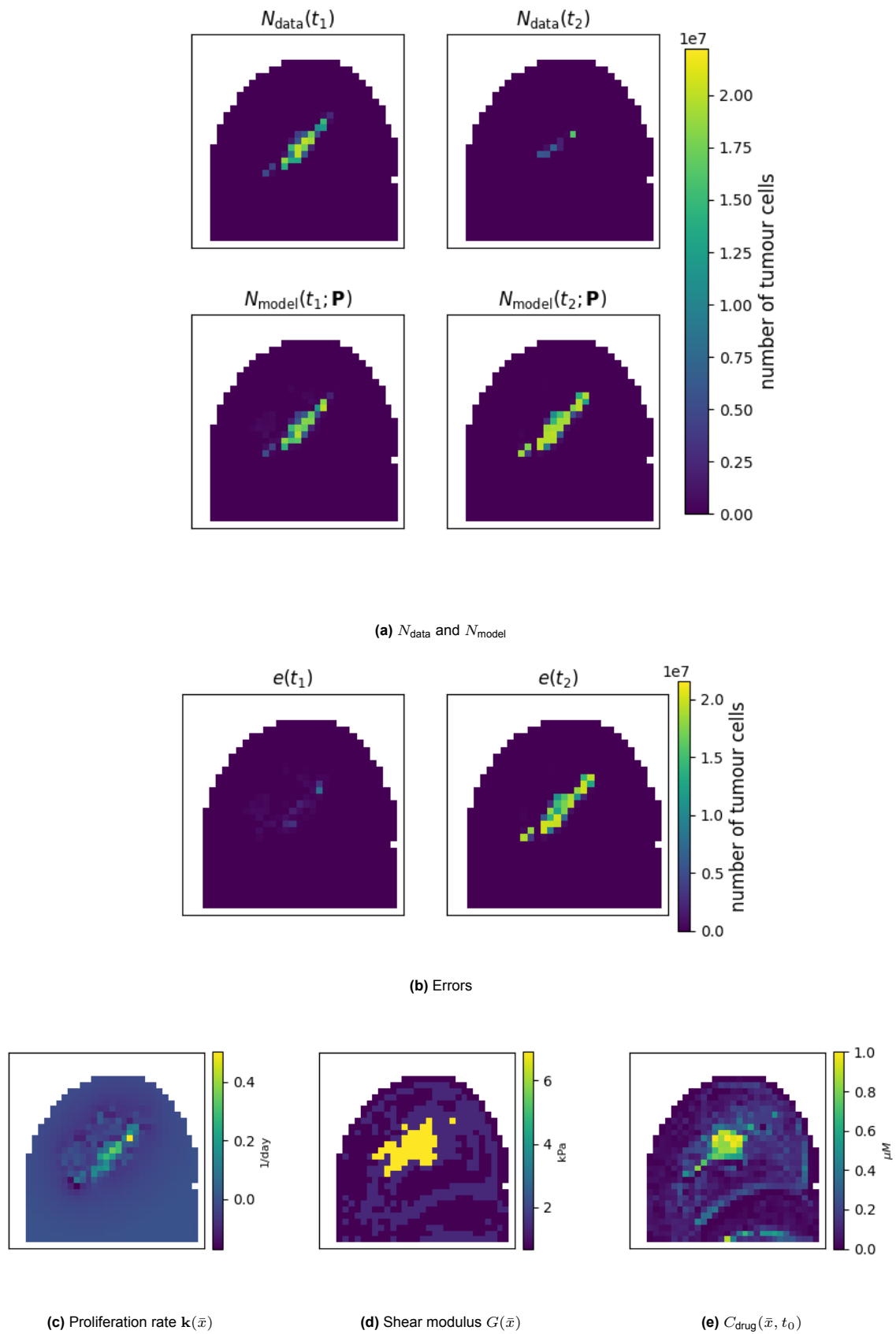
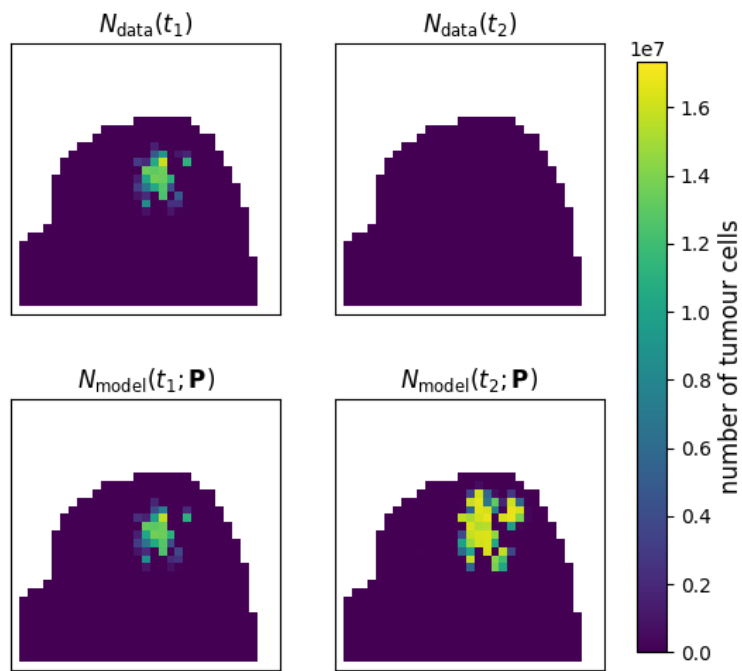
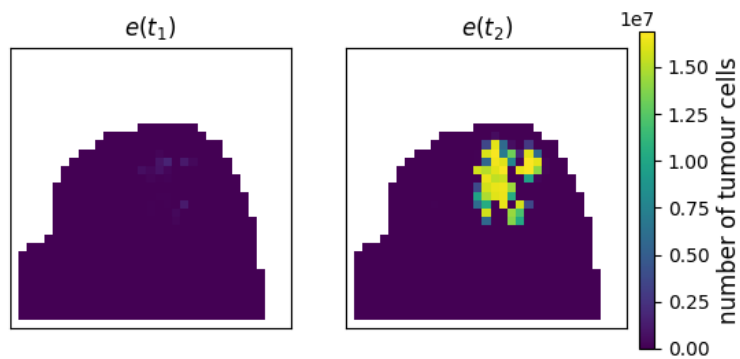


Figure C.8: Baseline results for p_{11} visualized using slices. (a) shows the N_{data} representation at t_1 and t_2 , along with $N_{\text{model}}(t_1)$, the calibrated number of tumour cells at t_1 , and $N_{\text{model}}(t_2)$, the prediction made by the DI-MCRD model at t_2 . (b) presents the errors between N_{data} and N_{model} at t_1 and t_2 . (c) visualizes the proliferation rate $k(\bar{x})$, (d) displays the shear modulus $G(\bar{x})$, and (e) displays the drug distribution $C_{\text{drug}}(\bar{x}, t_0)$.

(a) N_{data} and N_{model} 

(b) Errors

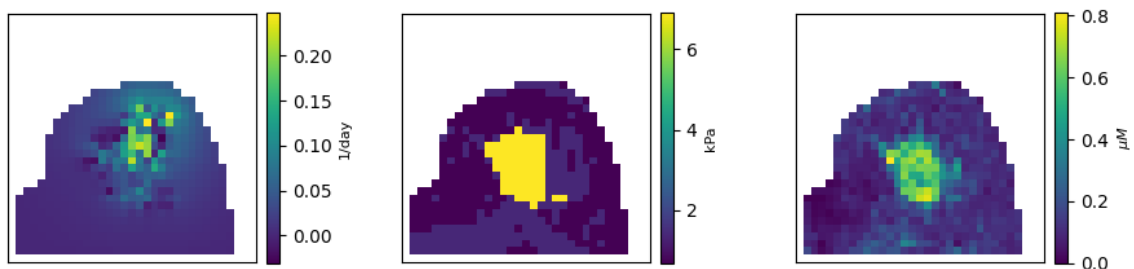
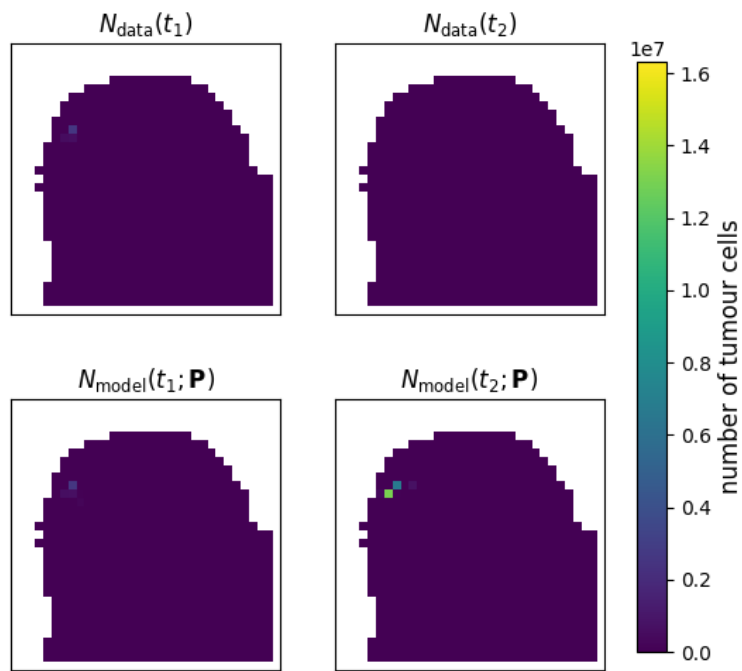
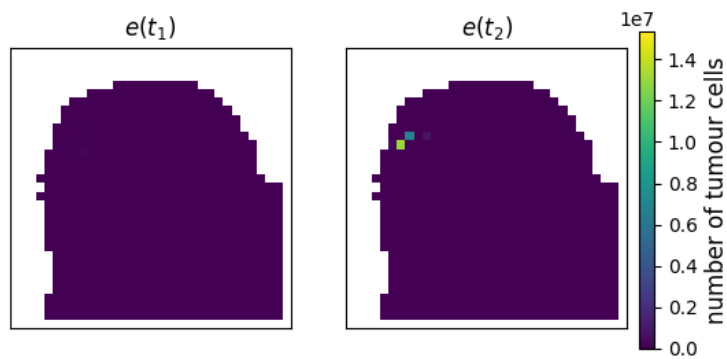
(c) Proliferation rate $k(\bar{x})$ (d) Shear modulus $G(\bar{x})$ (e) $C_{\text{drug}}(\bar{x}, t_0)$

Figure C.9: Baseline results for p_{15} visualized using slices. (a) shows the N_{data} representation at t_1 and t_2 , along with $N_{\text{model}}(t_1)$, the calibrated number of tumour cells at t_1 , and $N_{\text{model}}(t_2)$, the prediction made by the DI-MCRD model at t_2 . (b) presents the errors between N_{data} and N_{model} at t_1 and t_2 . (c) visualizes the proliferation rate $k(\bar{x})$, (d) displays the shear modulus $G(\bar{x})$, and (e) displays the drug distribution $C_{\text{drug}}(\bar{x}, t_0)$.

(a) N_{data} and N_{model} 

(b) Errors

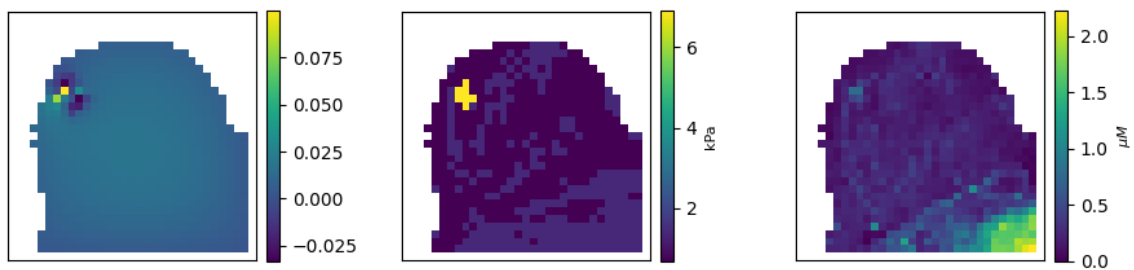
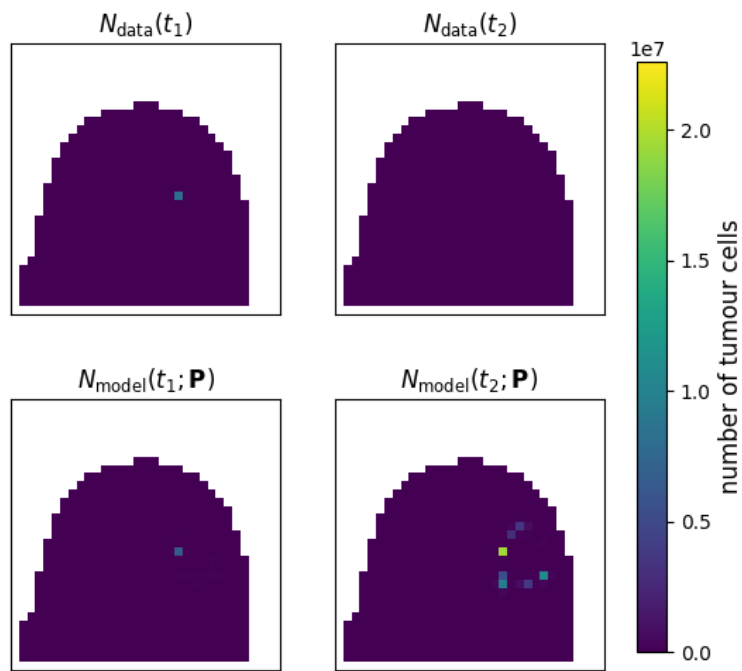
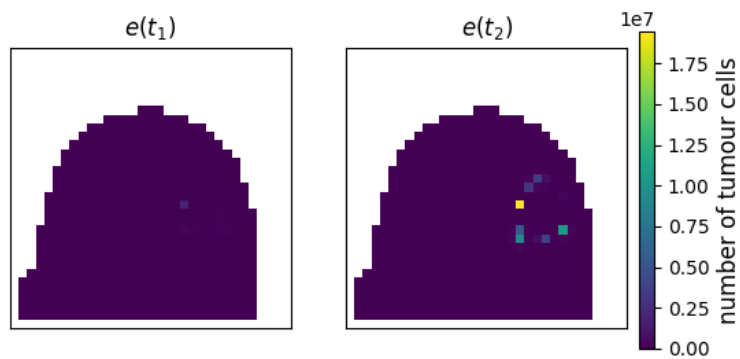
(c) Proliferation rate $k(\bar{x})$ (d) Shear modulus $G(\bar{x})$ (e) $C_{drug}(\bar{x}, t_0)$

Figure C.10: Baseline results for p_{16} visualized using slices. (a) shows the N_{data} representation at t_1 and t_2 , along with $N_{model}(t_1)$, the calibrated number of tumour cells at t_1 , and $N_{model}(t_2)$, the prediction made by the DI-MCRD model at t_2 . (b) presents the errors between N_{data} and N_{model} at t_1 and t_2 . (c) visualizes the proliferation rate $k(\bar{x})$, (d) displays the shear modulus $G(\bar{x})$, and (e) displays the drug distribution $C_{drug}(\bar{x}, t_0)$.

(a) N_{data} and N_{model} 

(b) Errors

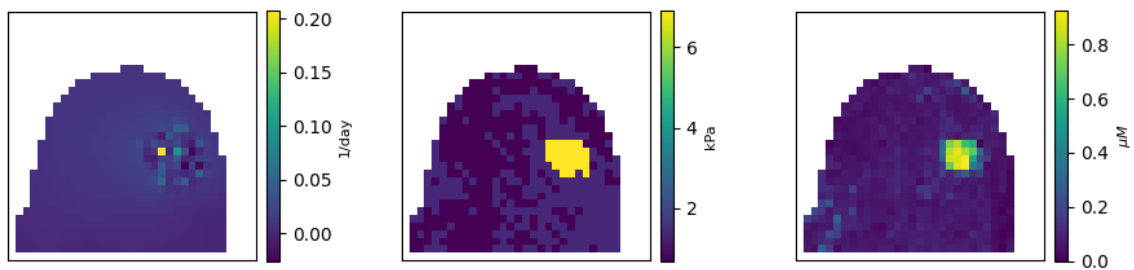
(c) Proliferation rate $k(\bar{x})$ (d) Shear modulus $G(\bar{x})$ (e) $C_{drug}(\bar{x}, t_0)$

Figure C.11: Baseline results for p_{18} visualized using slices. (a) shows the N_{data} representation at t_1 and t_2 , along with $N_{model}(t_1)$, the calibrated number of tumour cells at t_1 , and $N_{model}(t_2)$, the prediction made by the DI-MCRD model at t_2 . (b) presents the errors between N_{data} and N_{model} at t_1 and t_2 . (c) visualizes the proliferation rate $k(\bar{x})$, (d) displays the shear modulus $G(\bar{x})$, and (e) displays the drug distribution $C_{drug}(\bar{x}, t_0)$.

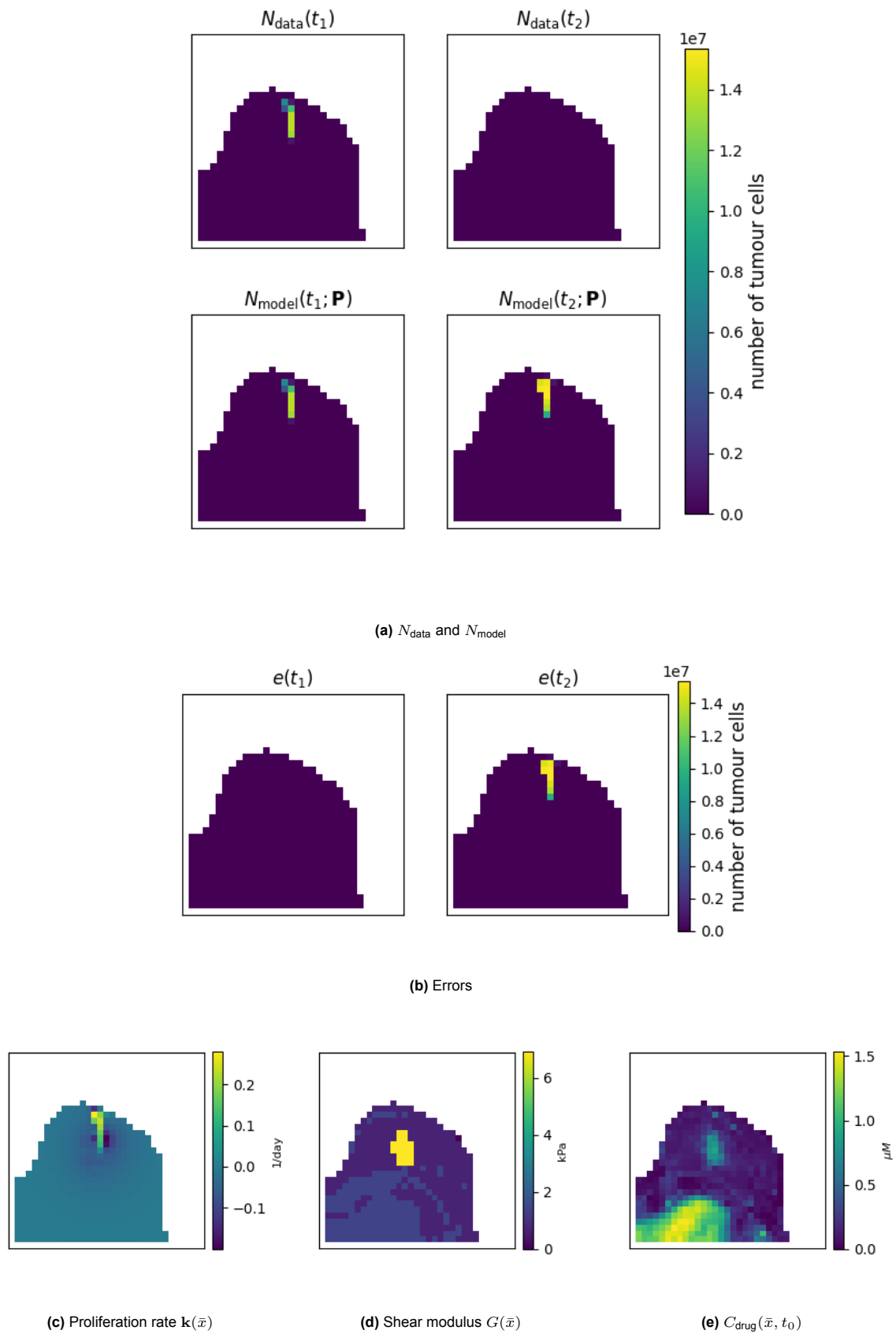
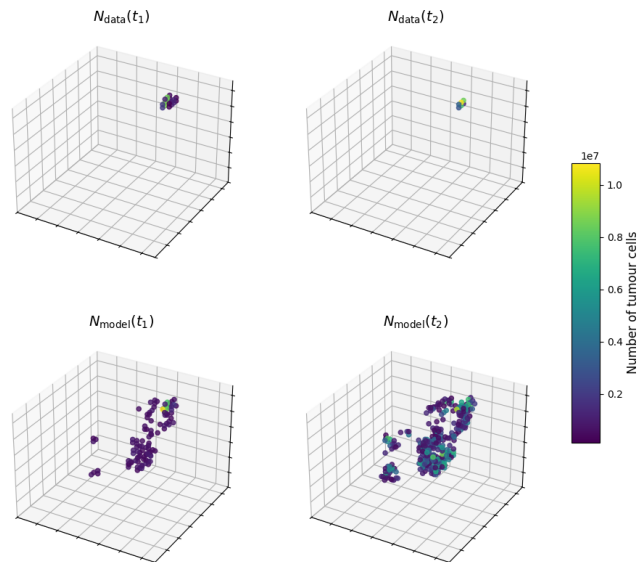


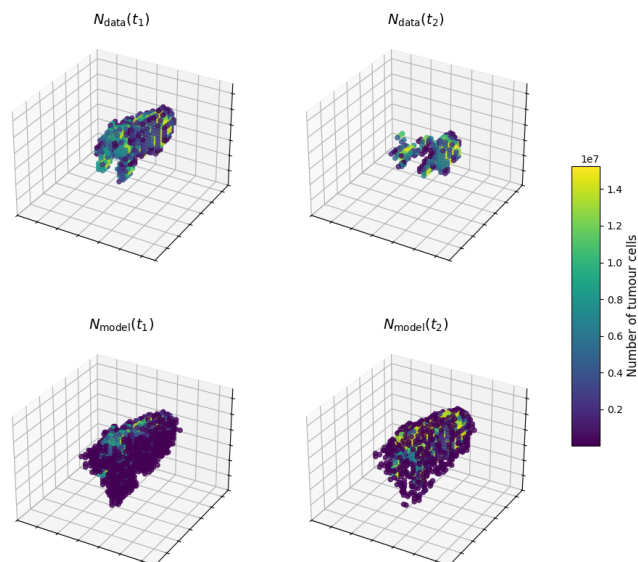
Figure C.12: Baseline results for p_{19} visualized using slices. (a) shows the N_{data} representation at t_1 and t_2 , along with $N_{\text{model}}(t_1)$, the calibrated number of tumour cells at t_1 , and $N_{\text{model}}(t_2)$, the prediction made by the DI-MCRD model at t_2 . (b) presents the errors between N_{data} and N_{model} at t_1 and t_2 . (c) visualizes the proliferation rate $k(\bar{x})$, (d) displays the shear modulus $G(\bar{x})$, and (e) displays the drug distribution $C_{\text{drug}}(\bar{x}, t_0)$.

C.1.3. 3D Visualization

This section presents the 3D visualization of the results for the patients not shown in Section 4.1.8. In all the subfigures, the top row shows the N_{data} representation at t_1 and t_2 , while the bottom row displays $N_{\text{model}}(t_1)$, the calibrated number of tumour cells at t_1 (left), and $N_{\text{model}}(t_2)$, the prediction made by the DI-MCRD model at t_2 (right). In the bottom row, all voxels with a tumour cell count below N_{min} are removed.

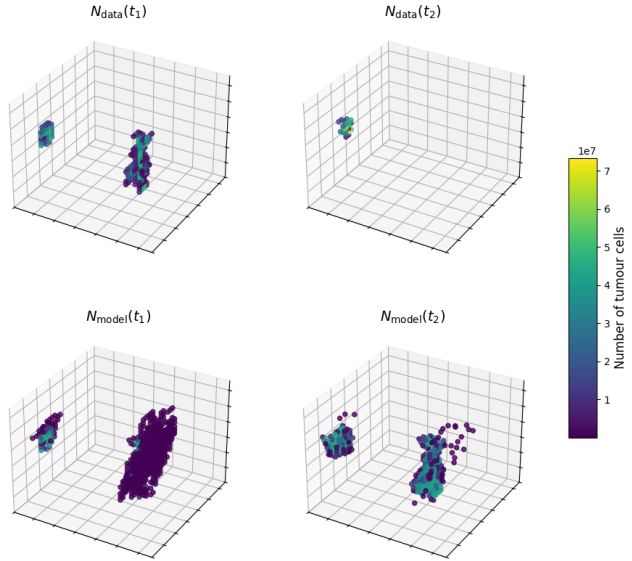


(a) p_1

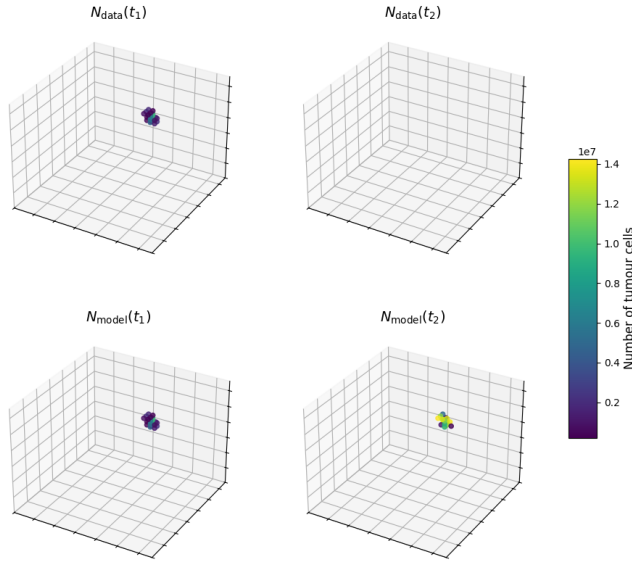


(b) p_3

Figure C.13: Visualization of the results from the baseline model using a 3D representation for a subset of the dataset (part 1).

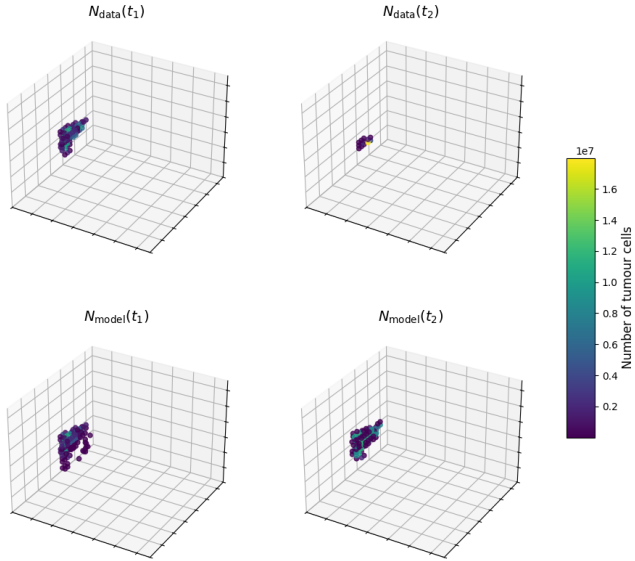


(a) p_4

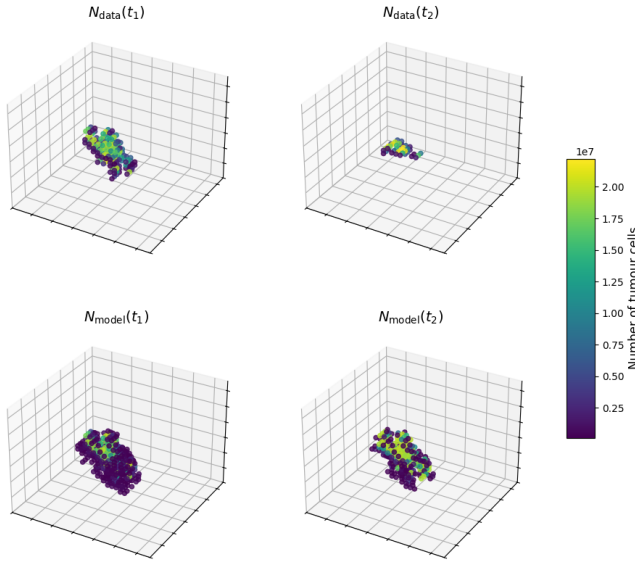


(b) p_6

Figure C.14: Visualization of the results from the baseline model using a 3D representation for a subset of the dataset (part 2).

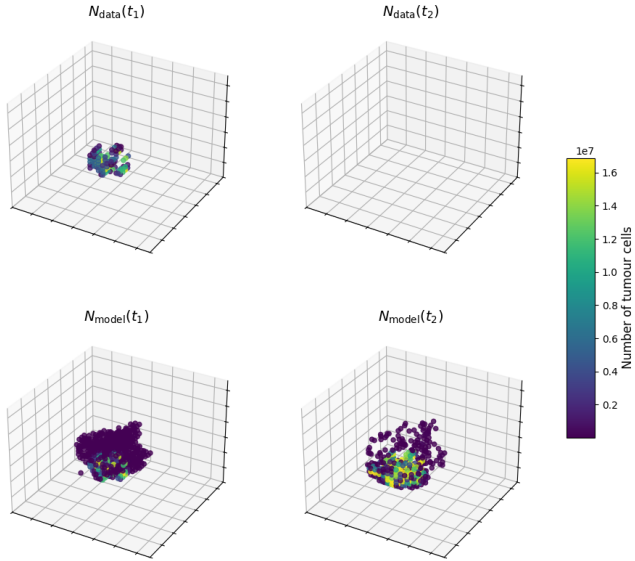


(a) p_{10}

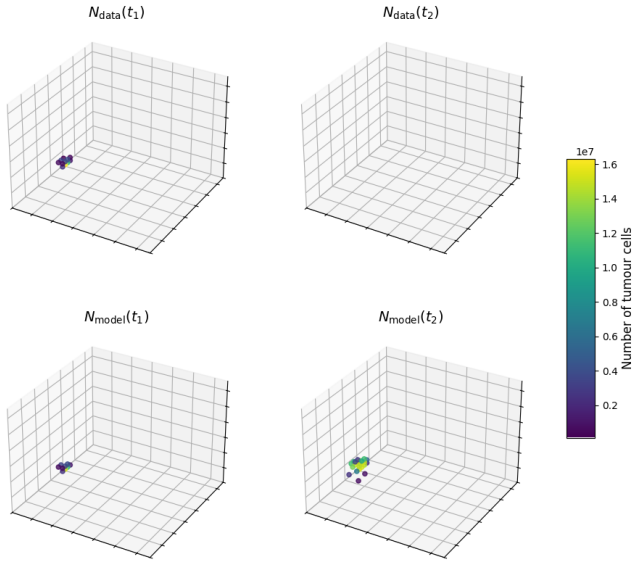


(b) p_{11}

Figure C.15: Visualization of the results from the baseline model using a 3D representation for a subset of the dataset (part 3).



(a) p_{15}



(b) p_{16}

Figure C.16: Visualization of the results from the baseline model using a 3D representation for a subset of the dataset (part 4).

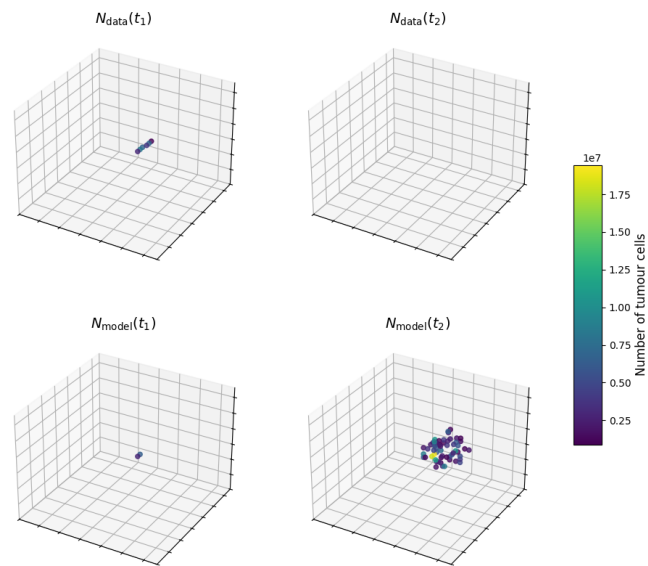
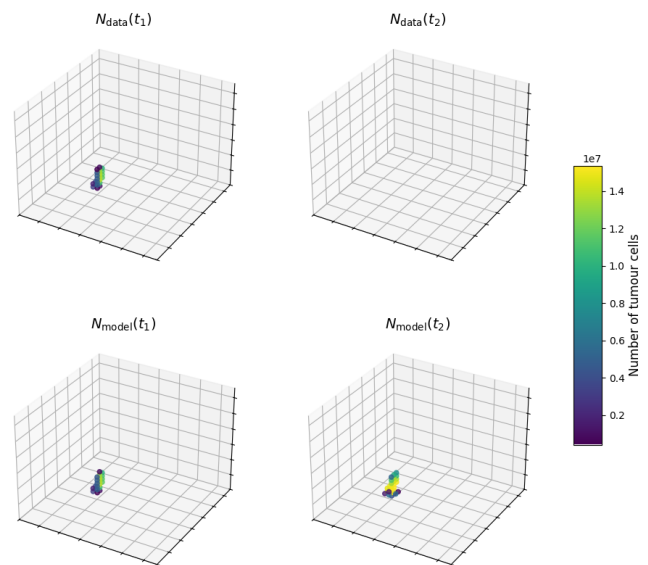
(a) p_{18} (b) p_{19}

Figure C.17: Visualization of the results from the baseline model using a 3D representation for a subset of the dataset (part 5).

C.2. Cycle I Results

C.2.1. Cycle Ia

In this section the visualizations of the results using the DI-MRCD model from cycle Ia that are not shown in Section 4.2.1 are shown.

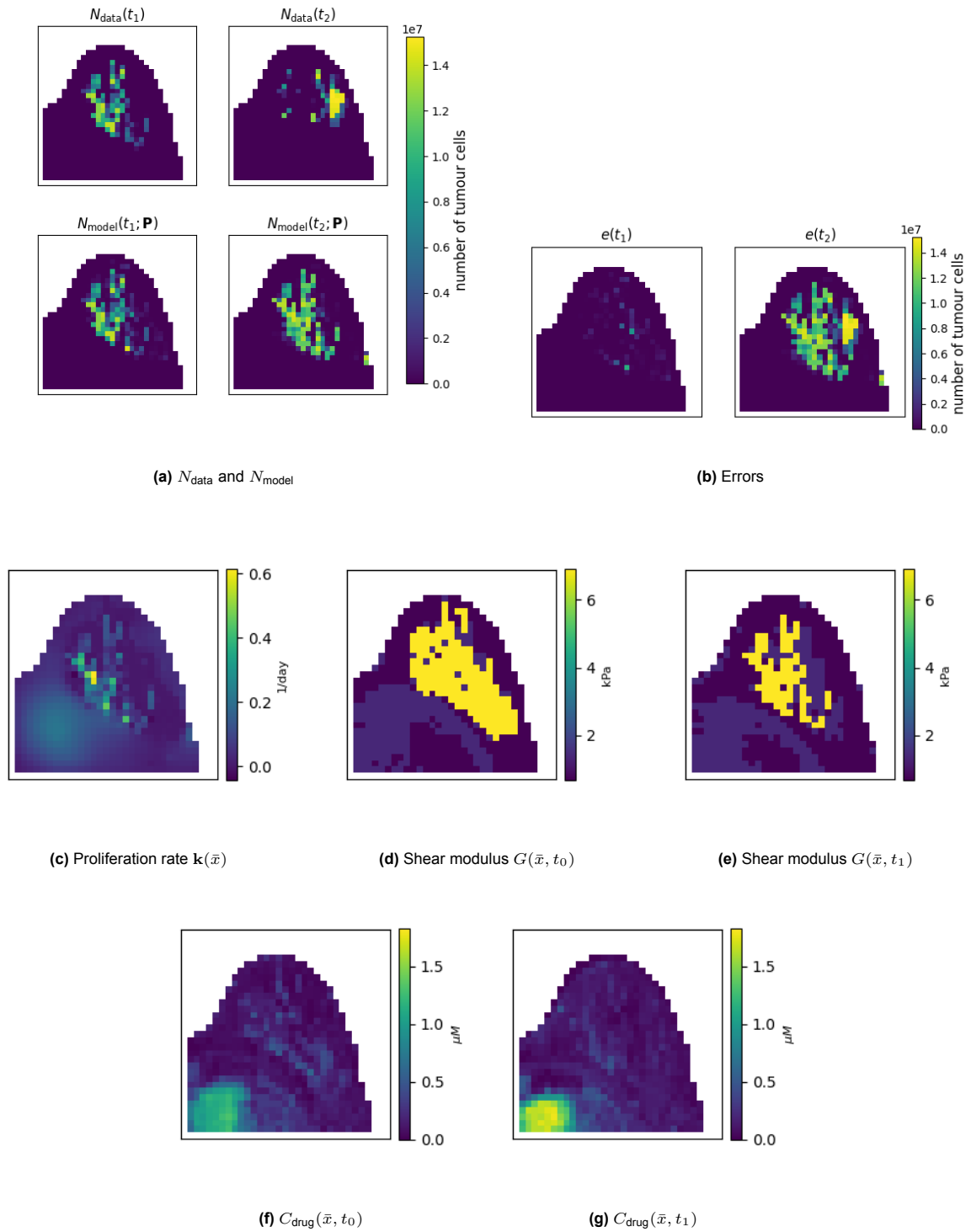


Figure C.1: Results from cycle Ia for p_3 visualized using slices. (a) shows the N_{data} representation at t_1 and t_2 , along with $N_{model}(t_1)$, the calibrated number of tumour cells at t_1 , and $N_{model}(t_2)$, the prediction made by the DI-MCRD model from cycle Ia at t_2 . (b) presents the errors between N_{data} and N_{model} at t_1 and t_2 . (c) visualizes the proliferation rate $k(\bar{x})$, (d) displays the shear modulus $G(\bar{x}, t_0)$, (e) displays the shear modulus $G(\bar{x}, t_1)$, (f) drug distribution $C_{drug}(\bar{x}, t_0)$, and drug distribution $C_{drug}(\bar{x}, t_1)$.

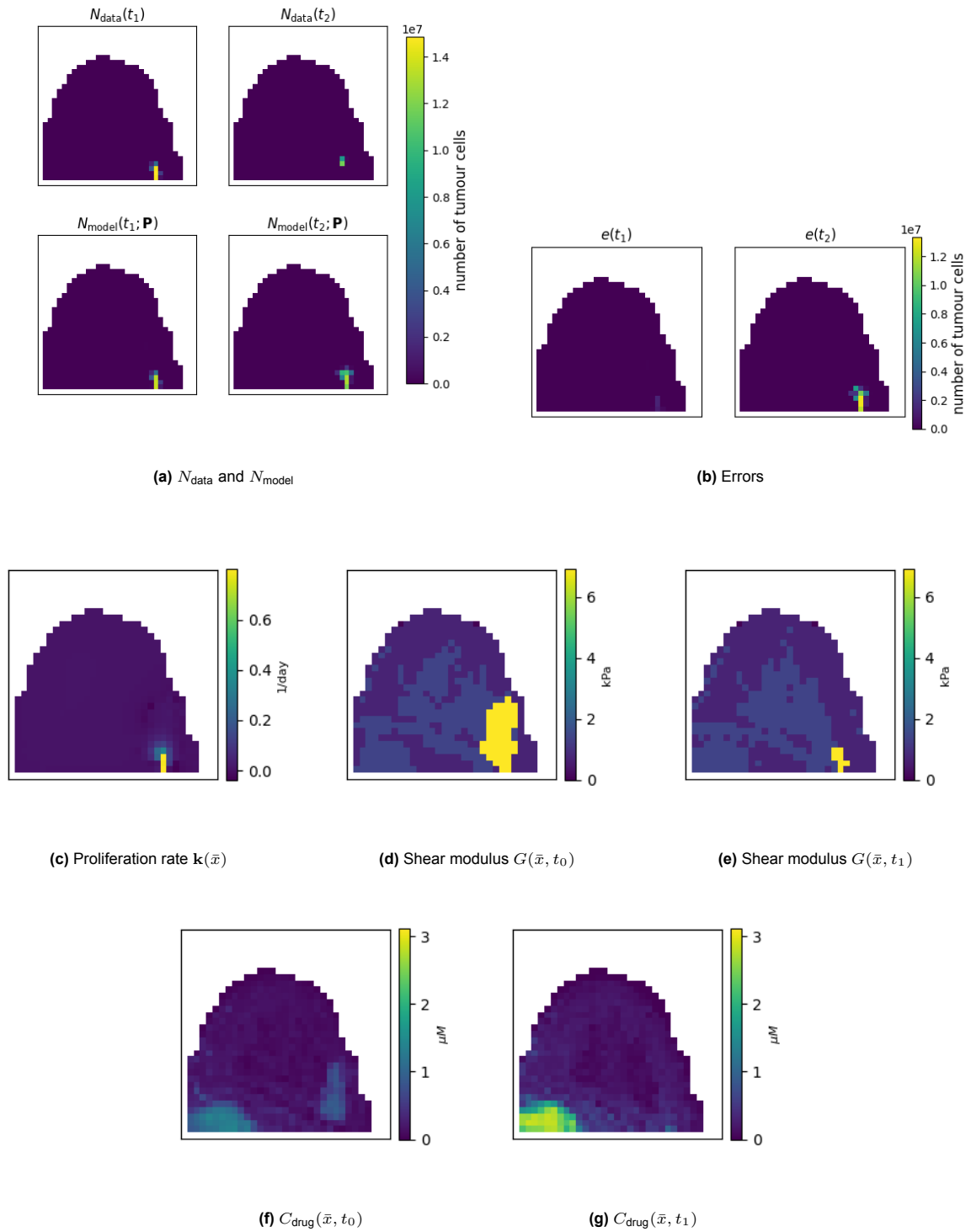


Figure C.2: Results from cycle Ia for ps visualized using slices. (a) shows the N_{data} representation at t_1 and t_2 , along with $N_{model}(t_1)$, the calibrated number of tumour cells at t_1 , and $N_{model}(t_2)$, the prediction made by the DI-MCRD model from cycle Ia at t_2 . (b) presents the errors between N_{data} and N_{model} at t_1 and t_2 . (c) visualizes the proliferation rate $k(\bar{x})$, (d) displays the shear modulus $G(\bar{x}, t_0)$, (e) displays the shear modulus $G(\bar{x}, t_1)$, (f) drug distribution $C_{drug}(\bar{x}, t_0)$, and drug distribution $C_{drug}(\bar{x}, t_1)$.

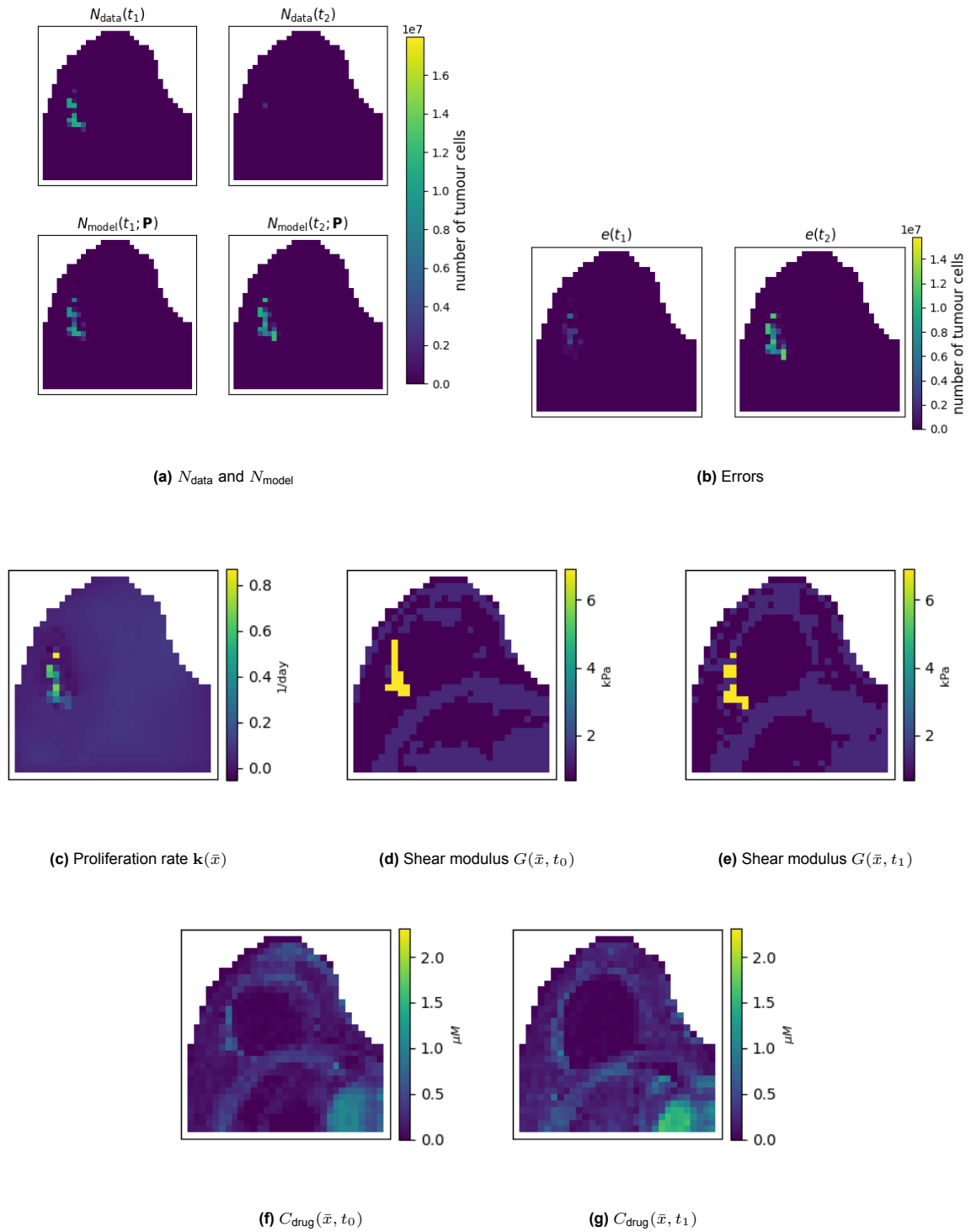


Figure C.3: Results from cycle Ia for p_{10} visualized using slices. (a) shows the N_{data} representation at t_1 and t_2 , along with $N_{\text{model}}(t_1)$, the calibrated number of tumour cells at t_1 , and $N_{\text{model}}(t_2)$, the prediction made by the DI-MCRD model from cycle Ia at t_2 . (b) presents the errors between N_{data} and N_{model} at t_1 and t_2 . (c) visualizes the proliferation rate $k(\bar{x})$, (d) displays the shear modulus $G(\bar{x}, t_0)$, (e) displays the shear modulus $G(\bar{x}, t_1)$, (f) drug distribution $C_{\text{drug}}(\bar{x}, t_0)$, and drug distribution $C_{\text{drug}}(\bar{x}, t_1)$.

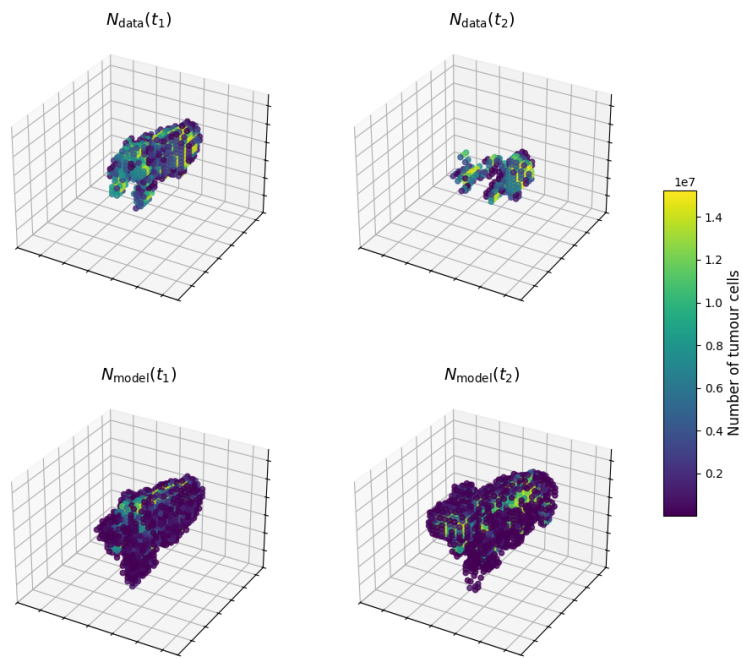
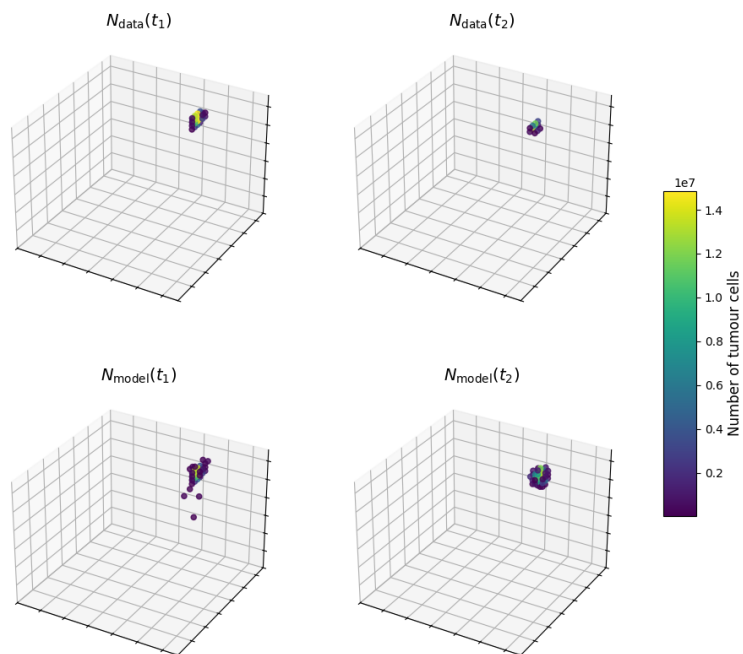
(a) p_3 (b) p_8

Figure C.4: 3D representation of the number of tumour cells for patients p_3 and p_8 obtained using the model from cycle Ia. Within each subfigure, the top row shows the N_{data} representation at t_1 and t_2 , while the bottom row displays $N_{\text{model}}(t_1)$, the calibrated number of tumour cells at t_1 , and $N_{\text{model}}(t_2)$, the prediction made by the DI-MCRD model at t_2 . In the bottom row, all voxels with a tumour cell count less than N_{min} are removed.

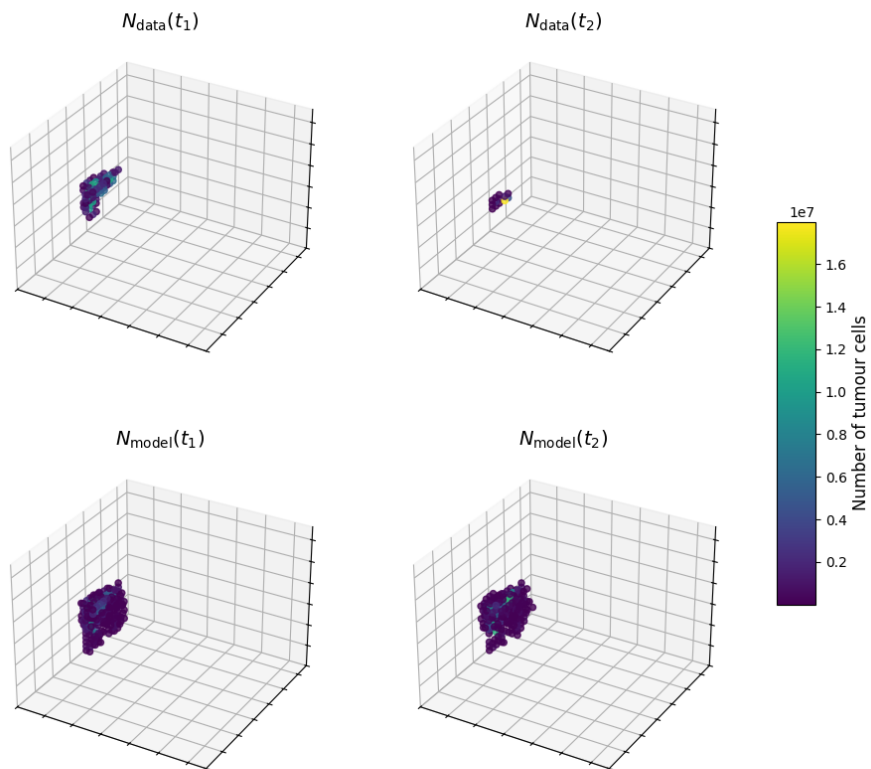


Figure C.5: 3D representation of the number of tumour cells for patient p_{10} obtained using the model from cycle Ia. The top row shows the N_{data} representation at t_1 and t_2 , while the bottom row displays $N_{\text{model}}(t_1)$, the calibrated number of tumour cells at t_1 , and $N_{\text{model}}(t_2)$, the prediction made by the DI-MCRD model at t_2 . In the bottom row, all voxels with a tumour cell count less than N_{min} are removed.

C.2.2. Cycle Ib

In this section the visualizations of the results using the DI-MRCD model from cycle Ia that are not shown in Section 4.2.2 are shown.

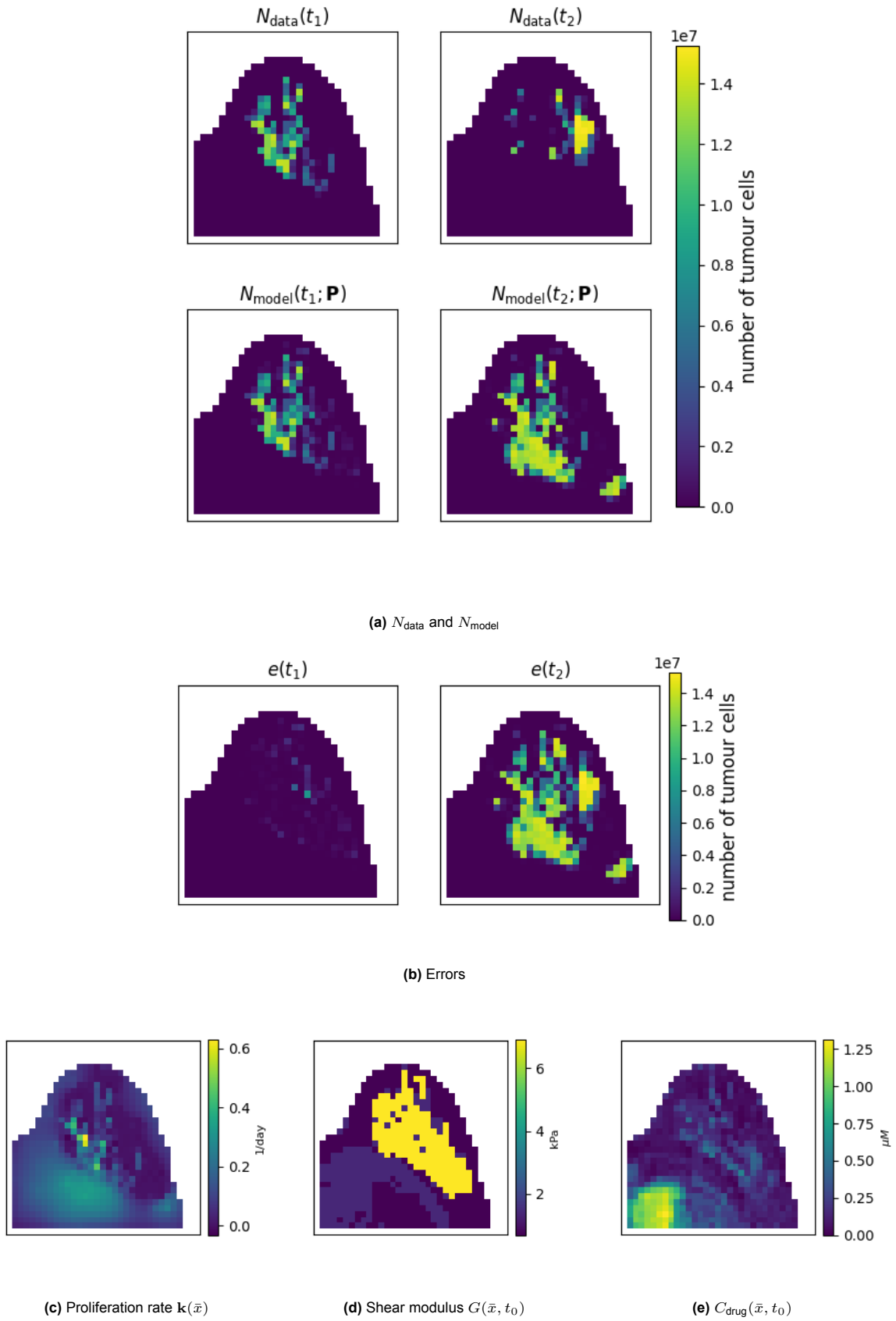
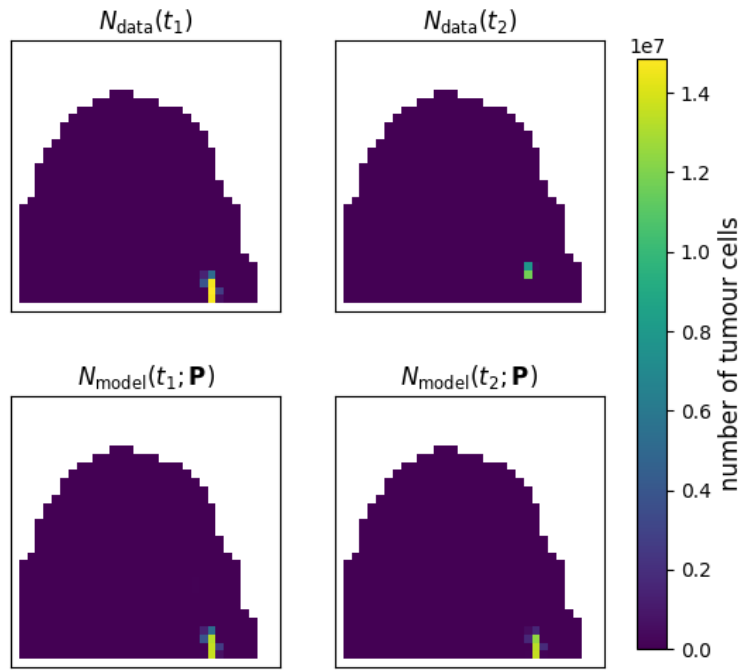
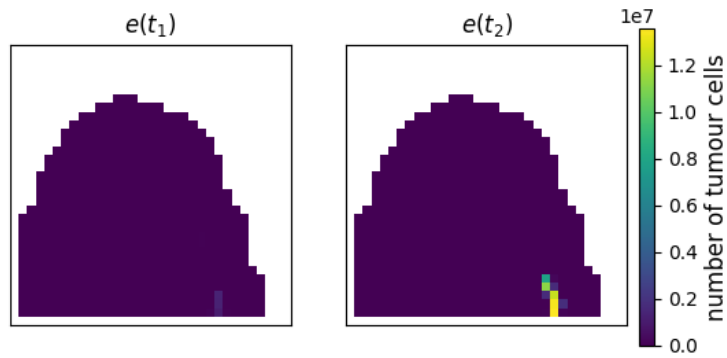


Figure C.6: Results from cycle Ib for p_3 using DL optimization visualized using slices. (a) shows the N_{data} representation at t_1 and t_2 , along with $N_{\text{model}}(t_1)$, the calibrated number of tumour cells at t_1 , and $N_{\text{model}}(t_2)$, the prediction made by the DI-MCRD model from cycle Ib at t_2 . (b) presents the errors between N_{data} and N_{model} at t_1 and t_2 . (c) visualizes the proliferation rate $k(\bar{x})$ (d) displays the shear modulus $G(\bar{x}, t_0)$ and (e), displays the drug distribution $C_{\text{drug}}(\bar{x}, t_0)$.

(a) N_{data} and N_{model} 

(b) Errors

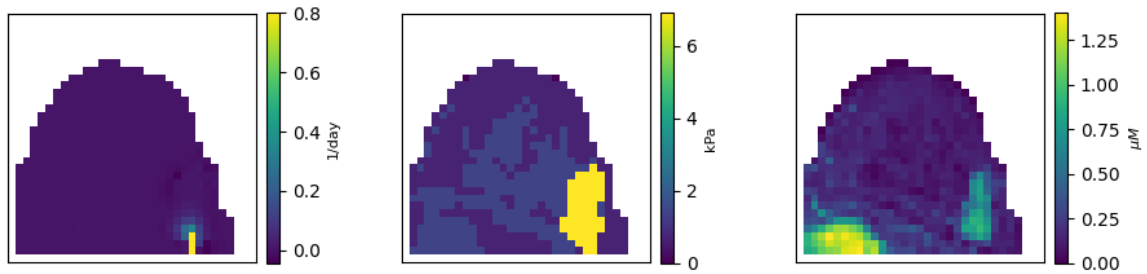
(c) Proliferation rate $k(\bar{x})$ (d) Shear modulus $G(\bar{x}, t_0)$ (e) $C_{drug}(\bar{x}, t_0)$

Figure C.7: Results from cycle Ib for p_8 using DL optimization visualized using slices. (a) shows the N_{data} representation at t_1 and t_2 , along with $N_{model}(t_1)$, the calibrated number of tumour cells at t_1 , and $N_{model}(t_2)$, the prediction made by the DI-MCRD model from cycle Ib at t_2 . (b) presents the errors between N_{data} and N_{model} at t_1 and t_2 . (c) visualizes the proliferation rate $k(\bar{x})$, (d) displays the shear modulus $G(\bar{x}, t_0)$ and (e), displays the drug distribution $C_{drug}(\bar{x}, t_0)$.

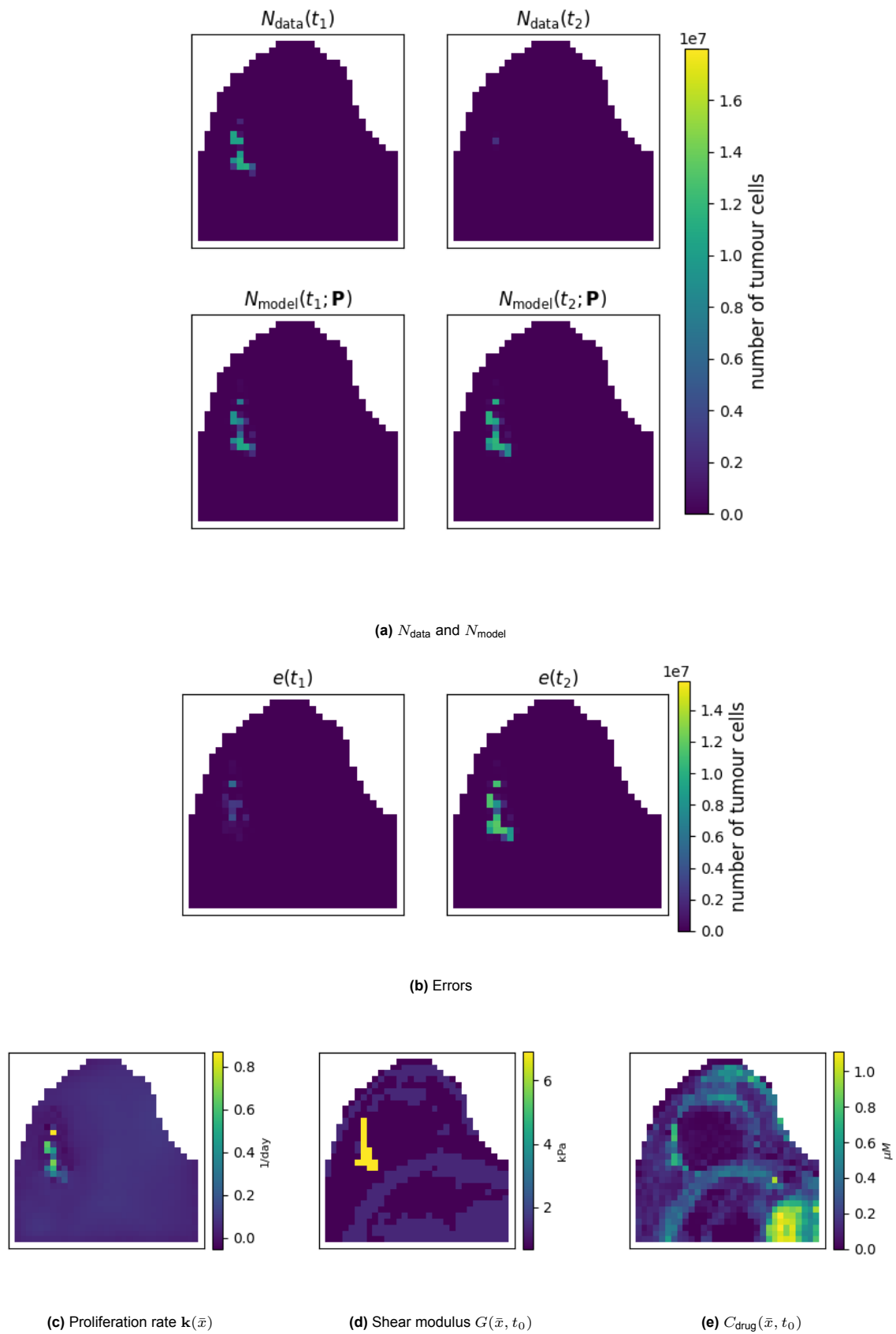


Figure C.8: Results from cycle Ib for p_{10} using DL optimization visualized using slices. (a) shows the N_{data} representation at t_1 and t_2 , along with $N_{\text{model}}(t_1)$, the calibrated number of tumour cells at t_1 , and $N_{\text{model}}(t_2)$, the prediction made by the DI-MCRD model from cycle Ib at t_2 . (b) presents the errors between N_{data} and N_{model} at t_1 and t_2 . (c) visualizes the proliferation rate $k(\bar{x})$, (d) displays the shear modulus $G(\bar{x}, t_0)$ and (e), displays the drug distribution $C_{\text{drug}}(\bar{x}, t_0)$.

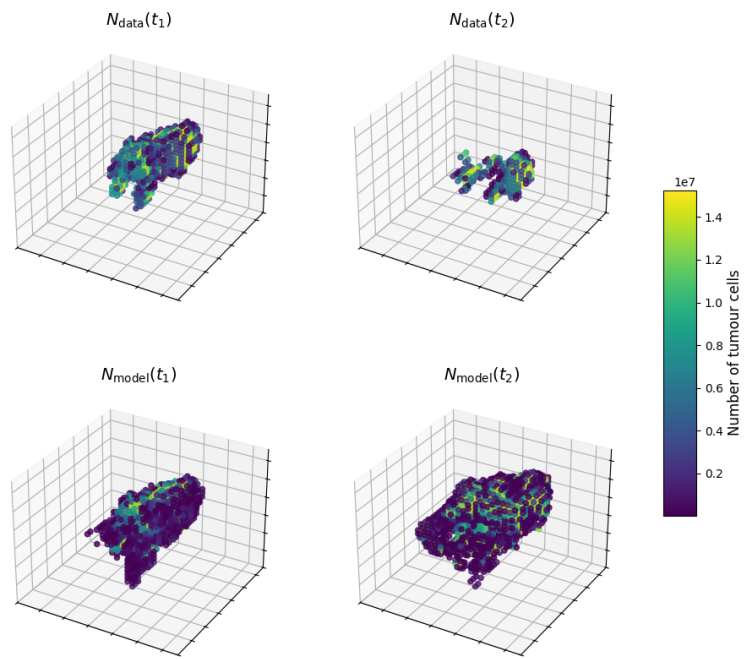
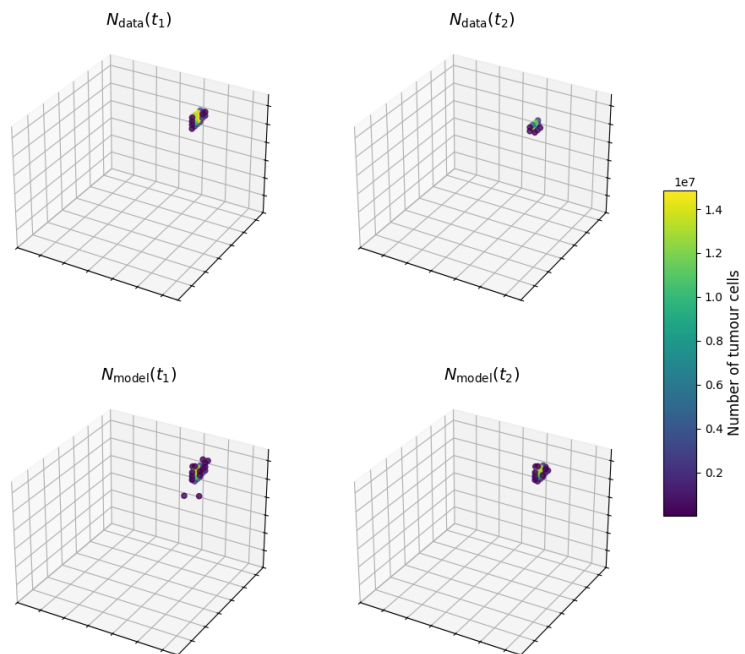
(a) p_3 (b) p_8

Figure C.9: 3D representation of the number of tumour cells for patients p_3 and p_8 obtained using the model from cycle Ib with DL optimization. Within each subfigure, the top row shows the N_{data} representation at t_1 and t_2 , while the bottom row displays $N_{model}(t_1)$, the calibrated number of tumour cells at t_1 , and $N_{model}(t_2)$, the prediction made by the DL-MCRD model at t_2 . In the bottom row, all voxels with a tumour cell count less than N_{min} are removed.

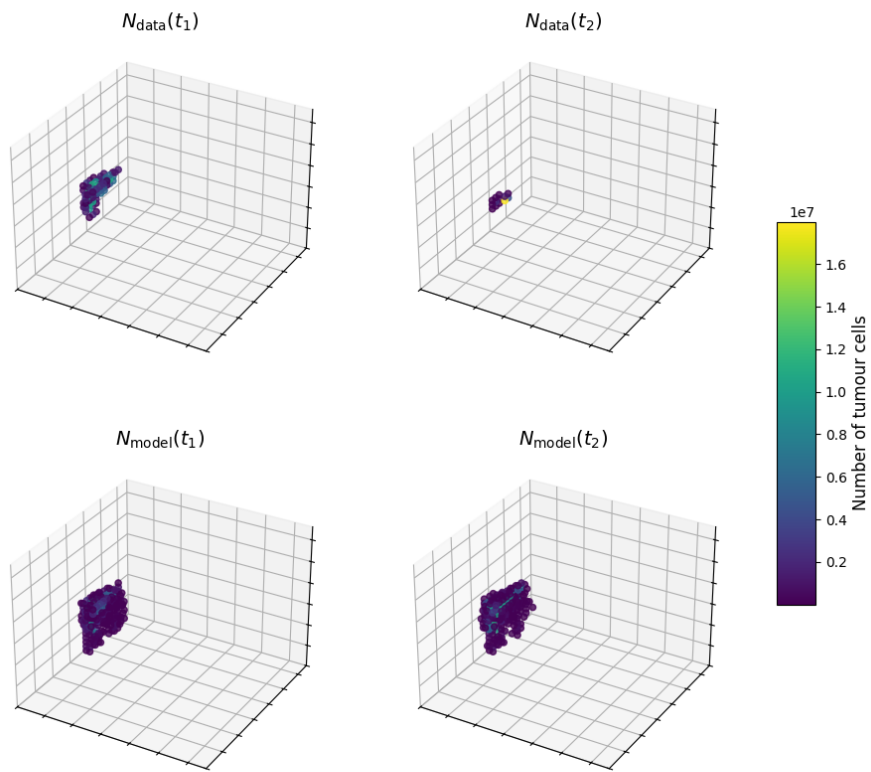


Figure C.10: 3D representation of the number of tumour cells for patient p_{10} obtained using the model from cycle Ib with DL optimization. The top row shows the N_{data} representation at t_1 and t_2 , while the bottom row displays $N_{\text{model}}(t_1)$, the calibrated number of tumour cells at t_1 , and $N_{\text{model}}(t_2)$, the prediction made by the DI-MCRD model at t_2 . In the bottom row, all voxels with a tumour cell count less than N_{min} are removed.

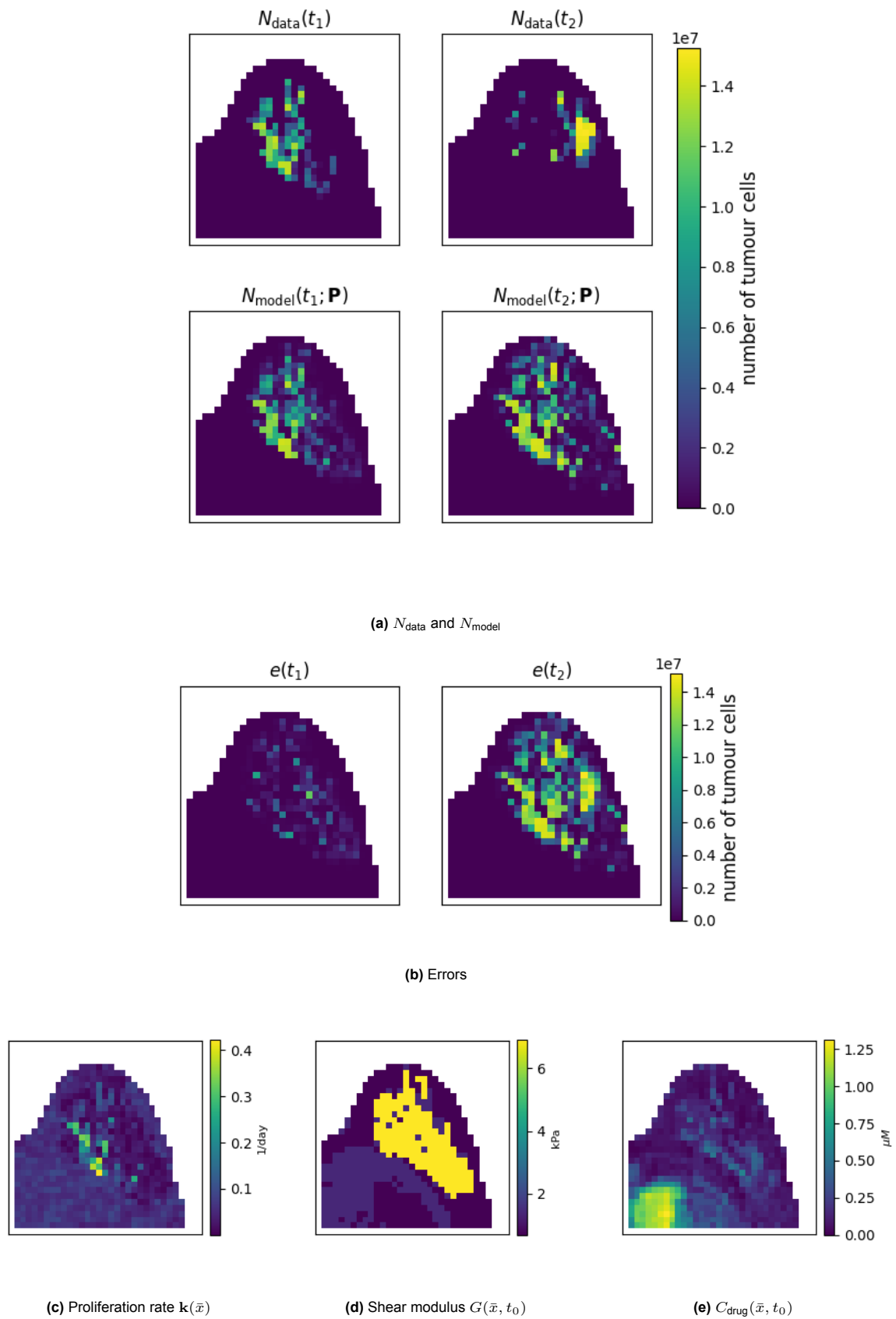


Figure C.11: Results from cycle Ib for p_3 using TRF optimization visualized using slices. (a) shows the N_{data} representation at t_1 and t_2 , along with $N_{\text{model}}(t_1)$, the calibrated number of tumour cells at t_1 , and $N_{\text{model}}(t_2)$, the prediction made by the DI-MCRD model from cycle Ib at t_2 . (b) presents the errors between N_{data} and N_{model} at t_1 and t_2 . (c) visualizes the proliferation rate $k(\bar{x})$, (d) displays the shear modulus $G(\bar{x}, t_0)$ and (e), displays the drug distribution $C_{\text{drug}}(\bar{x}, t_0)$.

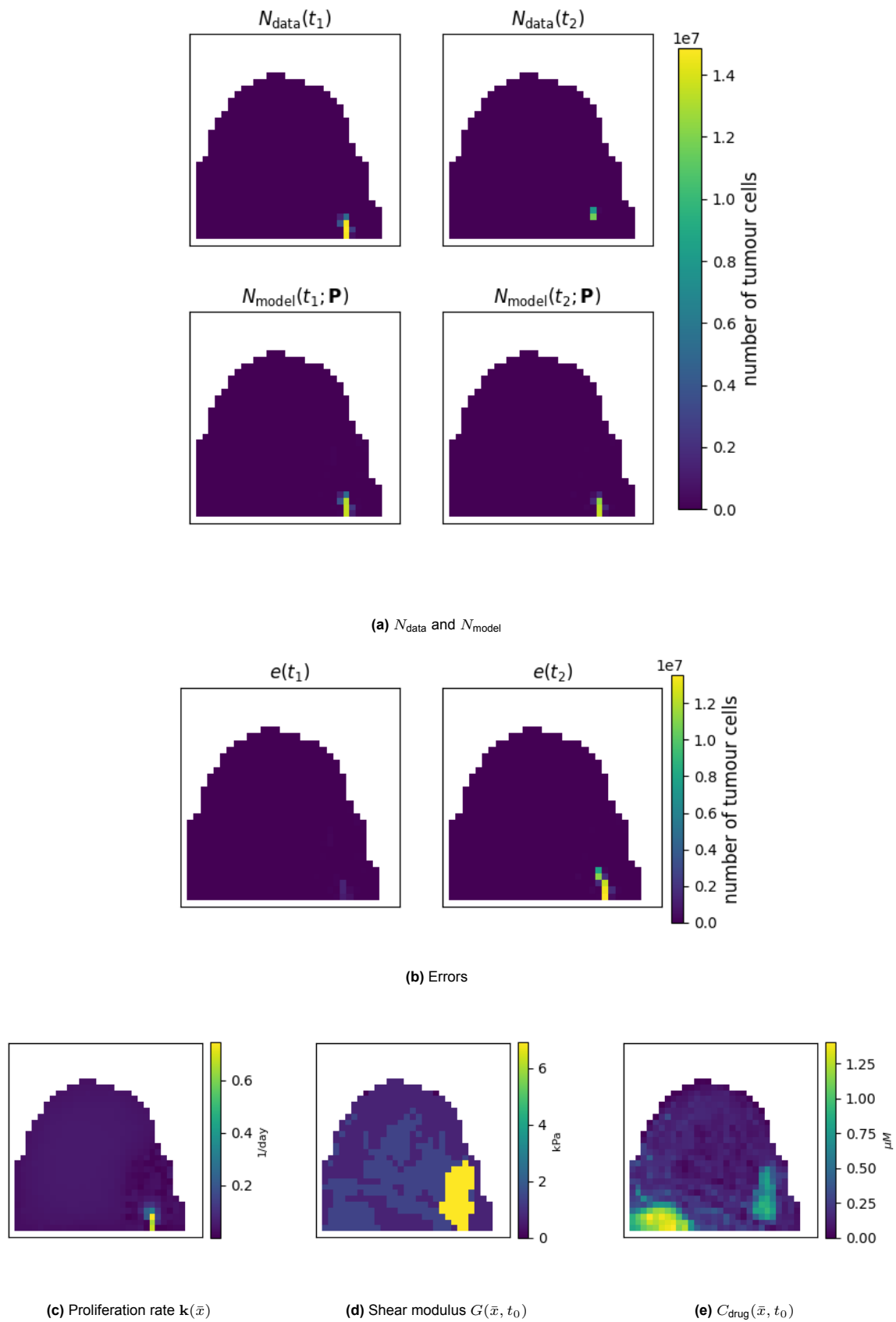


Figure C.12: Results from cycle Ib for p_8 using TRF optimization visualized using slices. (a) shows the N_{data} representation at t_1 and t_2 , along with $N_{\text{model}}(t_1)$, the calibrated number of tumour cells at t_1 , and $N_{\text{model}}(t_2)$, the prediction made by the DI-MCRD model from cycle Ib at t_2 . (b) presents the errors between N_{data} and N_{model} at t_1 and t_2 . (c) visualizes the proliferation rate $k(\bar{x})$, (d) displays the shear modulus $G(\bar{x}, t_0)$ and (e), displays the drug distribution $C_{\text{drug}}(\bar{x}, t_0)$.

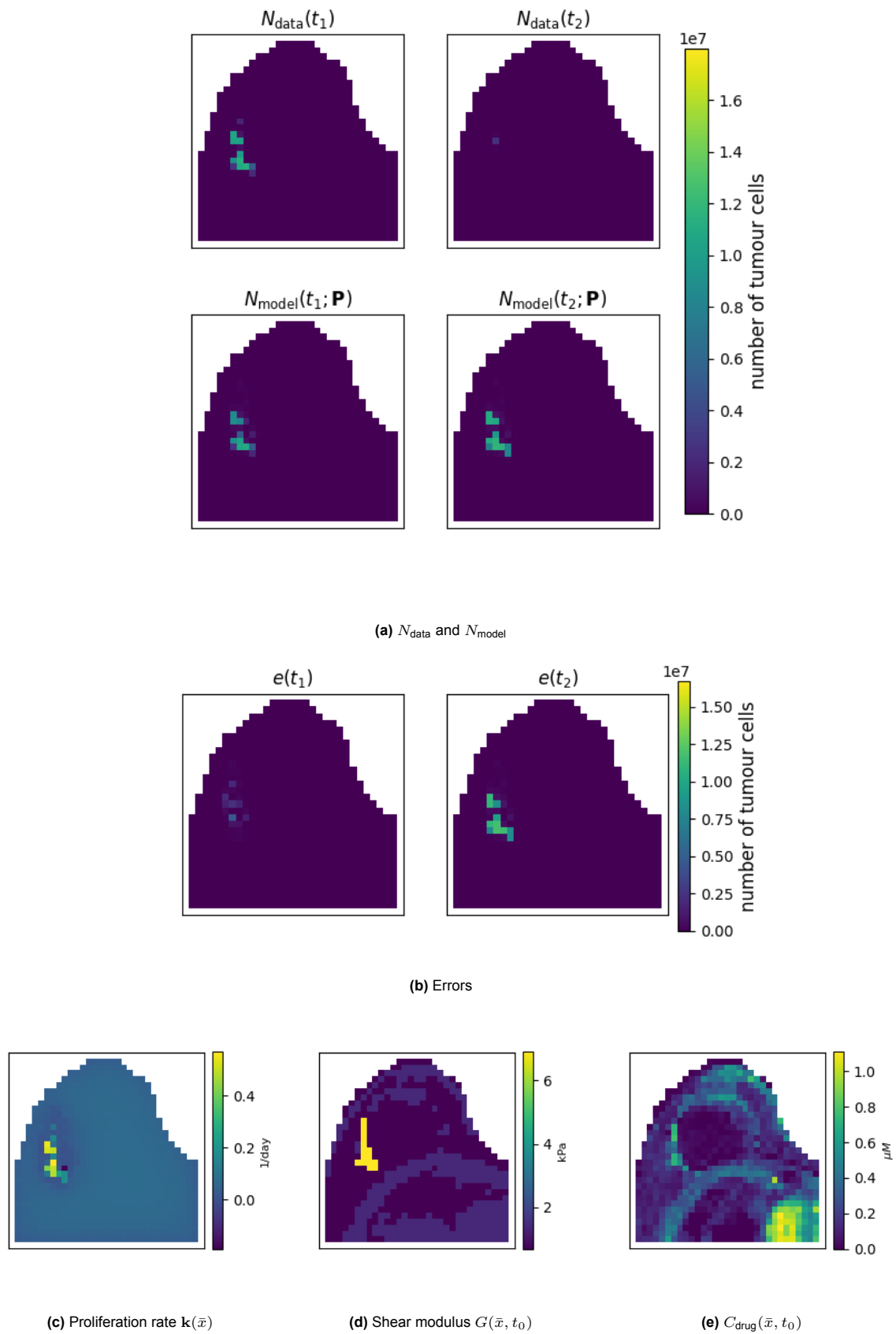


Figure C.13: Results from cycle Ib for p_{10} using TRF optimization visualized using slices. (a) shows the N_{data} representation at t_1 and t_2 , along with $N_{\text{model}}(t_1)$, the calibrated number of tumour cells at t_1 , and $N_{\text{model}}(t_2)$, the prediction made by the DI-MCRD model from cycle Ib at t_2 . (b) presents the errors between N_{data} and N_{model} at t_1 and t_2 . (c) visualizes the proliferation rate $k(\bar{x})$, (d) displays the shear modulus $G(\bar{x}, t_0)$ and (e), displays the drug distribution $C_{\text{drug}}(\bar{x}, t_0)$.

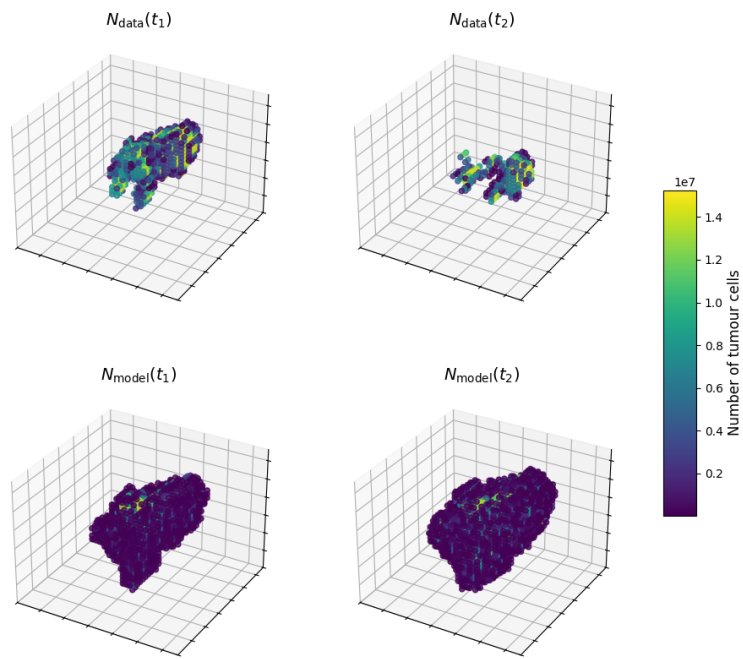
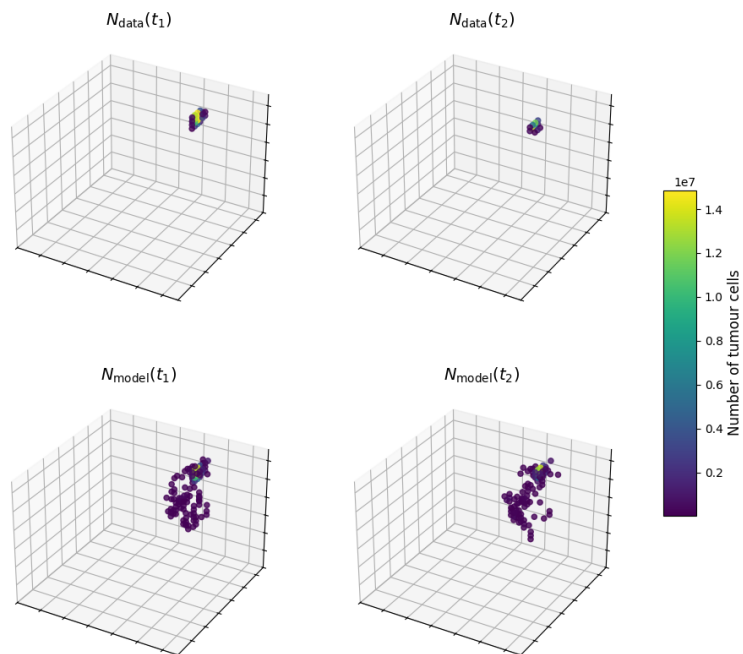
(a) p_3 (b) p_8

Figure C.14: 3D representation of the number of tumour cells for patients p_3 and p_8 obtained using the model from cycle Ib with TRF optimization. Within each subfigure, the top row shows the N_{data} representation at t_1 and t_2 , while the bottom row displays $N_{model}(t_1)$, the calibrated number of tumour cells at t_1 , and $N_{model}(t_2)$, the prediction made by the DI-MCRD model at t_2 . In the bottom row, all voxels with a tumour cell count less than N_{min} are removed.

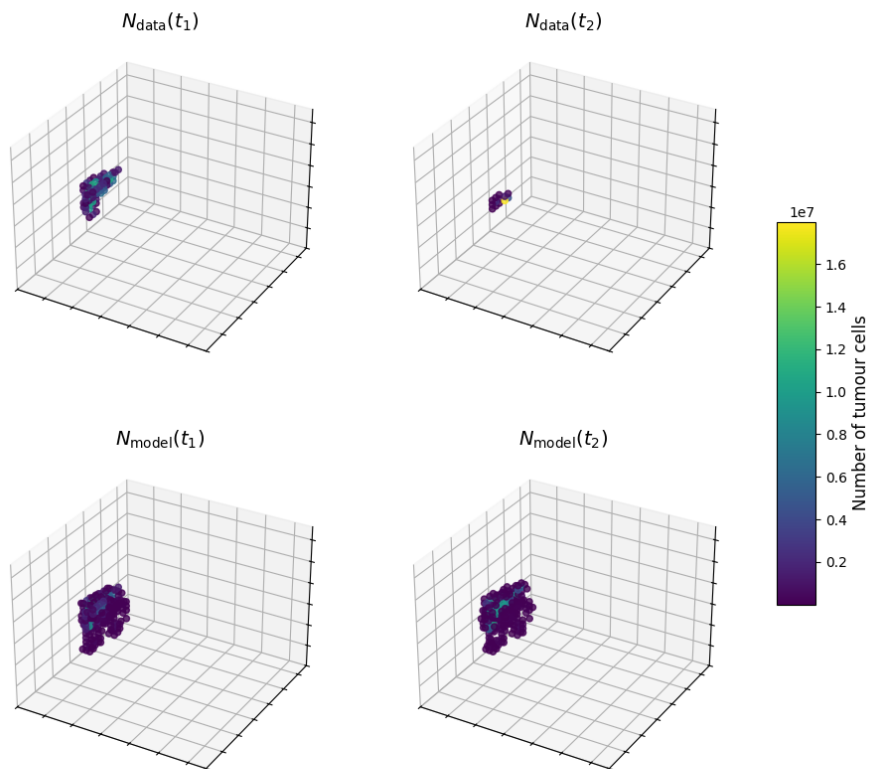


Figure C.15: 3D representation of the number of tumour cells for patient p_{10} obtained using the model from cycle Ib with TRF optimization. The top row shows the N_{data} representation at t_1 and t_2 , while the bottom row displays $N_{\text{model}}(t_1)$, the calibrated number of tumour cells at t_1 , and $N_{\text{model}}(t_2)$, the prediction made by the DI-MCRD model at t_2 . In the bottom row, all voxels with a tumour cell count less than N_{min} are removed.

C.3. Cycle II Results

In this section the visualizations of the results using the DI-MRCD model from cycle II that are not shown in Section 4.3 are shown.

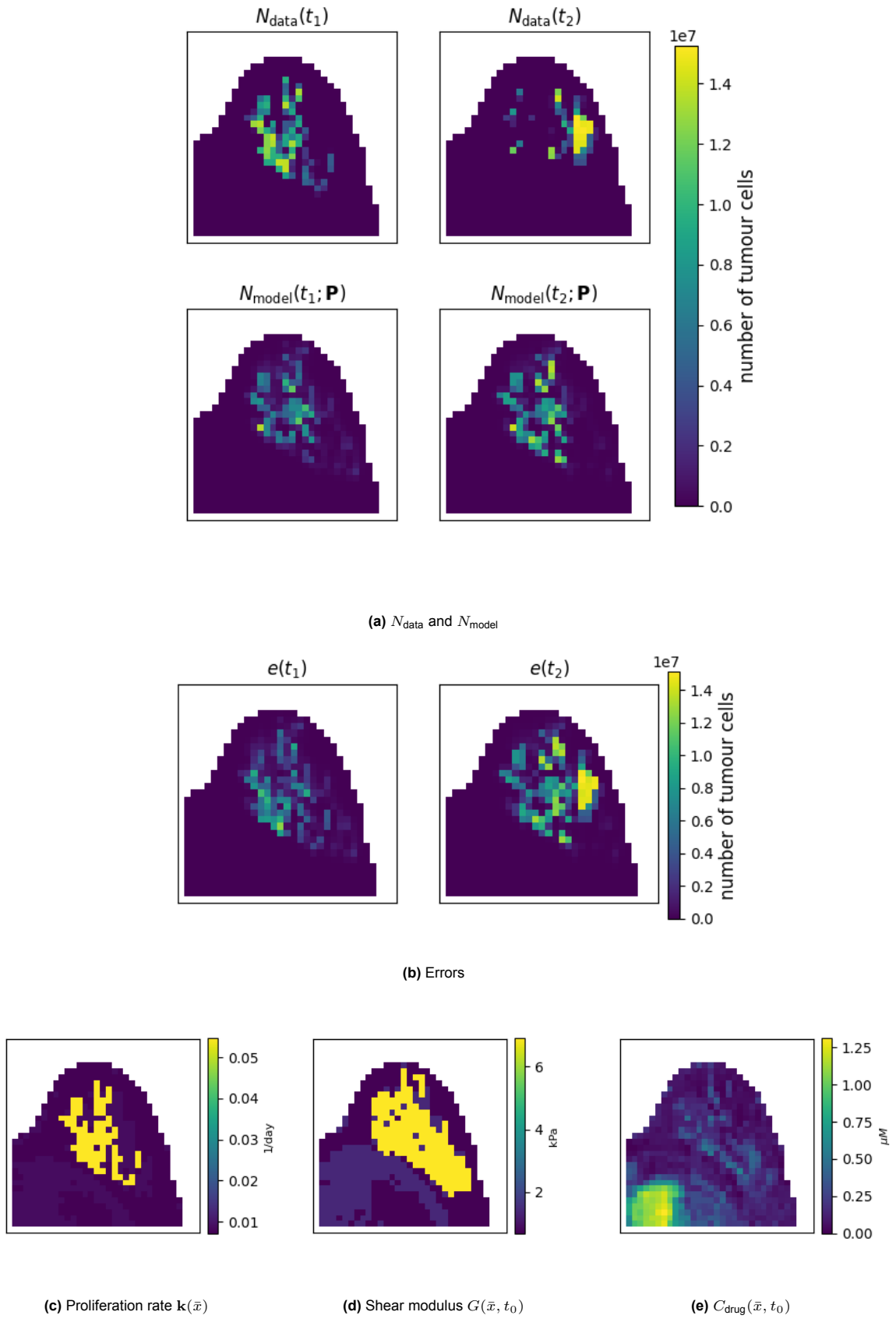
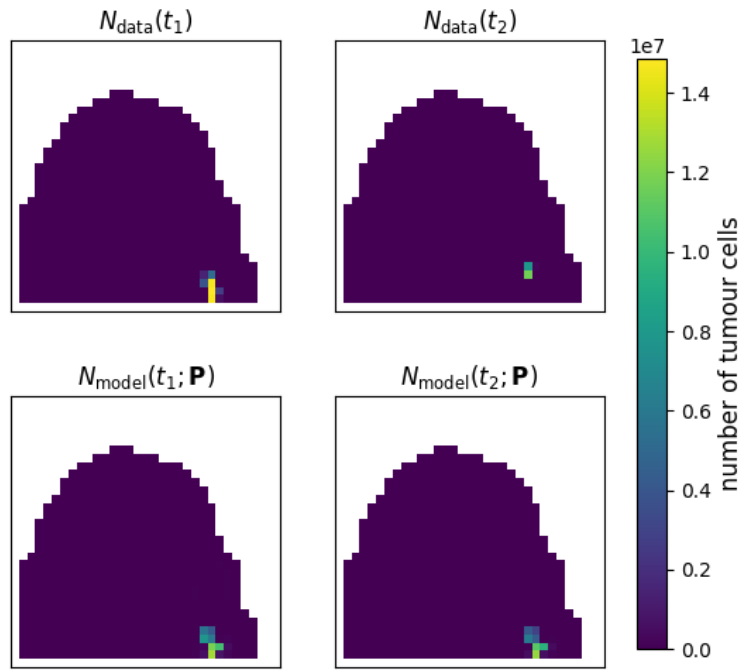
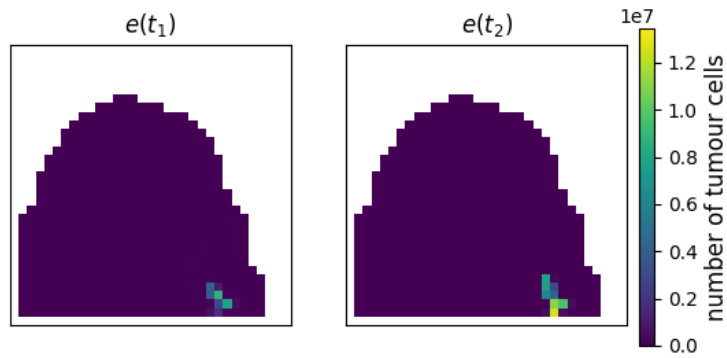


Figure C.1: Results from cycle II for p_3 using DL optimization visualized using slices. (a) shows the N_{data} representation at t_1 and t_2 , along with $N_{\text{model}}(t_1)$, the calibrated number of tumour cells at t_1 , and $N_{\text{model}}(t_2)$, the prediction made by the DI-MCRD model from cycle II at t_2 . (b) presents the errors between N_{data} and N_{model} at t_1 and t_2 . (c) visualizes the proliferation rate $k(\bar{x})$, (d) displays the shear modulus $G(\bar{x}, t_0)$, and (e) displays the drug distribution $C_{\text{drug}}(\bar{x}, t_0)$.

(a) N_{data} and N_{model} 

(b) Errors

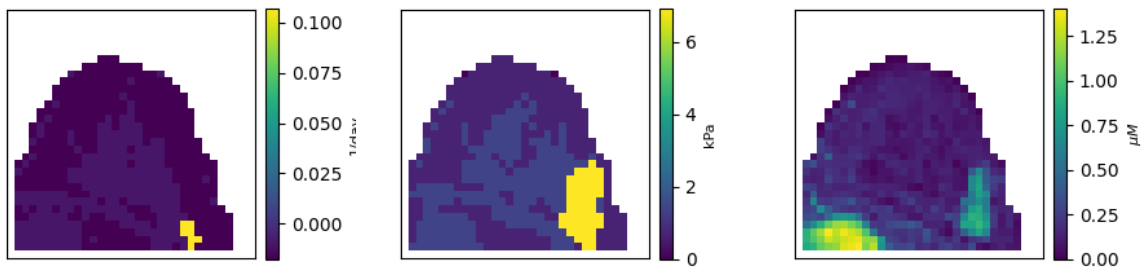
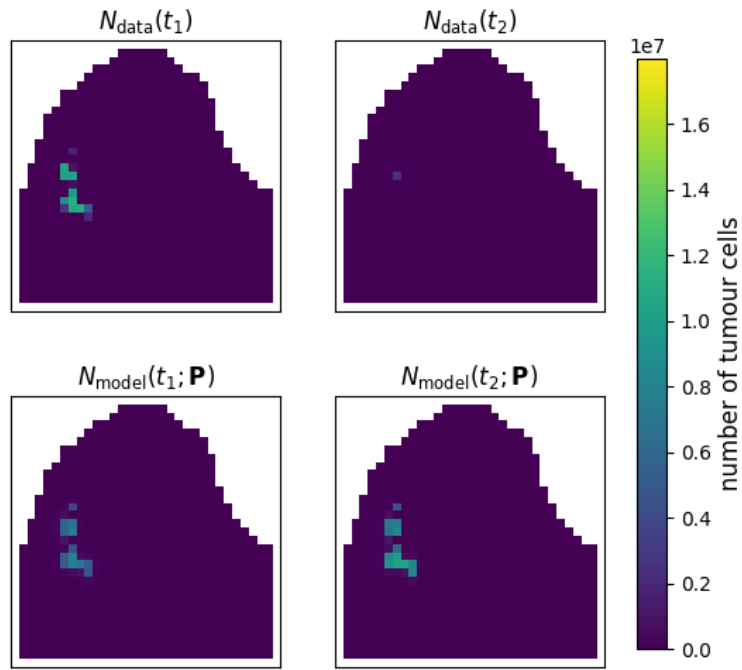
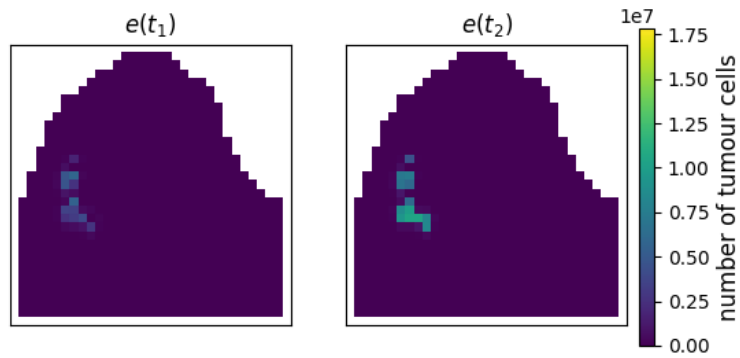
(c) Proliferation rate $k(\bar{x})$ (d) Shear modulus $G(\bar{x}, t_0)$ (e) $C_{drug}(\bar{x}, t_0)$

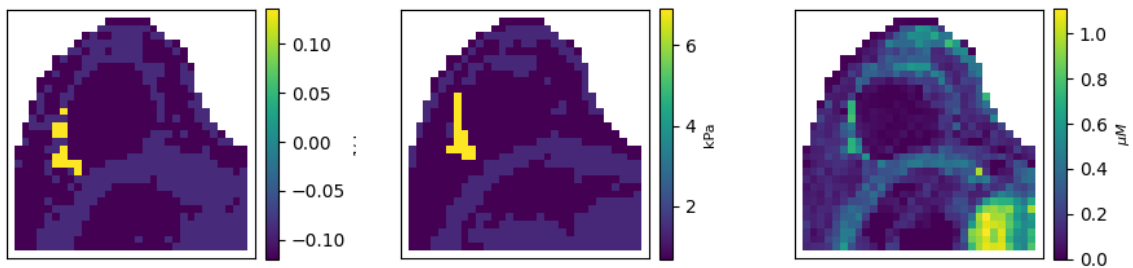
Figure C.2: Results from cycle II for p_8 using DL optimization visualized using slices. (a) shows the N_{data} representation at t_1 and t_2 , along with $N_{model}(t_1)$, the calibrated number of tumour cells at t_1 , and $N_{model}(t_2)$, the prediction made by the DI-MCRD model from cycle II at t_2 . (b) presents the errors between N_{data} and N_{model} at t_1 and t_2 . (c) visualizes the proliferation rate $k(\bar{x})$, (d) displays the shear modulus $G(\bar{x}, t_0)$, and (e) displays the drug distribution $C_{drug}(\bar{x}, t_0)$.



(a) N_{data} and N_{model}



(b) Errors



(c) Proliferation rate $k(\bar{x})$

(d) Shear modulus $G(\bar{x}, t_0)$

(e) $C_{\text{drug}}(\bar{x}, t_0)$

Figure C.3: Results from cycle II for p_{10} using DL optimization visualized using slices. (a) shows the N_{data} representation at t_1 and t_2 , along with $N_{\text{model}}(t_1)$, the calibrated number of tumour cells at t_1 , and $N_{\text{model}}(t_2)$, the prediction made by the DI-MCRD model from cycle II at t_2 . (b) presents the errors between N_{data} and N_{model} at t_1 and t_2 . (c) visualizes the proliferation rate $k(\bar{x})$, (d) displays the shear modulus $G(\bar{x}, t_0)$, and (e) displays the drug distribution $C_{\text{drug}}(\bar{x}, t_0)$.

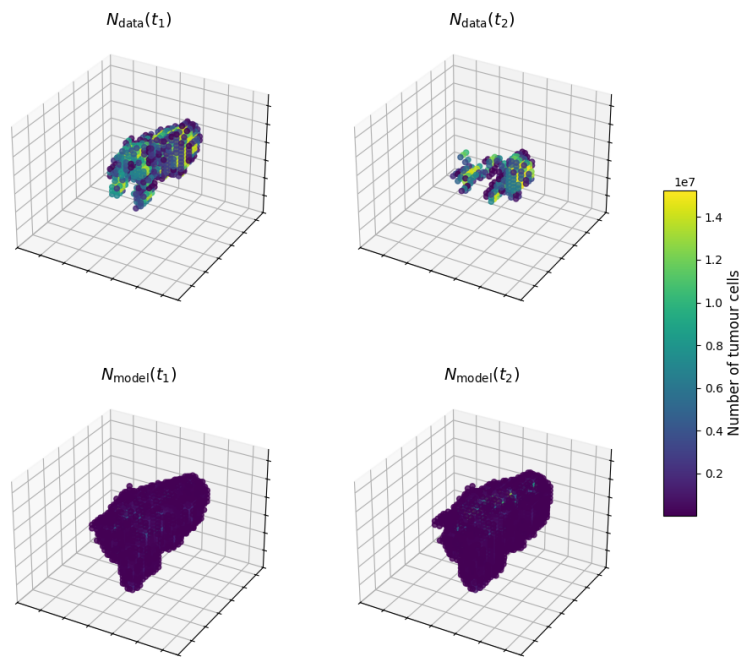
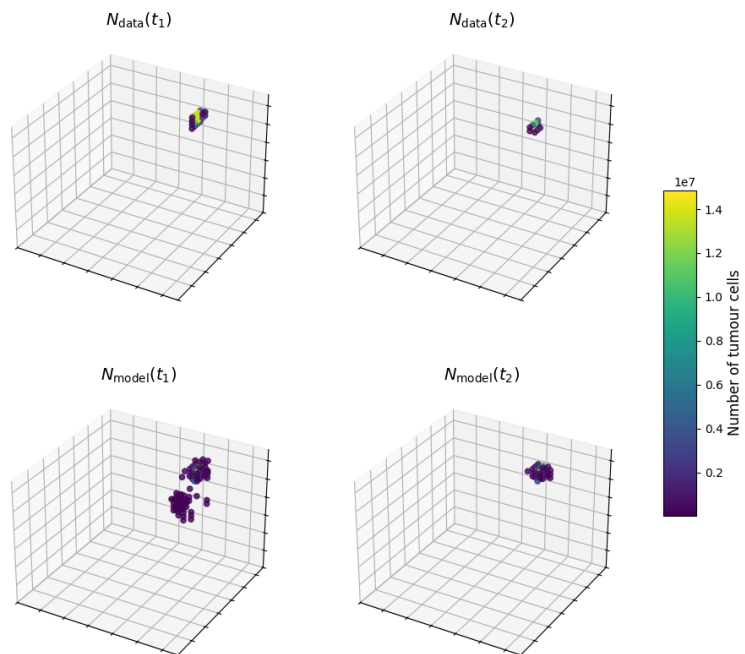
(a) p_3 (b) p_8

Figure C.4: 3D representation of the number of tumour cells for patients p_3 and p_8 obtained using the model from cycle II with DL optimization. Within each subfigure, the top row shows the N_{data} representation at t_1 and t_2 , while the bottom row displays $N_{\text{model}}(t_1)$, the calibrated number of tumour cells at t_1 , and $N_{\text{model}}(t_2)$, the prediction made by the DL-MCRD model at t_2 . In the bottom row, all voxels with a tumour cell count less than N_{min} are removed.

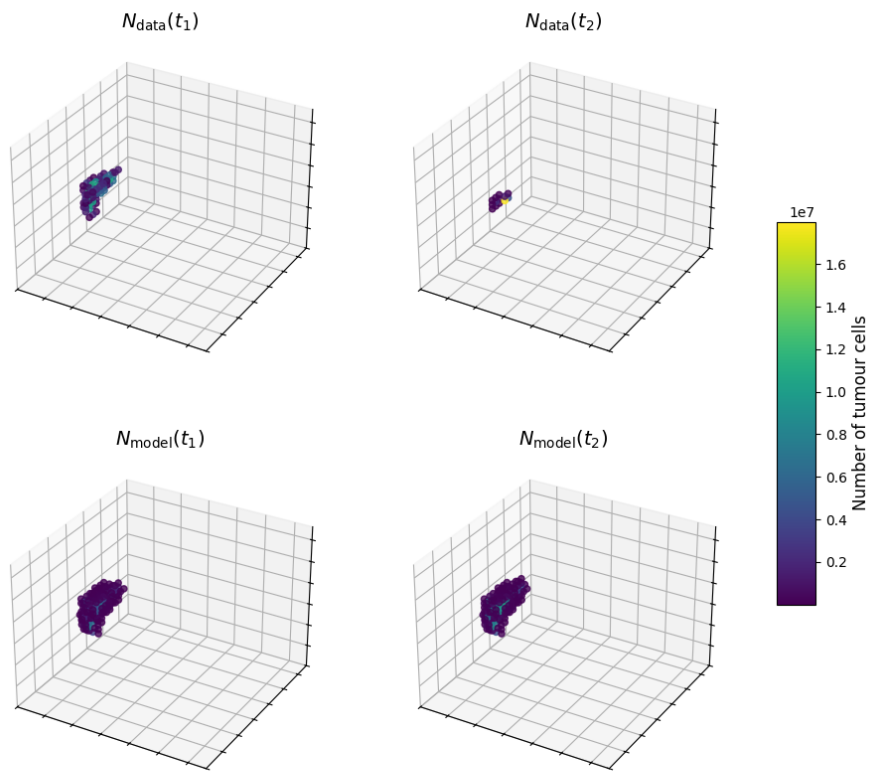


Figure C.5: 3D representation of the number of tumour cells for patient p_{10} obtained using the model from cycle II with DL optimization. The top row shows the N_{data} representation at t_1 and t_2 , while the bottom row displays $N_{\text{model}}(t_1)$, the calibrated number of tumour cells at t_1 , and $N_{\text{model}}(t_2)$, the prediction made by the DI-MCRD model at t_2 . In the bottom row, all voxels with a tumour cell count less than N_{min} are removed.

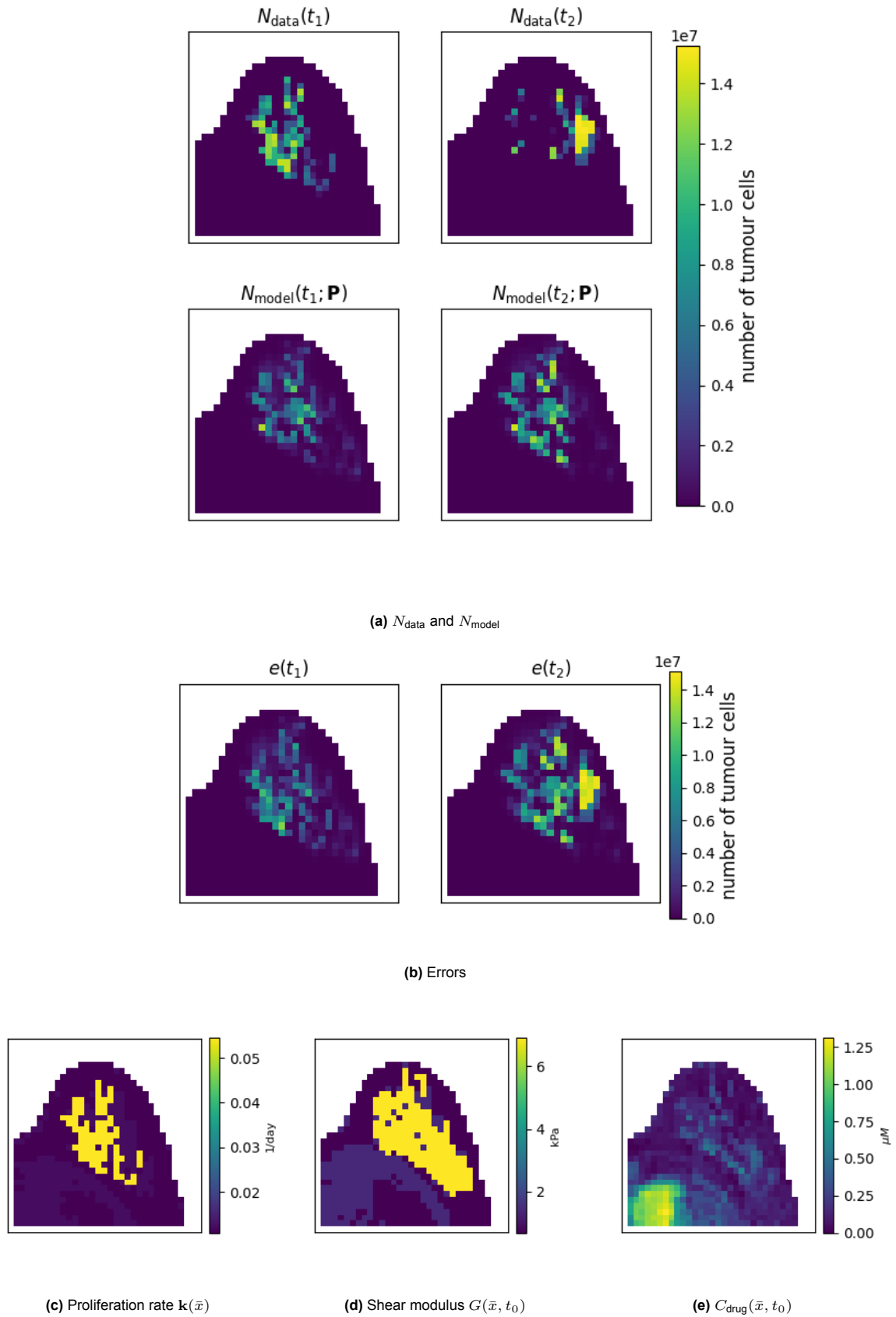
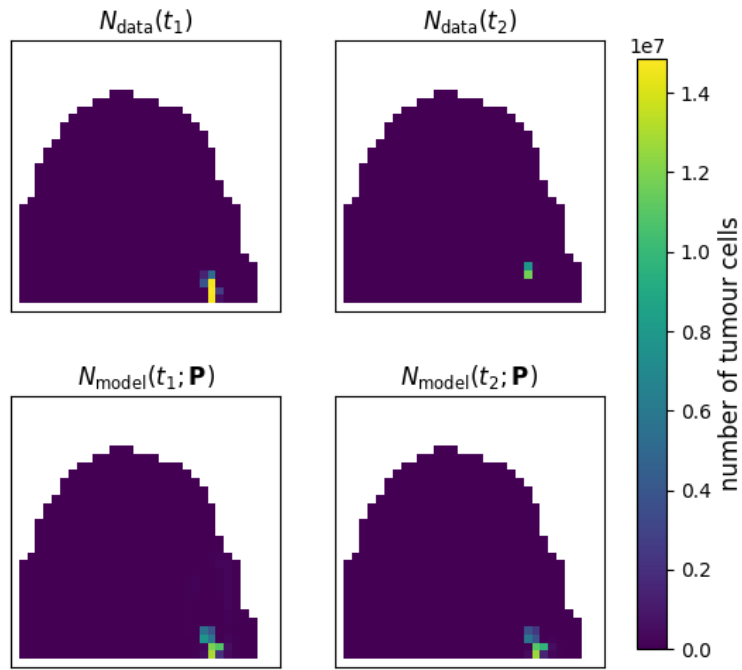
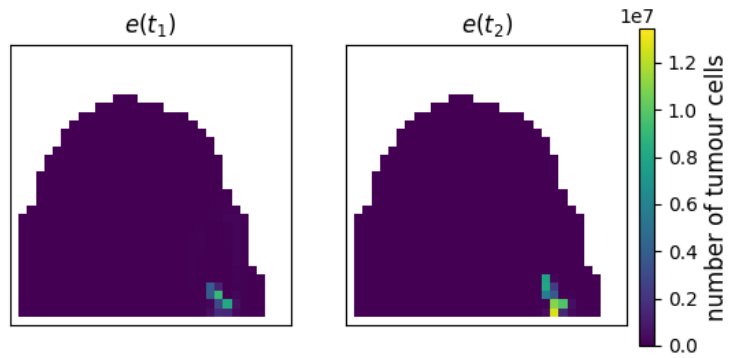


Figure C.6: Results from cycle II for p_3 using TRF optimization visualized using slices. (a) shows the N_{data} representation at t_1 and t_2 , along with $N_{\text{model}}(t_1)$, the calibrated number of tumour cells at t_1 , and $N_{\text{model}}(t_2)$, the prediction made by the DI-MCRD model from cycle II at t_2 . (b) presents the errors between N_{data} and N_{model} at t_1 and t_2 . (c) visualizes the proliferation rate $k(\bar{x})$, (d) displays the shear modulus $G(\bar{x}, t_0)$ and (e), displays the drug distribution $C_{\text{drug}}(\bar{x}, t_0)$.

(a) N_{data} and N_{model} 

(b) Errors

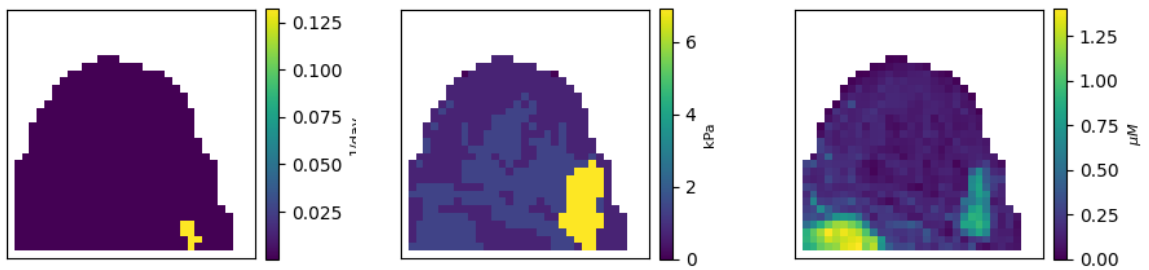
(c) Proliferation rate $k(\bar{x})$ (d) Shear modulus $G(\bar{x}, t_0)$ (e) $C_{drug}(\bar{x}, t_0)$

Figure C.7: Results from cycle II for p_8 using TRF optimization visualized using slices. (a) shows the N_{data} representation at t_1 and t_2 , along with $N_{model}(t_1)$, the calibrated number of tumour cells at t_1 , and $N_{model}(t_2)$, the prediction made by the DI-MCRD model from cycle II at t_2 . (b) presents the errors between N_{data} and N_{model} at t_1 and t_2 . (c) visualizes the proliferation rate $k(\bar{x})$, (d) displays the shear modulus $G(\bar{x}, t_0)$ and (e), displays the drug distribution $C_{drug}(\bar{x}, t_0)$.

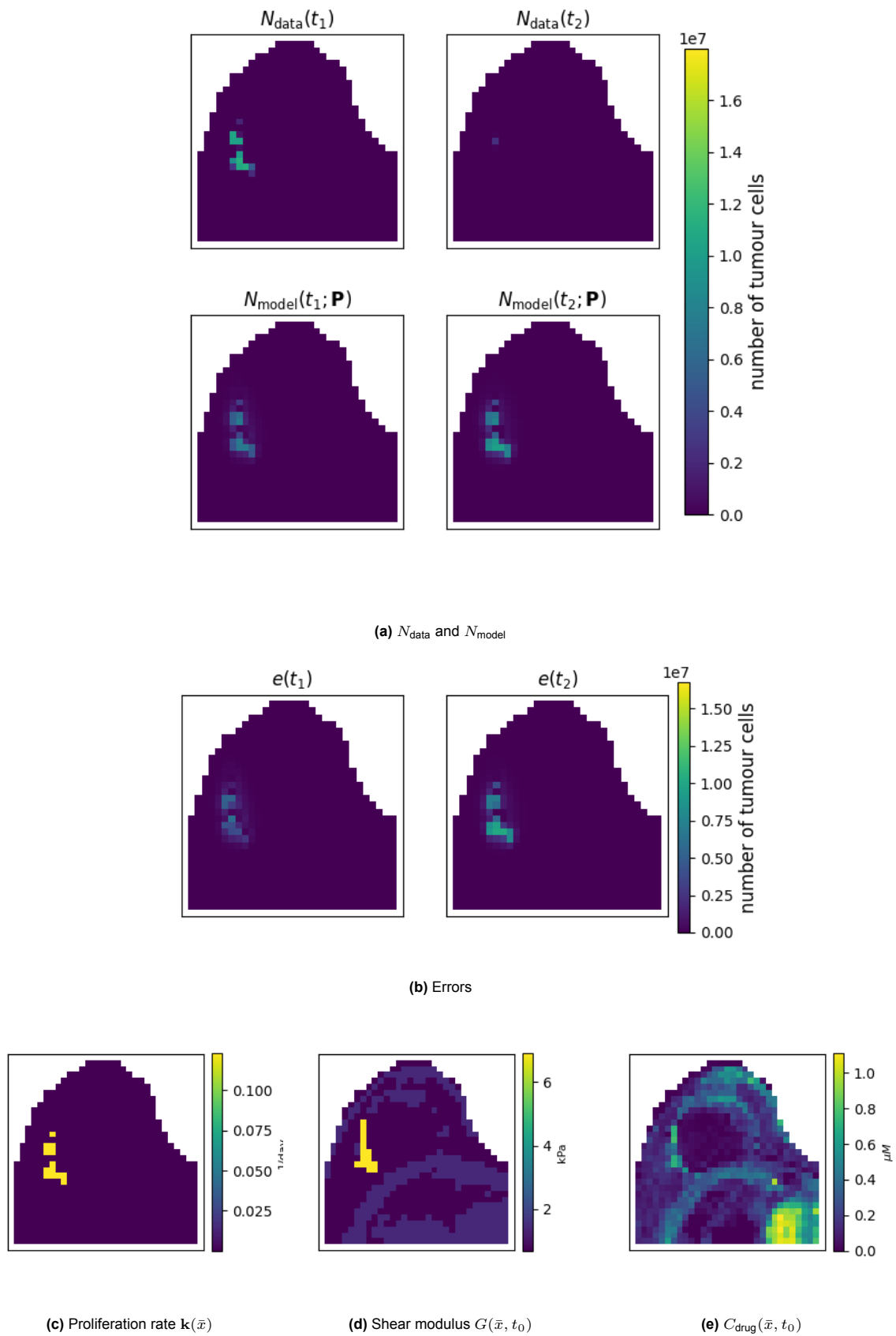


Figure C.8: Results from cycle II for p_{10} using TRF optimization visualized using slices. (a) shows the N_{data} representation at t_1 and t_2 , along with $N_{\text{model}}(t_1)$, the calibrated number of tumour cells at t_1 , and $N_{\text{model}}(t_2)$, the prediction made by the DI-MCRD model from cycle II at t_2 . (b) presents the errors between N_{data} and N_{model} at t_1 and t_2 . (c) visualizes the proliferation rate $k(\bar{x})$, and (d) displays the shear modulus $G(\bar{x}, t_0)$.

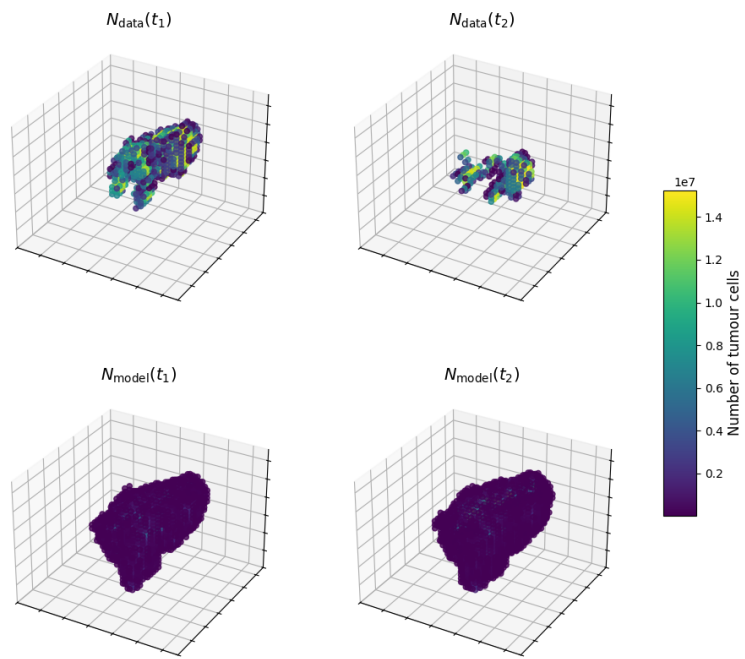
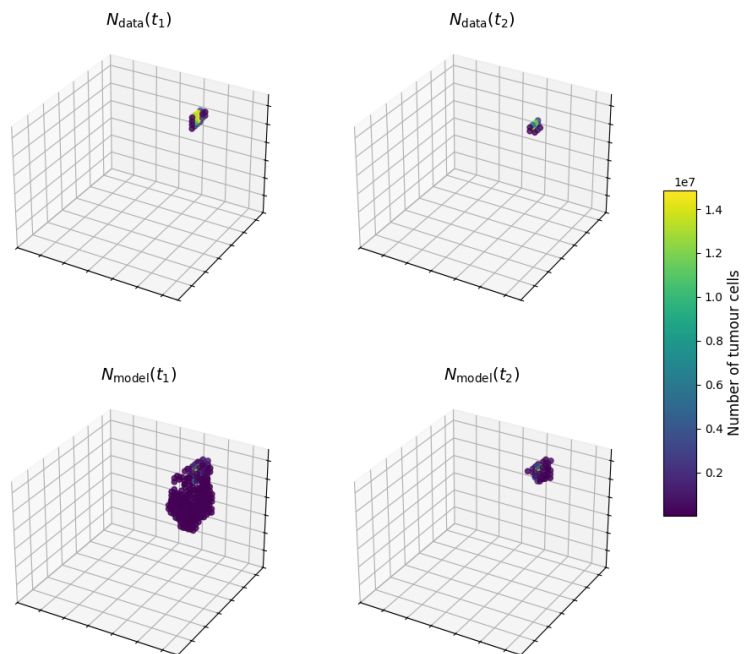
(a) p_3 (b) p_8

Figure C.9: 3D representation of the number of tumour cells for patients p_3 and p_8 obtained using the model from cycle II with TRF optimization. Within each subfigure, the top row shows the N_{data} representation at t_1 and t_2 , while the bottom row displays $N_{\text{model}}(t_1)$, the calibrated number of tumour cells at t_1 , and $N_{\text{model}}(t_2)$, the prediction made by the DI-MCRD model at t_2 . In the bottom row, all voxels with a tumour cell count less than N_{min} are removed.

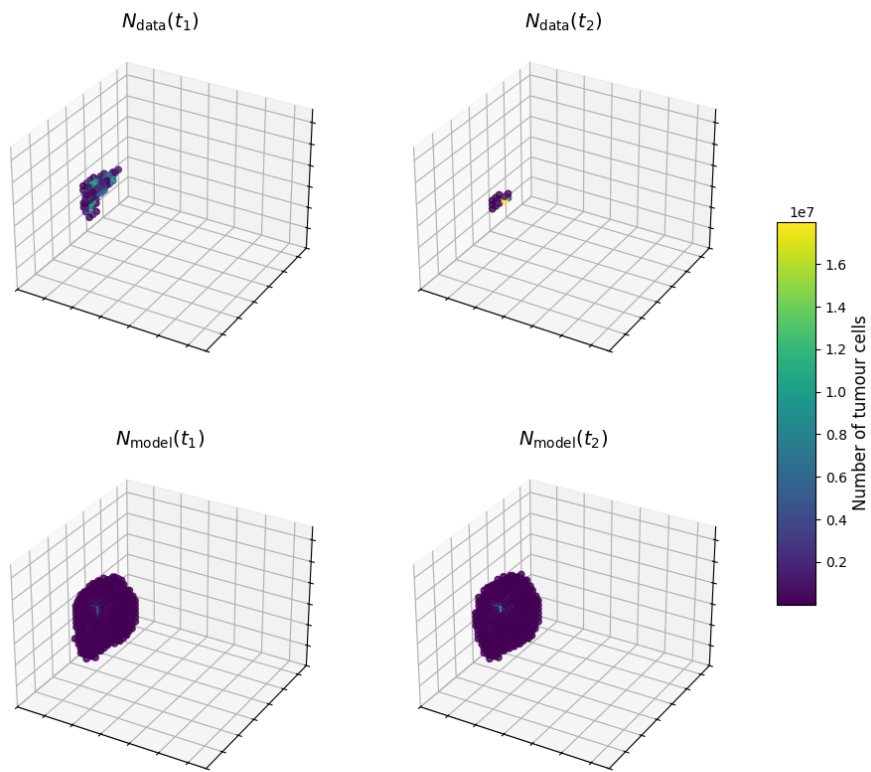


Figure C.10: 3D representation of the number of tumour cells for patient p_{10} obtained using the model from cycle II with TRF optimization. The top row shows the N_{data} representation at t_1 and t_2 , while the bottom row displays $N_{\text{model}}(t_1)$, the calibrated number of tumour cells at t_1 , and $N_{\text{model}}(t_2)$, the prediction made by the DI-MCRD model at t_2 . In the bottom row, all voxels with a tumour cell count less than N_{min} are removed.

C.4. Cycle III Results

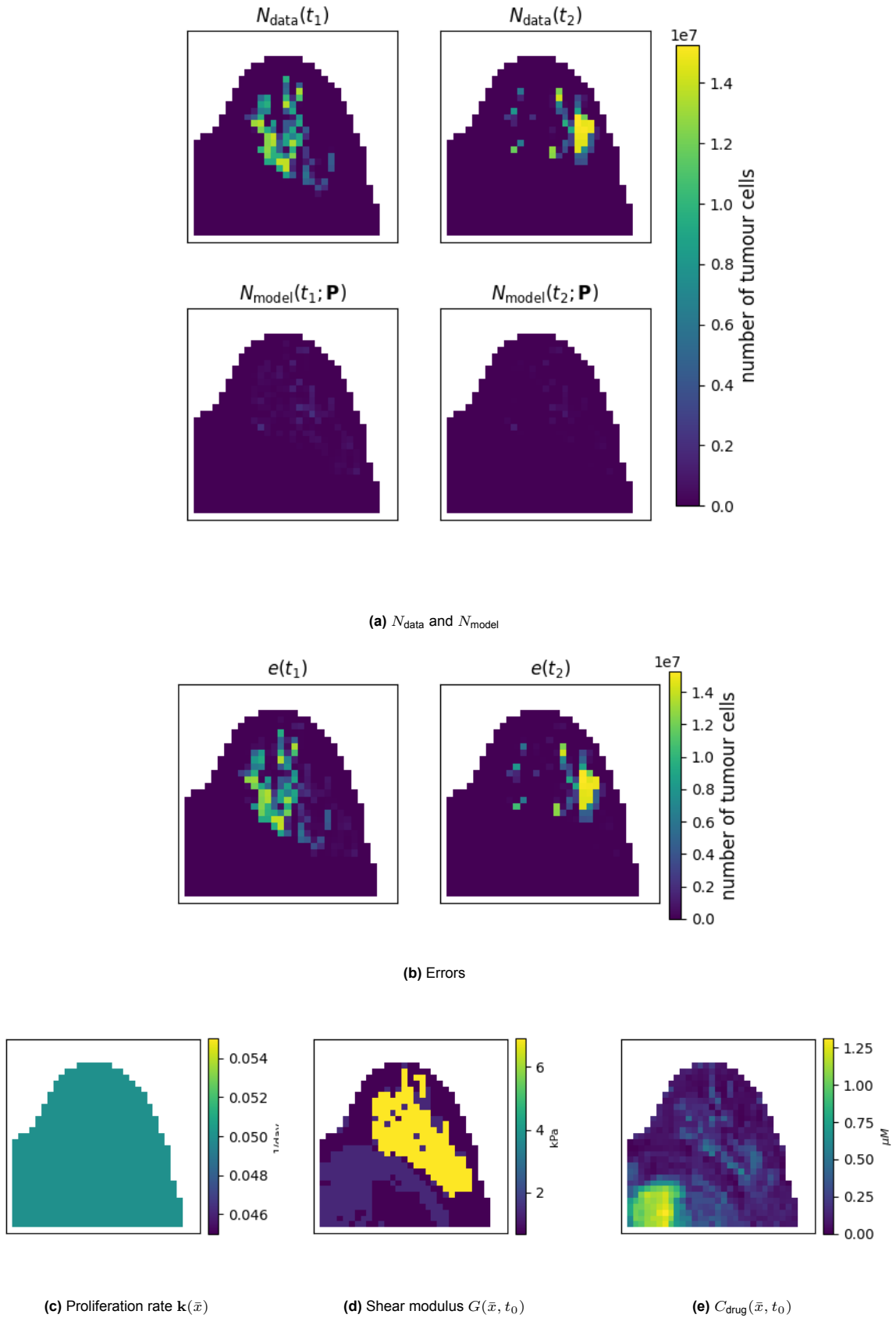


Figure C.1: Results from cycle III with $\gamma_0 = 0.05$ for p_3 using TRF optimization visualized using slices. (a) shows the N_{data} representation at t_1 and t_2 , along with $N_{\text{model}}(t_1)$, the calibrated number of tumour cells at t_1 , and $N_{\text{model}}(t_2)$, the prediction made by the DI-MCRD model from cycle II at t_2 . (b) presents the errors between N_{data} and N_{model} at t_1 and t_2 . (c) visualizes the proliferation rate $k(\bar{x})$, (d) displays the shear modulus $G(\bar{x}, t_0)$ and (e), displays the drug distribution $C_{\text{drug}}(\bar{x}, t_0)$.

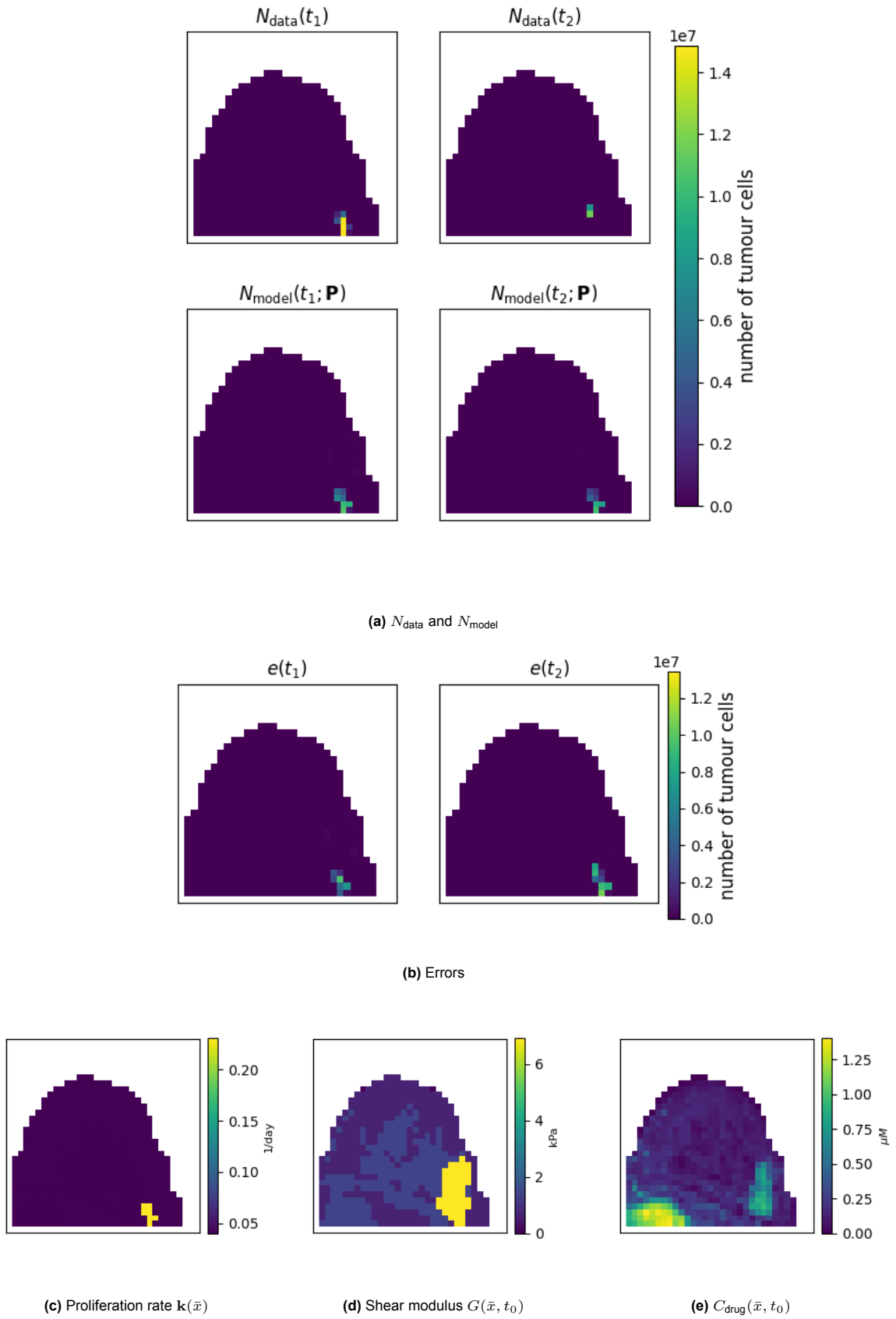


Figure C.2: Results from cycle III for p_8 with $\gamma_0 = 0.05$ using TRF optimization visualized using slices. (a) shows the N_{data} representation at t_1 and t_2 , along with $N_{\text{model}}(t_1)$, the calibrated number of tumour cells at t_1 , and $N_{\text{model}}(t_2)$, the prediction made by the DI-MCRD model from cycle II at t_2 . (b) presents the errors between N_{data} and N_{model} at t_1 and t_2 . (c) visualizes the proliferation rate $k(\bar{x})$, (d) displays the shear modulus $G(\bar{x}, t_0)$ and (e), displays the drug distribution $C_{\text{drug}}(\bar{x}, t_0)$.

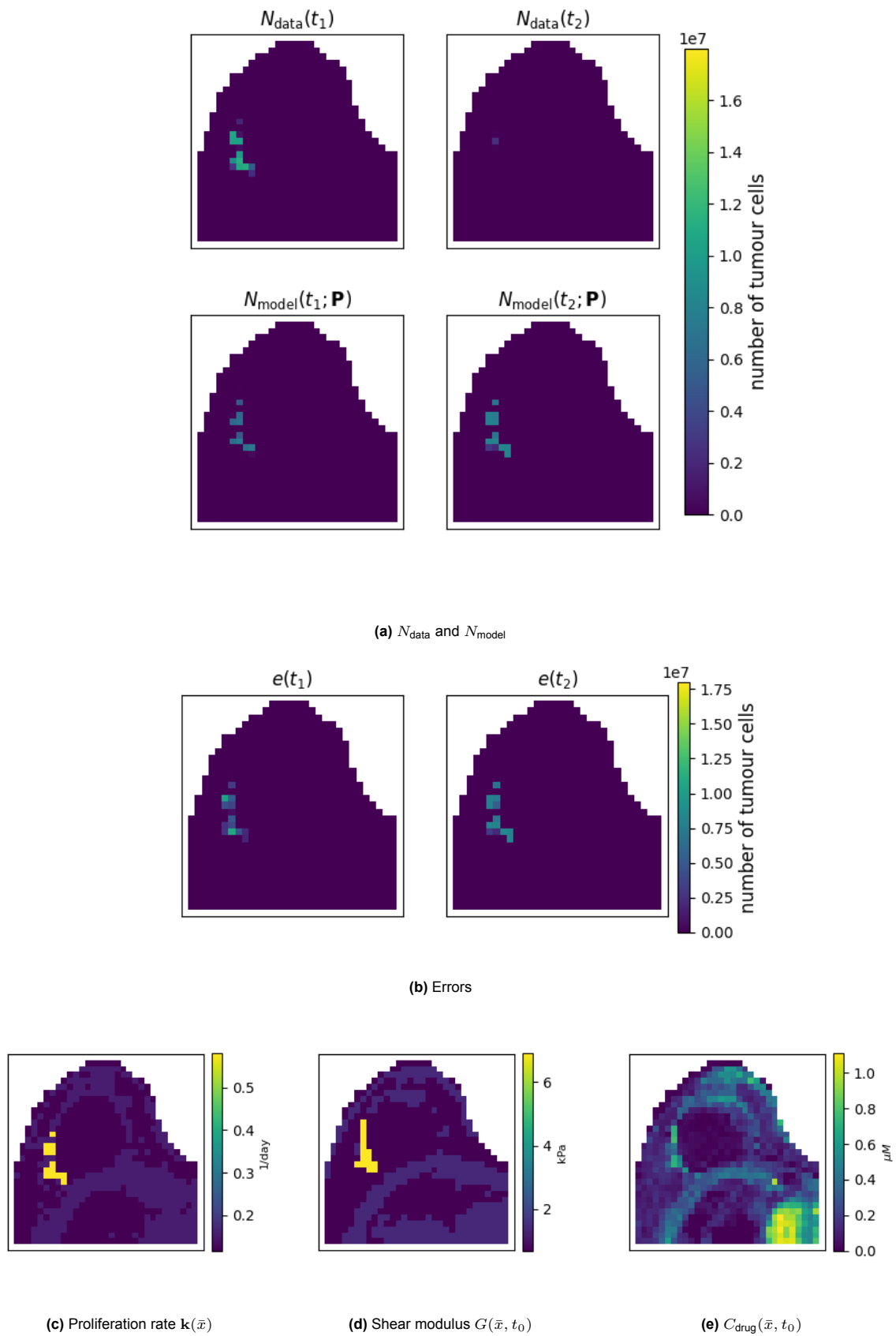


Figure C.3: Results from cycle III with $\gamma_0 = 0.05$ for p_{10} using TRF optimization visualized using slices. (a) shows the N_{data} representation at t_1 and t_2 , along with $N_{\text{model}}(t_1)$, the calibrated number of tumour cells at t_1 , and $N_{\text{model}}(t_2)$, the prediction made by the DI-MCRD model from cycle II at t_2 . (b) presents the errors between N_{data} and N_{model} at t_1 and t_2 . (c) visualizes the proliferation rate $k(\bar{x})$, and (d) displays the shear modulus $G(\bar{x}, t_0)$.

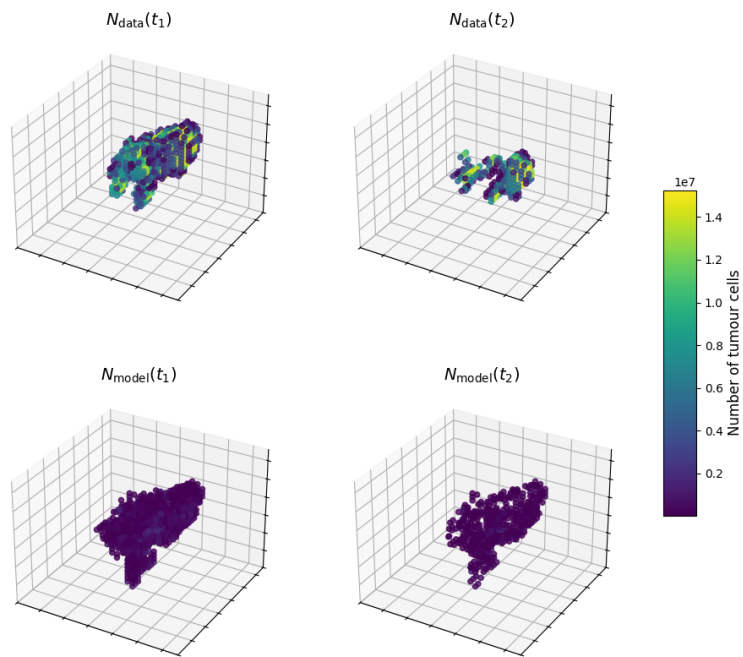
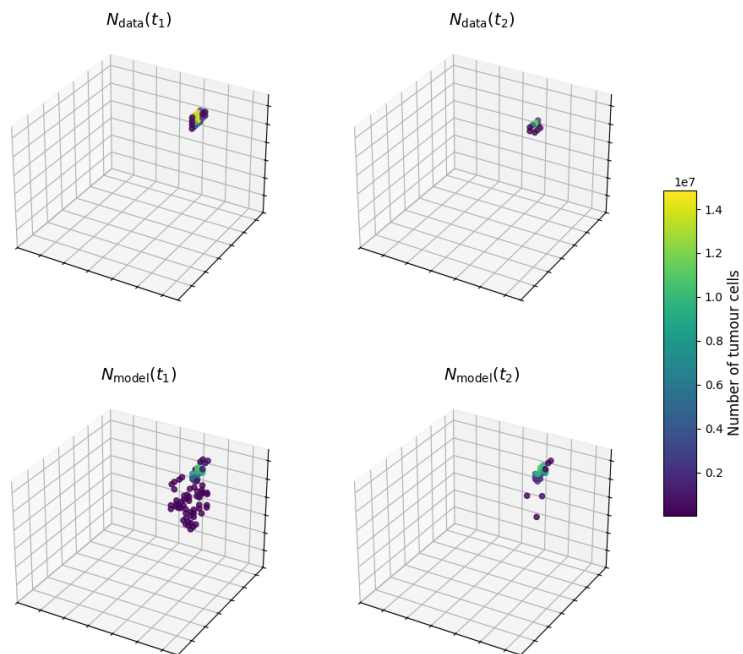
(a) p_3 (b) p_8

Figure C.4: 3D representation of the number of tumour cells for patients p_3 and p_8 obtained using the model from cycle III with $\gamma_0 = 0.05$ with TRF optimization. Within each subfigure, the top row shows the N_{data} representation at t_1 and t_2 , while the bottom row displays $N_{\text{model}}(t_1)$, the calibrated number of tumour cells at t_1 , and $N_{\text{model}}(t_2)$, the prediction made by the DI-MCRD model at t_2 . In the bottom row, all voxels with a tumour cell count less than N_{min} are removed.

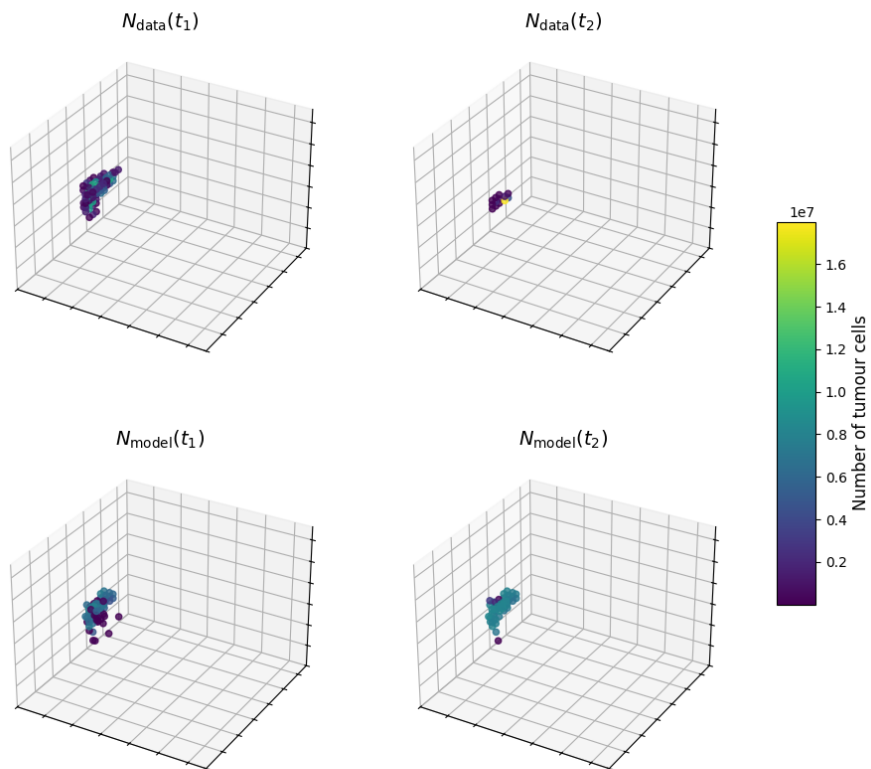


Figure C.5: 3D representation of the number of tumour cells for patient p_{10} obtained using the model from cycle III with $\gamma_0 = 0.05$ with TRF optimization. The top row shows the N_{data} representation at t_1 and t_2 , while the bottom row displays $N_{\text{model}}(t_1)$, the calibrated number of tumour cells at t_1 , and $N_{\text{model}}(t_2)$, the prediction made by the DI-MCRD model at t_2 . In the bottom row, all voxels with a tumour cell count less than N_{min} are removed.

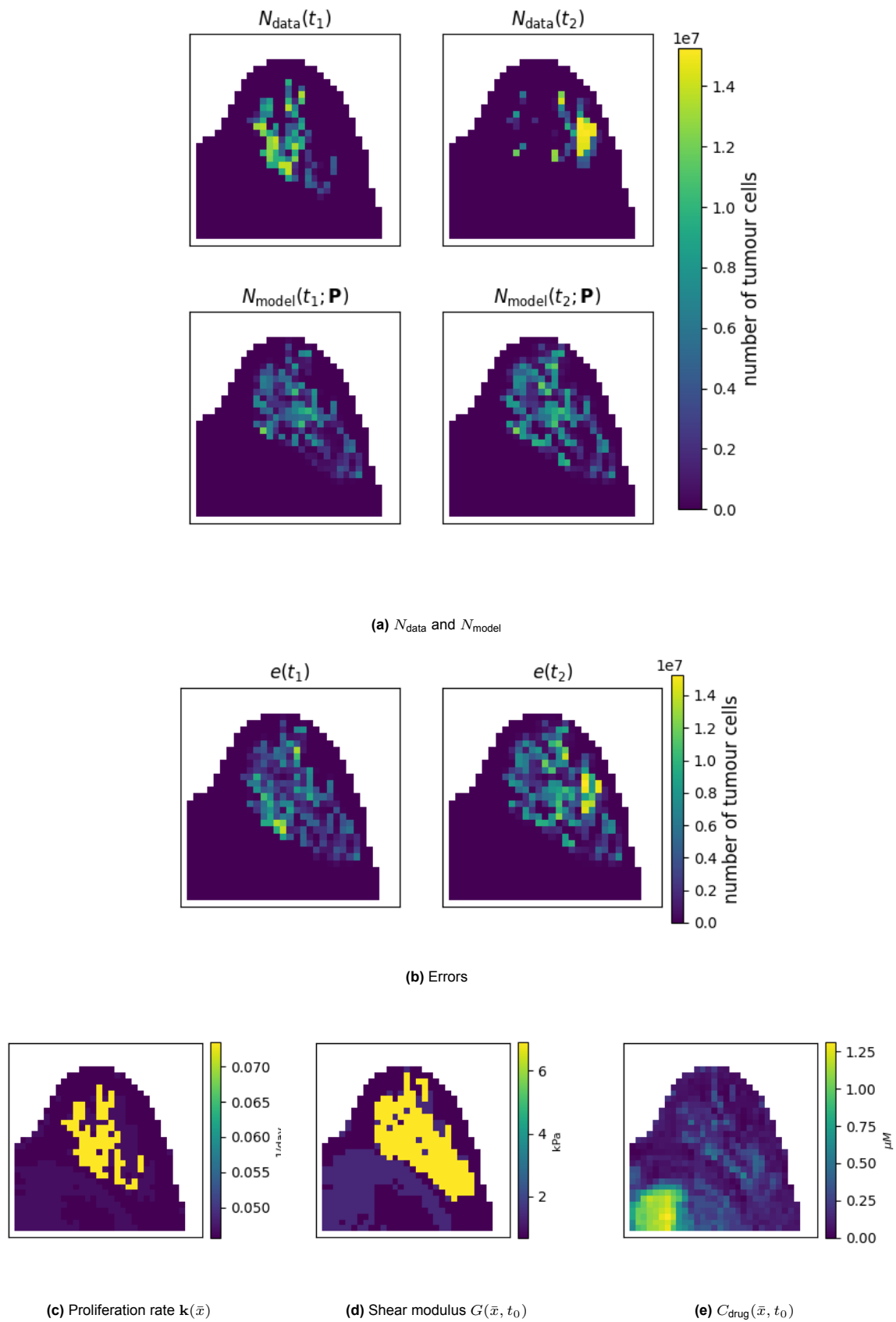


Figure C.6: Results from cycle III with $\gamma_0 = 0.005$ for p_3 using TRF optimization visualized using slices. (a) shows the N_{data} representation at t_1 and t_2 , along with $N_{\text{model}}(t_1)$, the calibrated number of tumour cells at t_1 , and $N_{\text{model}}(t_2)$, the prediction made by the DI-MCRD model from cycle II at t_2 . (b) presents the errors between N_{data} and N_{model} at t_1 and t_2 . (c) visualizes the proliferation rate $k(\bar{x})$, (d) displays the shear modulus $G(\bar{x}, t_0)$ and (e), displays the drug distribution $C_{\text{drug}}(\bar{x}, t_0)$.

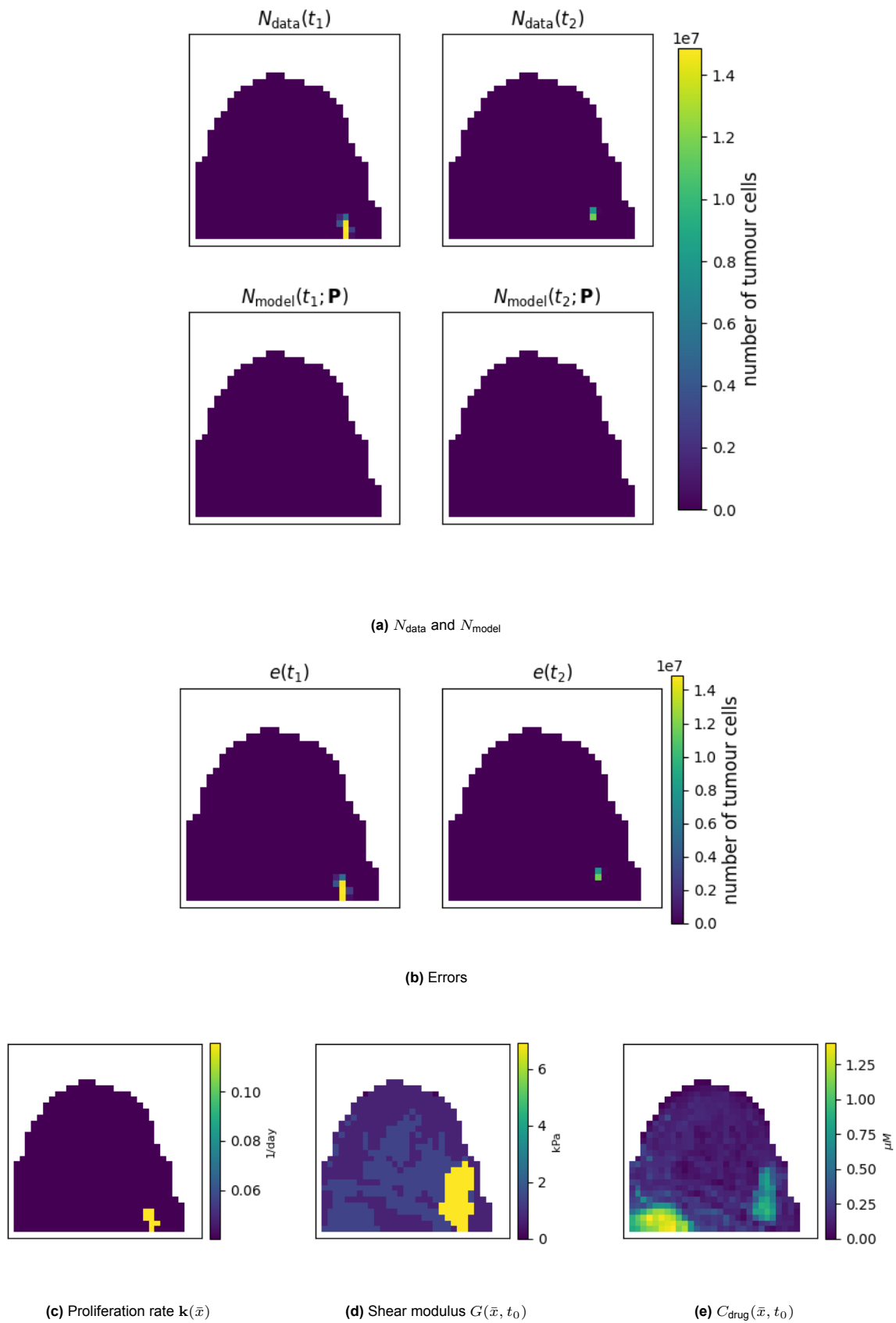
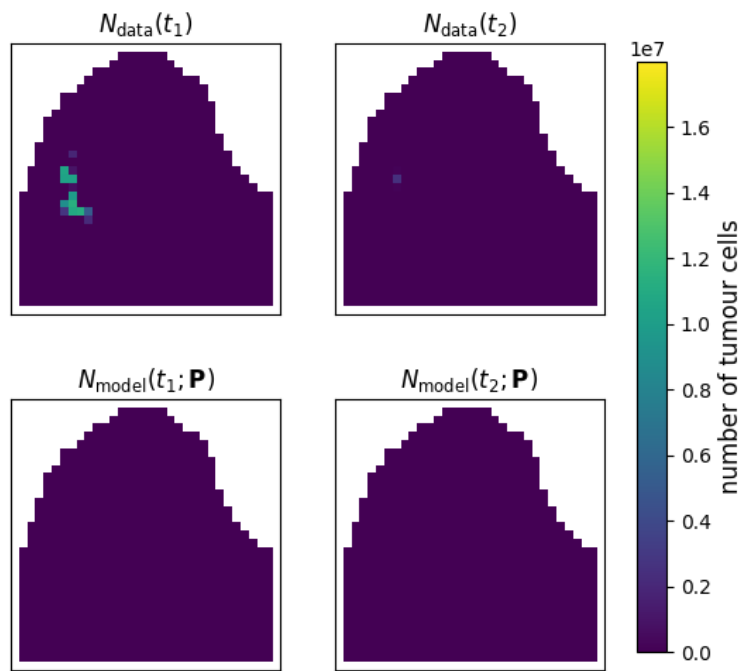
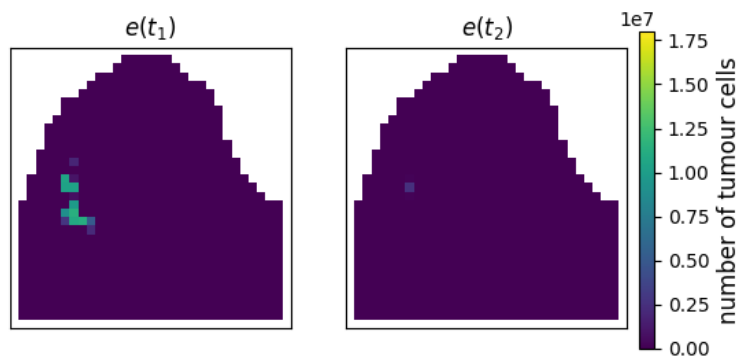


Figure C.7: Results from cycle III for p_8 with $\gamma_0 = 0.005$ using TRF optimization visualized using slices. (a) shows the N_{data} representation at t_1 and t_2 , along with $N_{\text{model}}(t_1)$, the calibrated number of tumour cells at t_1 , and $N_{\text{model}}(t_2)$, the prediction made by the DI-MCRD model from cycle II at t_2 . (b) presents the errors between N_{data} and N_{model} at t_1 and t_2 . (c) visualizes the proliferation rate $k(\bar{x})$, (d) displays the shear modulus $G(\bar{x}, t_0)$ and (e), displays the drug distribution $C_{\text{drug}}(\bar{x}, t_0)$.

(a) N_{data} and N_{model} 

(b) Errors

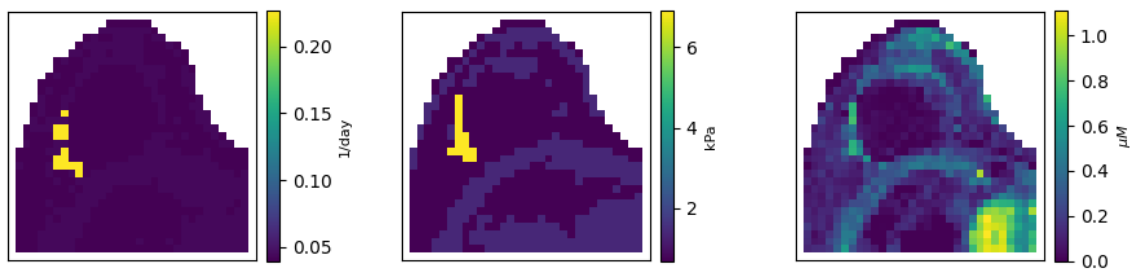
(c) Proliferation rate $k(\bar{x})$ (d) Shear modulus $G(\bar{x}, t_0)$ (e) $C_{drug}(\bar{x}, t_0)$

Figure C.8: Results from cycle III with $\gamma_0 = 0.005$ for p_{10} using TRF optimization visualized using slices. (a) shows the N_{data} representation at t_1 and t_2 , along with $N_{model}(t_1)$, the calibrated number of tumour cells at t_1 , and $N_{model}(t_2)$, the prediction made by the DI-MCRD model from cycle II at t_2 . (b) presents the errors between N_{data} and N_{model} at t_1 and t_2 . (c) visualizes the proliferation rate $k(\bar{x})$, and (d) displays the shear modulus $G(\bar{x}, t_0)$.

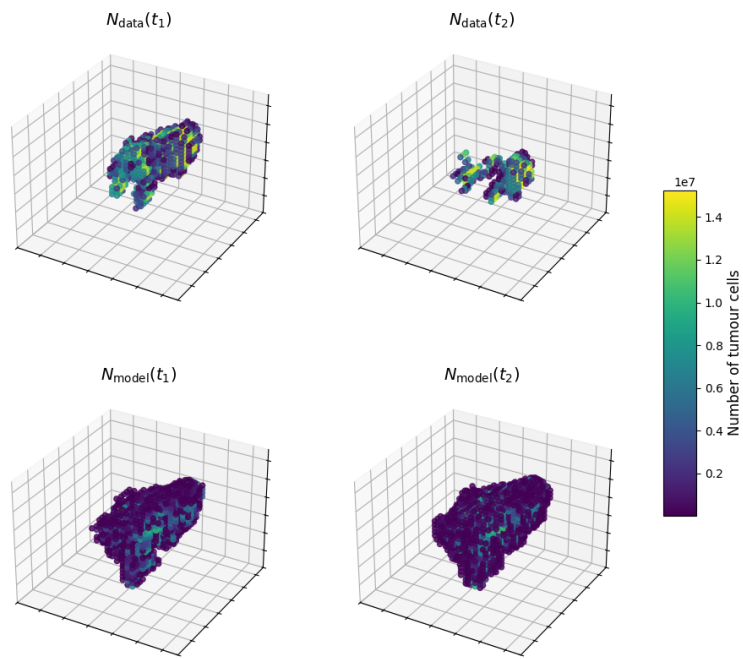
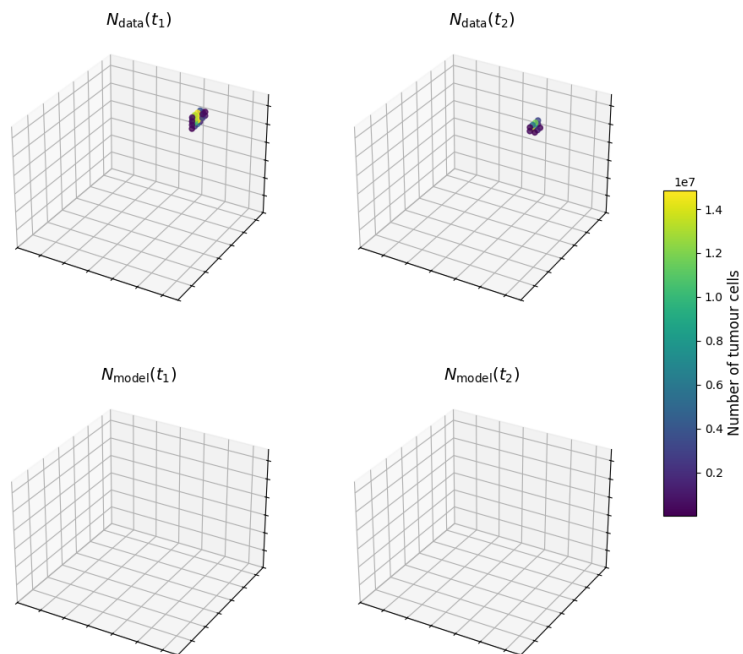
(a) p_3 (b) p_8

Figure C.9: 3D representation of the number of tumour cells for patients p_3 and p_8 obtained using the model from cycle III with $\gamma_0 = 0.005$ with TRF optimization. Within each subfigure, the top row shows the N_{data} representation at t_1 and t_2 , while the bottom row displays $N_{model}(t_1)$, the calibrated number of tumour cells at t_1 , and $N_{model}(t_2)$, the prediction made by the DI-MCRD model at t_2 . In the bottom row, all voxels with a tumour cell count less than N_{min} are removed.

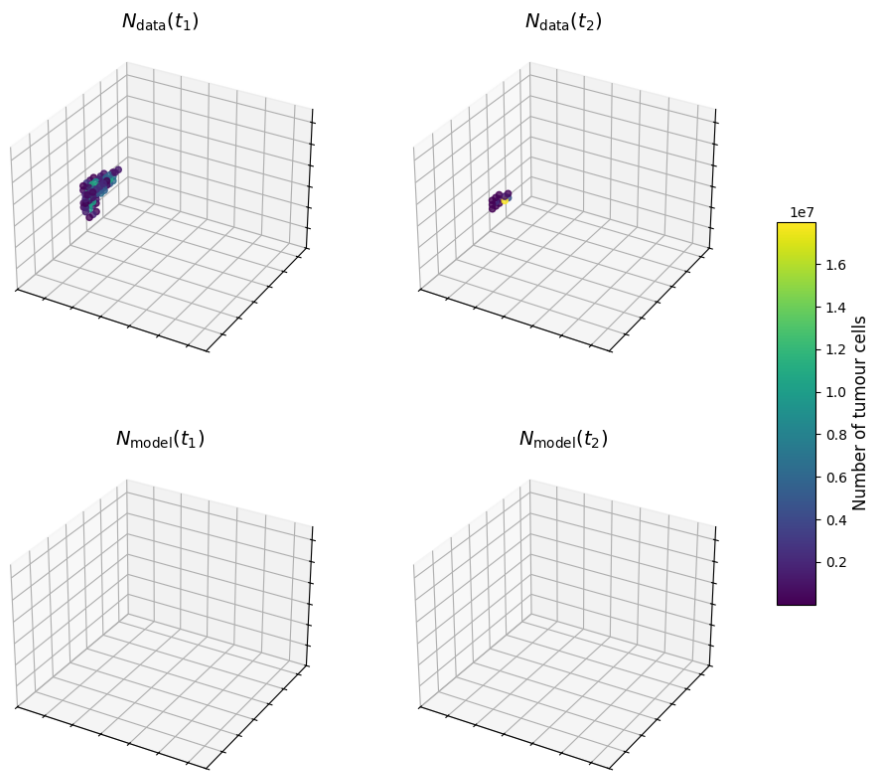
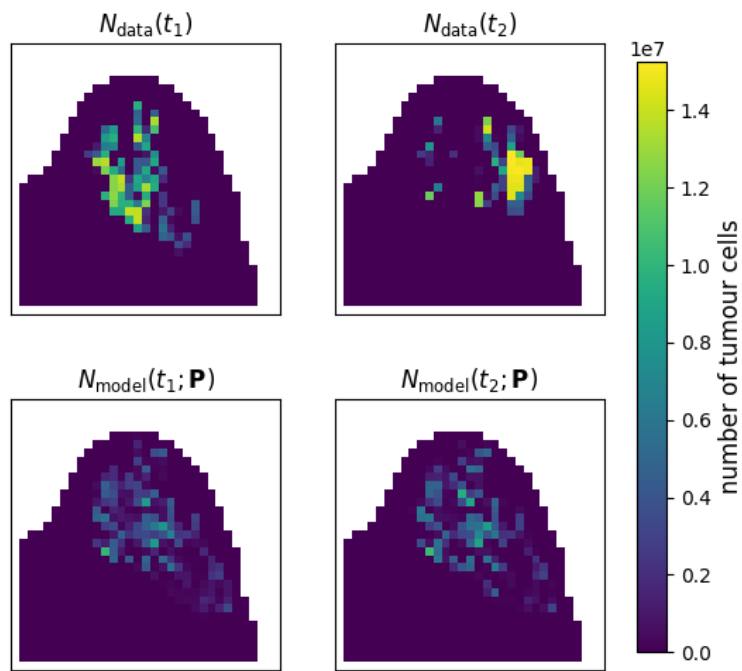
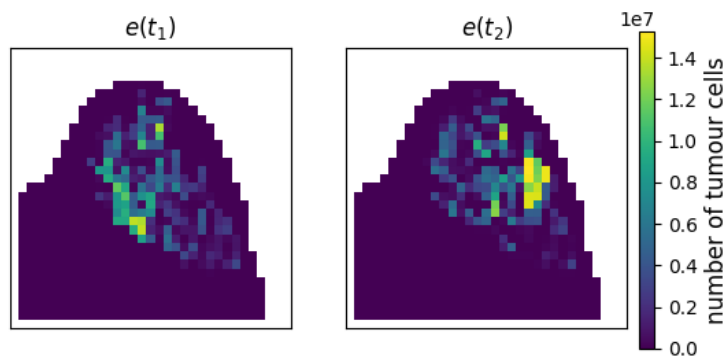


Figure C.10: 3D representation of the number of tumour cells for patient p_{10} obtained using the model from cycle III with $\gamma_0 = 0.005$ with TRF optimization. The top row shows the N_{data} representation at t_1 and t_2 , while the bottom row displays $N_{\text{model}}(t_1)$, the calibrated number of tumour cells at t_1 , and $N_{\text{model}}(t_2)$, the prediction made by the DI-MCRD model at t_2 . In the bottom row, all voxels with a tumour cell count less than N_{min} are removed.

(a) N_{data} and N_{model} 

(b) Errors

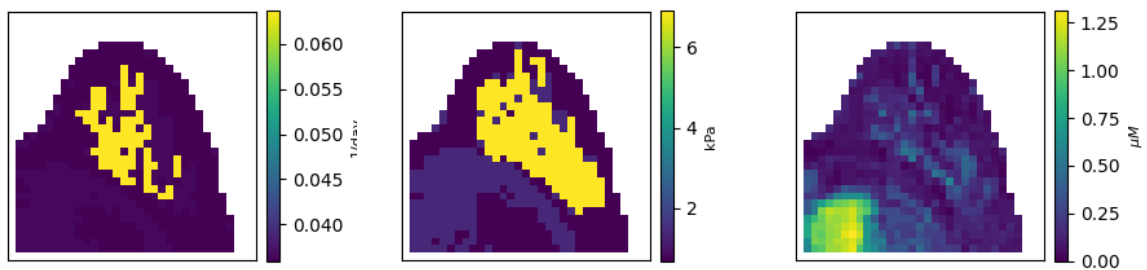
(c) Proliferation rate $k(\bar{x})$ (d) Shear modulus $G(\bar{x}, t_0)$ (e) $C_{\text{drug}}(\bar{x}, t_0)$

Figure C.11: Results from cycle III with $\gamma_0 = 0.0005$ for p_3 using TRF optimization visualized using slices. (a) shows the N_{data} representation at t_1 and t_2 , along with $N_{\text{model}}(t_1)$, the calibrated number of tumour cells at t_1 , and $N_{\text{model}}(t_2)$, the prediction made by the DI-MCRD model from cycle II at t_2 . (b) presents the errors between N_{data} and N_{model} at t_1 and t_2 . (c) visualizes the proliferation rate $k(\bar{x})$, (d) displays the shear modulus $G(\bar{x}, t_0)$ and (e), displays the drug distribution $C_{\text{drug}}(\bar{x}, t_0)$.

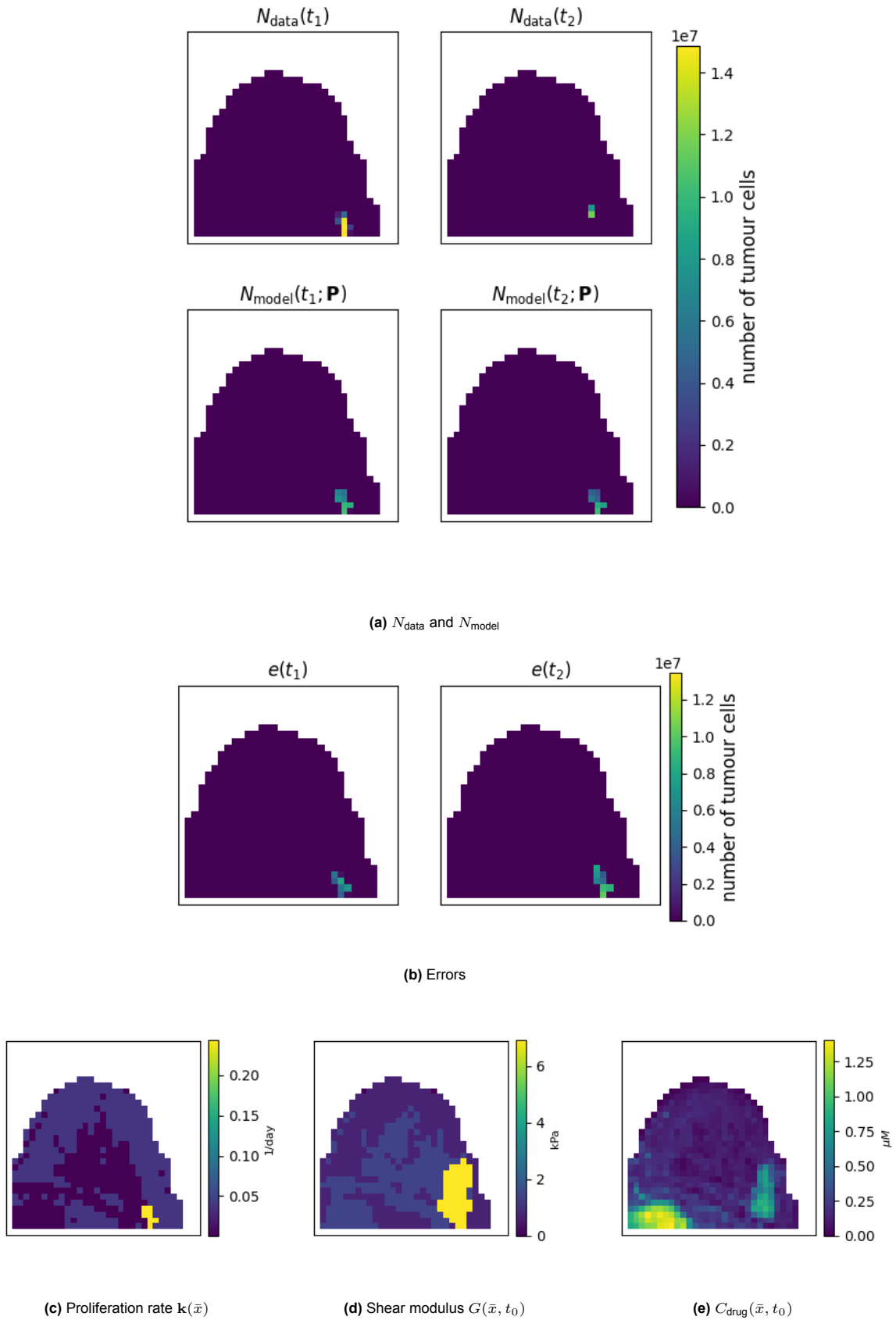


Figure C.12: Results from cycle III for p_8 with $\gamma_0 = 0.0005$ using TRF optimization visualized using slices. (a) shows the N_{data} representation at t_1 and t_2 , along with $N_{\text{model}}(t_1)$, the calibrated number of tumour cells at t_1 , and $N_{\text{model}}(t_2)$, the prediction made by the DI-MCRD model from cycle II at t_2 . (b) presents the errors between N_{data} and N_{model} at t_1 and t_2 . (c) visualizes the proliferation rate $k(\bar{x})$, (d) displays the shear modulus $G(\bar{x}, t_0)$ and (e), displays the drug distribution $C_{\text{drug}}(\bar{x}, t_0)$.

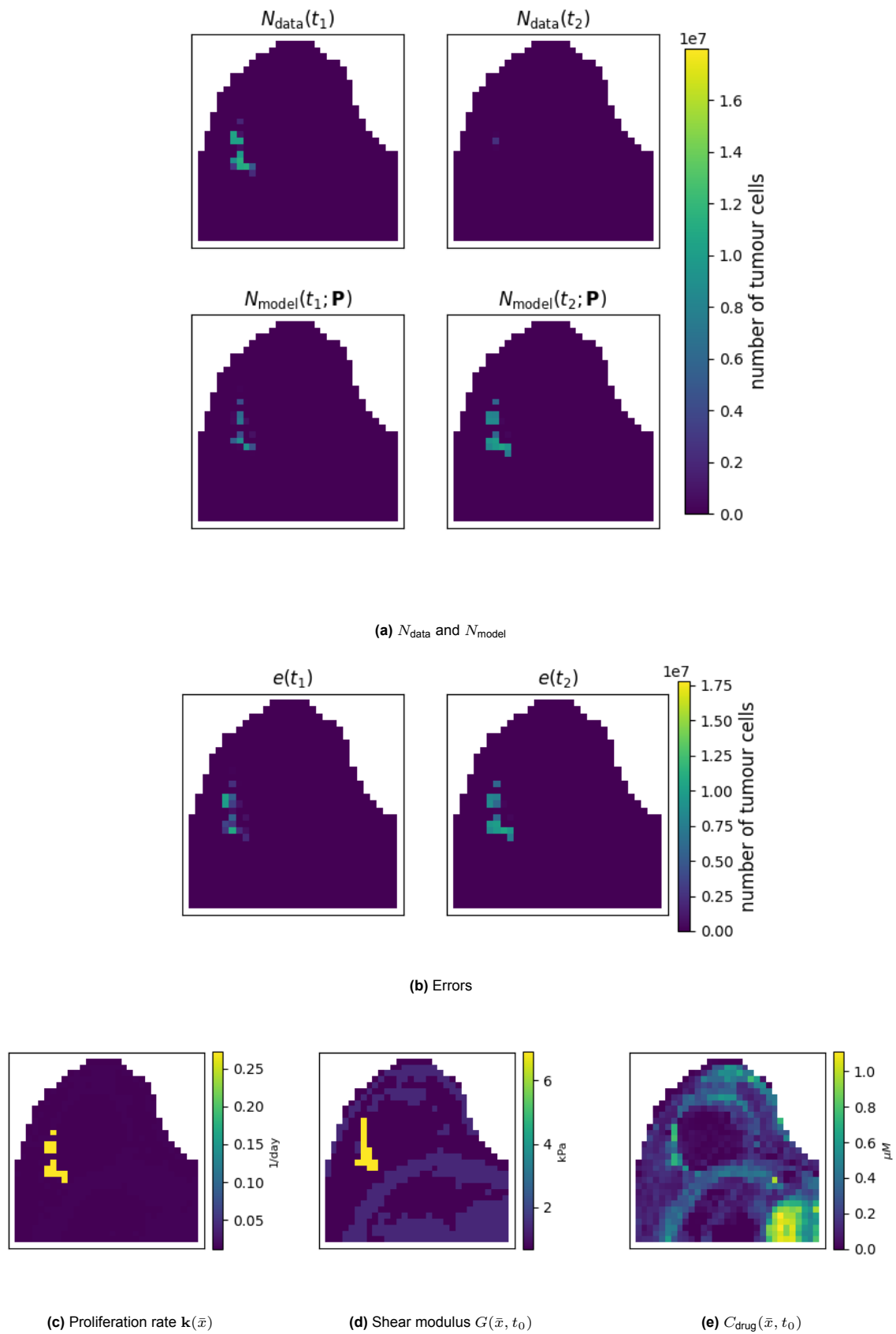


Figure C.13: Results from cycle III with $\gamma_0 = 0.0005$ for p_{10} using TRF optimization visualized using slices. (a) shows the N_{data} representation at t_1 and t_2 , along with $N_{\text{model}}(t_1)$, the calibrated number of tumour cells at t_1 , and $N_{\text{model}}(t_2)$, the prediction made by the DI-MCRD model from cycle II at t_2 . (b) presents the errors between N_{data} and N_{model} at t_1 and t_2 . (c) visualizes the proliferation rate $k(\bar{x})$, and (d) displays the shear modulus $G(\bar{x}, t_0)$.

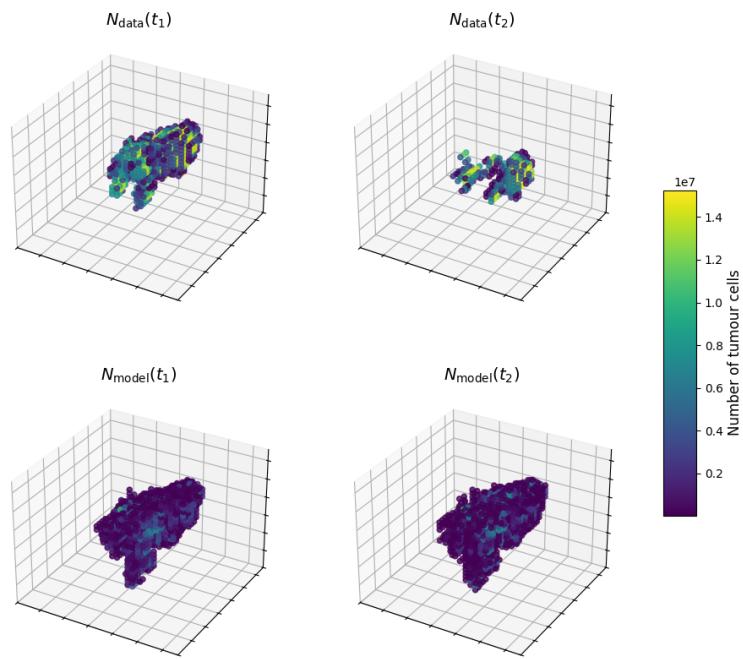
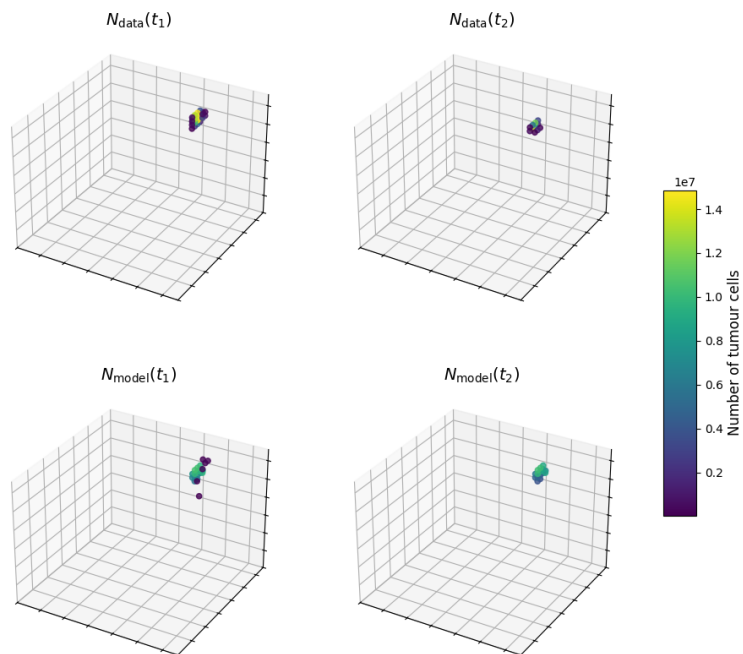
(a) p_3 (b) p_8

Figure C.14: 3D representation of the number of tumour cells for patients p_3 and p_8 obtained using the model from cycle III with $\gamma_0 = 0.0005$ with TRF optimization. Within each subfigure, the top row shows the N_{data} representation at t_1 and t_2 , while the bottom row displays $N_{\text{model}}(t_1)$, the calibrated number of tumour cells at t_1 , and $N_{\text{model}}(t_2)$, the prediction made by the DI-MCRD model at t_2 . In the bottom row, all voxels with a tumour cell count less than N_{min} are removed.

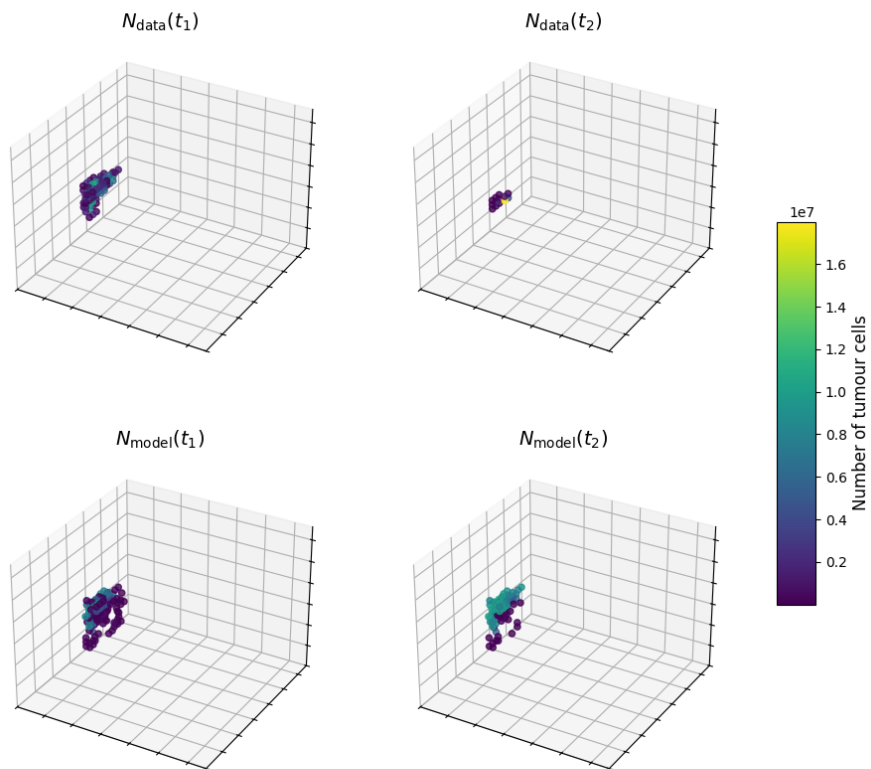


Figure C.15: 3D representation of the number of tumour cells for patient p_{10} obtained using the model from cycle III with $\gamma_0 = 0.0005$ with TRF optimization. The top row shows the N_{data} representation at t_1 and t_2 , while the bottom row displays $N_{\text{model}}(t_1)$, the calibrated number of tumour cells at t_1 , and $N_{\text{model}}(t_2)$, the prediction made by the DI-MCRD model at t_2 . In the bottom row, all voxels with a tumour cell count less than N_{min} are removed.